Scalable On-chip Platforms for Quantum Microwave-Optical Interface with Solid-State Ensembles

Thesis by
Tian Xie

In Partial Fulfillment of the Requirements for the
Degree of
Doctor of Philosophy

Caltech

CALIFORNIA INSTITUTE OF TECHNOLOGY
Pasadena, California

2025
Defended November 18th, 2024

ACKNOWLEDGEMENTS

First, I would like to thank my Ph.D. advisor, Prof. Andrei Faraon. Thank you so much for welcoming me into the group and the continuous support over years. I enjoyed the time when you randomly walked in to the lab or offices and started scientific discussions. Thanks for giving me the freedom in the lab and cleanroom to explore various ideas. Thank you for providing me opportunities for lots of conference. Thanks for the very helpful discussions inside and outside the lab.

Next, I would like to thank my thesis committee: Prof. Kerry Vahala, Prof. Oskar Painter, and Prof. Keith Schwab. I have attended classes from all of you in the early times. Thank you to Prof. Kerry Vahala for clearly teaching the laser optics and group theory, which helps my research directly. Thank you for your helpful discussion on the maser project. Thank you to Prof. Oskar Painter. I learned a lot from you on advanced quantum theory and the superconducting circuits. Thank you to Prof. Keith Schwab for letting me use the niobium sputter. Thank you for lots of discussions and help on the sputter operations and guide on the projects.

Thank you to Riku Fukumori. We worked together on the transduction project since 2022. I really appreciate your efficient working style and tireless effort. We together tried many different designs of the device. I enjoyed the time working and discussing questions with you. I'm happy to hand over the project to you.

Thank you to Prof. John Bartholomew and Dr. Jake Rochman. I worked with John when I joined the group for one year. I appreciate your mentoring and patience with me in the early stages. I learned a lot of rare-earth ion theories and experiment skills from you. Thank you for your continuous support over the years. I worked with Dr. Jake Rochman for three years. Thank you so much for developing and teaching me device design, cleanroom fabrications and niobium sputter operations. So many things would not be possible without your effort.

Thank you to Dr. Mi Lei, Dr. Andrei Ruskuc, Dr. Tianzhe Zheng, and Chunju Wu for lots of discussions inside and outside the lab during days and nights. Thank you to Dr. Jon Kindem for helping me understand the rare-earth ion energy structures and selection rules. Thank you to Dr. Ioana Craiciu for the help of telecomm optics. Thank you to Dr. Chengyi Luo for lots of discussions on the maser work. Thank you to Dr. Ding Zhong, Dr. Adrian Beckert, Will Pajak, Mccoy Lim for sharing the office with me and lots of triggered discussions. Thank you to Dr. Sophie

Hermans for scientific discussions and advice inside and outside the lab. Thank you to Jiahui Li for discussions, San Gabriel explorations, and billiards games. Thank you to Yiran Gu for fabrication discussions. Thank you to Emanuel Green for the discussions and 3D printing works. Thank you to Erin Liu for helping with organizing the group events. Thanks so much to the whole group. I enjoyed our hiking events, board game events, and meals together with you all!

Many thanks to my Caltech friends: Dr. Ruizhi Cao, Dr. Yang Zhang, Dr. Zhiquan Yuan, Dr. Lue Wu, Dr. Cheng Shen, Dr. Xiaoqiao Chen, Dr. Tianzhe Zheng, Dr. Ding Zhong, Yongzhao Guo, Duxing Hao. I enjoyed our weekly board game nights and explorations around LA areas. My scientific works would have slowed down a lot without these relaxing moments.

Many thanks to my friends from high school and undergrad: Dr. Yunshu Zhang, Bowen Feng, Yichao Hu, Haoqi Tong, and Zijie Yan. Thanks for keeping in touch with me and for a lot of games and chats. Thanks for providing me continuous help during the up and downs.

Thanks to Naj Alikhan. We've met in my early stage at Caltech. Thanks for providing continuous support over my whole Ph.D. I learned a lot every time from our discussions.

Last but not least, I would like to express my sincere gratitude to my family : my mom Ying Shen and my father Jilong Xie. I would not be here without all the support and care from you over the sea. Thanks a lot to my dear wife Yuchun Sun. Thanks for always being so supportive of me and your sincere love. Thanks for my upcoming baby Langkong Xie. You helped dad finish up the work before you are born.

ABSTRACT

Superconducting quantum circuits based on Josephson junctions are one of the most promising platforms for future quantum information processing. Tens of superconducting quantum bits have been integrated on a single chip with performances exceeding the most advanced classical computers. However, these new quantum machines operate at microwave frequencies, which have enormous thermal noise and photon loss at room temperature. This fundamentally limits the future application of this technology in distributed quantum computing and quantum networks. Conversely, optical photons are an ideal information carrier as the photon loss is extremely small in fibers and the thermal noise is negligible at room temperature. Therefore, a quantum transducer that converts between microwave and optical frequencies at the single-photon level is of great importance.

This thesis is centered on building such chip-scale interfaces with rare-earth ion (REI) doped crystals. First, we focus on developing a theoretical understanding of microwave-to-optical transducers. Based on coupled mode theories, we derive a clean theoretical result of the on-resonance transduction model. This allows us to condense the relevant material properties for transduction into a single parameter, effective $\chi^{(2)}$, describing the strength of the non-linearities provided by the rare-earth ion materials. Next, we designed, fabricated, and measured the chip under cryogenic temperatures, where percent-level efficiency and single-photon level of added noise referred to the input is achieved. To further demonstrate the unique advantage of atom-based platforms, we perform two transducer interference experiments, showing the scalability and capacity towards transducer-assisted remote entanglement of superconducting quantum bits. Lastly, with large microwave cooperativities achieved, we observe novel quantum electrodynamics enabled by controllable initialization of the excited-state spin system. By initializing the spins into spin-down and spin-up states, we observe collectively induced transparency and periodic superradiant emissions, respectively. Simulations are developed to explain the experimental results.

These results establish REI doped crystals as a highly competitive platform for microwave-optical quantum interfaces and pave the way toward remote transducer-assisted entanglement of superconducting quantum machines.

PUBLISHED CONTENT AND CONTRIBUTIONS

[1] T. Xie, R. Fukumori, J. Li, and A. Faraon. "A tunable on-chip superradiant light source from disordered quantum systems." In preparation.
T.X. designed and fabricated the device, performed the measurements, developed the simulations, processed the data, and wrote the manuscript.

[2] T. Xie, R. Fukumori, J. Li, and A. Faraon. "Scalable microwave-to-optical transducers at single photon level with spins." In: *arXiv:2407.08879* (2024). DOI: `10.48550/arXiv.2407.08879`.
T.X. designed and fabricated the device, performed the measurements, developed the simulations, processed the data, and wrote the manuscript.
T.X. and R.F. contributed equally to this work.

[3] J. Rochman, T. Xie, J. Bartholomew, K. Schwab, and A. Faraon. "Microwave-to-optical transduction with erbium ions coupled to planar photonic and superconducting resonators." In: *Nature Communications* 14.1 (2023), p. 1153. DOI: `10.1038/s41467-023-36799-0`.
T.X. contributed to the experimental setup, measurement and data analysis, and participated in writing the manuscript.
J.R. and T.X. contributed equally to this work.

[4] T. Xie, J. Rochman, J. Bartholomew, A. Ruskuc, J. Kindem, I. Craiciu, C. Thiel, R. Cone, and A. Faraon. "Characterization of Er^{3+}: YVO_4 for microwave to optical transduction." In: *Physical Review B* 104.5 (2021), p. 054111. DOI: `10.1103/PhysRevB.104.054111`.
T.X. built the experimental setup, performed the measurements, processed the data, and wrote the manuscript.

[5] J. Bartholomew, J. Rochman, T. Xie, J. Kindem, A. Ruskuc, I. Craiciu, M. Lei, and A. Faraon. "On-chip coherent microwave-to-optical transduction mediated by ytterbium in YVO_4." In: *Nature Communications* 11.1 (2020), p. 3266. DOI: `10.1038/s41467-020-16996-x`.
T.X. contributed to the measurements and data analysis, and participated in writing the manuscript.

TABLE OF CONTENTS

LIST OF ILLUSTRATIONS

LIST OF TABLES

Chapter 1

INTRODUCTION

Quantum information science, rooted in the foundational principles of quantum mechanics, computer science, and information theory, is driving a transformative shift toward building quantum machines capable of solving complex real-world problems across a broad range of fields. Quantum computing, as one of the field's most promising branches, has attracted significant scientific and financial resources over the past two decades. A notable quantum computing platform is based on superconducting circuits with Josephson junction, which has been largely explored and led to a milestone in 2019 with the demonstration of quantum supremacy – a quantum machine performing a specific task order-of-magnitude faster than most powerful classical computers. To fully harness the potential of quantum machines, it is essential to integrate superconducting systems into quantum networks, enabling connections between remote quantum systems. Within this framework, a quantum transducer capable of converting between microwave and optical fields will play an essential role in such hybrid networks, where the information can be processed at high speeds in the microwave domain and transmitted with high fidelity through optical channels. This thesis presents my research work on developing on-chip quantum transducers that convert between microwave and optical fields with solid-state spin ensembles.

This chapter will introduce the concept of quantum computing and quantum networks as the motivation of the thesis. It will be followed by a discussion of quantum transduction and the current state-of-the-art. Lastly, there will be a brief introduction of rare-earth ion doped crystals in the context of quantum information science.

1.1 Concept of quantum computing

Quantum computing, proposed by Prof. Richard Feynman in 1980s [1], leverages quantum mechanics to tackle problems beyond the reach of classical computation. The first question to consider is: why is quantum computing so powerful? A short answer is because nature itself operates according to quantum mechanical principles. A quantum system is inherently more complex than a classical one. For example, a system with 330 quantum bits (qubits) would require a vector with dimension $2^{330} \sim 10^{100}$ to fully describe its state – a number vastly exceeding the estimated number of atoms in the visible universe. The immense complexity arises from the unique properties of the qubit: each qubit can exist in a superposition state and can entangle with other qubits, creating correlations that cannot be represented classically. Mathematically, the state of a qubit can be represented as:

$$|\psi\rangle = \cos\frac{\theta}{2}\,|0\rangle + e^{i\phi}\sin\frac{\theta}{2}\,|1\rangle \tag{1.1}$$

up to a global phase factor. Here, the state $|0\rangle$ or $|1\rangle$ is an eigenstate of the measurement, meaning there is $\cos^2\frac{\theta}{2}$ probability to measure 0 or $\sin^2\frac{\theta}{2}$ probability to measure 1. With a fully entangled state from a n-qubit system, the system vector will be 2^n dimension where each parameter is a complex number, therefore leading to $2^{n+1}-2$ real parameters [1].

One prominent example of quantum computing's potential is Shor's algorithm [2] for integer factoring, which can find the prime factors of an integer in polynomial time – a vast contrast to the current most efficient classical algorithm which does it in sub-exponential time [3]. However, quantum computing is not a universal solution. Identifying problems that are classically hard but tractable with quantum resources remains an active research area.

Today, quantum processors have scaled up to hundreds of qubits on a single chip, marking a significant milestone with the demonstration of quantum supremacy [4], where a quantum processor outperformed a classical supercomputer by orders of magnitude for a specific task. While this task itself may not have immediate practical applications, its demonstration marks the potential of quantum computing and drives the community to develop larger-scale systems with reduced computational errors.

1.2 Quantum networks

To further leverage quantum advantage, one approach is to create a quantum network [5], conceptually similar to the current internet, where diverse quantum systems can be interconnected. In this framework, information station – quantum nodes need to be established at different locations, and information transfer – quantum channels needs to be developed to facilitate secure communications between the nodes. Such a network would enable quantum secure communication [6] by distributing entanglement across nodes, as well as distributed quantum computing [7] where not all qubits are housed on a single chip or in a single location. Hence, entangled states

---

[1] Each complex number needs two real parameters to describe. The total state will be normalized up to a global phase factor, leading to $2^{n+1}-2$.

can be shared among local quantum devices to collectively perform computational tasks.

On the quantum channel side, it would require high-fidelity quantum signal transmission, meaning low loss and low noise. Optical photons are a great information carrier, as photons in the telecom band through optical fibers experience little loss at room temperature [2] and optical frequencies have high enough energy to overcome room-temperature thermal noise ($\hbar\omega_{op} \gg k_b T$). Currently, people have demonstrated the distribution of entangled photon pairs across metropolitan distances [8]. On the quantum node side, finding and developing optical emitters for quantum nodes are an active research area, where defects in diamond [9, 10], trapped ions [11, 12] and rare-earth ion doped crystals [13, 14] are extensively studied for single-photon sources and entanglement generation.

Superconducting quantum circuits[15], though operating at microwave frequencies, are also attractive due to its outstanding computation capacities. Integrating these circuits into quantum nodes will be of great significance towards distributed quantum computing. However, the corresponding quantum channels for the microwave photons (typically gigahertz (GHz)) needs to be developed as the photons would suffer greatly from photon loss [3] and thermal noise ($\hbar\omega_{mw} \ll k_b T$) at room temperature. One idea to solve this issue is to build a cryogenic microwave link for microwave photon transmission, hence towards a local network. At low temperatures, photon loss can be significantly suppressed by using microwave waveguides or superconducting cables. The millikelvin temperature will at the same time suppress the thermal noise to be negligible. Pioneering works on this direction demonstrate local cryogenic quantum networks built over tens of meters and loophole-free Bell inequality has been tested to fully prove the channel capacity [16, 17]. Another solution is to build a transducer that could convert between microwave photons and optical photons. This would enable superconducting circuits with the existing developed optical networks and hence extend the capabilities of quantum computing. A schematic is shown in Fig. 1.1.

1.3 Quantum transduction

As motivated above, quantum transduction would enable superconducting qubits with an access to optical photons. On one hand, this could bring quantum informa-

---

[2] 0.2 dB/km from a fiber datasheet on Thorlabs website.

[3] 0.3 dB/m from a datasheet of a coax cable on Pasternack website, three orders of magnitude higher than an optical photon.

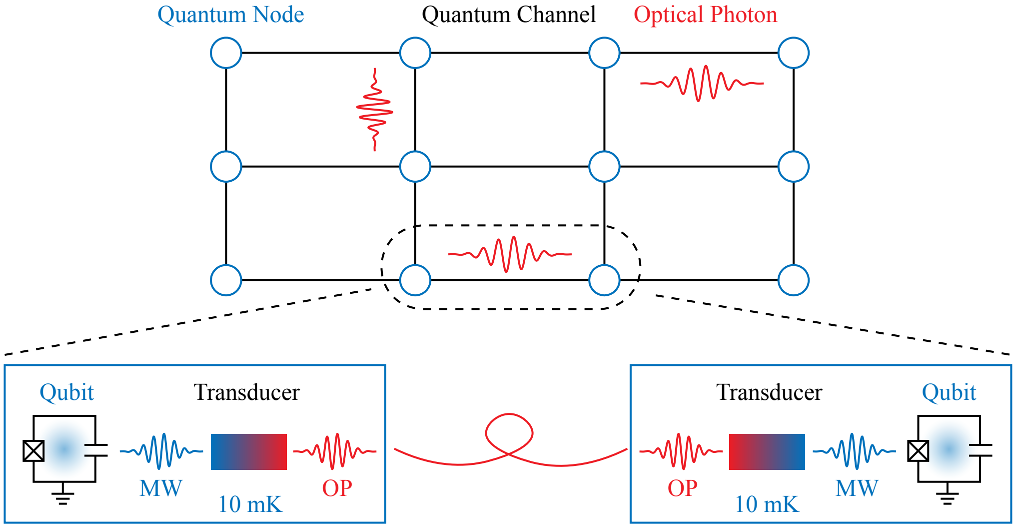

Figure 1.1: **Superconducting qubits inside optical quantum networks.** A schematic for integrate superconducting qubits with quantum transducers, where optical photons will be utilized for information transfer. MW: Microwave. OP: Optics.

tion outside the ultra-cold environment to room temperature transmission. On the other hand, by reversing the process, one would also be able to drive superconducting qubits via optical photons, which would not only reduce the complexity of bulky microwave cables inside a dilution refrigerator, but also significantly decrease the thermal load from the microwave coaxial cables.

Figure of merits

To build such transducers for useful tasks, there are a few figure-of-merits that one would like to optimize [18, 19]. I will summarize the key requirements here and discuss them one by one:

1. **Efficiency**
2. **Added noise**
3. **Bandwidth**
4. **Scalability**
5. **Synchronization**

First, efficiency is defined as $\eta = \frac{N_{out}}{N_{in}}$. It describes in photon number bases how many output photons there are compared to the number of input photons. The input and output could either be microwave or optical photons, as the transducer should be bidirectional. Unit efficiency would mean getting one optical photon per input microwave photon and vice versa. One thing worth noting is that, the efficiency at the single-photon level is relevant metric. Sometimes the efficiency listed in literature is not measured at the single-photon level. This is fine as long as the efficiency does not change with the input strength. However, if there are parasitic absorptions in the system, the efficiency would change at different input powers. This is analagous to the quality factor (Q) measurement of a superconducting resonator, lower power could give lower Q as one needs to saturate the other bathes (two-level systems, quasiparticles, etc.) first. Therefore, the efficiency at the single photon level would be quite informative as that will be the number for actual usage.

Second, the added noise describes the noise generated along the transduction process. There are different terms used here that one should be cautious of. The noise referred to the output (RTO) and the noise referred to the input (RTI) are totally different. Noise referred to the output describes the number of noisy photons measured just at the output port, whereas noise referred to the input describes the number of noisy photons at the input port, such that the process generated the noise on the output port from these RTI noise. Mathematically, the difference is

$$\begin{aligned} N_{add,RTO} &= N_{measure} \\ N_{add,RTI} &= N_{measure}/\eta \quad \Rightarrow N_{add,RTI} \cdot \eta = N_{measure} \end{aligned} \tag{1.2}$$

where $N_{measure}$ describes the measured noise from any detection method and η describes the transduction efficiency. As shown in the equation, by dividing the efficiency from the total measured noise, one would get effectively the noise on the input side. This is important, as when performing the actual tasks, one would like to convert a single microwave photon to a single optical photon (for example). Therefore, added noise referred to the input will tell you what the signal-to-noise ratio is in this case, in terms of effectively how many noisy input microwave photons exist at the input port when sending in the single coherent microwave photon. Therefore, $N_{add,RIT}$ would be the characteristic that one should care about. Specifically, considering a microwave-to-optical transduction case, a single microwave photon will have a temporal width when sending into the device. Assume a single optical photon detector is used to measure the transduced optical photon. In this case, the efficiency and added noise will be

$$\begin{aligned} \eta &= (R_{on} - R_{off})\delta t/1 = (R_{on} - R_{off})\delta t \\ N_{add,RTI} &= \frac{R_{off}\delta t}{\eta} = \frac{R_{off}}{R_{on} - R_{off}} \end{aligned} \tag{1.3}$$

where $R_{on,off}$ describes the photon count rate on the single photon detector with microwave photon input turned on or off. Therefore, by sending in a single microwave photon into the transducer, one would learn the system efficiency at the single photon level and the added noise referred to the input by analyzing the signal strength and the signal-to-noise ratio. One thing worth mentioning is that, this is usually not trivial to implement. On one side, there is always some noise flux on the detection side (e.g., dark counts) that might not related to the transducer by itself. If the efficiency is too low, then one could get a large number of $N_{add,RTI}$ by dividing a small efficiency. This is not necessarily true to represent the transducer performance, as it is originated from the detection method. Therefore, one needs to carefully calibrate the measured noise source to confirm this is truly coming from the transducer, but not other components. On the other side, an optical pump is usually required to perform transduction (e.g., to bridge the energy difference between microwave and optics). The optical pump will usually be in the same spatial and temporal mode as the transduced optical photons. To only measure the transduced optical photons, one needs to have an ultra-strong and narrow optical filter system, to attenuate the optical pump that is typically a few GHz away by $\sim 80 - 140$ dB, depending on the system efficiency. For one example of using such an optical filter, I recommend this thesis [20] for detailed descriptions.

A natural question here is: what is the requirement for the noise? As mentioned above, noise referred to the input describes the signal-to-noise ratio of a single input microwave photon. Therefore, for any quantum operation, one wants $N_{add,RTI}$ to be at the very least smaller than 1, such that the desired signal is higher than the noisy part. In other words, this serves as a prerequisite for transduction fidelity to be higher than 50%. For actual quantum error-corrected computational tasks, this should be below the error threshold (e.g., $\sim 0.1\%$ for surface code [21]).

Third, the bandwidth describes how narrow the temporal width of an input can be such that the transducer can capture it and convert it to the other frequency domain without losing the information (e.g., a lower efficiency). In the frequency domain, these two are related as:

$$BW = \Delta f = \frac{1}{\Delta t} \tag{1.4}$$

where higher bandwidth would allow a shorter pulse to be converted. Higher bandwidth is desirable, as it would allow faster operations compared to the qubit coherence time. Another advantage of higher bandwidth is that it could also help overcome the detection system noise. A shorter detection window effectively lowers the noisy photon getting detected and hence lowers the systematic noise. Lastly, a higher bandwidth would also allow a shorter optical pump pulse to appear on the transducer, which will lower the noise intrinsically as less heating would be generated. With less heating, one would be able to operate the system with a higher repetition rate, hence increasing the entanglement generation rate from the transducers.

Fourth, the scalability of the transducer reflects its potential for large-scale production and integration with superconducting qubit platforms. As the cooling power of a dilution refrigerator is limited, a bulky transducer setup would consume more cooling power and hence increase the fridge temperature. An ideal case would be an on-chip transducer that could be fabricated with the qubit on a single chip. But this inevitably brings optical photons directly to qubits, which could have adverse effects on the qubit performance. This is still an active research area on how to better shield the qubit from the optical photons. But in general, an on-chip transducer is preferred due to its small footprint and corresponding less required cooling power.

Fifth, the synchronization describes whether transducers from multiple productions would operate at the same frequency. The ability to convert between microwave and optical fields is important, but if the conversion happens at different frequencies for each transducer, it posts anther frequency-matching problem to solve before actual tasks for entanglement generation. One typical entanglement generation protocol is based on the heralding of a single photon. This relies on the photon indistinguishability between the two optical paths such that the information will coherently interfere with each other to establish entanglement. For lots of the current transduction platforms, which will be discussed later, the operation frequencies are determined from design and fabrication. Even for the same design and fabrication in different rounds, the resultant frequency will be different due to fabrication disorder. One solution is to post-tune the optical part of the device to manually satisfy the frequency matching condition. This has been demonstrated at least for one of the platforms [22] but it would complicate the fabrication process by another step and hence lower the yield and potentially lower the quality factors. Similarly, one could also post-shift the optical photon frequency via another quantum frequency conversion step between optical ranges. This is achievable via commercial products. Depending on the technical efforts, this may or may not be a bottleneck that finally limits the transducer performance (e.g., a 50% efficiency between optical ranges will put a ceiling of the total transducer efficiency to 50%). In addition to the post-tuning, a passive design can be considered as well. For atom-based systems, as the transduction process are based on atomic transitions, the operation frequencies are naturally lock the atomic transitions and hence the same for different transducers. This solves the problem fundamentally. But one thing that needs to be mentioned is that this transfers the frequency-matching problem to the fabrication side. Specifically, as the systems are operated with atoms, the cavities used for enhancing the light-matter interactions need to be on-resonance with the atom. This sets requirements on the fabrication side, where the frequency of each cavities needs to be either fabricated relatively precisely or actively tunable to make it on-resonance.

There are other aspects that need to be considered as well. Some of them are obvious that is not covered above. For example, the transduction process needs to be coherent to preserve the quantum information. Combining a single microwave photon detector (this by itself is also non-trivial) with a single optical photon source is not coherent, and hence losing the point of doing this. The transducer needs to operate in cryogenic environments, and at millikelvin temperatures for single-digit GHz transducers. As qubits are operated there and microwave photons are preserved in this low temperature environment, the conversion process should also happen in the same circumstance. Some platforms works at higher temperatures (e.g., room temperature [23]) needs further investigation to move into the cryogenic environment for actual usage.

As discussed above, there are lots of aspects to consider for an ideal quantum transducer, and hence there is not a clear choice for the 'best' platform, motivating the transduction community to explore different systems and different designs. For readers who are interested in further details, I recommend these two review papers [18, 19].

Transduction platforms

To achieve the conversion between microwave fields and optical fields, one needs to engineer a coupling directly or effectively between them. A general transducer can be understood as a two port device, as shown in Fig. 1.2. Specifically, the

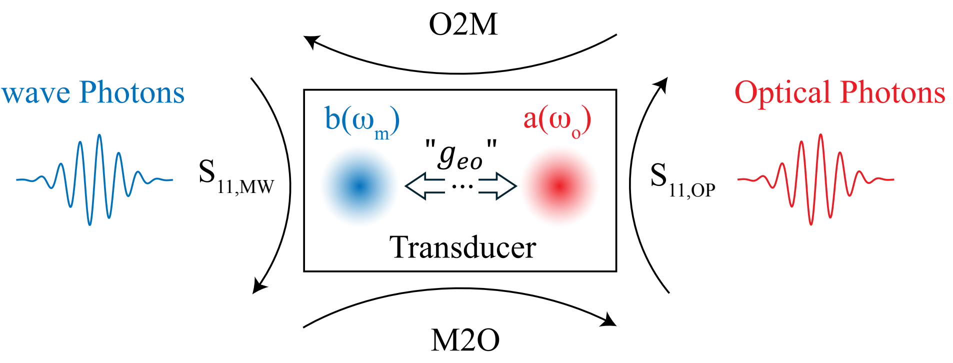

Figure 1.2: **Schematic for a general transducer between microwave and optical fields.** A transducer is generally a two-port device with four scattering parameters. The optical/microwave field interacts with mode a/b at ω_o/ω_μ frequency. The coupling between the two fields can be direct or via intermediate stages, creating a coupling g_{eo} directly or effectively. M2O: Microwave-to-optical transduction. O2M: Optical-to-microwave transduction.

Hamiltonian should have a beam-splitter term as:

$$\mathcal{H}_{eff} = \hbar g_{eo} a^\dagger b + h.c. \tag{1.5}$$

where g_{eo} describes the coupling strength between the two fields, a and b are the annihilation operators for optical and microwave fields. Various platforms have been theoretically proposed and experimentally studied. Here, I will go through the three most studied platforms and discuss the principles one by one:

1. **Electro-optic system**
2. **Mechanics-based system**
3. **Atom-based system**

First, the electro-optic system utilizes the nonlinearity of the material to directly couple microwave with optics. For example, with the Pockels effect where the refractive index of a material is linearly dependent with the applied voltage, one would apply an AC voltage at GHz frequency. This will imprint a rapid-phase shift on the input optical phase and generate sidebands. Hence, a commercial electro-optical modulator is technically a microwave-to-optical transducer. But the efficiency is quite low as the V_π is typically high. Since it utilizes the direct coupling between the microwave and optical system, the physics is relatively straightforward to understand. There are groups working on this platform [24–27]. As of writing the best on-chip result is [25], where 15% internal efficiency is measured, but added noise is not calibrated yet. By moving the system from an on-chip to a bulk setup, 8.7 % efficiency with 0.16 added noise has been achieved [24]. Further by using the spontaneous parametric down conversion (SPDC) process, microwave-optical entanglement has been demonstrated [28] via this platform.

Second, the mechanics-based system utilizes phonon as an intermediate stage between microwave and optics to realize the coupling between the fields. There are at least two different categories: piezo-electricity and electro-mechanics. By a piezo-electric material, the microwave photons can be directly coupled to resonant phonons. Next, the phonon could be converted to optical photons via opto-mechanical coupling due to radiation pressure [29]. For example, if readers are familiar with a piezoelectric element (piezo), one could think about a piezo attached to an optical cavity. Typically this is one way to realize a scannable Fabry-Perot cavity. Assuming the piezo can operate at high enough frequencies, one can apply a microwave signal to the piezo, effectively modulating the cavity length, and hence generating a sideband of the optical pump into the cavity. Hence, an acousto-optical modulator is also a microwave to optical transducer via acoustics. Systems with this piezo-electric platform have demonstrated results with percent-level efficiencies and single-photon level noise [30–34]. One ground-breaking experiment with this platform presented direct coupling of a superconducting qubit to a piezo-mechanical transducer, where the Rabi flopping of the qubit was detected via single optical photon detectors [30]. There are also experiments using SPDC process, where microwave and optical entangled photon pairs have been measured [35] and time-bin qubits based on two sequential SPDC photon pairs has been studied [36].

Another category here is based on electro-mechanical coupling. The idea behind is a vibrating capacitor, where electrical signals can be coupled to phonons via this element. A phonon converted to a photon can again be realized via opto-mechanical coupling. A bulk setup has been achieved first by this group [37, 38], where high efficiency up to $\sim$ 50% was measured. However, since the membrane used operates at MHz frequency, the thermal occupancy is high even at low temperatures. Therefore, feed-forward protocols were utilized in this system to demonstrate down to 3 noisy photons referred to the input. This system has also been coupled to a superconduting qubit [39] via a modular approach. By separating the qubit and the transducer setup, optical heating of the qubit is negligible, hence qubit operations could be done together with transduction. An on-chip version of this type of interaction has recently been realized in [40, 41]. By designing everything out of silicon, they avoid the piezo-electric material via heterogeneous chip architecture, potentially towards ultra-coherent mechanical quality factors. This device measured quantum-level noise with percent-level efficiency, as well as achieving 20% with higher noise. The advantage of this type of system is that the mechanical system can be ground-state cooled. Due to the strong coupling with microwave circuits, one can cool the mechanical mode (typically the dominant thermal bath) with the cold microwave bath. Utilizing this technique, the paper shows the percent-level efficiency with quantum-level noise under CW operation, improving the repetition rate to being limited by the bandwidth of the system instead of the repetition rates.

Lastly, the atom-based system, similar to the mechanics-based system, achieves an effective coupling via atomic couplings. Since atoms or ions can have both microwave and optical transitions, each atom can effectively serve as a non-linearity. Therefore, by using an ensemble of atoms or ions, typically ranging from thousands to billions, the effective non-linearity will go up due to the collective enhancement from the ensemble. Here, Rydberg atoms [23, 42–44] and solid-state defects [45–47] have been studied for the transduction purposes. For Rydberg atoms, since atoms are trapped and typically coupled to 3D cavities, the setup would be relatively bulky and multiple lasers are required to operate the system. With strong dipole moments and coherent atomic states, $50-80\%$ efficiency has been achieved at 4K or room temperature. The room temperature experiment needs further investigation towards cold temperature for coverting a real quantum microwave signal. The 4K realization requires qubits operating at millimeter-wave (hundreds of GHz), which is an active research area [48].

For solid-state defect systems, most of the research efforts are in rare-earth ion (REI) doped crystals. The reason is that REIs have narrow inhomogeneities in both the optical and microwave domains, with stable and coherent transitions at high concentrations, compared to other solid-state systems such as nitrogen-vacancy centers in diamond. Similar to the various platforms discussed above, bulk and on-chip setups have been studied here as well. For bulk setups, people have used cylindrical REI-doped crystals to fit inside a microwave loop-gap cavity and an optical Fabry-Perot cavity. Efficiency up to 10^{-5} has been demonstrated but the added noise is yet to be calibrated [45]. The limitation for the bulk setup is the drive Rabi frequency is small, as the optical beam radius is large and REIs typically have weak 4f-4f optical transitions. Sending higher optical pump power generates a trade-off between atomic cooperativity and material heating. For on-chip platforms, the

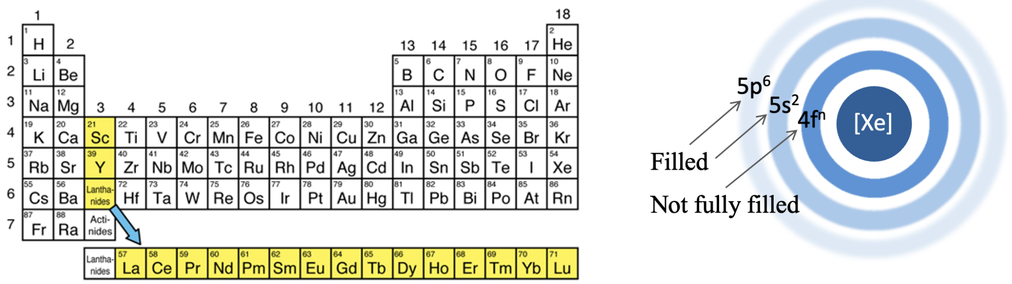

Figure 1.3: **Rare-earth elements in the periodic table and their electronic structures.** Rare-earth ions have transitions have a partially filled 4f electronic shell which is shielded by the outer 5s and 5p orbits. This results in weakly allowed, but highly coherent intra-4f shell transitions.

chip utilizes superconducting microwave resonators and photonic crystal cavities. The photonic modes can either be directly inside the material from a suspended structure, or evanescently coupled from a hybrid system [49–52]. The highest efficiency that has been achieved is 10^{-7} [46, 53]. However the added noise could not be measured accurately due to the low efficiency. The shortcomings and other details of previous on-chip REI-based demonstrations will be discussed in Chapter 4.

As discussed in the figure of merits section, the uniqueness of atom-based system is the natural frequency matching. This is an important aspect for entanglement generation between remote superconducting qubits. Also, with enough concentrations, REI systems would present an ultra-strong effective non-linearity for the transduction process (more than 4 orders of magnitude higher than $LiNbO_3$ [54]). Meanwhile, since REIs are already doped inside the crystal, one can fabricate any structures on the chip with a small footprint, advantageous for scalability. Lastly, REI-based quantum technologies have flourished across multiple areas which will be discussed in the next section. These reasons make REIs a promising and competitive platform among others. Further details will be discussed in Chapter 3 for theory and Chapter 6 for measurements.

1.4 Rare-earth ions platform

The rare-earth elements are highlighted in Fig. 1.3. After the atoms get ionized to 3+ charge, the electronic structures are shown on the right of Fig. 1.3. The optical transitions are between 4f to 4f orbitals. This is abnormal as typically this is electric-dipole forbidden. However, by doping the rare-earth ions in crystals, the surrounding crystal environment, specifically the crystal field, will Stark shift the energy levels as well as mix different orbitals together [55]. One example is Er:YVO$_4$, where theoretical calculations have shown how the different orbitals are mixed into different energy levels [56]. This level mixing allows the 4f to 4f transition to be dipole allowed, even though the represented angular momentum of the energy levels is unchanged ($\Delta L = 0$). This gives unique advantages to the REI system. Since the transitions are 4f to 4f, the filled electron shells outside 4f (5s and 5p) will shield the inner transitions, such that the 4f electronic states are highly coherent and the 4f to 4f transitions are highly radiative (less phonon coupling). However, this also comes with other effects. One is the weak transition dipole moments which is based on the level mixture. The other is that atomic properties such as transition frequency, dipole moments, and inhomogeneity can vary from crystal to crystal even with the same dopants, unlike in free atoms or ions.

There have been lots of studies on REI-doped materials, and a general finding is that REIs have narrow inhomogeneities in both the optical and microwave domains [57]. For example, erbium-doped crystals have typically around hundreds of MHz optical inhomogeneities (180 MHz for Er:YVO$_4$, 500 MHz for Er:YSO) and tens of MHz spin inhomogeneities (60 MHz for Er:YVO$_4$, 10 MHz for Er:YSO) [58–60]. Another finding is that REIs typically have long coherence times. A six-hour coherence time has been achieved with ^{151}Eu^{3+}:Y$_2$SiO$_5$ at a zero first-order Zeeman (ZEFOZ) point of a hyperfine transition [61]. A 30 ms spin coherence time has been measured with ^{171}Yb^{3+}:YVO$_4$ under a Carr-Purcell-Meiboom-Gill (CPMG) sequence [13]. Meanwhile, since REIs are doped in crystals, one can do micro- and nano-fabrication with it [49, 62–64]. This gives the REIs an access to small mode volume on-chip cavities, necessary for Purcell enhancement [13] and can lead to many-body physics studies [65]. With these on-chip technologies, REI-based quantum technologies have flourished across multiple areas including single photon sources [14], quantum memories [66, 67], and entanglement generation [68]. A necessary demand arises for a seamless link between various REI-based technologies and other leading microwave quantum platforms.

1.5 Outline of the thesis

With the above introduction covering the concept of quantum computing, quantum networks, quantum transduction, and REI systems, this thesis is focused on building an on-chip microwave-to-optical transducer at single photon level with REIs.

Chapter 2 will discuss the energy levels of rare-earth ion doped crystals. One would get the LSJ levels from the electronic structure and apply group theory to calculate the selection rules between different levels. Specific examples will be discussed.

Chapter 3 will focus on the theory of transduction using REIs. Specifically, an on-resonance regime with simple and intuitive equations will be derived to understand the system performance. From there, an effective $\chi^{(2)}$ non-linearity will be extracted to fully represent the REI material properties in terms of transduction. Meanwhile, an adiabatic model for off-resonance regime will be discussed.

Chapter 4 will go through the previous REI-based on-chip transducers. The design and measurement results for each individual demonstration are discussed and conclusions are drawn for future improvements.

Chapter 5 will introduce the latest design, by learning from the shortcomings of previous designs. The microwave and optical part will be discussed and the fabrication for each part will be described as well.

Chapter 6 describes all the experimental work for measuring the transducer. After going through the experimental setup, the efficiency and added noise will be measured. Detailed calibrations are performed in both microwave and optical detection methods. With these performance, photon interference between two independent transducers are measured. Finally, summaries and future improvements are discussed.

Chapter 7 explores another aspect of the transducer – what if a blue sideband is sent to the device rather than a red sideband. Novel physical phenomena will be discussed such as collectively-induced transparency and periodic synchronized pulsing in both microwave and optical domains.

Chapter 8 will summarize the thesis and point toward future directions with REI platforms for quantum technologies.

Chapter 2

RARE-EARTH IONS DOPED IN CRYSTALS

Here I will talk about the electronic configuration and derive the LSJ levels using Hund's rule. Next, I will cover how to use group theory to do the relevant calculations in REI crystals. Specifically, how to label an energy level with an irreducible representation and the selection rules. After a general methodology discussion, I will give two examples, Er^{3+}:YVO_4 and $^{171}Yb^{3+}$:YVO_4. Both of them have D_{2d} symmetry. The zero-nuclear spin erbium will be calculated and the selection rules under Zeeman splitting will be discussed via crystal field quantum number. ^{171}Yb has a nuclear spin 1/2, so hyperfine interactions need to be considered. I will cover both the group theory approach of the electron-nuclear hybridization and an analytical result from solving the $I \cdot A \cdot S$ Hamiltonian. This tutorial helps one understand the atomic energy levels of REI-doped crystals and the corresponding selection rules, setting up for the system control in the later experimental sections.

2.1 Electronic configuration

Here I will discuss the electronic structure and the LSJ quantum number of a rare-earth ion using Hund's rules. First, the electron configuration of rare earth elements are generally:

$$RE_N : [Xe]4f^N 6s^2 \tag{2.1}$$

where the 4f electrons will accumulate up to 14 along the Lanthanide series. When doped into solids, the rare-earth ion will usually lose three electrons and be in a positive charge 3 state:

$$REI_N^{3+} : [Xe]4f^{N-1}. \tag{2.2}$$

For example, the electron configuration of an erbium free atom is $[Xe]4f^{12}6s^2$. After becoming an ion in a crystal host, the electron configuration is $[Xe]4f^{11}$.

Then, we can apply Hund's rules to find the ground state angular momentum. In short, Hund's rule specifies that the ground state should have an electronic structure that features a maximum spin S index and an angular momentum L index. Also, for a less than half-filled electron shell, the energy increases with a higher J, whereas for an over half-filled electron shell, the energy decreases with a higher J.

With this, we can check the ground state level of erbium ions. Erbium ions have

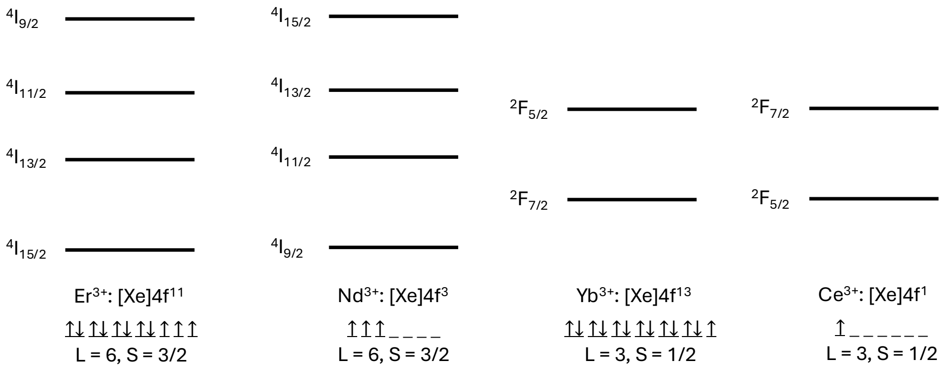

Figure 2.1: **Electron configuration and energy level ordering of different REIs.** Due to Hund's rule, REIs with the same S and L momentum will have a different energy ordering for J depending on whether the 4f shell is more than half-filled or not. Energy spacing is not to scale.

11 f-electrons. The f shell has L=3, with 7 different orbitals corresponding to $m_l = 0, \pm 1, \pm 2, \pm 3$. Following Hund's rule to maximize S and L, we obtain:

$$Er^{3+} : \underline{\uparrow\downarrow}\ \ \underline{\uparrow\downarrow}\ \ \underline{\uparrow\downarrow}\ \ \underline{\uparrow\downarrow}\ \ \underline{\uparrow}\ \ \underline{\uparrow}\ \ \underline{\uparrow} \tag{2.3}$$

where 4 pairs of electrons fill 4 orbitals and the remaining 3 electrons are aligned in the same direction. This gives $S = 3/2$ and $L = 3 + 2 + 1 = 6$. Lastly, since it filled more than a half-shell, the energy decreases with a higher J. Therefore, the ground state energy level will be

$$Er^{3+} :^4 I_{15/2}. \tag{2.4}$$

The same arguments can be applied to neodymium, whose ionic electronic configuration is $[Xe]4f^3$. This gives the same $S = 3/2$ and $L = 6$. However, since it has a less than half-filled electron shell, the ground state level is the one with the smallest J. This gives the ground level for Nd^{3+} as $^4I_{9/2}$. The same procedures can also applied to ytterbium ion (Yb^{3+} and Ce^{3+}). Results are summarized in the Fig. 2.1.

Following the energy ordering of the LSJ levels, the level degeneracy will be lifted by the crystal field splitting. However, for rare-earth ions with an odd number of electrons in the 4f shell, the 'Kramers' theorem' [69] results in each crystal field level being a doublet. This is particularly useful as this doublet can be tuned via an external magnetic field, forming an effective spin-1/2 system. This effective spin can be used for applications in quantum information processing due to its unique spin properties. Also, depending on the nuclear spin of the isotope, the levels will be further split under electron-nuclear interactions.

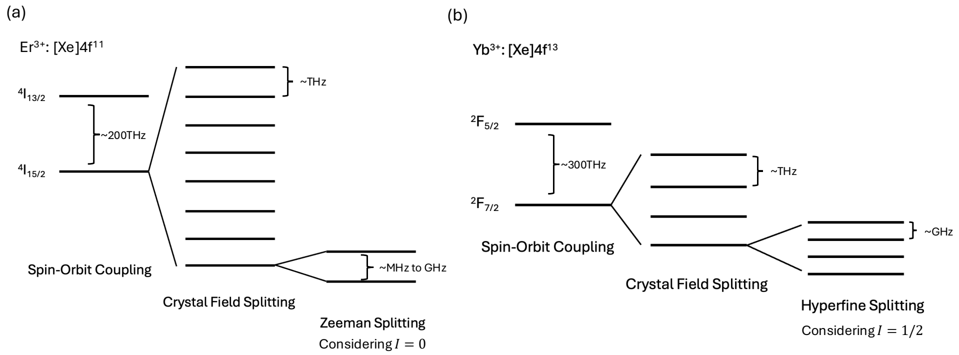

Figure 2.2: **A general energy level diagram of (a) erbium ions and (b) ytterbium ions.** Both of them are Kramers ions as the f-shell electron number is odd. Here, erbium with zero-nuclear spin is considered to show the Zeeman effect, whereas ytterbium with 1/2-nuclear spin is considered to show hyperfine splitting.

Finally, with the crystal field lifting the degeneracy, hyperfine splitting, and the external magnetic field to split the effective spin-1/2 levels further, all the levels are then non-degenerate as shown in Fig. 2.2

2.2 Group theory calculation

Here I will focus on how to use group theory to represent each energy level and further calculate selection rules between different energy levels.

First, the group here refers to the site symmetry of the REIs after substituting ions in a material. For example, in Er^{3+}:YVO_4, yttrium is substituted by erbium, where the site symmetry is D_{2d}. Further, because the erbium has effective electron spins, the group that needs to be considered is the D_{2d} double group. After the site symmetry is known, one can find the group character table and learn each irreducible representation. I recommend the following book [70] for all thirty-two point group properties. Here I will use D_{2d} double group for demonstration purposes, as this will be used in the next two subsections for calculation. With the character table, one can calculate the character of a rotational operation at angle ψ for a LSJ level using the following equation:

$$\chi^j(\psi) = \frac{\sin\left[(j+1/2)\psi\right]}{\sin\frac{\psi}{2}} \tag{2.5}$$

where ψ is the rotation angle of each operation. For example, $\psi = \pi$ for a C_2 operation. σ operation has $\psi = \pi$, but also has a spatial inversion P (-1 for an odd number of 4f electrons). S_4 operation has $\pi/2$ and a spacial inversion. With the characters calculated for each group operation, one can decompose it under the

D_{2d}	E	E’	S$_4$	E’S$_4$	C$_{2z}$ / E’C$_{2z}$	C$_{2x,y}$ / E’C$_{2x,y}$	$\sigma_{1,2}$ / E’$\sigma_{1,2}$
Γ_1	1	1	1	1	1	1	1
Γ_2	1	1	1	1	1	-1	-1
Γ_3	1	1	-1	-1	1	1	-1
Γ_4	1	1	-1	-1	1	-1	1
Γ_5	2	2	0	0	-2	0	0
Γ_6	2	-2	$\sqrt{2}$	-$\sqrt{2}$	0	0	0
Γ_7	2	-2	-$\sqrt{2}$	$\sqrt{2}$	0	0	0

Table 2.1: Character table for D$_{2d}$ double group.

bases of all the group irreducible representations and hence find the irreducible representations of the energy levels:

$$\chi^j(\overrightarrow{\psi}) = \Gamma_{k_1} \oplus \ldots \oplus \Gamma_{k_l}. \tag{2.6}$$

We note that this decomposition can also be found in the compatibility table in [70]. $\oplus$ operator means a sum of individual characters of all k_l irreducible representations. Then, one can calculate the irreducible representation of the electric and magnetic dipole moment, which is equivalent to an L=1 operator and the electric dipole has spatial inversion, but the magnetic dipole does not. This is also represented in the group compatibility table with electric dipole as D_1^- and magnetic dipole as D_1^+. Finally, we consider the selection rules. In quantum mechanics, one performs the state integral to see if the result is nonzero to learn if a transition is allowed:

$$\int \psi_f^* O_T \psi_i d^3r \neq 0 \tag{2.7}$$

where $\psi_{f,i}$ labels the final and initial quantum state, respectively, and O_T is the transition operator. The idea is similar in group theory, but instead we must check if the multiplication of the irreducible representations contains the identity operation:

$$\Gamma_f^* \otimes \Sigma_j \Gamma_j \otimes \Gamma_i \supseteqq \Gamma_1 \tag{2.8}$$

where Γ_i is the irreducible representation of the initial state. $\Sigma_j \Gamma_j$ is the decomposition of the transition operator into its irreducible representations. Γ_f^* is the complex conjugate irreducible representation of the final state. $\otimes$ operator means a multiplication of individual characters between the two irreducible representations. From the books [71] and [72], this selection rule is equivalent to

$$\Gamma_f^* \otimes \Gamma_i \supseteqq \Sigma_j \Gamma_j. \tag{2.9}$$

With all of the above results, one should be able to use the character table and the compatibility table to perform the group theory calculation for REI-doped crystals. Next, I will give two examples of the materials I have worked with.

2.3 Example of Er^{3+}:YVO_4

From the above electronic structure calculation, we know Er^{3+} will have $J = 15/2$ for the ground state and $J = 13/2$ for the excited state. So first, we use equation 2.5 to decompose the energy levels into irreducible representations as shown in table 2.2.

J	Equation	E($\psi = 2\pi$)	C_2($\psi = \pi$)	$\sigma(P, \psi = \pi)$	$S_4(P, \psi = \frac{\pi}{2})$
15/2	$\frac{\sin[8\psi]}{sin[\frac{\psi}{2}]}$	16	0	0	0
13/2	$\frac{\sin[7\psi]}{sin[\frac{\psi}{2}]}$	14	0	0	$\sqrt{2}$

Table 2.2: Character table of different J.

From this, we can get

$$\begin{aligned} \Gamma_{J=15/2} &= 4\Gamma_6 \oplus 4\Gamma_7 \\ \Gamma_{J=13/2} &= 4\Gamma_6 \oplus 3\Gamma_7. \end{aligned} \tag{2.10}$$

We note that this calculation result can also be found in the compatibility table shown in the book [70]. We then know the Z_1 and Y_1 levels will be either Γ_6 or Γ_7. For the transition dipole moment, one can calculate it based on a J = 1 format, as summarized in table 2.3

J	Equation	E($\psi = 2\pi$)	C_2($\psi = \pi$)	$\sigma(P, \psi = \pi)$	$S_4(P, \psi = \frac{\pi}{2})$
1 (ED, P=-1)	$\frac{sin[\frac{3\psi}{2}]}{sin[\frac{\psi}{2}]}$	3	-1	1	-1
1 (MD, P=1)	$\frac{sin[\frac{3\psi}{2}]}{sin[\frac{\psi}{2}]}$	3	-1	-1	1

Table 2.3: Character table of transition dipole moment in D_{2d}.

This decomposes the electric dipole and magnetic dipole selection rules into:

$$\begin{aligned} \Gamma_{ED} &= \Gamma_4 \oplus \Gamma_5 \\ \Gamma_{MD} &= \Gamma_2 \oplus \Gamma_5. \end{aligned} \tag{2.11}$$

Specifically, we note $E(\Gamma_2) = E(\Gamma_4) = 1$ and $E(\Gamma_5) = 2$ from table 2.1. This means Γ_2 and Γ_4 are both one-dimensional representations, corresponding to π

polarization, whereas Γ_5 is a two-dimensional representation, corresponding to σ polarization. Therefore, we get a summary of the correspondence between the transition dipole selection rules and the individual irreducible representations, shown in Table 2.4.

Dipole moment	π	σ
ED	Γ_4	Γ_5
MD	Γ_5	Γ_2

Table 2.4: One-to-one correspondence between transition dipole moment selection rule and irreducible representation.

Finally, we can apply these selection rules to the state of Γ_6 and Γ_7. As an example, I will show how to use equation 2.9 to perform this calculation between Γ_6 and Γ_7. We first write down the characters of Γ_6 and Γ_7^*. Note that in D_{2d} group, all the characters are real, so $\Gamma_7^* = \Gamma_7$. We next multiply each character together and get another character vector row here. Then by doing the character decomposition, we can find what this multiplication consists of. Since it contains a Γ_4 and Γ_5, that means the transition is allowed via π_{ED}, π_{MD}, and σ_{ED}. Each procedure is shown in table 2.5.

D_{2d}	E	E'	S_4	E'S_4	C_{2z} / E'C_{2z}	$C_{2x,y}$ / E'$C_{2x,y}$	$\sigma_{1,2}$ / E'$\sigma_{1,2}$
Γ_6	2	-2	$\sqrt{2}$	$-\sqrt{2}$	0	0	0
Γ_7	2	-2	$-\sqrt{2}$	$\sqrt{2}$	0	0	0
$\Gamma_6 \otimes \Gamma_7$	4	4	-2	-2	0	0	0
$\Gamma_3 \oplus \Gamma_4 \oplus \Gamma_5$	4	4	-2	-2	0	0	0

Table 2.5: Example of a selection rule calculation between Γ_6 and Γ_7.

By performing this calculation between different pairs, we finally have a table for all allowed transitions between Γ_6 and Γ_7.

Levels	Γ_6	Γ_7
Γ_6	$\sigma_{MD}, \sigma_{ED}, \pi_{MD}$	$\pi_{ED}, \pi_{MD}, \sigma_{ED}$
Γ_7	$\pi_{ED}, \pi_{MD}, \sigma_{ED}$	$\sigma_{MD}, \sigma_{ED}, \pi_{MD}$

Table 2.6: Summary of all allowed transitions between Γ_6 and Γ_7 in D_{2d}.

We note these results agree with this paper [73], where the authors perform the same calculation in Er^{3+}:YPO_4 with the same D_{2d} symmetry. Also, this book [72] gives electric-dipole selection rule tables for a few different groups, which could also be

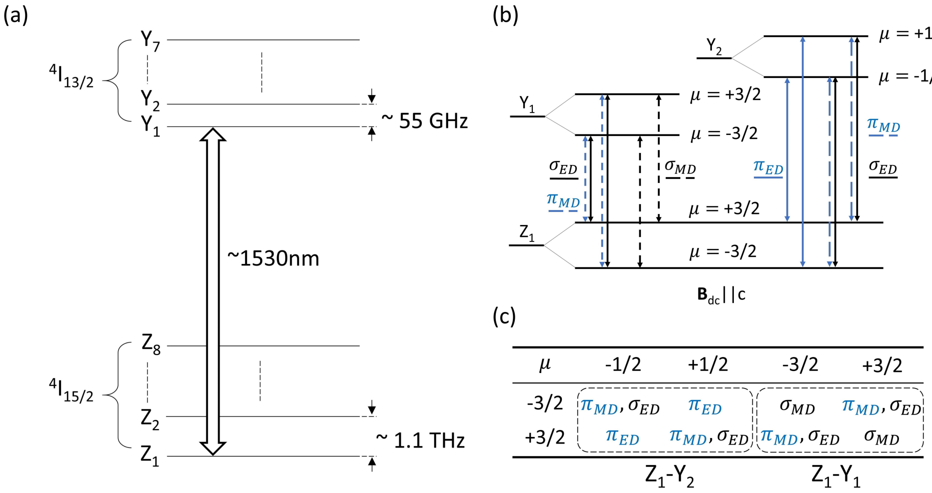

Figure 2.3: **Er^{3+}:YVO_4 energy levels and selection rules.** (a) The energy-level diagram of Er^{3+}:YVO_4 at zero applied magnetic field. (b) Partial diagram of Er^{3+}:YVO_4 crystal field and Zeeman levels with the crystal field quantum number and the selection rules under external magnetic field along the crystal symmetry c-axis ($B_{dc}//c$). π and σ indicate $E_{ac}//c$ and $E_{ac}//a$ polarization.

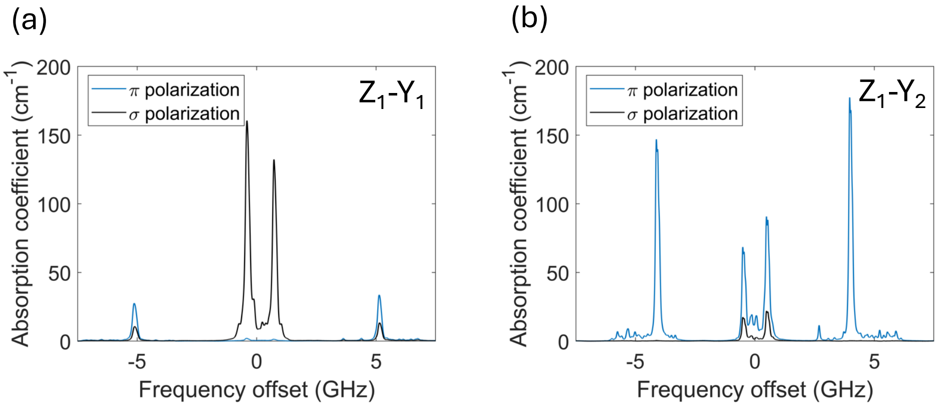

Figure 2.4: **The high-resolution optical transmission spectrum of 140 ppm Er^{3+}:YVO_4.** (a) and (b) show the optical transmission spectrum of Z_1-Y_1 and Z_1-Y_2, respectively, at an applied field of 90 mT at 1 K. The blue line labels π polarization and the black line labels σ polarization.

helpful. One small thing worth mentioning is that the π and σ are all referred to the input electric field. π here means $E//c$ and σ means $E//a$, where c and a are crystal axes.

These results are already useful for understanding the zero-field optical spectroscopic results. To further understand the selection rules under Zeeman splitting, one needs to know the crystal field quantum number of each individual level. As after Zeeman splitting, the single degenerate transition will split into four transitions based on the difference in the g-factors between the ground and excited state spin. The selection rules of these four transitions can also be addressed with the tool of crystal field quantum number. By looking into this paper [56], we learn Z_1 is Γ_7, Y_1 is Γ_7 and Y_2 is Γ_6. Checking with book [72], we found that Γ_6 corresponds to $\mu = \pm\frac{1}{2}$ and Γ_7 corresponds to $\mu = \pm\frac{3}{2}$, where μ labels the crystal field quantum number. Each irreducible representation corresponds to a pair of positive and negative μ, as $\Gamma_{6,7}$ are two-dimensional for a spin-1/2 system. With this and the selection rules using μ in this paper [74], one can get the full selection rule picture under Zeeman splitting, as shown in Fig. 2.3.

With these calculations, one can perform optical spectroscopy on Er^{3+}:YVO_4 at different magnetic fields. Based on the experimental data at different polarizations, one can find a configuration where all the selection rules are met with each level corresponding to a crystal field quantum number. We note there will be two configurations satisfying this, up to a global factor of -1 (e.g., add a minus sign to all the crystal field quantum numbers together).

2.4 Example of $^{171}\mathrm{Yb}^{3+}$:YVO_4

Now I will talk about the application of group theory calculation in $^{171}\mathrm{Yb}^{3+}$:YVO_4. Specifically, here $^{171}\mathrm{Yb}^{3+}$ has a nuclear spin 1/2. Another hyperfine splitting term $I \cdot A \cdot S$ needs to be considered. In group theory language, the electronic states need to $\otimes$ another nuclear spin 1/2 irreducible representation.

Following the logic explained above, we again first find the electronic state of the energy levels. From the electronic configuration, $^{171}\mathrm{Yb}^{3+}$ will have $^2F_{7/2}$ as the ground state and $^2F_{5/2}$ as the excited state. One can perform the calculation using equation 2.5 or check the group compatibility table. We follow the table in [70] and found Γ_6 and Γ_7 are the irreducible representations to use. The nuclear spin 1/2 will behave as Γ_6 ($D^+_{1/2}$). Therefore, the hybridized electron-nuclear state will be:

$$\begin{aligned} \Gamma_6 \otimes \Gamma_6 &= \Gamma_1 \oplus \Gamma_2 \oplus \Gamma_5 \\ \Gamma_7 \otimes \Gamma_6 &= \Gamma_3 \oplus \Gamma_4 \oplus \Gamma_5. \end{aligned} \tag{2.12}$$

We note that Γ_5 corresponds to the doubly degenerate state. In the electron ($|\uparrow\rangle$) - nuclear ($|\Uparrow\rangle$) language, it corresponds to $|\uparrow\Uparrow\rangle$ and $|\downarrow\Downarrow\rangle$ state. Also, Γ_1 and Γ_3 behaves as D_0, which corresponds to $\frac{1}{\sqrt{2}}(|\uparrow\Downarrow\rangle - |\downarrow\Uparrow\rangle)$. And Γ_2 as well as Γ_4 behave as D_1, which corresponds to $\frac{1}{\sqrt{2}}(|\uparrow\Downarrow\rangle + |\downarrow\Uparrow\rangle)$. And Γ_2. This is summarized in table 2.7.

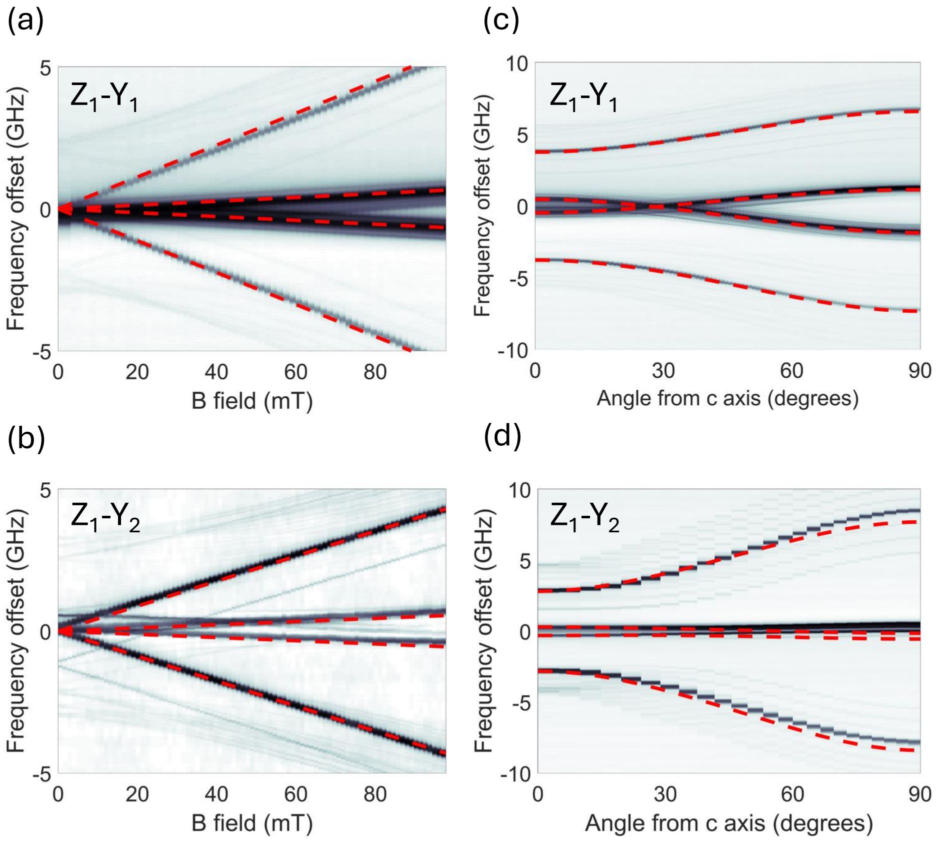

Figure 2.5: **Optical transmission spectrum of 140 ppm Er^{3+}:YVO_4 at various magnetic field.** (a) and (b) show the magnetic field ramp of Z_1-Y_1 and Z_1-Y_2 transmission spectra with σ and π polarization, respectively. The red dashed lines are the fitting from the effective spin Hamiltonian. (c) and (d) show the transmission spectra as a magnetic field of 75 mT rotated from parallel to the crystal c- axis to parallel with crystal a-axis. The red dashed lines are the fitting from the effective spin Hamiltonian.

Irreducible representation	Electron-nuclear wavefunction
Γ_1,Γ_3	$\frac{1}{\sqrt{2}}(\lvert\uparrow\Downarrow\rangle - \lvert\downarrow\Uparrow\rangle)$
Γ_2,Γ_4	$\frac{1}{\sqrt{2}}(\lvert\uparrow\Downarrow\rangle + \lvert\downarrow\Uparrow\rangle)$
Γ_5	$\lvert\uparrow\Uparrow\rangle$ and $\lvert\downarrow\Downarrow\rangle$

Table 2.7: Irreducible representation to electron-nuclear wavefunction for $^{171}Yb^{3+}$:YVO_4.

Since the group is still D_{2d}, we re-use the electric dipole and magnetic dipole correspondence results from the erbium calculation in table 2.6. We then calculate the electric dipole and magnetic dipole selection rule between all Γ_i, shown in table 2.8 and table 2.9.

ED	Γ_1	Γ_2	Γ_3	Γ_4	Γ_5
Γ_1				π	σ
Γ_2			π		σ
Γ_3		π			σ
Γ_4	π				σ
Γ_5	σ	σ	σ	σ	π

Table 2.8: Electric dipole selection rule between different Γ_i in ^{171}Yb^{3+}:YVO$_4$.

MD	Γ_1	Γ_2	Γ_3	Γ_4	Γ_5
Γ_1		σ			π
Γ_2	σ				π
Γ_3				σ	π
Γ_4			σ		π
Γ_5	π	π	π	π	σ

Table 2.9: Magnetic dipole selection rule between different Γ_i in ^{171}Yb^{3+}:YVO$_4$.

We note these two tables are symmetric and the transitions are between two levels, unrelated to the ordering. Therefore, we can just focus on half of them. From electric dipole calculations, there are totally four σ transitions and three π transitions, whereas in the magnetic dipole calculation, there are three σ transitions and four π transitions.

We can compare the above calculations with experimental data and gather more information. First, we observe four σ transitions and three π transitions in the experiment. This indicates the ground state and excited state must be one Γ_6 and one Γ_7, not the same representation. Also, this means the electric dipole is what we observed. Furthermore, as experimentally the transition between Γ_5 and Γ_5 are easy to identify (will split into four transitions under external magnetic field), there are only π transitions allowed from the measurement. This again supports the fact that the magnetic dipole moment might be zero or negligible. For these reasons, we neglect the magnetic dipole contribution in the later calculations and consider the ground state as Γ_7 and excited state as Γ_6 (the reverse is the same as we only consider transitions connected by two levels).

With the above conclusions, we can draw the ^{171}Yb^{3+}:YVO$_4$ energy levels with irreducible representation and allowed transitions properly labeled. This agrees with the experimental measurements pretty well, as initially measured in [75]. Since ^{171}Yb^{3+}:YVO$_4$ only has electron spin 1/2 and nuclear spin 1/2, the Hamiltonian is relatively simple. From this book [55], there is already an analytical equation

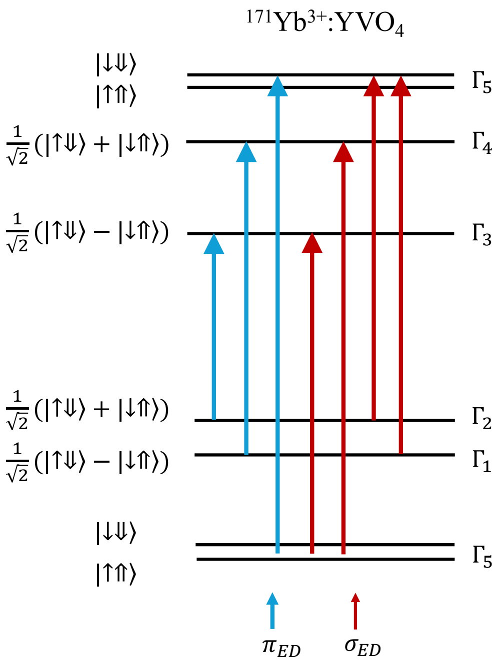

Figure 2.6: **Energy levels of ^{171}Yb^{3+}:YVO$_4$ with group theory labelling and allowed transitions** Each level is labeled by both the irreducible representation in D_{2d} group and also the electron-nuclear wavefunction.

derived from solving the Hamiltonian with an external magnetic field along c-axis. Here I further simplify the results from the book, assuming nuclear spin is 1/2 and zero-field. With these assumptions, one gets:

$$E = -\frac{1}{4}A_{//} \pm \frac{1}{2}[A_{//}^2 m_F^2 + A_{\perp}^2(1 - m_F^2)]^{1/2} \tag{2.13}$$

where $A_{//}$ and $A_{\perp}$ are the elements in the A tensor ($\mathcal{H} = I \cdot A \cdot S$). m_F is the magnetic quantum number of the combined angular momentum ($F = S + I$). Two spin 1/2 systems will combine to a spin-1 and spin-0 system, which corresponds to the four different hybridized functions. Therefore, we get

$$\begin{aligned} |F = 1, m_F = 1\rangle &: E = \frac{A_{//}}{4} \\ |F = 1, m_F = -1\rangle &: E = \frac{A_{//}}{4} \\ |F = (1,0), m_F = 0\rangle &: E = \frac{-A_{//} \pm 2A_{\perp}}{4}. \end{aligned} \tag{2.14}$$

We see that the two $|\uparrow\Uparrow\rangle$ and $|\downarrow\Downarrow\rangle$ are degenerate. The energy of the two $m_F = 0$ states needs to be assigned based on the sign of $A_{//}$ and $A_{\perp}$.

Chapter 3

TRANSDUCTION THEORY

In this chapter, I will discuss the transduction theory in detail. A perfect model will include everything (both cavity modes and each individual atom) and solve all of the individual differential equations together. However, this is numerically intensive and lacks intuition. Below, I will discuss two models, capturing the physics of the transduction process in two different regimes. One is originally presented in [76] and the other is adapted from a general mode coupling theory [77] as presented in the supplementary information of our work [78]. Then, examples will be given to show how to use the tool to solve the electro-optical system, the piezo-opto-mechanical system and the atomics system. Towards the end, since there are different atomic regimes to be work with, we have a discussion on the difference between them. Finally, an important parameter, the effective $\chi^{(2)}$ will be derived, based on the efficiency equation derived here.

3.1 General method

In the quantum picture, a transduction process is basically a beam-splitter Hamiltonian between the two modes. Following the description in [77], let us consider a system consisting of a microwave mode $(b, b^\dagger)$, an optical mode $(a, a^\dagger)$, and N other intermediate modes $(m_i, m_i^\dagger)$. The whole system conceptually forms a chain where each mode is coupled to its two neighbors via a beam splitter Hamiltonian:

$$\begin{aligned}\mathcal{H} =& \hbar\omega_{MW} b^\dagger b + \hbar\omega_{OP} a^\dagger a + \Sigma_i \hbar\omega_i m_i^\dagger m_i \\ &+ \hbar g_b (b^\dagger m_1 + m_1^\dagger b) + \Sigma_i \hbar g_i (m_i^\dagger m_{i+1} + m_{i+1}^\dagger m_i) + \hbar g_a (a^\dagger m_n + m_n^\dagger a)\end{aligned} \tag{3.1}$$

where ω_{MW} and ω_{OP} are the microwave and optical mode frequencies and g_k's are the mode coupling strengths between different modes. First, if there is no intermediate mode, the modes are only microwave and optics. This simplifies back to a direct microwave-optical coupling via an electro-optic material. Second, the mode coupling forms a chain and only couples to its nearest two neighbors is also experimentally reasonable. Typically, a mode can be supported by the geometry of a material, which can at the same time be the building blocks of another mode (e.g., electromechanical[41] and optomechanical[30] effect).

With this Hamiltonian, we use input-output theory to solve the mode dynamics.

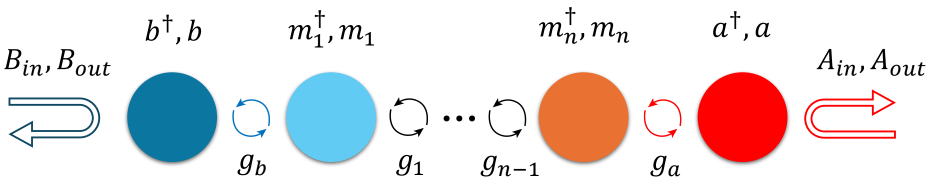

Figure 3.1: **A general mode coupling mode for transduction calculation.** Each mode couples to nearest neighbors via beam-splitter Hamiltonian.

Writing each mode in vector format, we have:

$$\begin{aligned} \dot{k}(t) &= Pk(t) + QK_{in}(t) \\ where \quad k(t) &= (a, m_1, ..., m_N, b)^T \\ K_{in}(t) &= (A_{ext}, A_{int}, M_1, ..., M_N, B_{ext}, B_{int})^T \\ K_{out}(t) &= Q^T k(t) - K_{in}(t) \end{aligned} \tag{3.2}$$

where $B_{in,out}$ and $A_{in,out}$ are the microwave and optical input output fields, M_i's are the input intermediate fields. $K_{in,out}$ is a collective vector of all the relevant input output fields. With these notations, one can solve the dynamics in frequency domain, where all of the useful information is contained in the scattering matrix:

$$\begin{aligned} K_{out}[\omega] &= S[\omega]K_{in}[\omega] \\ where \quad S[\omega] &= Q^T[-i\omega I_{N+2} - P]^{-1}Q - I_{N+4} \end{aligned} \tag{3.3}$$

where I_j is the identity matrix of dimension j.

Electro-optic system

Here we use the above generalized mode coupling theory to calculate the transduction process of an electro-optic (EO) system. For the EO system, we have

$$\begin{aligned} P &= \begin{pmatrix} -\kappa_o/2 & ig_{eo} \\ ig_{eo} & -\kappa_e/2 \end{pmatrix} \\ Q &= \begin{pmatrix} \sqrt{\kappa_{o,ext}} & \sqrt{\kappa_{o,int}} & 0 & 0 \\ 0 & 0 & \sqrt{\kappa_{e,ext}} & \sqrt{\kappa_{e,int}} \end{pmatrix} \end{aligned} \tag{3.4}$$

where κ_i is the total dissipation rates of the resonators and g_{eo} is the coupling strength between the microwave and optical mode. The efficiency is the S-parameter connecting the two output ports of the microwave and optics, which is:

$$\eta_{m2o} = |S(1,3)|^2 = |S(3,1)|^2 = \eta_o\eta_e\frac{4C_{eo}}{(1+C_{eo})^2} \tag{3.5}$$

where $\eta_i = \frac{\kappa_{i,ext}}{\kappa_i}$ is the extraction factor of microwave or optical resonator. $C_{eo} = \frac{4g_{eo}^2}{\kappa_e\kappa_o}$ is the cooperativity. As the system should behave reciprocally, the conversion efficiency from microwave-to-optical and optical-to-microwave should be the same, which is captured in the formalism as $|S(1,3)|^2 = |S(3,1)|^2$. Clearly, the system reaches unit efficiency when $C_{eo} = 1$ and $\eta_i = 1$. This is called the impedance matching condition. The efficiency will not keep increasing with an increased coupling after the matching point. Intuitively, when the coupling is much higher than the decay rate of the mode, one can think about the mode conversion keeps going on between the microwave and optics, back and forth, but not have enough time to emit out. Therefore, the efficiency is only optimized when the conversion speed matches the emission speed. In the language of all the parameters, that means the coupling induced conversion speed $\frac{4g_{eo}^2}{\kappa_e}$ is equal to the emission rate of the optical cavity κ_o, which is the same as $C_{eo} = 1$.

The scattering matrix is also useful to understand the noise process. Considering there are some noise photons in the microwave port, one can calculate how many noisy optical photons get converted through the process. As the noise is incoherent, one can add up the noise from different sources. For example, considering there are n_e noisy photons in the microwave waveguide and n_i noisy photons from the intrinsic microwave bath (e.g., quasiparticle environment), the noise contribution will be:

$$\begin{aligned} n_o &= n_{th,e} + n_{th,i} \\ &= |S(1,3)|^2 n_e + |S(1,4)|^2 n_i. \end{aligned} \tag{3.6}$$

The noisy photons just populated in the optical modes are usually ignored, as optical frequencies are much higher than the room temperature, where the thermal population is negligible ($\hbar\omega_{op} \gg k_b T$). This above equation links the experimentally measured optical photons to the source of the noisy microwave photons. From this, one can get a key parameter called - added noise referred to the input as:

$$\begin{aligned} n_{add,RTI} &= \frac{n_o}{\eta_{m2o}} \\ &= \frac{|S(1,3)|^2 n_e + |S(1,4)|^2 n_i}{|S(1,3)|^2} \\ n_{add,RTI} &= n_e + \frac{\kappa_{e,int}}{\kappa_{e,ext}} n_i. \end{aligned} \tag{3.7}$$

The above result is quite meaningful. First, the added noise referred to the input is the key parameter to describe whether the system operates at the single-photon level (‘quantum regime’) or not, as it divides the efficiency away. Second, the first part of the result is n_e which is the same as the number of coherent microwave photons sent into the waveguide for conversion. The next part is $\frac{\kappa_{e,int}}{\kappa_{e,ext}} n_i$, as one can not directly send photons into the intrinsic bath, but the difference is only the κ ratio factor.

Piezo-opto-mechanical system

Similarly, we can derive the transduction dynamics in a piezo-optomechanical system via this mode coupling theory. We note that the Hamiltonian of the optomechanical coupling is parametric (e.g., $a^\dagger a(m + m^\dagger)$). One needs to first consider a red-detuned optical pump to reduce it to a beamsplitter Hamiltonian. Details can be found in [29]. With these assumptions, one gets:

$$\begin{aligned} P &= \begin{pmatrix} -\kappa_o/2 & ig_{om} & 0 \\ ig_{om} & -\kappa_m/2 & ig_{em} \\ 0 & ig_{em} & -\kappa_e/2 \end{pmatrix} \\ Q &= \begin{pmatrix} \sqrt{\kappa_{o,ext}} & \sqrt{\kappa_{o,int}} & 0 & 0 & 0 \\ 0 & 0 & \sqrt{\kappa_m} & 0 & 0 \\ 0 & 0 & 0 & \sqrt{\kappa_{e,ext}} & \sqrt{\kappa_{e,int}} \end{pmatrix} \end{aligned} \tag{3.8}$$

where $g_o m$ is the coupling strength between the optical and mechanical mode, g_{em} is the coupling strength between the microwave and mechanical mode. With this, one can calculate the efficiency as:

$$\begin{aligned} \eta_{m2o} &= |S(1,4)|^2 = |S(4,1)|^2 \\ &= \eta_o \eta_e \frac{4C_{om}C_{em}}{(1 + C_{om} + C_{em})^2} \end{aligned} \tag{3.9}$$

where $C_{om} = \frac{4g_{om}^2}{\kappa_o \kappa_m}$ is the optomechanical cooperativity and $C_{em} = \frac{4g_{em}^2}{\kappa_e \kappa_m}$ is the piezoelectric cooperativity. Notice again that here the impedance matching condition appears again. The conversion efficiency will be low if only one of the cooperativities is increased while the other one is fixed. The optimal condition is when the $C_{om} = C_{em} \gg 1$. The physical intuition behind this is also clear. First, one needs to have $C_{em} = C_{om}$ such that the process between the two stages is connected fully, otherwise the coherence will be converted back and forth in one stage but not transferred to the next one. Second, the mechanical mode is simply an intermediate stage that connects the microwave and optical modes. Any coherence that leaks out at this stage through mechanical dissipation is harmful. Therefore, one wants the coupling induced conversion speed in each stage to be much higher than the mechanical decay rate, as $\frac{4g_{em}^2}{\kappa_e} \gg \kappa_m$ and $\frac{4g_{om}^2}{\kappa_o} \gg \kappa_m$. These two requirements together give

$C_{om} = C_{em} \gg 1$.

The amount of noise can also extracted from the S matrix. Assuming all of the noise sources are independent and incoherent with respect to each other, then we have

$$\begin{aligned} n_o &= |S(1,4)|^2 n_{e,ext} + |S(1,5)|^2 n_{e,int} + |S(1,3)|^2 n_m \\ \Rightarrow \quad n_{add,RTI} &= \frac{n_o}{\eta_{m2o}} \\ &= n_{e,ext} + \frac{\kappa_{e,int}}{\kappa_{e,ext}} n_{e,int} + \frac{1}{\eta_e C_{em}} n_m \end{aligned} \tag{3.10}$$

where n_m is the thermal occupancy in the mechanical mode. The first two terms are the same as the electro-optic system. The last term is a new term introduced by the mechanical mode. As mechanical devices are typically suspended by design, this term is normally the dominant thermal contribution. However, as the efficiency is referred to the microwave input, the n_m can be suppressed by the strong cooperativity between the microwave and mechanical modes, which can be understood as mechanical cooling from the cold microwave resonator.

3.2 Atomic on-resonance regime

Based on the method discussed in 'General Method', we adapted it into the atomic system with reasonable assumptions as shown below.

Setup of the problem

The system Hamiltonian with both microwave and optical cavity-ion coupling is:

$$\begin{aligned} \mathcal{H} =& \hbar\omega_{o,c} a^\dagger a + \hbar\omega_{e,c} b^\dagger b + \sum_k E_{g,k}\sigma_{gg,k} + \sum_k E_{e_1,k}\sigma_{e_1e_1,k} + \sum_k E_{e_2,k}\sigma_{e_2e_2,k} \\ &+ \sum_k \hbar g_{o,k}(a^\dagger \sigma^-_{o,k} + h.c.) + \sum_k \hbar g_{e,k}(b^\dagger \sigma^-_{s,k} + h.c.) \\ &+ \sum_k \hbar\Omega_k(\sigma^-_{p,k} + h.c.) \end{aligned} \tag{3.11}$$

where a is the optical mode at frequency $\omega_{o,c}$, b is the microwave mode at frequency $\omega_{e,c}$, E are the energies of the level denoted in the subscript, g are the optical or microwave coupling rates, Ω is the pump Rabi frequency, and σ are the atomic operators for the transition denoted in the subscript (e.g. $\sigma^-_{p,k} = |g\rangle\langle e_1|$ for the k-th atom). Implementing the Heisenberg equations of motion, we get

$$\begin{aligned}
\dot{a} &= -\frac{i}{\hbar}[a,\mathcal{H}] = -i\omega_{o,c}a - \frac{\kappa_o}{2}a - i\sum_k g_{o,k}\sigma^-_{o,k} \\
&\quad + \sqrt{\kappa_{o,ext}}a_{in,ext} + \sqrt{\kappa_{o,int}}a_{in,int} \\
\dot{\sigma}^-_{o,k} &= -\frac{i}{\hbar}[\sigma^-_{o,k},\mathcal{H}] = -i\omega_{o,k}\sigma^-_{o,k} - \frac{\gamma_o}{2}\sigma^-_{o,k} \\
&\quad - ig_{o,k}(\sigma_{gg,k} - \sigma_{e_2e_2,k})a + i\Omega_k\sigma^-_{s,k} - ig_{e,k}\sigma^-_{p,k}b \\
\dot{\sigma}^-_{s,k} &= -\frac{i}{\hbar}[\sigma^-_{s,k},\mathcal{H}] = -i\omega_{s,k}\sigma^-_{s,k} - \frac{\gamma_s}{2}\sigma^-_{s,k} \\
&\quad - ig_{e,k}(\sigma_{e_1e_1,k} - \sigma_{e_2e_2,k})b + i\Omega_k\sigma^-_{o,k} - ig_{o,k}\sigma^+_{p,k}a \\
\dot{b} &= -\frac{i}{\hbar}[b,\mathcal{H}] = -i\omega_{e,c}b - \frac{\kappa_e}{2}b - i\sum_k g_{e,k}\sigma^-_{s,k} \\
&\quad + \sqrt{\kappa_{e,ext}}b_{in,ext} + \sqrt{\kappa_{e,int}}b_{in,int},
\end{aligned} \tag{3.12}$$

where we introduce γ and κ, the atomic dephasing rates and cavity decay rates, respectively. Here, we make two assumptions for simplicity: (1) We assume $\langle a\sigma_{ii}\rangle = \langle a\rangle\langle\sigma_{ii}\rangle$, where quantum correlations have been ignored [65]. (2) We ignore the last terms for $\dot{\sigma}^-_{(s,o),k}$, as they simply impose a frequency shift that does not affect the conversion process (e.g. $a \sim \sigma^-_o, \sigma^+_p a \sim \sigma^-_s$).

With the above assumptions, we can rewrite the differential equations into a matrix with the following definitions:

$$\begin{aligned}
V_m &= (a, \sigma^-_{o,1}, \cdots, \sigma^-_{o,k}, \sigma^-_{s,1}, \cdots, \sigma^-_{s,k}, b)^T \\
V_{m,in} &= (a_{in,ext}, a_{in,int}, 0, \cdots, 0, 0, \cdots, 0, b_{in,ext}, b_{in,int})^T \\
V_{m,out} &= (a_{out,ext}, a_{out,int}, 0, \cdots, 0, 0, \cdots, 0, b_{out,ext}, b_{out,int})^T
\end{aligned} \tag{3.13}$$

where V_m is a vector with $2k+2$ elements, $V_{m,in/out}$ is a vector with $2k+4$ elements. Next we rewrite the system dynamics in the frequency domain, going into the rotating frame of the input optical and microwave frequencies, and use the input-output formalism. The equations of motion will become:

$$\begin{aligned}
\dot{V}_m &= AV_m + BV_{m,in} \\
V_{m,out} &= B^TV_m - V_{m,in} \\
V_{m,out} &= SV_{m,in} \\
S &= B^T[-i\omega I_{2k+2}A]^{-1}B - I_{2k+4},
\end{aligned} \tag{3.14}$$

where I_d is the d-dimensional identity matrix. The system can then be solved via matrix operations, and the conversion efficiency is the relevant matrix element of the total scattering matrix S (e.g., $\eta_{M2O} = |S_{1,5}|^2$).

Single atom case

To gain some physical intuition, we start by just considering a single atom:

$$
\begin{aligned}
A &= \begin{pmatrix} -i\delta_{oc} - \frac{\kappa_o}{2} & -ig_o & 0 & 0 \\ -ig_o(n_g - n_{e_2}) & -i\delta_o - \frac{\gamma_o}{2} & i\Omega & 0 \\ 0 & i\Omega & -i\delta_e - \frac{\gamma_s}{2} & -ig_e(n_{e_1} - n_{e_2}) \\ 0 & 0 & -ig_e & -i\delta_{e,c} - \frac{\kappa_e}{2} \end{pmatrix} \\
B &= \begin{pmatrix} \sqrt{\kappa_{o,ext}} & \sqrt{\kappa_{o,int}} & 0 & 0 & 0 & 0 \\ 0 & 0 & 0 & 0 & 0 & 0 \\ 0 & 0 & 0 & 0 & 0 & 0 \\ 0 & 0 & 0 & 0 & \sqrt{\kappa_{e,ext}} & \sqrt{\kappa_{e,int}} \end{pmatrix}.
\end{aligned}
\tag{3.15}
$$

Setting the detunings to zero, we obtain the microwave to optical conversion efficiency as:

$$
\begin{aligned}
\eta_{M2O} = |S_{1,5}|^2 &= \frac{\kappa_{o,ext}}{\kappa_o} \frac{\kappa_{e,ext}}{\kappa_e} \frac{n_{e1} - n_{e2}}{n_g - n_{e2}} \frac{4C_{e,s}C_{o,s}C_{a,s}}{[(1 + C_{e,s})(1 + C_{o,s}) + C_{a,s}]^2} \\
&= \frac{\kappa_{o,ext}}{\kappa_o} \frac{\kappa_{e,ext}}{\kappa_e} \frac{n_{e1} - n_{e2}}{n_g - n_{e2}} \frac{C_{e,s}}{1 + C_{e,s}} \frac{4 * C'_{a,s}}{(1 + C'_{a,s})^2} \frac{C_{o,s}}{1 + C_{o,s}},
\end{aligned}
\tag{3.16}
$$

where the cooperativity is the single-atom cooperativity with dephasing rate γ in the denominators ($C_{o,s} = \frac{4g_o^2(n_g - n_{e_2})}{\kappa_o \gamma_o}$, $C_{e,s} = \frac{4g_e^2(n_{e_1} - n_{e_2})}{\kappa_e \gamma_e}$, $C_{a,s} = \frac{4\Omega^2}{\gamma_o \gamma_e}$). $C'_{a,s}$ is again the modified atomic cooperativity with $(1 + C_{e,s})(1 + C_{o,s})$ in the denominator.

The first two terms are the external coupling rates of each resonator. The third term appears due to the fermionic nature of the atoms, and depends on the population distribution between the three energy levels. However, if the optical pumping is strong enough such that it equalizes the pump transition ($n_g = n_{e_1} = \frac{1}{2}$, $n_{e_2} = 0$), the third term goes to unity. This makes sense since in this scenario, the population of the two fermionic modes (optical and spin) are equivalent and their effects cancel each other out. The remaining three terms involving the cooperativities are the efficiencies which can be understood as the three stages as shown in the left part of Fig. 3.2: a microwave photon to spin coherence, spin coherence to optical coherence (same as electro-optics), and optical coherence to an optical photon.

Also, since the microwave coplanar waveguide connects to the resonator with rate $\kappa_{e,ext}$ and the resonator internal reservoir contributes with rate $\kappa_{e,int}$, the contribution

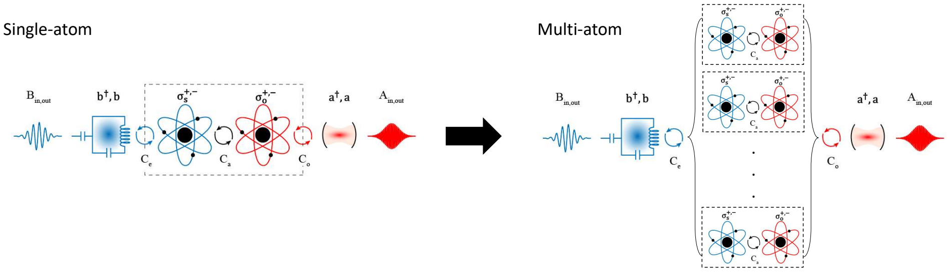

Figure 3.2: **Conversion diagram for single-atom and multi-atom case.** In the multi-atom case, each atom can individually couple to the resonator mode, but the mode only couples to the entire ensemble.

to the microwave noise from the resonator thermal reservoir is:

$$\begin{aligned} N_{measured} &= |S(1,5)|^2 N_{wg} + |S(1,6)|^2 N_{res,int} \\ N_{add,RTI} &= \frac{N_{measured}}{\eta} = N_{wg} + \frac{|S(1,6)|^2}{|S(1,5)|^2} N_{res,int} \\ &= N_{wg} + \frac{\kappa_{e,int}}{\kappa_{e,ext}} N_{res,int}. \end{aligned} \tag{3.17}$$

Multiple atoms case

Now we consider the more general ensemble case, where there are multiple atoms that can each individually couple to the optical and microwave resonator mode. However, as we have ignored quantum correlations and consider only the atoms as a collective, the resonator couples to the total contribution of the ensemble, illustrated in the right part of Fig. 3.2. In this case, the matrix can be rewritten as:

$$\begin{aligned} A &= \begin{pmatrix} -i\delta_{oc} - \frac{\kappa_o}{2} & -ig_{o,1} & \cdots & -ig_{o,k} & & & & \\ -ig_{o,1}(n_{g,1} - n_{e_2,1}) & -i\delta_{o,1} - \frac{\gamma_o}{2} & & & i\Omega_1 & & & \\ \cdots & & \cdots & & & \cdots & & \\ -ig_{o,k}(n_{g,k} - n_{e_2,k}) & & & -i\delta_{o,k} - \frac{\gamma_o}{2} & & & i\Omega_k & \\ & i\Omega_1 & & & -i\delta_{e,1} - \frac{\gamma_e}{2} & & & -ig_{e,1}(n_{e_1,1} - n_{e_2,1}) \\ & & \cdots & & & \cdots & & \cdots \\ & & & i\Omega_k & & & -i\delta_{e,k} - \frac{\gamma_e}{2} & -ig_{e,k}(n_{e_1,k} - n_{e_2,k}) \\ & & & & -ig_{e,1} & \cdots & -ig_{e,k} & -i\delta_{ec} - \frac{\kappa_e}{2} \end{pmatrix} \\ B &= \begin{pmatrix} \sqrt{\kappa_{o,ext}} & \sqrt{\kappa_{o,int}} & & & & & & & & \\ & & 0 & & & & & & & \\ & & & \cdots & & & & & & \\ & & & & 0 & & & & & \\ & & & & & 0 & & & & \\ & & & & & & \cdots & & & \\ & & & & & & & 0 & & \\ & & & & & & & & \sqrt{\kappa_{e,ext}} & \sqrt{\kappa_{e,int}} \end{pmatrix} \end{aligned} \tag{3.18}$$

where A is a $(2k + 2) \times (2k + 2)$ matrix and B is a $(2k + 2) \times (2k + 4)$ matrix.

To get a sense of the analytical form of the conversion efficiency, we can consider just two identical atoms. Then, A will be a 6×6 matrix and B a 6×8 matrix. Assuming no detunings again, the matrix will become:

$$
\begin{gathered}
A = \begin{pmatrix}
-\frac{\kappa_o}{2} & -i\frac{g_o}{\sqrt{2}} & -i\frac{g_o}{\sqrt{2}} & & & \\
-i\frac{g_o}{\sqrt{2}}(n_g - n_{e_2}) & -\gamma_o/2 & & i\Omega & & \\
-i\frac{g_o}{\sqrt{2}}(n_g - n_{e_2}) & & -\gamma_0/2 & & i\Omega & \\
 & i\Omega & & -\gamma_e/2 & & -i\frac{g_e}{\sqrt{2}}(n_{e_1} - n_{e_2}) \\
 & & i\Omega & & -\gamma_e/2 & -i\frac{g_e}{\sqrt{2}}(n_{e_1} - n_{e_2}) \\
 & & & -i\frac{g_e}{\sqrt{2}} & -i\frac{g_e}{\sqrt{2}} & -\frac{\kappa_e}{2}
\end{pmatrix} \\
B = \begin{pmatrix}
\sqrt{\kappa_{o,ext}} & \sqrt{\kappa_{o,int}} & & & & & & \\
 & & 0 & & & & & \\
 & & & 0 & & & & \\
 & & & & 0 & & & \\
 & & & & & 0 & & \\
 & & & & & & \sqrt{\kappa_{e,ext}} & \sqrt{\kappa_{e,int}}
\end{pmatrix}
\end{gathered}
\tag{3.19}
$$

where we have added a factor of $\frac{1}{\sqrt{2}}$ to g_o and g_e to conserve the total coupling strength ($g_{o,tot} = \sqrt{\sum_i g_{o,i}^2}$). Then, the efficiency is:

$$
\eta_{M2O} = |S_{1,7}|^2 = \frac{\kappa_{o,ext}}{\kappa_o}\frac{\kappa_{e,ext}}{\kappa_e}\frac{n_{e1} - n_{e2}}{n_g - n_{e2}}\frac{4C_eC_oC_a}{[(1 + C_e)(1 + C_o) + C_a]^2}, \tag{3.20}
$$

where the cooperativities are now ensemble cooperativities, and the coupling strength in the numerator is the sum of squares of the individual coupling strengths. Similarly, the added noise referred to the input can be found as:

$$
\begin{aligned}
N_{add,RTI} = \frac{N_{measured}}{\eta} &= N_{wg} + \frac{|S(1,8)|^2}{|S(1,7)|^2}N_{res,int} \\
&= N_{wg} + \frac{\kappa_{e,int}}{\kappa_{e,ext}}N_{res,int}.
\end{aligned}
\tag{3.21}
$$

These results are exactly the same as the single atom case due to the symmetry of the S-matrix. Increasing the number of atoms will yield the same results. This indicates that atoms with the same properties (detunings, coupling strengths) can be considered as a single atom with coupling strength equal to ensemble coupling strength to solve the conversion process.

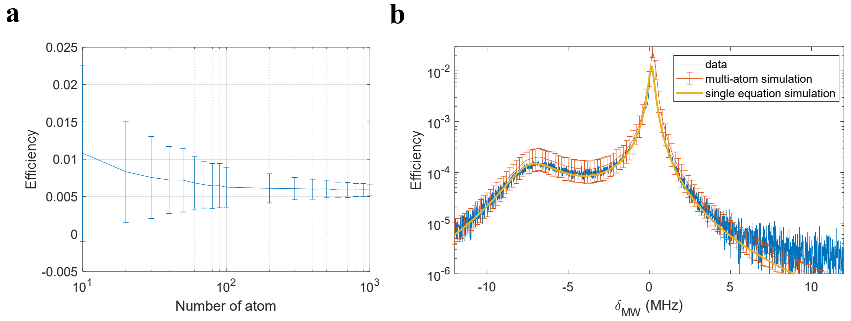

Figure 3.3: **Multi-atom simulations.** (a) The convergence test. Parameters used are the same parameters used in the main experiment presented in Fig. 6.2, but with zero spin detuning. Each simulation is repeated 1000 times and the error bars reflect the finite sampling. (b) Comparison between data, multi-atom simulation and the single-atom equation. For the multi-atom simulation, each point consists of 200 atoms and is averaged over 1000 simulations from which error bars are calculated.

For a large number of atoms with inhomogeneities, deriving an analytical expression becomes intractable, and numerical simulations must be implemented. To do this, we first assign a random optical and microwave detuning to each atom from a Gaussian distribution with width equal to the respective inhomogeneous linewidths. Additionally, random horizontal and vertical coordinates are assigned taking into account a Gaussian distribution based on the optical beam radius. Therefore, from the beam edge to the center, a corresponding optical and microwave coupling strength can be assigned to each sampled atom using the Gaussian beam profile and simulated microwave mode profile. Since we have billions of atoms, we cannot simulate each atom individually. Instead, we group the atoms with similar properties together to reduce the total number of calculated atoms. In doing so, we perform a convergence test to see how many groups of atoms we must sample in order for the result to converge. As shown in Fig. 3.3a, around 100 atoms sufficiently capture the system behavior.

Finally, we compare the multi-atom simulation with the single-atom simulation with the same parameters used in the experiments. As shown in Fig. 3.3b, the results are similar and overlap within a factor of 2. This validates the usage of the simple, single-atom equation as discussed earlier. However, it is worth noting that these two simulations need not necessarily agree with each other. This is because the single-atom equation uses ensemble cooperativity with inhomogeneous linewidth instead of atomic dephasing in the denominator, which is technically an approximation. Specifically, when the homogeneous linewidth of each individual atom (equivalently, T_2) is much narrower than the inhomogeneous linewidth, the result of the single-atom equation deviates from the multi-atom results, due to the fact that the more accurate multi-atom case only addresses a narrow subset of the ensemble. In this case, the denominator of the ensemble cooperativity should be modified to include a contribution from both the homogeneous and inhomogeneous linewidths. In our case, the homogeneous and inhomogeneous linewidths differ by a factor of 40, where the single equation and multi-atom results still agree with each other.

3.3 Atomic adiabatic regime

We note there is also an atomic adiabatic regime originally proposed in [76]. Although so far experiments have operated with small cooperativities and hence are captured by the atomic on-resonance model, the adiabatic model results in clean and intuitive expressions. The comparison between the two regimes will be discussed in the next section. Here I will describe this adiabatic calculation using the excited state spins.

Setup of the problem

The system Hamiltonian to start with is the same as calculated in 3.11 in the on-resonance regime:

$$\begin{aligned}\mathcal{H} =& \hbar\omega_{o,c}a^\dagger a + \hbar\omega_{e,c}b^\dagger b + \sum_k E_{g,k}\sigma_{gg,k} + \sum_k E_{e_1,k}\sigma_{e_1e_1,k} + \sum_k E_{e_2,k}\sigma_{e_2e_2,k} \\ &+ \sum_k \hbar g_{o,k}(a^\dagger\sigma^-_{o,k} + h.c.) + \sum_k \hbar g_{e,k}(b^\dagger\sigma^-_{s,k} + h.c.) \\ &+ \sum_k \hbar\Omega_k(\sigma^-_{p,k} + h.c.).\end{aligned} \tag{3.22}$$

Then we calculate the dynamics of each relevant operator in the Heisenberg picture:

$$\begin{aligned}\dot{a} &= \frac{i}{\hbar}[\mathcal{H}, a] = -i\omega_{o,c}a - \frac{\kappa_o}{2}a - i\Sigma g_{o,k}\sigma^-_{o,k} \\ \dot{b} &= -i\omega_{e,c}b - i\Sigma g_{e,k}\sigma^-_{s,k} - \frac{\kappa_e}{2}b - \sqrt{\kappa_{e,c}}B_{in} \\ \dot{\sigma}^-_{o,k} &= -i\omega_{e2,g}\sigma^-_{o,k} + ig_{o,k}(n_{e_2,k} - n_{g,k})a - ig_{e,k}\sigma^-_{p,k}b + i\Omega_k\sigma^-_{s,k} \\ \dot{\sigma}^-_{p,k} &= -i\omega_{e_1,g}\sigma^-_{p,k} + ig_{o,k}\sigma^+_{s,k}a - ig_{e,k}b^\dagger\sigma^-_{o,k} + i\Omega_k(n_{e_1,k} - n_{g,k}) \\ \dot{\sigma}^-_{s,k} &= -i\omega_{e_2,e_1}\sigma^-_{s,k} - ig_{o,k}\sigma^+_{p,k}a + ig_{e,k}(n_{e_2,k} - n_{e_1,k})b + i\Omega_k\sigma^-_{o,k}.\end{aligned} \tag{3.23}$$

Calculation via Integral

We can apply the rate equation approximation to carry out the integral of each equation. For example, to learn the optical field a, we need to calculate $\sigma^-_{o,k}$, which can then be used to directly link to optical field a via either rate equation approximation or by adiabatically eliminating the cavity. To find $\sigma_{o,k}$, we need to find $\sigma^-_{p,k}$ and $\sigma^-_{s,k}$, which can integral out. Therefore, we get

$$\sigma^-_{o,k} \approx \frac{g_{e,k}\Omega_k}{\delta_{ec,k}+\delta_p}\left(\frac{n_{e_2,k}-n_{e_1,k}}{\delta_{ec,k}} - \frac{n_{e_1,k}-n_{g,k}}{\delta_{p,k}}\right)b + (i\omega+\Gamma)a. \tag{3.24}$$

We note that there are two different terms here. The first term is linear with microwave field b. This term is useful as $\sigma^-_{o,k}$ will be plugged into the equation of optical field a, which will finally become $a = Mb$ term, where M is just a complicated parameter from the system. This is the beam-splitter Hamiltonian effectively connecting mode a and mode b. The second term is not useful, as I only write it generally as $(i\omega + \Gamma)$. The reason is that this term is linear with mode a, which will finally become a frequency shift/mode broadening term, not contributing to the beam-splitter Hamiltonian.

With the equation of $\sigma^-_{o,k}$, one can get the optical mode a:

$$\begin{aligned} a &= \Sigma \frac{-ig_{o,k}}{-i\delta_{oc,k}+\kappa_o/2}\sigma^-_{o,k} \\ &= \Sigma \frac{g_{o,k}g_{e,k}\Omega_k}{(i\delta_{ec,k}+i\delta_p)(i\delta_{oc,k}-\kappa_o/2)}\left(\frac{n_{e_1,k}-n_{g,k}}{\delta_{p,k}} - \frac{n_{e_2,k}-n_{e_1,k}}{\delta_{ec,k}}\right)b. \end{aligned} \tag{3.25}$$

Similarly, with the same method, one can get the mode b equation via calculating $\sigma^-_{s,k}$:

$$\begin{aligned} b &= \Sigma \frac{-g_{o,k}g_{e,k}\Omega_k}{(i\delta_{ec,k}-\kappa_e/2)(i\delta_{oc,k}-i\delta_{p,k})}\left(\frac{n_{g,k}-n_{e_1,k}}{\delta_{p,k}} + \frac{n_{e_2,k}-n_{g,k}}{\delta_{oc,k}}\right)a \\ &- \frac{\sqrt{\kappa_{e,c}/2}}{i(\delta_{e,k}-\delta_{ec,k})+\kappa_e/2}B_{in}. \end{aligned} \tag{3.26}$$

We note there are many detunings and it might introduce confusions to readers. For clarity, all the detuning definitions are as follows:

$$\begin{aligned} \delta_{oc,k} &= \omega_{e_2,g,k} - \omega_{o,c} \\ \delta_{ec,k} &= \omega_{e_2,e_1,k} - \omega_{e,c} \\ \delta_{p,k} &= \omega_{e_1,g,k} - \omega_p \\ \delta_{o,k} &= \omega_{e_2,g,k} - \omega_o \\ \delta_{e,k} &= \omega_{e_2,e_1,k} - \omega_e \\ \omega_o &= \omega_e + \omega_p. \end{aligned} \tag{3.27}$$

All the cavity-related detunings are referred to the cavity frequencies $\omega_{o/e,c}$. All the other detunings are referred to the input microwave/pump frequencies $\omega_{e/p}$. The last equation from above is energy conservation, where we label the transduced optical photon frequency as ω_o.

To further simplify the prefactors in the equations, we now assume the microwave input frequency is on-resonance with the microwave cavity frequency ($\omega_e = \omega_{e,c}$), the optical output frequency is on-resonance with the optical cavity frequency ($\omega_o = \omega_{o,c}$). And further assume the optical detuning (usually a few optical inhomogeneous linewidth) is much larger than the microwave detuning (usually a few spin inhomogeneous linewidth). This is valid for $^{171}Yb^{3+} : YVO_4$ where the spin linewidth is only ~100 kHz where the optical linewidth is ~100 MHz. Also, this will eliminate the detuning difference between each atom, as the detuning is much large than the inhomogeneous linewidths. With these assumptions, one can then get a much simpler version of the equation:

$$\begin{aligned} a &= \Sigma \frac{-g_{o,k} g_{e,k} \Omega_k}{(i\delta_{oc} - \kappa_o/2) i\delta_{o,k}} \frac{n_{e_2,k} - n_{e_1,k}}{\delta_e} b \\ b &= \Sigma \frac{-g_{o,k} g_{e,k} \Omega_k}{(i\delta_{ec} - \kappa_e/2) i\delta_{e,k}} \frac{n_{e_2,k} - n_{e_1,k}}{\delta_o} a - \frac{\sqrt{\kappa_{e,c}/2}}{\kappa_e/2} B_{in}. \end{aligned} \tag{3.28}$$

With this, one can get the efficiency equation as

$$\begin{aligned} \eta &= \frac{A_{out}^\dagger A_{out}}{B_{in}^\dagger B_{in}} = \frac{\kappa_{o,c} a^\dagger a}{B_{in}^\dagger B_{in}} \\ &= \eta_a \eta_b \frac{16|S|^2 \kappa_o \kappa_e}{|4S^2 + \kappa_o \kappa_e|^2} \\ &= \eta_a \eta_b \frac{4R^2}{|1 + R^2|^2} \\ where \quad S &= \Sigma \frac{g_{o,k} g_{e,k} \Omega_k}{\delta_o \delta_e} (n_{e_2,k} - n_{e_1,k}) \\ and \quad R &= \frac{2S}{\sqrt{\kappa_o \kappa_e}}. \end{aligned} \tag{3.29}$$

This recovers back the adiabatic result as shown in [76]. However, one main difference is that there is a population difference term in parameter S, $n_{e_2} - n_{e_1}$, that does not appear in the result using ground state spins. The reason is that under the adiabatic approximation of ground state spins, all the populations are originally in the ground state $n_g = 1$. This makes all the relevant population difference terms to 1 as $n_g - n_{e_1} = 1$ and $n_g - n_{e_2} = 1$. The factor of 1 will not show up, therefore the population difference terms are hidden. One thing should be acknowledged is

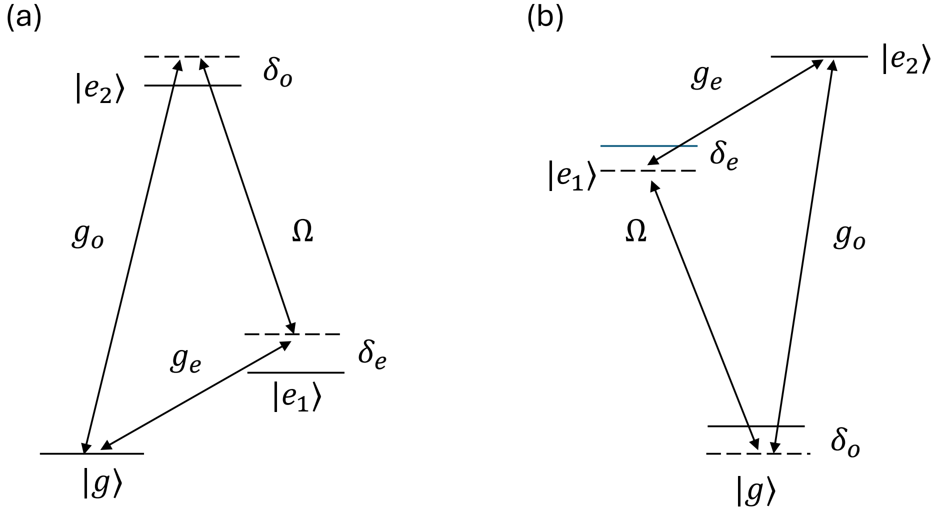

Figure 3.4: **Diagrams of adiabatic regimes.** (a) Diagram using ground state spin and (b) using excited state spin. One can understand the excited state spin case is exactly the ground state but with the energy flipped.

that this type of integral calculation is messy. The reader should remember how many assumptions we need to have, to reach this final clean results. Also, lots of frequency shifts and cavity-broadening terms are neglected as it does not contribute to the effective beam-splitter Hamiltonian.

Below, I will discuss another easier method to get the adiabatic results and capture some important frequency shift terms back.

Calculation via Optical Bloch Equation

We notice that the optical field a is only coupled via σ_o^- (equivalently ρ_{g,e_2}) and the microwave field is only coupled via σ_s^- (equivalently ρ_{e_1,e_2}). Therefore, it is enough to calculate the efficiency as long as we learn the equation of ρ_{g,e_2} and ρ_{e_1,e_2}. To achieve this, one can perform the optical block equation and calculate the steady-state solution:

$$\begin{aligned}\dot{\rho}_{g,e_2} &= 0 = i\delta_o\rho_{g,e_2} - iA^*(n_{e_2} - n_g) + iB^*\rho_{g,e_1} - i\Omega\rho_{e_1,e_2}\\ \dot{\rho}_{e_1,e_2} &= 0 = i\delta_e\rho_{e_1,e_2} + iA^*\rho_{e_1,g} - iB^*(n_{e_2} - n_{e_1}) - i\Omega\rho_{g,e_2}.\end{aligned} \tag{3.30}$$

Here, we take $A = g_o a$ and $B = g_e b$ to assume they are actual steady-state values instead of operators. Also, we neglect the term that consists of ρ_{g,e_1} or $\rho_{e_1,g}$ as the pump coherence is generally small in the adiabatic limit (e.g., pump is far off-resonance).

Under the above adiabatic limit, we can then solve ρ_{g,e_2} and ρ_{e_1,e_2} as:

$$\begin{aligned}\rho_{g,e_2} &= \frac{1}{\delta_o\delta_e}[A^*\delta_e(n_{e_2}-n_g)+B^*\Omega(n_{e_2}-n_{e_1})]\\ \rho_{e_1,e_2} &= \frac{1}{\delta_o\delta_e}[A^*(n_{e_2}-n_{e_1})\Omega+B^*\delta_o(n_{e_2}-n_{e_1})].\end{aligned} \tag{3.31}$$

Combined with the input-output equations in steady state, one gets:

$$\begin{aligned}0 &= -i\delta_{co}a-iSb(n_{e_2}-n_{e_1})-i\omega_a a(n_{e_2}-n_g)-\frac{\kappa_o}{2}a\\ 0 &= -i\delta_{ce}b-iSa(n_{e_2}-n_g)-i\omega_b a(n_{e_2}-n_{e_1})-\frac{\kappa_e}{2}b-\sqrt{\kappa_{b,c}}B_{in}\\ here \quad S &= \Sigma\frac{g_o g_e\Omega}{\delta_o\delta_e}.\end{aligned} \tag{3.32}$$

Here, we capture two frequency shifting terms due to the ion-cavity coupling as $\omega_a = \Sigma\frac{g_o^2}{\delta_o}$ and $\omega_b = \Sigma\frac{g_e^2}{\delta_e}$. We notice the S definition does not contain any population difference term here, so we can clearly write it down in the full equation now. From the above equation, one can plug the first into the second one, and get the efficiency equation as:

$$\begin{aligned}\eta_{e-spin} &= \frac{A_{out}^\dagger A_{out}}{B_{in}^\dagger B_{in}} = \frac{\kappa_{o,c}a^\dagger a}{B_{in}^\dagger B_{in}}\\ &= |\frac{\sqrt{\kappa_{o,c}}\sqrt{\kappa_{e,c}}S(n_{e_1}-n_{e_2})}{(-i\delta_{oc}+i\omega_a(n_g-n_{e_2})-\kappa_o/2)(-i\delta_{ec}+i\omega_b(n_{e_1}-n_{e_2})-\kappa_e/2)+S^2(n_g-n_{e_2})(n_{e_1}-n_{e_2})}|^2\end{aligned} \tag{3.33}$$

where we use η_{e-spin} to label this is the adiabatic result using the excited state spins. The above result is quite meaningful. First, if we take $n_{e_2} = 1$ and $n_{e_1} = n_g = 0$, this simply recovers the normal adiabatic equation where all the population difference terms disappear. This means the excited state calculation is exactly the same as the ground state calculation, by inverting the system up to down (e.g., flip any subscript of e_2 into g and vice versa). Because the Hamiltonian is the same, any mode coupling is also the same, but only up a negative sign in energy to flip the whole diagram. Second, following what we have discussed, the ground state adiabatic regime calculation can be then easily derived from the excited-state result above, with the interchange of $n_{e_2} \Leftrightarrow n_g$ as:

$$\begin{aligned}\eta_{g-spin} &= \frac{A_{out}^\dagger A_{out}}{B_{in}^\dagger B_{in}} = \frac{\kappa_{o,c}a^\dagger a}{B_{in}^\dagger B_{in}}\\ &= |\frac{\sqrt{\kappa_{o,c}}\sqrt{\kappa_{e,c}}S(n_{e_1}-n_g)}{(-i\delta_{oc}+i\omega_a(n_{e_2}-n_g)-\kappa_o/2)(-i\delta_{ec}+i\omega_b(n_{e_1}-n_g)-\kappa_e/2)+S^2(n_{e_2}-n_g)(n_{e_1}-n_g)}|^2\end{aligned} \tag{3.34}$$

where we use η_{g-spin} to label this is the adiabatic result using the ground state spins, separating from the excited state spin result.

Now the population difference terms are captured well. Readers should be able to derive the result in [76] using 3.34. One thing worth noting is that in 3.33, even if it is in the adiabatic regime, one always needs to do on-resonance optical pumping to put populations in the excited state spin manifold. Ideally, the populations are all in n_{e_2}, as it is a full inversion of the ground state condition. However, this might trigger superradiance effect if the microwave cooperativity is large enough. This effect is observed in the experiment and will be discussed in Section 8 in detail.

Here we finish all the theoretical calculations of the transduction process in the on-resonance regime and adiabatic regime. Clearly, there are differences between the two regimes and also differences between the choice of using ground state spin or excited state spin. Below we will have a brief discussion on the difference.

3.4 Comparison of transduction schemes

The on-resonance regime vs adiabatic regime

First with excited state spins, one always needs to do on-resonance optical initialization to initiate the system non-linearity. Then, with large optical and microwave cooperativities ($C \gg 1$), the adiabatic regime is great as it puts a loose requirement on the pump rabi frequency. However, if the platform does not have large microwave and optical cooperativities (e.g., $C \leq 1$), then the largest transduction signal will be on-resonance with the transitions, where the detuning will only hurt the system as it drives weaker. Meanwhile, the on-resonance regime has a stronger requirement on the pump rabi drive: to reach 100% efficiency, one needs not only $C_e, C_o \gg 1$, but also $C_a = C_e * C_o \gg 1$. This is technically difficult to achieve and could also introduce high noise as the pump power increases. It is fair to say that when all the cooperativities are ~ 1, the on-resonance case is best, as the efficiency is $\sim 20\%$. But with further improvements in cooperativity, the adiabatic regime is preferable as noise can potentially be reduced.

The choice between ground state spins and excited state spins

There is a trade-off between the two options. With ground state spins, any imperfection in mode overlap between the microwave and optical fields will result in parasitic spins. These parasitic spins are spins that only absorb microwave photons but do not contribute to the transduction process as they are not exposed to the optical pump. This is a critical issue for single-photon level transduction, as the parasitic spins will put a hard cap on the efficiency in the single-photon regime. Meanwhile, for excited state spins, only the ions being optically excited can interact with the microwave photon. Therefore, the parasitic spins are inherently avoided. However, the drawback is the requirement of optical initialization at the beginning, to initiate the system non-linearity. This can lead to extra heating of the system, hurting the noise performance. But with a thinner crystal, the initialization pulse can be shorter, and the noise generated by the initialization pulse could potentially be small and not be a problem for the noise.

3.5 Effective $\chi^{(2)}$ calculation

Here we derive the effective $\chi^{(2)}$ nonlinearity of a three-level REI system. We start with the transduction efficiency of an electro-optical (EO) system in the low cooperativity regime:

$$\eta = \frac{4C_{eo}}{(1+C_{eo})^2} \sim 4C_{eo}. \tag{3.35}$$

Similarly, in the low cooperativity regime, the atomic system efficiency is

$$\eta = \frac{4C_e C_o C_a}{((1+C_e)*(1+C_o)+C_a)^2} \sim 4C_e C_o C_a. \tag{3.36}$$

Therefore, an effective $C_{eo} = C_e C_a C_o$ can be found, which leads to an effective coupling rate as

$$g_{eo} = \frac{4 g_{e,tot} g_{o,tot} \Omega_{pump}}{\Gamma_s \Gamma_o}. \tag{3.37}$$

The EO coupling rate is related to the material non-linearity as [79, 80]

$$h g_{eo} = \chi^{(2)} V_0 \epsilon_0 E_o E_p B_{mw} c \tag{3.38}$$

where V_0 is the mode volume, E_o/B_{mw} is the amplitude of the quantized optical/microwave field, and E_p is the pump field strength. Inserting the above equation into the effective EO coupling rate, one finds

$$\chi^{(2)}_{eff} = \frac{h g_{eo}}{V_0 \epsilon_0 c \frac{h g_{o,tot}}{\sqrt{N} d_o} \frac{h\Omega}{d_p} \frac{h g_{e,tot}}{\sqrt{N} \mu_{spin}}} = \frac{4}{\epsilon_0 c h^2} \frac{\rho\, d_p\, d_o\, \mu_{spin}}{\Gamma_s \Gamma_o} \tag{3.39}$$

where d is the electric dipole moment for each optical transition and μ is the spin magnetic dipole moment. This should be compared to the $\chi^{(2)}$ of EO materials. Also, given the relationship between g_{eo} and $\chi^{(2)}$, one can find an equation linking $\chi^{(2)}$ to efficiency in low cooperativity regime as

$$\eta \sim 4C_{eo} = \frac{16 g_{eo}^2}{\kappa_e \kappa_o} = \frac{4\omega_e \omega_o}{\epsilon_0 V_t} \frac{(\chi^{(2)})^2 P_p U_m U_o^2}{\kappa_e \kappa_o \kappa_p} \tag{3.40}$$

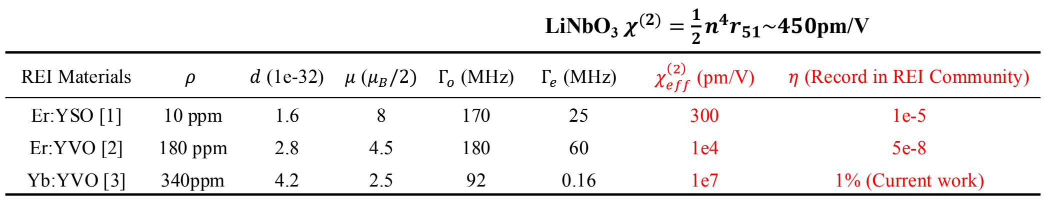

LiNbO$_3$ $\chi^{(2)} = \frac{1}{2} n^4 r_{51} \sim 450$pm/V

REI Materials	ρ	d (1e-32)	μ ($\mu_B/2$)	Γ_o (MHz)	Γ_e (MHz)	$\chi^{(2)}_{eff}$ (pm/V)	η (Record in REI Community)
Er:YSO [1]	10 ppm	1.6	8	170	25	300	1e-5
Er:YVO [2]	180 ppm	2.8	4.5	180	60	1e4	5e-8
Yb:YVO [3]	340ppm	4.2	2.5	92	0.16	1e7	1% (Current work)

Figure 3.5: **Effective $\chi^{(2)}$ among different REI materials.** [1] Er:YSO data comes from [45]. [2] Er:YVO data comes from [58]. [3] Yb:YVO data is from this thesis and our paper [78].

where P_p is the pump power, κ_p is the optical cavity decay rate at the pump frequency, V_t is the transduction zone volume, and $U_m(U_o)$ is the energy fraction of microwave (optical) resonator inside V_t. The above equation is meaningful as it indicates the efficiency changes quadratically with the non-linearity $\chi^{(2)}$. Therefore, with a stronger non-linearity, requirements on the quality factors of both microwave and optical resonators are less stringent.

One can also extract the $\chi^{(2)}$ non-linearity from measurements, which is

$$\chi^{(2)}_{exp} = \frac{\rho d^2 \mu_{spin}}{4h^2 \epsilon_0 c} \frac{\sqrt{\eta \kappa_e \kappa_o}}{g_{o,tot} g_{e,tot} \Omega} \tag{3.41}$$

where the parameters in the second term can all be independently measured.
We note this $\chi^{(2)}$ is only an effective calculation number. Since the spin linewidth is too narrow, this nonlinearity is only valid within a narrow window (~ spin inhomogeneity). Therefore, this may not be that useful for other nonlinear physics applications. However, for the transduction process, as long as there is a strong nonlinearity within the transduciton bandwidth (here, is determined by the spin linewidth), the process will work with whatever nonlinearity is inside this frequency range, without caring what is the nonlinearity outside this range. In other words, this is the transduction nonlinearity, that is concentrated around the spin transitions.

Lastly, one can gather the informations for different REI materials and compare the $\chi^{(2)}_{eff}$, as shown in Fig. 3.5

Chapter 4

PREVIOUS REI-BASED ON-CHIP TRANSDUCERS

Before we dive into the new designs of a microwave-to-optical transducer based on rare-earth ion crystals, learning how the previous transducers work and what the shortcomings of each different design are is valuable. Here, I will go through the previous on-chip designs and measurements.

4.1 Previous on-chip design v1

The first version of the device we have been working on is shown in Fig. 4.1 [53]. The microwave driving is from a coplanar waveguide made from gold. On the optical side, the waveguide is directly fabricated from focus-ion-beam milling out of the rare-earth ion doped crystal (^{171}Yb^{3+}:YVO$_4$). The physics is straight-forward, but the operation efficiency $\eta \sim 10^{-13}$ is quite low. The main reasons are three-fold: First, there are no microwave and optical resonators to enhance the light-matter interaction. The optical part is a waveguide directly inside the nanobeam. On the microwave side, the CPW drives a large portion of the chip, where the mode overlap between the driving volume and the nanobeam volume is tiny.

Second, the chip is operated at a finite magnetic field. This will broaden the spin linewidth and hence lower the microwave and atomic cooperativity. This leads to a smaller efficiency as well. The reason for a finite magnetic field is that the three-level system used to do transduction protocol needs a magnetic field to break the forbidden transition due to the selection rule. Details can be found in the supplementary information of the paper [53]. If the system uses π-polarization ($E//c-axis$), then a magnetic field is needed due to a forbidden transition at zero-field. If the system uses σ- polarization ($E//a-axis$) and only can optically access to one type of σ between σ_x and σ_y, phase cancellation will happen. Hence, a magnetic field is needed to split the levels and avoid signal cancellation.

Third, the optical nanobeam limits the optical pump power that can be sent into the device. This is because the nanobeam is a suspended structure and YVO and an insulating material, so the heat capacity is also not great at low temperatures. Since the pump will be absorbed by the ions, the heat generated heat can only dissipated via the two connecting bridge on the side. In the paper [53], the pump power used is only μW-level due to this reason.

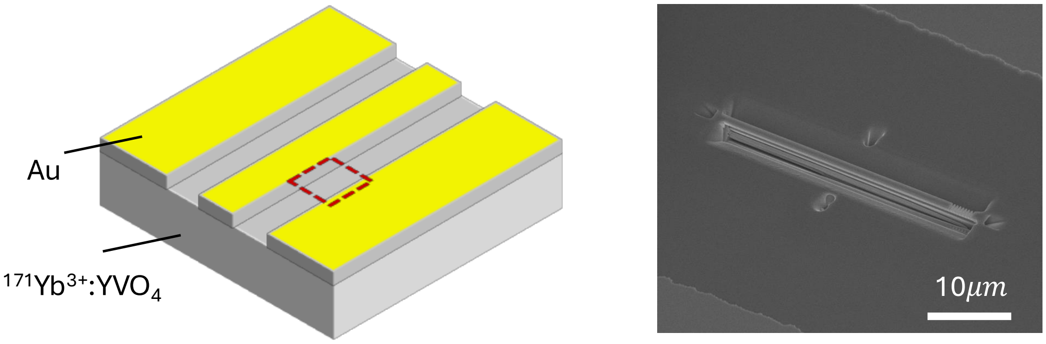

Figure 4.1: **Previous design v1.** The device consists of a coplanar waveguide (CPW) for microwave driving and a nanobeam optical waveguide for optical access. The CPW is fabricated out of Au. The nanobeam is fabricated from focus ion beam milling. The substrate is ytterbium-171 doped in yttrium orthovanadate crystal. More details can be found in [53].

4.2 Previous on-chip design v2

Learning from the first version of the device, the second device we have worked on aims to solve the heating issue and move the optical wavelength to the telecom-band. The device is shown in Fig. 4.2 [46]. The microwave side has a lumped-element resonator that capacitively couples to a CPW with an external coupling rate determined by the gap distance. The optical side has a photonic crystal cavity fabricated out of amorphous silicon (a-Si). Two photonic crystal mirrors are designed and fabricated to define a Fabry-Perot optical mode with the free-spectral range determined by the distance between the two mirror areas. More design and measurement details can be found in Dr. Jake Rochman's thesis [20]. Here, I will broadly discuss the result and what we can learn from this version of the device.

In this work, the REI-material used is Er:YVO_4, where the spins for the microwave interface are from the electronic spin states, not the electron-nuclear hyperfine transition. Therefore, to match the electron spin frequency to the microwave resonator frequency, an external magnetic field is utilized to Zeeman split the electronic state. Due to this reason, the spin transition linewidth is naturally broad ($\sim$ 65 MHz) contrasting to the hyperfine transition linewidth of typically sub MHz. With this in mind, the efficiency achieved with this design is $\eta = 5 \times 10^{-8}$, where the internal efficiency is around $\eta_{int} = 10^{-5}$ due to the non-ideal optical/microwave resonator couplings and optical grating coupler efficiency. The efficiency is largely improved from the first version design by five orders of magnitude. But it is still far away from any further applications with the transducers. The main limiting factor here is three-fold:

First, the microwave and optical mode overlap is small. Intuitively, the microwave wavelength is on the order of centimeters, whereas the optical wavelength is on the order of micrometers. Specifically, the optical mode is confined inside the a-Si waveguide, which the penetration is on the order of optical wavelength. Although the microwave field here is on-chip, the penetration depth is not the microwave wavelength scaling, but it will still spread out over 10 μm level both horizontally and vertically. This primarily limits the number of atoms that are actually involved in the transduction process. In other words, the actual microwave cooperativity is much smaller than measured numbers. In the paper [46], although we measured C_e=340 with the ground state spin. The actual used cooperativity is estimated as ~0.1 due to this huge mode mismatching reason.

Second, the REI-material used here is Er:YVO_4. Though it is a promising REI-material for transduction, it has a few orders of magnitude lower effective second-order non-linearity for the transduction process (see Section 3.5) than $^{171}Yb^{3+}$:YVO_4. The main reason for the smaller $\chi^{(2)}_{eff}$ is from the fact of using an electronic spin instead of the electron-nuclear type transition. The spin inhomogeneity is 65 MHz compared to 160 kHz, significantly lowering both C_e and C_a and hence decreasing the efficiency of the whole conversion process.

Third, there is a large factor between total efficiency (5×10^{-8}) and the internal efficiency (10^{-5}). This comes from the non-ideal couplings from both resonators and the optical grating coupler. This is mostly an engineering problem in the design and fabrication. But as the fabrication on both the microwave and optical sides require high quality factors, over-coupled regimes and near-unity efficiency on the grating coupler side, the yield of the production will inevitably become low due to the complexity from the fabrication side.

4.3 Previous on-chip design v3

With the previous experience in mind, I start to work with materials with high $\chi^{(2)}$ and also avoid utilizing the evanescent coupling on the optical side. This leads to combining the idea of a nanobeam optical resonator with microwave resonators together. With this idea, the chip is shown in Fig. 4.3 (unpublished). The microwave resonator is similar as the previous lumped-element design, but now with a U-shape inductor to surround the nanobeam for increasing the move overlap. On the optical part, learning from the worse evanescent coupling from hybrid systems, now the mode is fully inside the $^{171}Yb^{3+}$:YVO_4 crystal. The nanobeam is either with a

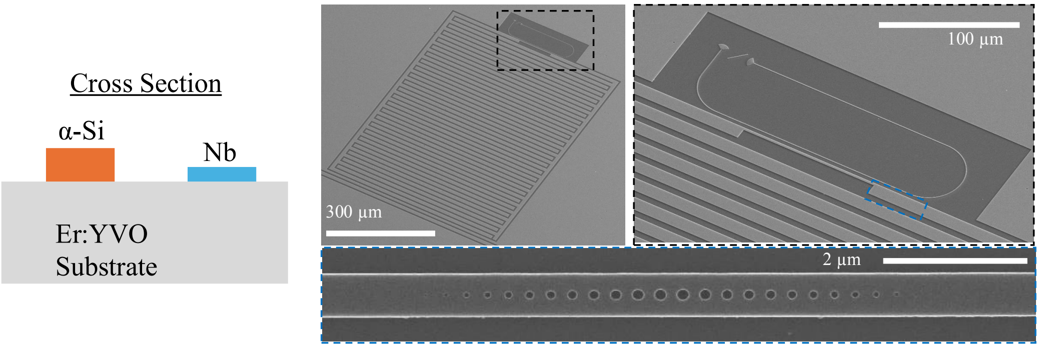

Figure 4.2: **Previous design v2.** The device consists of a lumped-element microwave resonator and photonic crystal cavity on top of doped in yttrium orthovanadate crystal. More details can be found in [46]

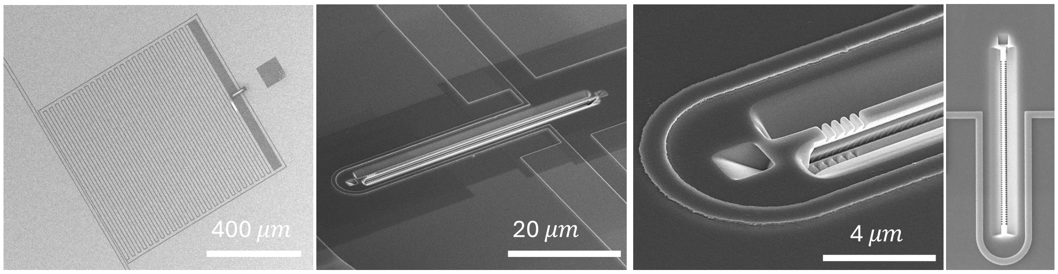

Figure 4.3: **Previous design v3.** The device consists of a nanobeam with either an optical waveguide or photon crystal cavity. A microwave resonator is formed by an interdigitated capacitor and a U-shape inductor. The whole pattern is on top of the yttrium-171 orthovanadate crystal.

photonic crystal mirror on the very end or with the full photonic crystal cavity milled on the whole nanobeam. The two preparations are because milling the full photonic crystal on a long suspended nanobeam is technically low-yield. It usually destroys the nanobeam due to the strong torque during milling. Another difficulty here is the double frequency matching on the optical and microwave sides. As the REI-material used here is with electron-nuclear typer transition, the frequencies are fixed. However, tuning both microwave and optical cavities in the current design are almost impossible. The way we have is the gas-tuning method. A layer of nitrogen will condense on top of the chip such that it changes the refractive index and hence shifts the mode frequency. Here, this gas-tuning can only bring one resonator on resonance, but not together. However, we can still investigate the system efficiency and see if this is a promising way to move forward with enough engineering efforts.

With the above discussions in mind, some calibration and measurements will be discussed below. Unlike the former two designs where the results could be found in each paper, the result of this design is unpublished. First, the device calibration results are shown in Fig. 4.4. After gas-tuning the optical resonator, the microwave resonance is at 3.56GHz with Q around 16k, about 1000 times spin inhomogeneity detuned from the excited state spin transition. At this large detuning, the coupling to ground state spin will happen at round 17 milli-Tesla as a 45-cut ^{171}Yb^{3+}:YVO$_4$ is used. By tuning the current to a pair of superconducting coils around the device, an anti-crossing coupling pattern appears on the microwave resonance, showing the ensemble ground-state spin coupling. A fitting pattern of this anti-crossing has been calculated which gives the spin ensemble coupling strength as 2.2MHz. This is about what we expect. A quick calculation is to compare with the previous on-chip device v2, where an ensemble coupling strength as 105 MHz is measured. Based on the g-factor differences, concentration differences and the angle misalignment due to the 45-cut, the ensemble coupling strength here is expected to be 3.7MHz. This is within a factor of 2 from the measurement results. However, as the ground state spin gets coupled here is not a ZEFOZ (zero first-order-Zeeman) transition, the spin inhomogeneity is much larger. A 70 MHz linewidth is extracted from the fitting, contrasting to a 200 kHz linewidth of the excited state spin clock transition. This number is also within the expectation, as again in the previous on-chip device v2, the spin transition used is with 65 MHz inhomogeneity, also not a ZEFOZ transition. On the optical side, the optical photonic crystal cavity after gas-tuning shows a quality factor of 3K. However, as the device is a long suspended nanobeam, the heating is quite significant. An optical inhomogeneity measured inside the nanobeam is 560 MHz with μW level optical power, contrasting to the 120 MHz linewidth measured from a cold bulk sample.

Having the optical and microwave resonator ready, the microwave-to-optical transduction signals are shown in Fig. 4.5. Even though the resonator is 1000 times the inhomogeneity detuned from the excited-state spin transition, transduction signal is still measured clearly from the excited-state spin at 3.37GHz. However, as the nanobeam can only access one type of σ transitions optically, The signal only happens at a finite magnetic field, which is a trade-off between the spin inhomogeneity and the separation from phase cancellation (see Supplementary materials of [53]) for more information). A simulation curve of this excited-state spin transition at different magnetic fields is plotted on top of the measurement results. The overlap proves that the signal is from the excited-state spins. However, since the transduction happened at some magnetic field, the spin linewidth will be broadened inevitably

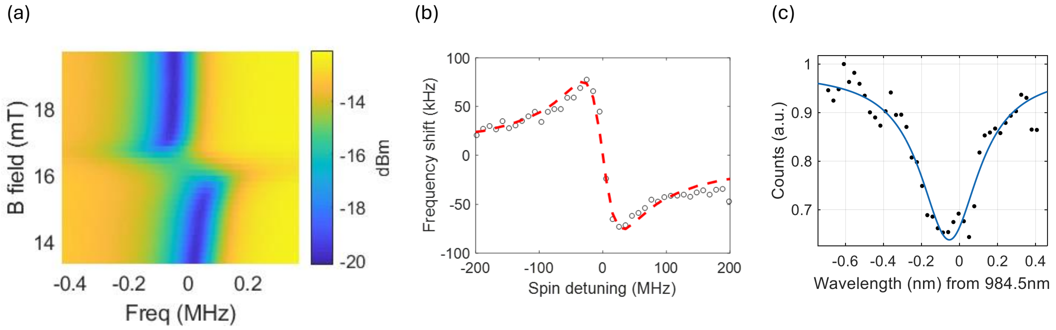

Figure 4.4: **Previous design v3 calibration.** (a) Microwave resonator transmission measurement at different external magnetic field. An anti-crossing happens when the resonator is aligned with the ground-state spin transition. (b) The fitted coupling pattern, showing the ensemble coupling strength as 2.2 MHz and ground-state spin inhomogeneity as 70 MHz. (c) The optical spectrum after gas tuning, showing the photonic mode with quality factor ~ 3000.

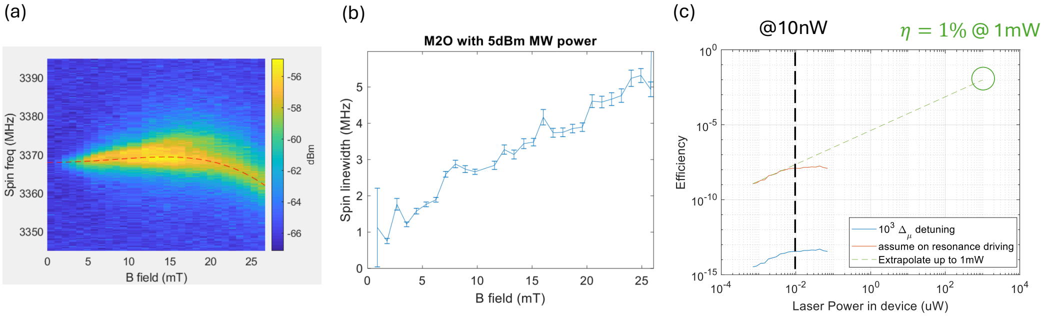

Figure 4.5: **Previous design v3 results.** (a) Microwave-to-optical transduction signal at the different external magnetic fields and input microwave frequencies. The red dashed line represents a simulation curve, calculating the spin transition frequency. (b) The spin inhomogeneity at different magnetic field, measured from the transduction signal in (a). (c) The measured transduction efficiency at different input pump powers.

to a few MHz level. Lastly, the transduction efficiencies are calibrated at different pump powers, shown in Fig. 4.5(c). The blue line represents the raw measurement results without any shifting or extrapolation. Based on the detuning we know, we can then calculate the expected efficiency if the resonator is on-resonance with the spin transition frequency. This is shown in the red line, where an expectation of 10^{-8} efficiency is expected at around 10 nW laser power to the device (after an estimate of the 45 coupler efficiency and the kappa ratio of the cavity). The dashed green line represents an extrapolation of the red line trend, which arrives at 1 % efficiency at 1 mW pump power in the device.

With these results presented, a conclusion can be drawn here that this design is still not promising. The reasons are three-fold.

First, the suspended nanobeam structure fundamentally limits the pump power to the device. As we saw from the pump power dependence measurements, the efficiency are promising if 1 mW pump power can be sent in. However, the heat dissipation is not ideal as there are only two connecting ports on each side for cooling down the long nanobeam. Optical inhomogeneities are measured to be broad with μW level before the device. The heating issue also will be present in the added noise property. As the efficiency is low, the added noise is not measured but is expected to be high. One solution to the heating problem is to fill in the milled trench with some materials such that the nanobeam is more thermally connected. One thought would be a spin-on glass, which has a smaller refractive index than YVO_4. However details need to be explored as the nanobeam will be unlikely to survive under the spin-coating process.

Second, the nanobeam only gives access to a single σ transition. This limits the operation to be with a finite external magnetic field, instead of a true zero-field operation. On the other side, the spin inhomogeneity will be broadened to a few MHz, which then losing the point of utilizing the narrow spin inhomogeneity, or equivalently large $\chi^{(2)}$, for the conversion process. A solution for this would be to use an a-cut crystal such that the two σ polarizations can be driven and collected together, but the oscillating magnetic field from the planar microwave resonator for the spin driving will be perpendicular to the allowed transition direction, hence, not working for this design.

Third, the microwave and optical resonance can not be tuned individually. From the data, the extrapolation and signal shifting by taking out the detuning factor shows 1% at 1 mW pump power, which looks promising. But the fact is the resonator is 1000 times spin inhomogeneity detuned from the actual spin transition frequency. More fabrication can be done to finally have a device with the correct microwave resonator frequency after gas-tuning, but the yield will be quite low. Another thought would be to post-tuning the microwave resonator frequency via a permanent way, such as shortening the capacitor length via focus ion beam milling. This should be doable in principle, but only a few chances at most, as the wire-bonding to the coplanar waveguide area is limited and each time the wires need to be cut off.

4.4 Motivation to the next generation device

Based on all the previous iterations shown in the above sections, we learn the suspended nanobeam structure is not ideal due to the limited cooling channel to the device. The hybrid device is also not ideal as the mode overlap from the evanescent coupling is very small, limiting the total number of REIs used in the conversion process. Better on-chip photonic structures are required, such as having an optical mode directly inside the REI material but not suspended. However, the fabrication methods that can be done will REI-materials are limited. On one side, there is still no published result on how to etch the usual host material (e.g., YSO and YVO). On the other side, there is no thin film of REI material commercially available. So all fabricated structures are from a bulk chip.

Therefore, instead of diving into the on-chip photonic mode limited by the fabrication methods currently, switching to a free-space optical mode would be beneficial. Because the structure will not rely on any suspended structure or evanescent coupling, the optical mode will be large to match the microwave mode. One would also get access to both σ polarizations by using a c-cut crystal and shining light in and out via the z-axis. In the future, incorporating an optical cavity is also doable as many groups in the world have demonstrated free-space optical cavities with REI-systems [45, 81, 82]. On the microwave side, we can still use the on-chip microwave resonator and coupling to the optical illumination area via a surrounding inductor to maximize the mode overlap.

With these thoughts, in the next chapter, I will focus on the next-generation device using free-space optical mode.

Chapter 5

NEW GENERATION TRANSDUCERS: DESIGN AND CALIBRATION

Here I will go through the design and calibrations in the microwave and optical domain of the new device. This is mostly adapted from the supplementary materials of our paper [78].

As discussed in the previous chapter, a free-space optical mode is chosen to work with instead of an on-chip photonic mode. With this, the fabrication process of the new chip design is largely simplified, which only consists of one layer of electron-beam lithography.

5.1 The microwave part

Design and fabrication

We start with a c-cut $^{171}\mathrm{Yb}^{3+}$:YVO_4 chip with 500 μm thickness. A c-cut crystal will allow us to drive the spin transition with σ_z polarization and also to access both σ-polarized optically. For the fabrication, 150 nm niobium is sputtered on top of the chip. The microwave resonator is fabricated based on the niobium layer with MaN-2403, which is then transferred to a 25 nm evaporated aluminum layer after lift-off. The aluminum behaves as a hard mask for the subsequent dry etch of niobium by reactive-ion etching in SF_6+Ar chemistry. The aluminum is finally removed with wet etch in aluminum etchant and hydrofluoric acid. The microwave resonator consists of an interdigitated capacitor and a circle-shaped inductor, as shown in Fig. 5.1. The capacitor is made by 10 μm wide niobium fingers and the inductor is made by 1 μm thin niobium wire. As the spin couples to the oscillating magnetic field, the circle-shaped inductor is used to confine the magnetic field and surround the optical mode. We notice the microwave is a single-port device, where a coplanar waveguide is directly connected to the shunt capacitor via a coupling capacitance. In this manner, we can change the coupling capacitance and hence making the resonator to be over-coupled regime for better microwave power injection to the resonator.

Meanwhile, the resonator aims to couple the excited-state spin transition at 3.3685 GHz. To make the resonance correct, other than fabricating the device to be roughly around the frequency, we also controllably shift the resonance frequency up closer

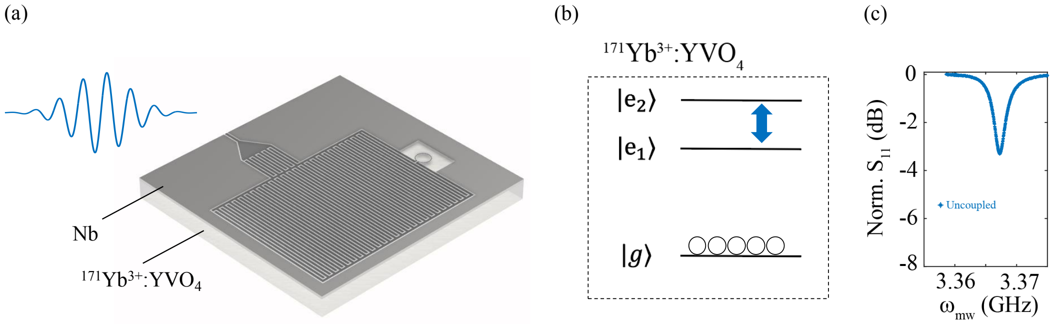

Figure 5.1: **The microwave part of the new transducer.** (a) The microwave resonator on top of ^{171}Yb^{3+}:YVO$_4$ chip. (b) Relevant energy levels for transduction. The microwave resonator aims to couple the excited-state spin transition between $|e_1\rangle$ and $|e_2\rangle$. (c) The microwave resonator calibration. At cold temperatures and no optical pumping, a bare resonator lineshape is measured with $Q_t = 1.1$K.

to our spin frequency after measuring once at base temperature. We used a Ga$^+$ focused ion-beam to mill parts of the interdigitated capacitor fingers away, which changed the shunt capacitance and thus the resonance frequency. The niobium layer is 150 nm, here we mill 250 nm to deterministically break the capacitor finger. A SEM picture of this focus ion beam (FIB) milling the capacitor is shown in Fig. 5.2. One can always run the simulation and find the exact length to cut on the capacitor for a precise frequency shifting. Here, a rough guidance for the milling is from the relationship between the capacitor finger length and the resonator frequency. We found about -6 MHz per μm in our design with a fixed 25 capacitor finger pairs and 30 μm inductor radius. The minus sign comes from the fact that a larger capacitor leads to a lower resonator frequency. Therefore, if we plan to shift the resonance by 20 MHz, then totally the capacitor needs to be shorter by ~ 3.3 μm, corresponding to $3.3\times50=167$ μm on a single capacitor finger. Experimentally, we only did a few times of this type of shifting and reached the correct frequency. With the limited number of data points, we found cutting 200 μm of the capacitor finger corresponds to 18 MHz and 400 μm corresponds to 42 MHz shifting, which roughly agrees with the quick calculation.

Another thing to mention is the quality factor before and after the FIB. The starting internal quality factors are already low, only a few thousand due to either a not prefect niobium film stress or the etcher condition. So we did not observe a clear change of the internal Q before and after this permanent tuning.

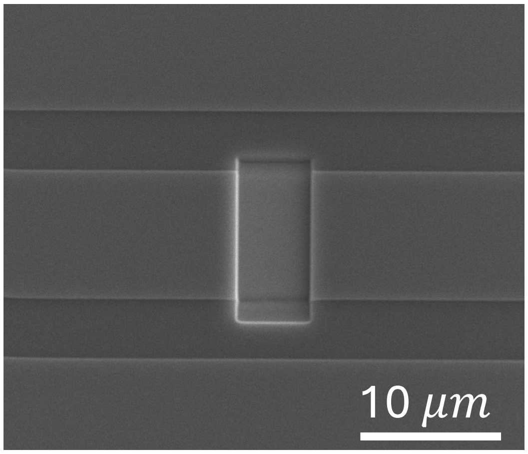

Figure 5.2: **Tuning the resonance via focus ion beam milling.** A SEM picture illustrating a capacitor finger after milled by Ga$^+$ focus ion beam, to shift the resonator frequency.

Simulation

As mentioned before, each resonator has an interdigitated capacitor formed by 25 capacitor finger pairs with 570 um in length and an inductor formed by a 1 um wide line with a 30 um bending radius. We simulate the microwave resonator mode profile as shown in Fig. 5.3. The coupling strength is almost constant within the 20 um beam radius (Fig. 5.3b). To get an estimate of the effective crystal length participating in transduction, we consider a cutoff at half of the cooperativity ($\sim \Sigma_i g_{e,i}^2$), where the center position shows $\sim$ 8 μm penetration depth (Fig. 5.3d). Out of the total magnetic field energy along all directions, $\sim$ 0.27 % of it is confined inside a 20 μm-radius 8 μm depth cylinder. In reality, there are complications due to the optical reabsorption of the crystal. Even with 8 μm thickness, the reabsorption is $\sim$ 35%. This roughly balances the 50% cutoff of the magnetic energy. Without unraveling the balance between the microwave mode cut-off and reabsorption, we find that using this 8 μm effective length in the simulations predicts the system behaviors well.

To calculate the ensemble coupling strength, we need to integrate all the atoms that couple to the microwave field. Although the single-atom coupling strength is inversely proportional to the mode volume of a cavity, the ensemble coupling strength is only related to the energy confinement ratio inside the REI material. Specifically, the total coupling strength goes as:

$$g_{e,tot}^2 = \sum_i g_i^2 \tag{5.1}$$

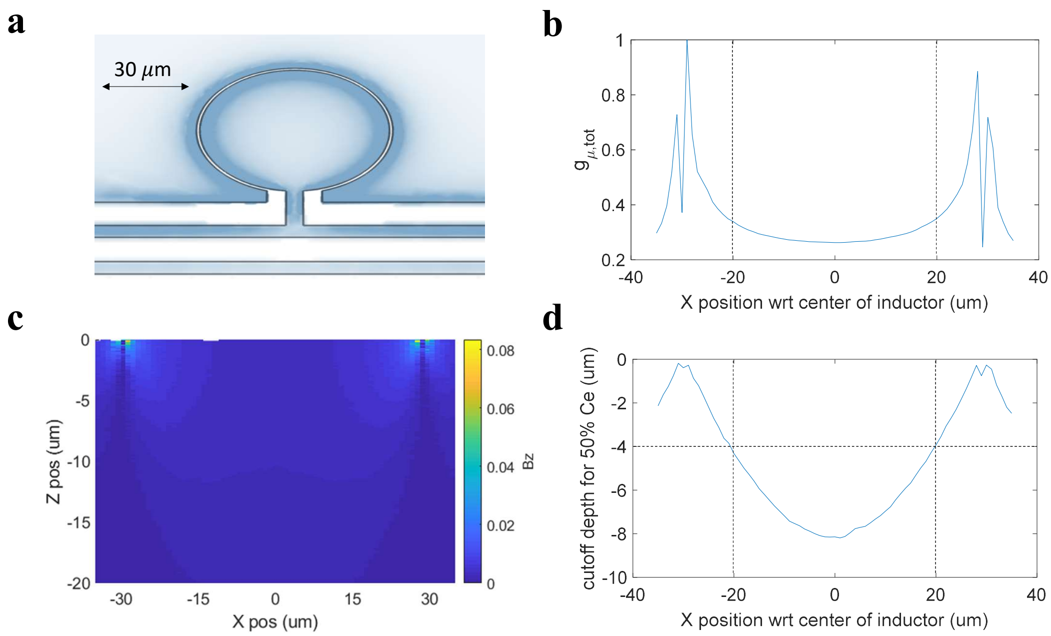

Figure 5.3: **Microwave resonator mode simulation.** (a) Top view showing the out-of-plane oscillating magnetic field, which couples to the excited state spin transition. (b) A horizontal cut through the center of the circular inductor, showing the coupling strength at each position on the diameter. (c) A vertical 2D plot showing the penetrating magnetic field strength through the center of the circular inductor. Note that there is no magnetic field along the z-axis right under the inductor as it is purely along the x-axis. (d) The cutoff depth for half of the ensemble cooperativity ($\sim \Sigma_i g_{e,i}^2$).

where the single spin coupling strength is

$$g_i = \sqrt{\frac{\omega_e \mu_0}{2\hbar}} \mu_{spin} \frac{1}{\sqrt{V_0}} \frac{B_i}{\sqrt{(|B_i|^2)_{max}}} \tag{5.2}$$

and μ_0 is the vacuum permeability. Putting the above equation into the ensemble equation and converting the discrete sums to integrals,

$$g_{e,tot}^2 = \frac{\omega_e \mu_0}{2\hbar} \mu_{spin}^2 \rho \eta \tag{5.3}$$

where we define the ratio of the resonator energy confinement to the transduction material η as,

$$\eta = \frac{\int_{mat} B^2 dV}{\int_{V_{tot}} |B|^2 dV}. \tag{5.4}$$

Apart from material properties, we find that the total ensemble spin-resonator coupling strength is only related to the energy confinement ratio, which has been

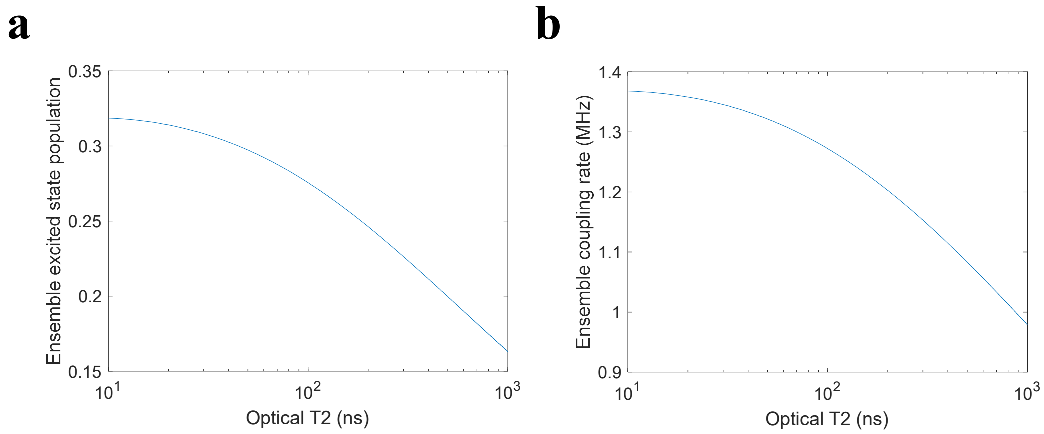

Figure 5.4: **Calculations on excited state population from optical pumping in the CW regime.** (a) The ensemble excited state population in the ensemble vs the optical T_2 of the transition, considering $\Omega = 1$ MHz optical pump. (b) The ensemble spin-resonator coupling strength ($g_{e,tot}$) vs the optical T_2 of the transition, considering $\Omega = 1$ MHz optical pump.

simulated to be 0.27% by considering the transduction volume to be a cylinder with radius 20 μm (equal to beam radius) and length of 8 μm (from the microwave mode simulations). Therefore, if all of the population is in the excited state, $g_{e,all} = 2.42$ MHz.

Next, we consider the population fraction pumped to the excited state, which depends on the optical pump power. To calculate this, we use the optical Bloch equations in steady state [83]:

$$\rho_{ee}(t \rightarrow \infty) = \frac{\Omega^2}{2\gamma_2\gamma_1} \frac{1}{1 + \frac{\Delta^2}{\gamma_2^2} + \frac{\Omega^2}{\gamma_2\gamma_1}} \tag{5.5}$$

where $\gamma_{1,2}$ are the population decay and coherence dephasing rates, respectively. Therefore, the ensemble excited state population for a given pump power can be calculated as:

$$\rho_{ee} = \frac{\int [\rho_{ee}(\Delta) \frac{1}{\sigma\sqrt{2\pi}} e^{-\frac{1}{2}\frac{\Delta^2}{\sigma^2}}] d\Delta}{\int [\frac{1}{\sigma\sqrt{2\pi}} e^{-\frac{1}{2}\frac{\Delta^2}{\sigma^2}}] d\Delta}. \tag{5.6}$$

Using $T_1 = 267$ μs measured from a thin crystal (avoiding radiative trapping) [75] and $T_2 = 140$ ns measured in another coherence experiment, we get $\rho_{ee} = 0.39$. With a CW pump, the crystal heating will cause the other ground states to be equally populated, and thus the remaining population in the transduction manifold will be

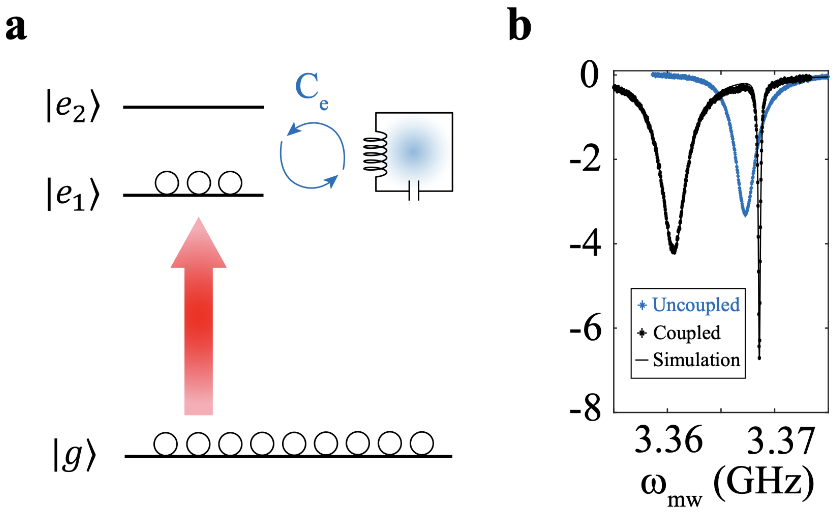

Figure 5.5: **Microwave spin-resonator coupling under a CW optical pump.** (a) The relevant energy levels and the schematic for the spin-resonator coupling. (b) Microwave resonator and ion-cavity coupling spectra. The blue curve shows the uncoupled microwave resonator with no pump light. The black curve shows the hybridized ion-cavity coupling, obtained by turning the 1 mW optical pump on and transferring the population to $|e_1\rangle$. The narrow dip corresponds to the spin and the broad dip to the resonator.

2/3. With this number, we get $g_{e,tot} = 2\pi \times 1.24$ MHz under an optical pump with strength $\Omega = 2\pi \times 1$ MHz.

Calibration

As the microwave resonator is fabricated to be on-resonance with the excited-state spin transition, there are no spin-resonator couplings when no optical pump is applied, as shown in Fig. 5.5. The bare cavity has a decay rate $\kappa_e = 2\pi \times$ 3MHz, which was deliberately designed to be broad enough to interface with most superconducting qubits [84]. With the pump light turned on, some populations is transferred to $|e_1\rangle$ from $|g\rangle$ and coupling to the microwave resonator is observed. To understand the data, we use the same model as built in Section 3.2. The efficiency can be calculated by an element inside the scattering matrix from the microwave input port to the optical output port. The microwave coupling pattern is basically another element inside the scattering matrix from the microwave input port to the microwave input port (e.g., S(5,5)). We fit the data with this theoretical model and extract the ensemble microwave cooperativity $C_e = 2.3$, where the coupling strength is 1.3 MHz under a 1 mW CW pump. We note the resonator frequency is shifted by a few MHz due to the CW light illumination, similarly as observed in [46]. Note

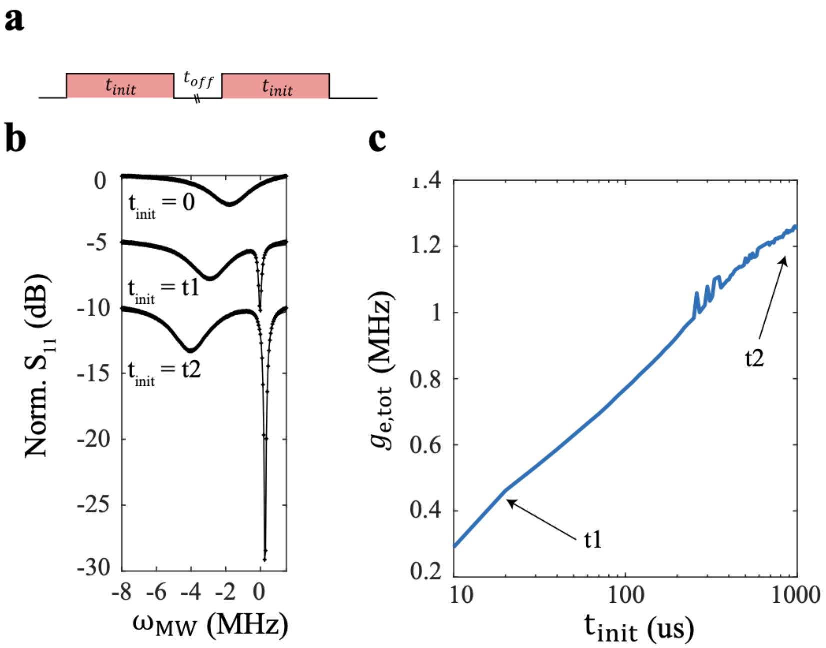

Figure 5.6: **Microwave spin-resonator coupling under a pulsed optical pump.** (a) Pulse sequence used in the experiments. (b) Microwave reflection spectra at different initialization times. Fits are plotted as solid lines on top of the data. Total coupling strength $g_{e,tot}$ is then extracted from each fit. (c) Fitted total coupling strength $g_{e,tot}$ at various initialization times.

that the expected coupling strength from the above calculation is 1.24 MHz, which matches the experimentally extracted value well.

To further understand the spin-resonator coupling in the time domain, we pulse the optical pump (400 μW) and measure the microwave reflection spectra at each 10us time window. At each time, a simulation of the microwave coupling pattern is generated to match the experimental data. The corresponding microwave resonator coupling strength, kappa ratio, and other relevant parameters are then extracted. First, the microwave resonator coupling spectral at different times is shown in Fig. 5.6. We did observe the separation between the broad resonator and the narrow spin is becoming further apart as the coupling strength increases. From the fit, we get the coupling strength at the very beginning is only about 0.3 MHz and finally saturates to the CW level.

Lastly, by running the fitting at each time, we also extract the microwave resonator frequency shifts due to the optical light illumination. We observe about 1 MHz frequency shift in 1 ms time with 400 μW optical pump power. The shift is not very

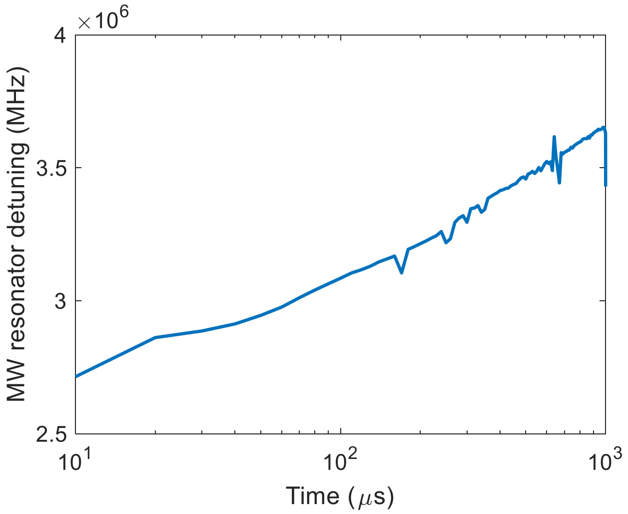

Figure 5.7: **Microwave resonator detuning under a pulsed optical pump].** The microwave resonator frequency versus the optical illumination time. About 1 MHz frequency shift is observed in 1 ms time with 400 μW optical pump power.

significant, likely due to the factor that the optical beam waist is 20 μm whereas the inductor circle has a radius of 30 μm. Therefore, the light that overlapped with the niobium inductor is small. From Gaussian beam calculation, the overlapped area corresponds to 0.15% of the input optical power (e.g., 0.6 μW overlapped on the inductor when shining 400 μW optical power).

5.2 The optical part

Design and fabrication

As discussed in Section 4.4, on-chip photonic modes have various problems based on the current fabrication techniques we have on REI materials. Therefore, here we move forward with the free-space optical mode. Specifically, we evaporate a 100 nm layer of gold on the back of the double-side polished chip, as shown in Fig. 5.8. One thing needs to mention is that a gold layer deposited directly on the REI material is not very sticky. Typically one would first evaporate a layer of another metal to link the chip and the gold. However, as we aim to use the good reflectivity of gold, another layer of metal will block the gold interface. Since the only step after gold evaporation is the wire bonding, no chemical process will be done afterward, so the gold layer can survive.

Using the Fresnel equation, one can get the reflectivity of the front surface and the

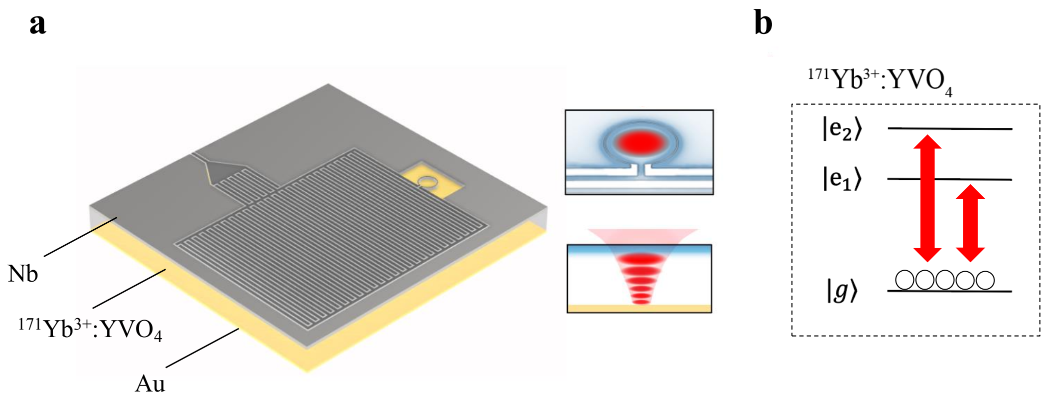

Figure 5.8: **Free-space optical mode.** (a) The free-space optical mode is formed by the front surface and gold layer reflection. (b) As the optical mode is broad, it couples to both the optical pump and transduction arm at the same time.

back surface as:

$$R = |\frac{n_1 - n_2}{n_1 + n_2}|^2 \tag{5.7}$$

where we only consider the perpendicular illumination case. With the equation, we get the front chip reflection is 11% and the gold layer reflection is 96% at 984 nm. Therefore, the optical finesse is determined based on the two reflectivities as:

$$\begin{aligned} \mathcal{F}_L &= \frac{2\pi}{-ln(R_1 R_2)} \\ \mathcal{F}_{airy} &= \frac{\pi}{2}[arcsin(\frac{1-\sqrt{R_1 R_2}}{2\sqrt[4]{R_1 R_2}})]^{-1} \end{aligned} \tag{5.8}$$

where the $\mathcal{F}_L$ labels the Lorentzian finesse and $\mathcal{F}_{airy}$ describes the linewidth from airy distribution (considering a sum of adjacent mode profiles) [85]. We note that at low finesse, it is better to consider the airy distribution as it captures the broadening from the surrounding modes as well. Based on the numbers we have, $\mathcal{F}_L = 2.8$ and $\mathcal{F}_{airy} = 2.5$, not much different.

Optical cooperativity

Remember cooperativity is the parameter we care about in the transduction process. Here we need to derive the ensemble optical cooperativity. Similar to the microwave domain, the ensemble cooperativity is also not dependent on mode volume, but only related to the energy confinement ratio.

We start with the ensemble total optical coupling strength, which can be written down as:

$$
\begin{aligned}
g_{o,tot}^2 &= \frac{\omega_o}{2\hbar\epsilon_r\epsilon_0} d_o^2 \rho\eta \\
\eta &= \frac{\int_{mat} E^2 dV}{\int_{V_{tot}} |E|^2 dV}
\end{aligned}
\tag{5.9}
$$

where d_o is the electric dipole moment for a certain transition, η is the electric field energy confinement ratio inside the REI material and ϵ_r is the relative permittivity. Then, by relating the optical dipole moment to the oscillator strength [58], we connect $g_{o,tot}$ to the optical absorption coefficient α:

$$
\begin{aligned}
C_o &= \frac{4g_{o,tot}^2}{\kappa_o\Gamma_o} = \frac{4g_{o,tot}^2\mathcal{F}}{2\pi \cdot FSR \cdot \Gamma_o} = \frac{4g_{o,tot}^2\mathcal{F} \cdot 2nL}{2\pi c\Gamma_o} \\
&= \frac{4\mathcal{F} \cdot 2nL}{2\pi c\Gamma_o} \cdot \frac{\omega_o}{2\hbar\epsilon_r\epsilon_0} d_o^2 \rho\eta \\
d_o^2 &= \frac{\hbar e^2}{2m\omega_o} f \\
f &= 4\pi\epsilon_0 \frac{mc}{\pi e^2} \frac{1}{\rho} n\pi\alpha_{peak} \frac{\Gamma_o}{2} \frac{1}{2\pi}.
\end{aligned}
\tag{5.10}
$$

And finally, we get:

$$
C_o = \frac{\alpha_{peak}\lambda Q\eta}{2n\pi} = \frac{\alpha_{peak}L\mathcal{F}\eta}{\pi}. \tag{5.11}
$$

We note that this result assumes no local correction factor in the oscillator strength equation and a Lorentzian lineshape of the absorption profile. We check this equation by comparing it with the measured C_o in previous works on similar REI systems [46, 65]. Both of them show a good agreement within a factor of 2. We note that for our transducer, the optical mode is fully inside the YVO$_4$ material, which gives $\eta = 1$.

Calibration

With the gold layer evaporated on the back of the chip, we can measure the optical Fabry-Perot effect from the two surface interferences, as shown in Fig. 5.9. Here, we clearly see the oscillation pattern measured on a optical spectrometer. The oscillation pattern is around every 0.5 nm which matches the chip thickness $FSR = \frac{c}{2nL}$. The Finesse from the fit gives $\mathcal{F} = 1.6$, similar to what we expected from the reflection of the two interfaces. On top of the oscillation pattern, we observe a small dip that corresponds to the optical absorption lines. Since the data is taken with a spectrometer with limited resolution ($\sim$ 10 GHz), the optical linewidths are not well resolved ($\sim$ 100 MHz). To better resolve the lines, we use a narrow linewidth Toptica

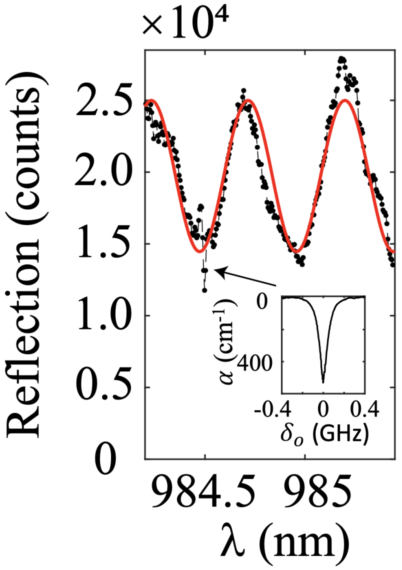

Figure 5.9: **Optical interference.** The oscillations show a period of ~ 0.5 nm, characteristic of a weak Fabry-Perot mode formed between the gold back mirror and the top surface of the 500 μm thick substrate. The red line shows a fit of $\mathcal{F}$ = 1.6. The zoom-in figure shows a finer scan on the optical lines, presenting a 92 MHz inhomogeneous linewidth and peak absorption coefficient at 530 cm^{-1}.

laser and scan the frequency across the optical absorption of a thinner sample (200 μm), detecting the transmitting light via an optical heterodyne measurement. This gives the inset figure of Fig. 5.9.

A full optical spectrum is shown in Fig. 5.10. As the crystal is c-cut, perpendicularly shining the optical light will only excite the E//a (σ) polarizations, which gives four lines in the optical spectra. For the transduction process, we only need to access two optical lines (labeled in red) and a microwave transition (labeled in blue). By scanning the laser across the lines, we observe the four transitions, with Γ_o = 92 MHz optical inhomogeneity and peak absorption coefficient α = 530 cm^{-1}. Based on the optical cooperativity equation derived above, we get $C_o = \frac{\alpha_{peak} L \mathcal{F} \eta}{\pi} = 0.22$ considering 8 μm microwave field penetration depth calculated in the Section 5.1.

Lastly, based on the laser beam waist (20 μm) shining on the chip, we can also calculate the free-space optical Rabi frequency for each pump power. Specifically, we have

$$\begin{aligned} \Omega &= \frac{d_o E}{h} \\ U &= \frac{1}{2}\epsilon E^2 V + \frac{1}{2\mu} B^2 V \end{aligned} \tag{5.12}$$

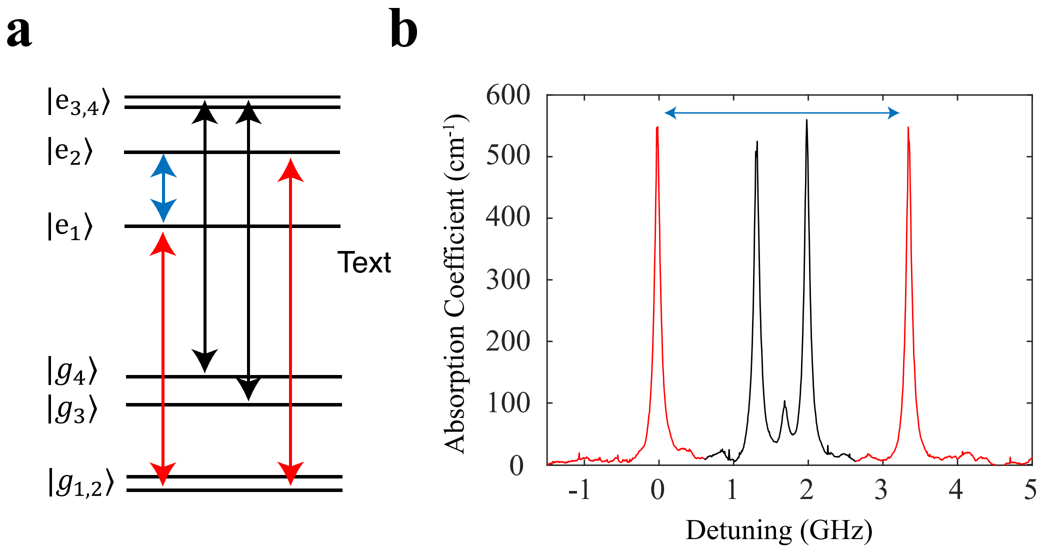

Figure 5.10: **Full energy levels and optical absorption spectrum.** (a) Energy levels of the $^2F_{7/2}(0)$ ($|g\rangle$) and $^2F_{5/2}(0)$ ($|e\rangle$) manifolds in $^{171}Yb^{3+}$:YVO4. The optical and microwave transitions used in the experiments are labeled red and blue, respectively. (b) Corresponding optical absorption spectrum, where red transitions are used for transduction. To better resolve the lines, this data was taken on a much thinner sample (200 μm) than the one used for transduction.

where V is the volume and U is the total electromagnetic energy. As the electric field and magnetic field energy are evenly split, we have

$$E = \sqrt{\frac{nP}{\epsilon Ac}} \tag{5.13}$$

where n is the refractive index of the REI material, P is the input optical power, A is the cross-section area and c is the speed of light. From a rough calculation, we have $A = \pi r_0^2$ where $r_0 = \frac{\omega_0}{2}\sqrt{2ln2}$ is the beam half-width half maximum. ω_0 is the beam waist of a Gaussian beam. Therefore, we get

$$\Omega = \frac{d}{h}\sqrt{\frac{nP}{\epsilon Ac}}. \tag{5.14}$$

Using our beam waist of 20 μm, we get the Rabi frequency as 1.2 MHz for 1 mW optical input power. However, we need to keep in mind that what we calculate here is an averaged Rabi frequency by assuming the cross-section area is πr_0^2 from the Gaussian beam. Different locations of the ions will experience different Rabi frequencies. For simplicity, we take the Rabi frequency as 1 MHz for the following calculations. With this, we get the atomic cooperativity is

$$C_a = \frac{4\Omega^2}{\Gamma_e \Gamma_o} = 0.22 \quad at \quad 1mW. \tag{5.15}$$

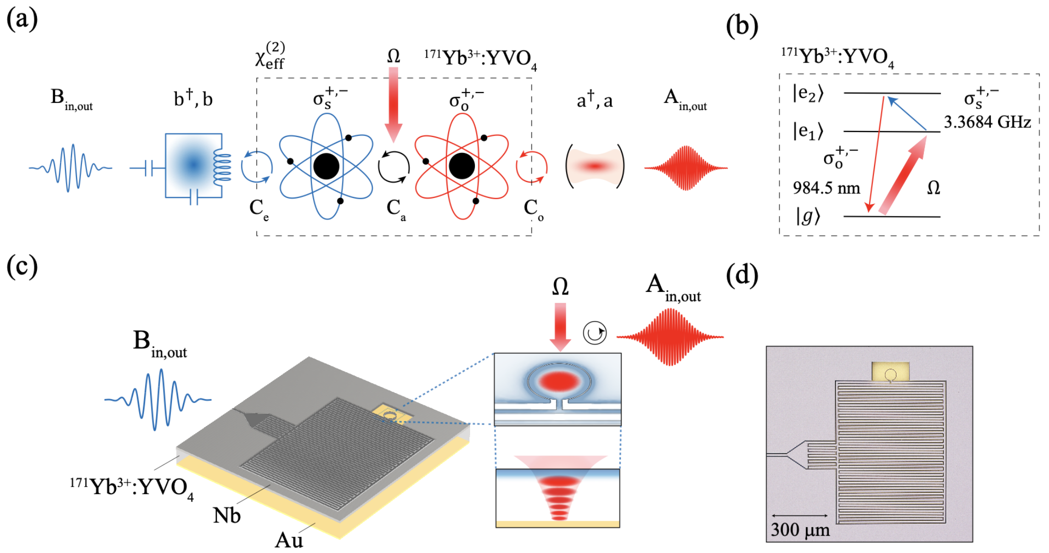

Figure 5.11: **Implementation of a REI-based on-chip microwave-to-optical transducer.** (a) Concept of REI-based transducer. $B_{in,out}$ and $A_{in,out}$ are the input/output microwave and optical modes, $b^\dagger, b$ and $a^\dagger, a$ are the microwave and optical cavity modes, C_e, C_a, and C_o are microwave, atomic and optical cooperativities, $\sigma_s^{+,-}$ and $\sigma_o^{+,-}$ are the spin and optical coherence operators. The black dashed box indicates the atomic part of the transduction process, where we define a material-dependent parameter $\chi^{(2)}_{eff}$. (b) The relevant energy levels of ^{171}Yb^{3+} :YVO$_4$, forming a V-system for transduction. (c) Transducer device schematic. Microwave photons are sent in and emitted out via a coplanar waveguide and coupling capacitor. The magnetic energy for coupling to spins is confined within the circular inductor, where the optical pump is focused through the center of the circle. A weak optical mode is formed between the front interface and the back gold mirror. (d) Optical image of a fabricated device.

5.3 The whole transducer

With the microwave and optical parts covered in the above sections, here is the whole transducer chip schematic, shown in Fig. 5.11. The microwave photon is first swapped into the excited-state spin coherence, converted into optical coherence via the optical pump, and finally swapped into the optical field. An optical image of the fabricated device is shown in Fig. 5.11d, where the gold color can be visually seen as the YVO$_4$ material is transparent in the visible wavelength. Notably, the whole chip absorption depth is $\alpha L = 26.5$. Any optical pump or transduced optical signal will be on-resonance with the atomic transitions, therefore experiencing these absorptions. However, the high optical depth can be avoided by utilizing the reflected optical pump, as shown in Fig. 5.12. Here, the transduced photons are generated based

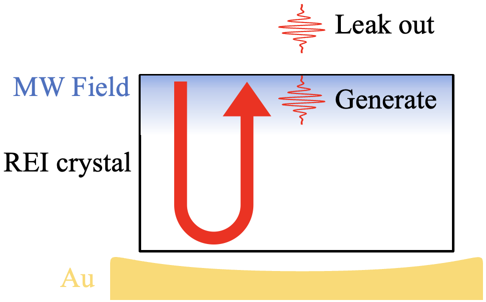

Figure 5.12: **Transduction process avoiding the high absorption.** By utilizing the reflected optical pump in the second path, transduction photons will be generated near the top surface of the chip and leak out without experiencing the high absorption profile of the REI material.

on the reflected pump in the second path, traveling towards the collection lens and exiting the chip close to the top surface, such that they experience little reabsorption.

Finally, the chip will be wire-bonded (3 wires on the signal pins and ≥ 10 wires on the ground) and clamped onto a homemade mount out of oxygen-free copper. Based on the calibrations on the microwave and optical parts, all the relevant parameters are listed in Fig. 5.13. With this, the chip is ready to perform transduction. The measurement results will be presented in the next chapter.

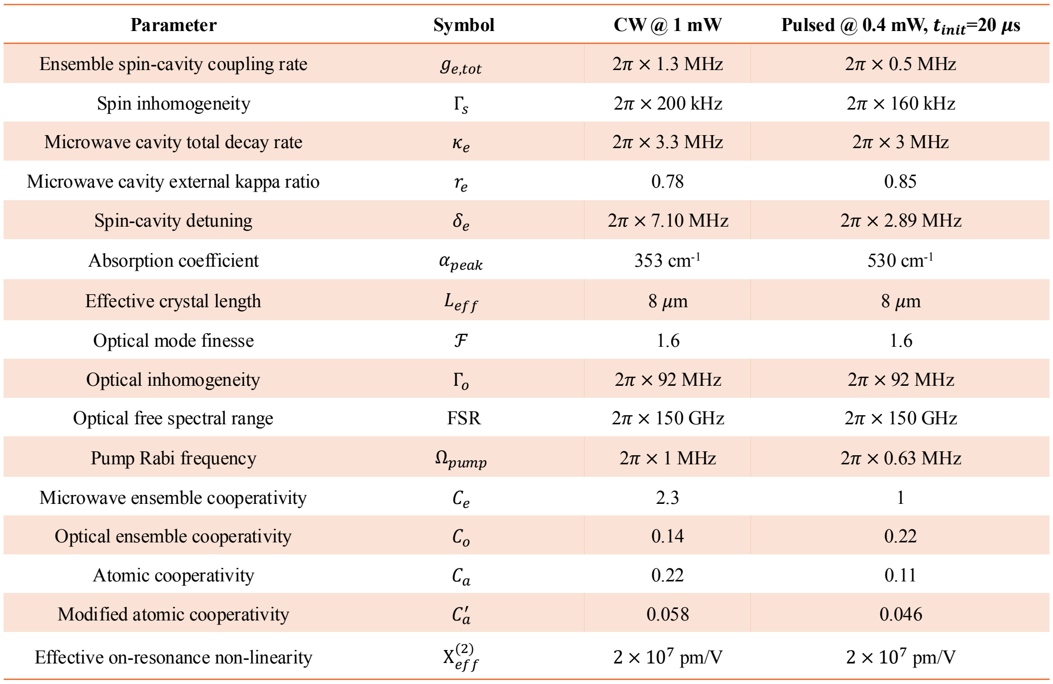

Parameter	**Symbol**	**CW @ 1 mW**	**Pulsed @ 0.4 mW, t_{init}=20 μs**
Ensemble spin-cavity coupling rate	$g_{e,tot}$	$2\pi \times 1.3$ MHz	$2\pi \times 0.5$ MHz
Spin inhomogeneity	Γ_s	$2\pi \times 200$ kHz	$2\pi \times 160$ kHz
Microwave cavity total decay rate	κ_e	$2\pi \times 3.3$ MHz	$2\pi \times 3$ MHz
Microwave cavity external kappa ratio	r_e	0.78	0.85
Spin-cavity detuning	δ_e	$2\pi \times 7.10$ MHz	$2\pi \times 2.89$ MHz
Absorption coefficient	α_{peak}	353 cm^{-1}	530 cm^{-1}
Effective crystal length	L_{eff}	8 μm	8 μm
Optical mode finesse	$\mathcal{F}$	1.6	1.6
Optical inhomogeneity	Γ_o	$2\pi \times 92$ MHz	$2\pi \times 92$ MHz
Optical free spectral range	FSR	$2\pi \times 150$ GHz	$2\pi \times 150$ GHz
Pump Rabi frequency	Ω_{pump}	$2\pi \times 1$ MHz	$2\pi \times 0.63$ MHz
Microwave ensemble cooperativity	C_e	2.3	1
Optical ensemble cooperativity	C_o	0.14	0.22
Atomic cooperativity	C_a	0.22	0.11
Modified atomic cooperativity	C_a'	0.058	0.046
Effective on-resonance non-linearity	$\mathrm{X}_{eff}^{(2)}$	2×10^7 pm/V	2×10^7 pm/V

Figure 5.13: **All relevant parameters of the transducer.** L_{eff} is obtained from microwave mode simulation. Ω_{pump} is calculated from the beam diameter. All other parameters are measured from independent experiments. The difference between the absorption coefficient α_{peak} is because of the difference of total populations inside the transduction manifold between CW and pulse mode.

Chapter 6

TRANSDUCER MEASUREMENTS

The chip design and calibration have been discussed in the previous chapter. Here, I will focus on the experimental results of the transduction measurements. Specifically, I will describe the experimental setup for the measurements, the transduction efficiency calibration in CW and pulsed operations, the added noise of the process and experiments towards the remote entanglement of superconducting qubits – transducer photon interference. This chapter is adapted from the main text of our paper [78].

6.1 Experimental setup

The experimental setup diagram is shown in Fig. 6.1. A master laser (Toptica DL Pro) is locked to a custom reference cavity (Stable laser systems) with 100 kHz linewidth via Pound-Drever-Hall (PDH) method. The pump laser (Moglabs CEL) is offset phase-locked (with Vescent D2-135) to the master laser. An AOM (Aerodiode model 6) shapes the optical pulses, and additionally provides a small frequency offset, useful for instance in creating the beatnote in Fig. 4a,b. An optical circulator (Precision micro-optics) sends light to the device and collects the reflected light. For CW M2O measurements the reflected light is beat with a local oscillator path from the same pump laser and the beatnote measured on a high speed photodiode (ALPHALAS UPD-35-IR-2), amplified and sent to a vector network analyzer (VNA, Copper Mountain C1209).

For pulsed, low photon count measurements, the reflected light is sent to a pump filtering setup shown in Fig. 6.1. Two narrow optical cavities (Stable laser systems) each with a linewidth of $\sim$ 2MHz and a free-spectral range of 20GHz do the majority of the filtering. Theoretically this provides $\sim$ 140dB of pump extinction, however there is still some residual leakage from unknown sources, possibly defects in fiber components that emit at frequencies outside the bands of the cavities. Thus an additional set of tunable broadband low and high pass filters (Semrock TLP01-995-25X36 and TSP01-995-25X36) placed between the two cavities are used to further extinguish the unwanted photons. Fiber isolators (OF-Link RHPII-980-H6-L-10-FA-Z5) are placed before the cavities to prevent back-reflections. To stabilize the cavities to the transduction frequency, they are periodically offset-locked (1s lock, 5s free-running). Fiber optical switches (Agiltron) are used to switch between the lock and free-running modes, and in the lock mode the cavities are locked to the pump laser, shifted up by the microwave frequency using an EOM (iXBlue NIR-MPX-LN-10). The filtered light is sent to a superconducting nanowire single photon detector (SNSPD, Photonspot), where the events are time-tagged (Swabian Time Tagger 20).

On the microwave side, the microwave input is generated by a CW source (BNC Model 845) and gated by a high-speed switch (Kratos F192A-9) for pulsed operation. The input line in the dilution refrigerator (Bluefors LD250) is attenuated as shown in Extended Data Fig. 9 for a total of 70dB attenuation down to the mixing chamber (MXC) plate held at 14mK with the laser off. Two circulators (LNF-CIC2.8_4.3A) each with approximately 20dB isolation block the thermal noise coming from the un-attenuated output line. The second port on the first circulator is connected to the device coplanar waveguide to send in and read out the microwave photons in reflection. The output line consists of superconducting NbTi cables connected from the MXC plate to the HEMT (LNF-LNC2_6B), which is then connected up to room-temperature amplifiers. See Supplementary Information section 1 for detailed calibration on the exact gains and losses of the microwave lines.

For pulsed microwave resonator thermometry measurements, microwave resonator mode occupation is detected via mixing (Marki Microwave IQ0307LXP) the signal coming from the HEMT down to 20MHz. This is amplified (2x SRS-445A) and measured on a digitizer (Alazar ATS9130).

The device is mounted in the MXC onto a copper post. The light is coupled from a 1060xp fiber to the device and back via a pair of aspheric lenses, focusing the light to a 4μm beam waist at the gold layer, resulting in a 20μm beam waist at the chip surface.

For the interconnected transducer experiment (both operating with CW M2O), we simultaneously send in weak microwave photons to each transducer with two synchronized microwave generators. Separate optical pumps are also generated by splitting the pump lasers into two optical paths, each focused onto the circular transduction zone of the respective transducers. Due to the limited laser power, each transducer operates with $\sim 400\ \mu$W pump power. The transduced photons from each transducer, along with the reflected pumps, are collected and combined via a beam-splitter. On one of the output ports, we measure the pump photon interference. The other output port goes through a high-extinction spectral filter

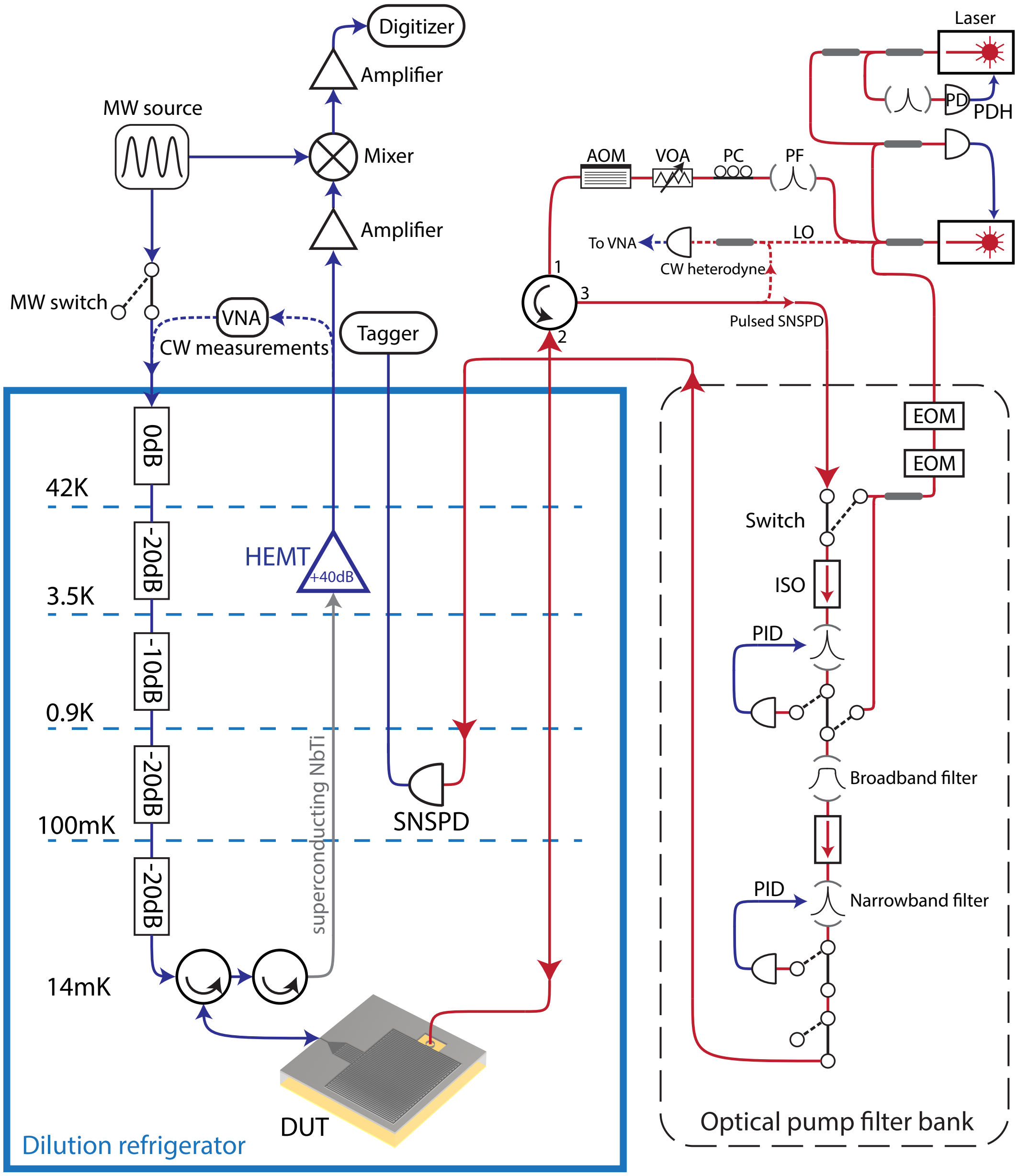

Figure 6.1: **Experimental setup.** BS: beamsplitter of various ratios. PD: photodetector. PF: optical pre-filter. LO: Local oscillator. PC: Polarization controller. PDH: Pound-Drever-Hall locking. VOA: variable optical attenuator. AOM: Acousto-optic modulator. ISO: optical isolator. PID: proportional integral derivative locking. EOM: electro-optic modulator. SNSPD: superconducting nanowire single photon detector. HEMT: high electron-mobility transistor. DUT: device under test. Blue lines indicate microwave cables, red lines indicate optical fibers.

to another SNSPD to detect only the interference between two transduced photons (Fig. 4a). Based on the phase measured on the pump interference, we correct the initial phase and average the interference over 1000 data traces for both the pump detection and the transduction detection.

For the cascaded O2M and M2O experiments, separate optical pumps are generated by splitting the pump lasers into two optical paths. The O2M path goes through an EOM and is sent to the O2M chip. Similarly, due to the limited laser power, each transducer operates with $\sim 400\ \mu$W pump power. The output of the final M2O signal is split into two paths for heterodyne detection of the cascaded O2M-M2O, and transduced photon interference through a high-extinction spectral filter.

6.2 Efficiency

CW regime

We characterize transduction first with a continuous-wave (CW) optical pump and microwave input (Fig. 6.2). With optical heterodyne measurements, we obtain a peak chip transduction efficiency of 1.1% under 1 mW of pump power ($C_a = 0.22$), calibrated by two different methods that will be discussed later in this chapter. The narrower peak at the center of Fig. 6.2 corresponds to the spin transition and the broader peak at $\delta_{MW} = 2\pi \times -7.1$ MHz corresponds to the microwave resonator. The data agrees with the simulation using

$$\eta = \eta_e \eta_o \frac{4 C_e C_a C_o}{((1 + C_e) * (1 + C_o) + C_a)^2} \tag{6.1}$$

where $\eta_{e,o}$ is the kappa ratio on the optical and microwave ports. Details can be found in Chapter 3. As the conversion process is reciprocal, similar efficiency is also achieved by sending in optical photons and detecting the transduced microwave signal (Fig. 6.2b).

At the same pump power, both input microwave and pump frequencies are scanned to reveal the signal structure, where the maximum appears when both the optical pump and microwave input are on resonance with the atomic transitions (Fig. 6.3).

Lastly, with a magnetic coil surrounding the chip, we scan the external magnetic field strength and found the highest efficiency is at zero-field. Therefore, here and in all further experiments, no external magnetic field is used. The spin transition frequency is shifted at different magnetic fields, which is well simulated from the effective spin Hamiltonian model [55].

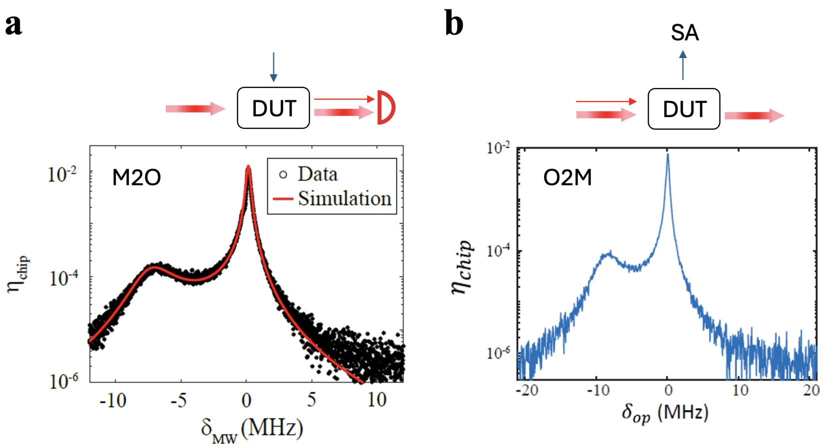

Figure 6.2: **Conversion between microwave and optical fields in CW regime.** (a) CW mode microwave-to-optical (M2O) transduction efficiency with 1 mW optical pump at different input microwave frequencies. The two peaks correspond to the spin at the center and microwave resonator at $\delta_{MW} = 2\pi\times-7.1$ MHz. (b) Optical-to-Microwave (O2M) chip efficiency at various input optical frequencies. The optimal point is when the difference between the input and pump frequencies is equal to the spin frequency. The two peaks correspond to the spin and resonator contributions, similar to (a). Here the pump is on the $|g\rangle - |e_1\rangle$ transition, and the input optical photons are on the $|g\rangle - |e_2\rangle$ transition. SA: spectrum analyzer.

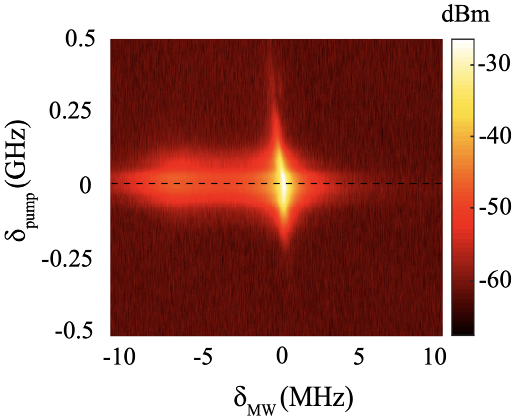

Figure 6.3: **Double frequency scan of the on-resonance transduction signal.** Microwave-to-optical transduction signals under various optical pump and microwave input frequencies. The dashed line is the data shown in Fig. 6.2a, which is also the pump frequency used in later experiments.

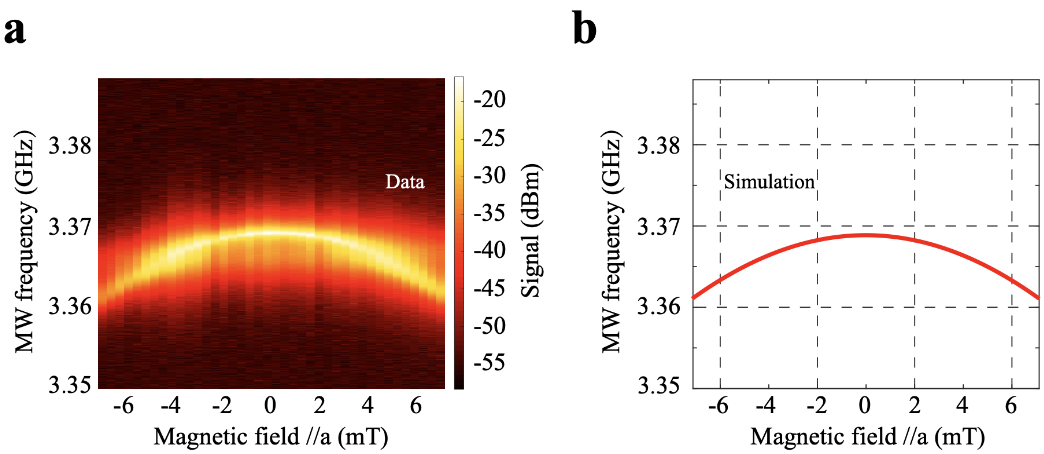

Figure 6.4: **Double frequency scan of the on-resonance transduction signal.** (a) Transduction signal measured by heterodyne with varying offset magnetic field along crystal a-axis. The signal broadens at ± 4mT due to the resonant spin and resonator coupling. (b) Simulated excited state spin transition frequency under different offset magnetic fields.

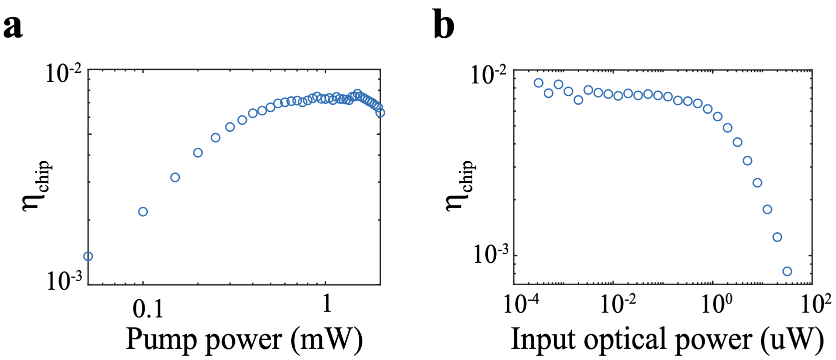

Figure 6.5: **Optical to microwave transduction at various pump power and input photon flux.** (a) Efficiency vs. pump power. (b) Efficiency vs. input optical power. A drop in efficiency is observed when input powers are higher than $\sim 1\ \mu$W due to the finite number of atoms in the system.

On the O2M side, we scan the input optical pump power and the input optical strength. A linear increase between the O2M efficiency and the pump power is found. On the input optical strength side, we found a saturation level of about 1 μW, which is due to the finite atomic ensemble size. We note that a similar effect has been observed in the microwave domain as well when performing the M2O experiments [46].

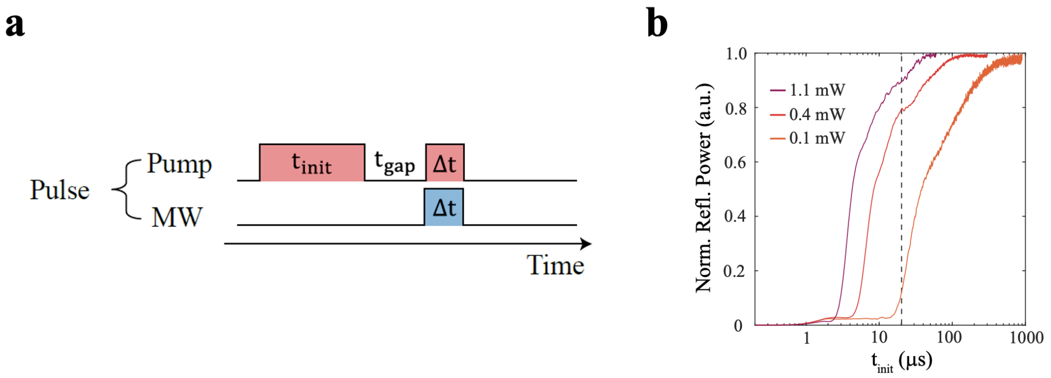

Figure 6.6: **Pulse sequence and optical initialization.** (a) Pulse sequence consisting of an optical initialization and short transduction window. (b) Optical saturation effect with different pump powers. The dashed vertical line indicates the initialization time used in the experiments.

Pulsed regime

To minimize the added noise generated from undesirable heating of the system under CW operation, we implement a pulsed protocol. The protocol consists of two parts, optical initialization with duration t_{init} and a transduction probe with duration Δt separated from the initialization pulse by t_{gap} (Fig. 6.6a). The initialization pulse is required in order to initialize the system with high enough C_e (as shown in Fig. 5.6), and to saturate the strong crystal absorption which enables round trip propagation of the pump (Fig. 5.12). To further study round-trip propagation, we send in an optical pulse, and detect the output optical signal on a single photon detector. As the optical frequency is on resonance with the atomic transitions, photons will be absorbed and hence no light will pass through the crystal until the absorption is saturated by enough pump power or pulse time due to the optical saturation effect. The data is shown in Fig. 6.6b where the initialization time and different optical pump power are explored. With enough pump power (≥0.4 mW), an initialization time of 20 μs is enough to enable the round-trip propagation of the pump.

To investigate the actual required initialization time in M2O experiments, we scan it with a fixed $\Delta t = 2$ μs, where the increasing trend is due to the combination of the aforementioned optical saturation and increasing population of $|e_1\rangle$ (Fig. 6.7). One question would be asked is that: what if there is no optical initialization? This question can be answer by sweeping the t$_{gap}$ in the pulse sequence, as the gap time is longer, the initialization effect will be diminishing. The data is shown in Fig. 6.7, where a fast exponential decay on the time scale of 40 μs is measured. The optical T$_1$

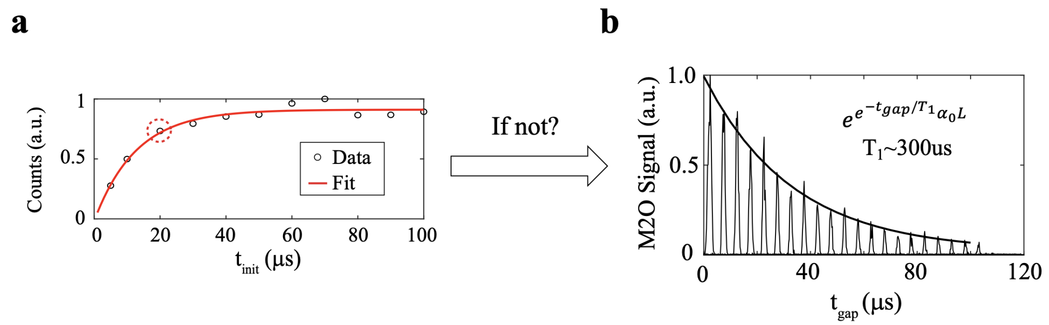

Figure 6.7: **Transduction signal versus optical initialization and gap time.** (a) Sweep of initialization time t_{init} with transduction time Δt = 2 μs, and a phenomenological exponential fit. (b) Experimental data for case (a) with $t_{init} = 20\mu s$ and $\Delta t = 2\mu s$. The decreased transduction signal is due to a combination of the optical T1 decay of the excited state population and the recovered optical absorption of the pump. In this regime, the transduction efficiency is linear with the pump power. Therefore, $\eta \propto P_{pump} \propto e^{-N\alpha_0 L} \propto e^{e^{-t_{gap}/T_1}\alpha_0 L}$. This 'exponential of exponential' behavior makes the decay faster than the optical T_1 time.

is 300 μs level without coherence trapping, much longer than this decay pattern. The reason here is the optical absorption. As illustrated in Fig. 5.12, the transduction is generated based on the reflected pump. As the initialization effect disappears, the pump experiences an absorption with the format of $e^{-\alpha L}$, where α is linear with the number of atoms. Therefore, the alpha is undergoing another exponential decay with the optical T_1. This leads to this 'exponential-of-exponential' behavior. This measurement also supports the reasoning for an initialization in the beginning of the pulses.

After understanding the initialization pulse, we study the microwave bandwidth of the transducer by sweeping the transduction probe length with fixed $t_{init} = 20$ μs, where a 3 dB suppression time of $\sim$ 2 μs was measured (Fig. 6.8a), showing a 500 kHz operation bandwidth. Finally, the pump power is swept, where each data point is optimized for the highest efficiency with respect to the input microwave frequency and initialization time between 10 μs and 1 ms (Fig.6.7). The initialization time must be increased for lower powers in order to sufficiently saturate the atoms and populate the excited state. A simulation (red) is shown on top of the data points. In this power regime, the efficiency changes roughly linearly with pump power. To obtain the highest efficiencies, we set $t_{gap} = 0$, and the pump and microwave pulses with duration Δt are temporally overlapping for all experiments above.

However, these parameters can be tuned. As the pump and input photons are first

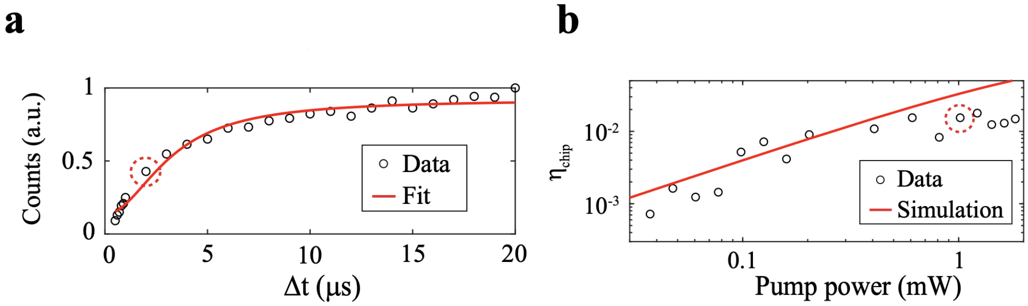

Figure 6.8: **Transduction signal versus optical initialization and gap time.** (a) Bandwidth characterization by sweeping Δt with t_{init} = 20 μs, and a bandwidth fit in the frequency domain. (f) Pulse mode efficiency with varying pump power and a simulation. The red circles in (a), (b) and Fig. 6.7a are under the same experimental conditions, e.g., (a) is measured with t_{init} = 20 μs and a pump power of 1 mW.

converted to atomic coherence, photons can be temporarily stored in the atoms. We demonstrate this by adding a temporal offset between the optical pump and microwave input during the transduction probe window and find that the efficiency decays due to the decoherence of the optical and spin transitions, depending on whichever pulse comes first (Fig. 6.9). This is potentially useful in temporally separating the optical pump, alleviating the need for spectral filtering, and also may lead to a transducer with a built-in quantum memory.

6.3 Added noise referred to the input

To characterize the added noise during the transduction process, we send in a single classical microwave photon per pulse and measure the transduced optical photon on a superconducting nanowire single photon detector (SNSPD) through a high-extinction spectral filter that selectively attenuates the reflected pump light. With a 20 μs initialization time, 2 μs transduction window, and 10 ms wait time, we measure the transduced photon with an added noise referred to the input of 1.24 photons ($N_{add,RTI}$ = 1.24(9)) and an efficiency of 0.76‰, shown in Fig. 6.10.

A zoom-out data from Fig. 6.10 is shown in Fig. 6.11a, two distinct noise processes are observed with different time-domain responses, as visualized in Fig. 6.11b. The population is originally in the ground state where part of it gets excited to $|e_1\rangle$ during the initialization pulse. Even in the absence of an input microwave photon, that population can undergo further processes to produce transduced noise photons.

One type of process is spin-phonon coupling, where the spins couple to a phonon bath, transferring some population to $|e_2\rangle$. Then the population decays from $|e_2\rangle$ to

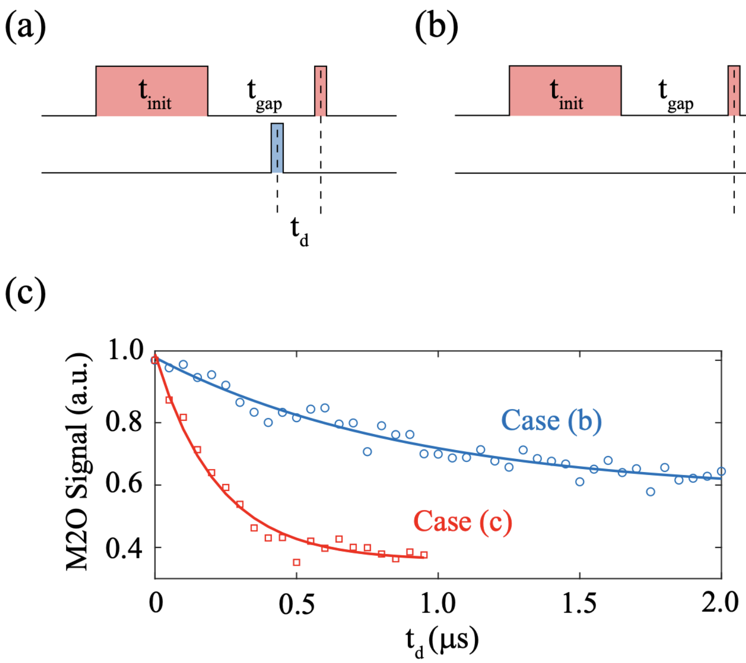

Figure 6.9: **Different pulse sequences for transduction.** (a) Transduction pulse sequence with a delay t_d between an early microwave input and late optical pump. (b) Transduction pulse sequence with a delay t_d between an early optical pump and a late microwave input. Because the optical/microwave photons will be first converted to optical/spin coherence, a delay to temporally separate the two short transduction pulses will preserve the efficiency as long as it is within the system coherence time. (c) Experimental data for cases (a) and (b) with $t_{init} = 20\mu s$ and $\Delta t = 200ns$. A $t_{gap} = 10\mu s$ is used here to significantly separate the transduction window away from the optical initialization pulse. With an early microwave input, a spin memory time of $T_{m,spin}$ = 910 ± 140 ns is measured. Whereas with an early optical pump, an optical memory time of $T_{m,op}$ = 140 ± 25 ns is measured.

$|g\rangle$, which produces photoluminescence (PL) at the transduction frequency (Supplementary Information section 9). We note that because of the large optical depth, the PL will experience radiation trapping [86] which results in an extended decay time (from 267 to 672 μs) and an increase of the PL before the trapping time. PL measurements in bulk material yield the same count rates (the black line in Fig. 6.11), thus confirming that this process is independent of the transducer. Furthermore, we calculate an order-of-magnitude estimate of about 1 to 100 Hz of PL given an estimated spin-phonon coupling rate and our detection efficiencies (discussed later in this chapter), which roughly agrees with our measured count rates.

Another type of coupling is spin-resonator coupling, the same mechanism by which input microwave photons are transduced, where any thermal photons will also be

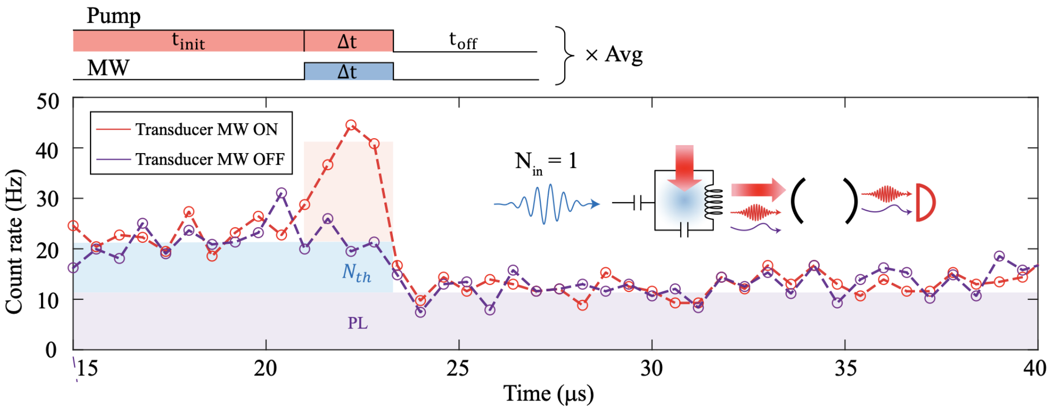

Figure 6.10: **Transduction from a single classical microwave photon.** Transduced optical photon detection on a superconducting nanowire single photon detector (SNSPD) with a single classical microwave input photon per pulse. The pulse sequence is composed of a 20 μs-long initialization time and a 2 μs-long transduction probe with 0.4 mW peak pump power.

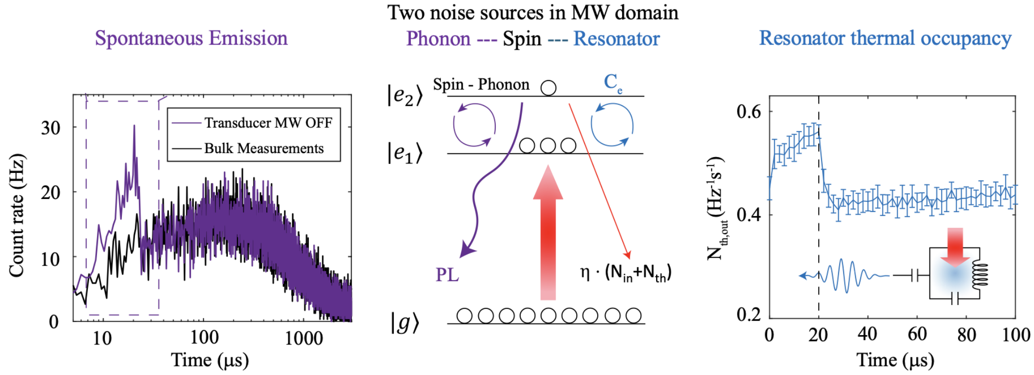

Figure 6.11: **Noise model of the transducer.** (a) Zoomed-out histogram of Fig. 6.10, revealing the photo-luminescence (PL) noise in the transduction zone (purple), and PL measured in bulk under the same conditions (black). (b) Diagram of transduction noise composition. An optical pump populates $|e_1\rangle$ and noise photons can be generated in two ways: thermal microwave photons converted out via transduction (blue), and spin-phonon coupling that generates PL (purple). (c) Microwave resonator thermometry with 20 μs initialization time and 10 ms wait time.

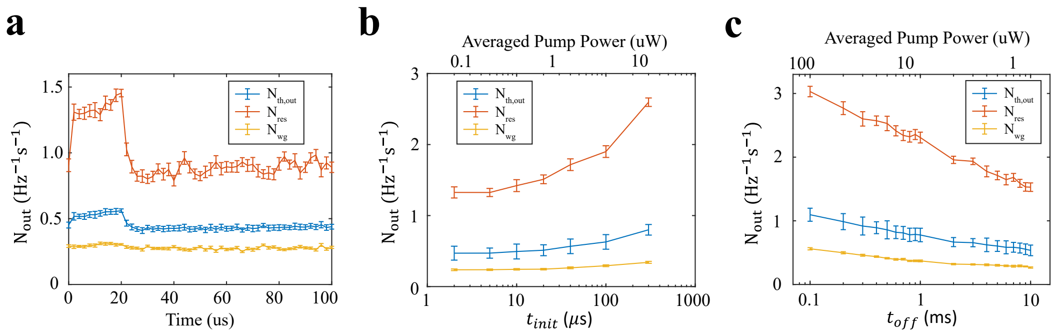

Figure 6.12: **Thermal noise characterization with different pulse parameters.** (a) N_{out} from microwave thermometry measurements vs. time, where $N_{th,out}$ is the same curve as shown in Fig. 3d. (b) N_{out} at various initialization times with fixed t_{off}=10 ms. (c) N_{out} at various t_{off} with fixed t_{init}=20 μs.

transduced out, similarly as any input microwave photons. This noise is only present when the pump is on, in contrast to the PL. To investigate this, we directly measure the microwave output noise power from the chip under 20 μs initialization time and 10 ms wait time (Fig. 6.11). From the calibrated gain and added noise of the output chain, we extract $N_{th,out}$ from resonator thermometry, which roughly matches the detected noise photons in SNSPD measurements (discussed later in this chapter). Thus, there are two ways the resonator can be heated: direct absorption of light by the superconductor, or indirectly from the substrate. In the regime where the superconductor absorbs the light, there is a sudden heating and cooling as the light is turned on and off. On the other hand, there is a slower heating from the substrate that increases as the wait time between pulses is decreased (Fig. 6.12). From this, we conclude that the measured N_{th} in Fig. 6.10 is transduced noisy photons from the thermal bath of the microwave resonator and waveguide.

To determine the optimal parameters with the smallest added noise summarized in Fig. 6.13, we measure the noise at various experimental parameters. First, we sweep the off times t_{off} between the pulses and observe an increase of the noise at a turning point of around 1 ms (Fig. 6.14). This indicates the average heating can be suppressed by longer off time, but finally, the noise will be limited by the instantaneous heating.

Returning to t_{off} = 10 ms, we also sweep the peak pump power (Fig. 6.15). In the high-power regime, thermal noise is dominant as expected as the instantaneous heating is related to the peak power. However, in the low-power regime, PL is dominant as efficiency drops quickly due to the de-population and re-absorption

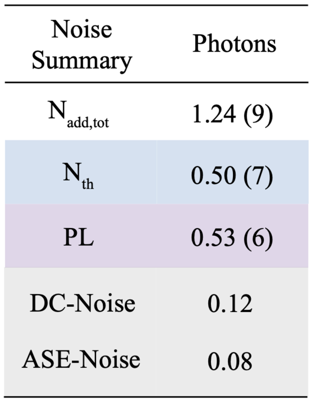

Noise Summary	Photons
$N_{add,tot}$	1.24 (9)
N_{th}	0.50 (7)
PL	0.53 (6)
DC-Noise	0.12
ASE-Noise	0.08

Figure 6.13: **Added noise summary.** A decomposition of all the added noise sources.

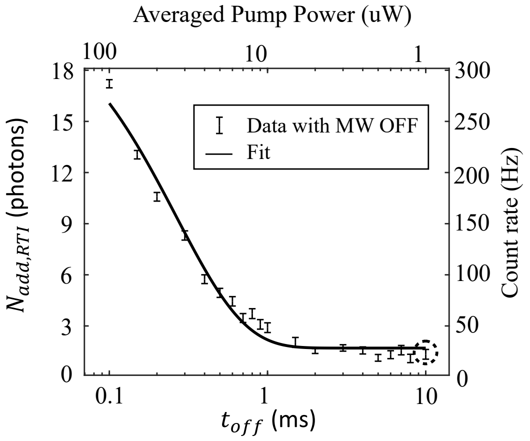

Figure 6.14: **Total added noise at various pulse off times.** Noise measurements with fixed t_{init}=20 μs using photon counting measurements. An increase of the noise flux is observed at a turn-over time of around 1 ms. We use a phenomenological exponential curve to fit and capture the key feature.

processes. The PL scattering rate gets lower linearly with the population, but the absorption goes exponentially with the population. This makes the refer-to-input PL noise goes up at lower power.

Higher pump powers lead to higher efficiencies, at the cost of increased added noise. Due to this interplay, the optimal peak power is found at an intermediate 400 μW. Additionally, for applications, a high repetition rate is desirable. To increase this while still keeping the noise reasonably low, we can first shorten t_{off} to 2 ms, then add multiple consecutive transduction pulses after a single initialization. The benefit here is that multiple attempts of transduction can be applied while the effect

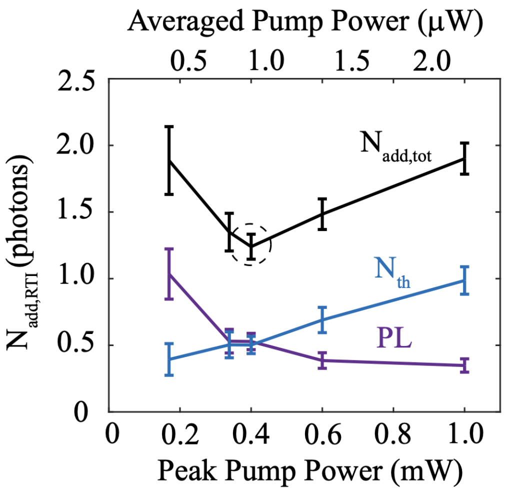

Figure 6.15: **Total added noise at various pump powers.** An optimal pump power is found due to the interplay between higher thermal noise in high-power regime and higher PL noise referred to the input in low-power regime.

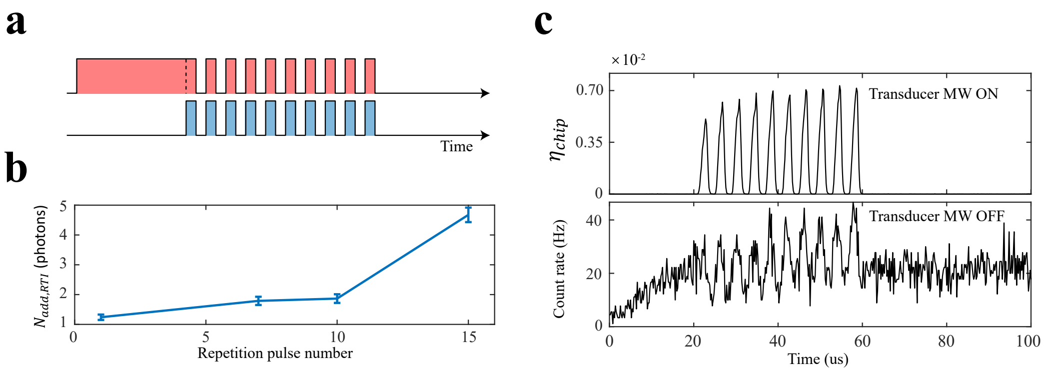

Figure 6.16: **Consecutive transduction pulses for high repetition rates.** (a) Pulse diagram of the experiment, consisting of an optical initialization pulse t_{init} = 20 μs and multiple transduction probes with Δt = 2 μs and a separation of 2 μs in between. (b) The total added noise for varying pulse repetitions. (c) An example of 10 consecutive transduction pulses. The top panel is with microwave input on for efficiency calibration. The bottom panel is with the microwave input off, measuring the added noise induced by the optical pump.

of initialization is still active, avoiding the noise from additional initialization pulses. We achieve $N_{add,tot} < 2$ for 10 pulses with 2 ms t_{off}, for a repetition rate of 5 kHz (Fig. 6.16).

More study on photo-luminescence noise

The spin-phonon relaxation process for REIs doped in solids at low temperatures is typically dominated by the direct process, in which phonons resonantly interact with the spins [55]. The rate of this process R is [55]

$$R = \frac{1}{\tau_1 + (1+b)\tau_{ph}} \tag{6.2}$$

where τ_1 is the time constant of heat transfer from the spins to the phonons, τ_{ph} the phonons to the bath, and b is the bottleneck coefficient.

For order of magnitude estimates of these numbers, we first note that τ_1 is fast for REIs in solids under 1K, typically on the order of μs [55, 87]. The bottleneck of the thermalization process, as the name suggests, comes from the heat transfer between the phonons and the bath. Specifically, since this is a resonant transfer of heat, we should only consider the phonons resonant within our spin inhomogeneous linewidth, greatly reducing the coupling rate, hence increasing the relaxation time. This is described by the bottleneck coefficient b, which is the density of states of the phonon bath resonant with our spins [55]:

$$b = \frac{\rho * 2\pi v^3}{2\omega^2\Gamma} tanh^2(\frac{\hbar\omega}{k_B T}) \sim 10^8 \tag{6.3}$$

where $\rho = 4 \times 10^{24}$ m^{-3} is the REI density, $v \sim 4$ km/s is the speed of sound in the substrate, and T is the spin temperature. Here we have assumed a spin temperature of 0.5 K, however this is dependent on how well our sample is thermalized and how much laser power we apply to the chip. Meanwhile the temperature independent parameter τ_{ph} represents the lifetime of the phonon before it hits a boundary, and can be estimated as $\tau_{ph} \sim L/(2v) \sim 500$ ns, where L is the length scale of the crystal. Using these estimates, we obtain $R \sim 50$ mHz.

Using this coupling strength, we can also obtain an order-of-magnitude estimate on the expected PL count rate as $\frac{t_{init} R \rho V \rho_e}{T_1}$, where we assume spin-phonon coupling occurs during $t_{init} = 20$ μs while the laser is on and the sample is getting heated up, $V \sim \pi(20\ \mu\text{m})^2 \times 8\ \mu$m is the volume of ions, $\rho_e \sim 0.05$ is the fraction of ions in the optical excited state after the initialization, and $T_1 \sim 600$ μs is the optical lifetime. Under these assumptions, we estimate a few Hz to ~ 100 Hz PL count rates depending on the spin temperature (Fig. 6.17). We emphasize again that this is an order-of-magnitude estimate, and we cannot extract a spin temperature from the measured count rate by comparing it to Fig. 6.17. Rather, this estimation gives some confidence that the PL noise we detect is indeed due to spin-phonon coupling.

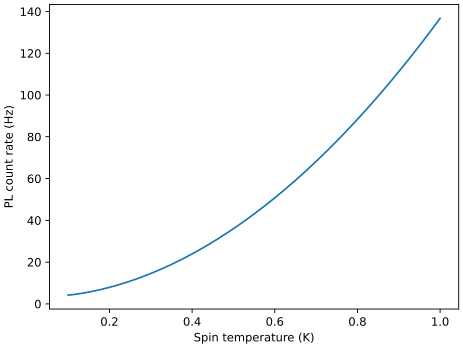

Figure 6.17: **Estimated PL strength versus temperature.** Modeled spin temperature vs. PL count rate expected at the detector, for experimental conditions in Fig. 6.10 in the main text.

From the above spin-phonon coupling rate estimation, we believe the PL should be coming from the spin-phonon coupling which transfers population from $|e_1\rangle$ to $|e_2\rangle$. To further confirm this, we pulse the pump with 200 μs on and 2 ms off, and leave the narrow filters (2 MHz linewidth) at the same detection frequency (from $|e_2\rangle$ to $|g\rangle$), but sweep the excitation frequency. If it is from spin-phonon coupling, then the PL strength should have a lineshape centered on the atomic transition frequency of $|g\rangle$ to $|e_1\rangle$, whereas if it is from direct off-resonant excitation of $|e_2\rangle$, the PL strength should be featureless and flat within the experimental scanning range (tail of a Lorentzian lineshape that is 3.37 GHz away). The results are shown in Fig. 6.18a, which indeed shows a Lorentzian-shaped PL centered on the transition between $|g\rangle$ and $|e_1\rangle$, with a linewidth of 68 MHz. This is slightly smaller than the optical inhomogeneous linewidth because the spin-phonon coupling rate also depends on the population within that manifold. Moreover, to distinguish the noisy photons between the transduced microwave thermal bath and PL noise photons, we fix the pump frequency and scan the filter frequency, effectively tracing out the spectral lineshape of the noise. Then, we separately integrate the PL counts right before turning off the pump (duration when pump on), and right after turning off the pump (duration when pump off). As shown in Fig. 6.18b, we see the broad PL profile is the same between the pump light on and off cases. However, there is an additional narrow peak only for the emission during the pump. We identify this narrow peak as not PL, but rather noisy photons transduced from the microwave resonator bath, as it is much narrower than the PL due to the narrow microwave resonator linewidth. We note that the exact linewidth of this feature is a convolution between the resonator

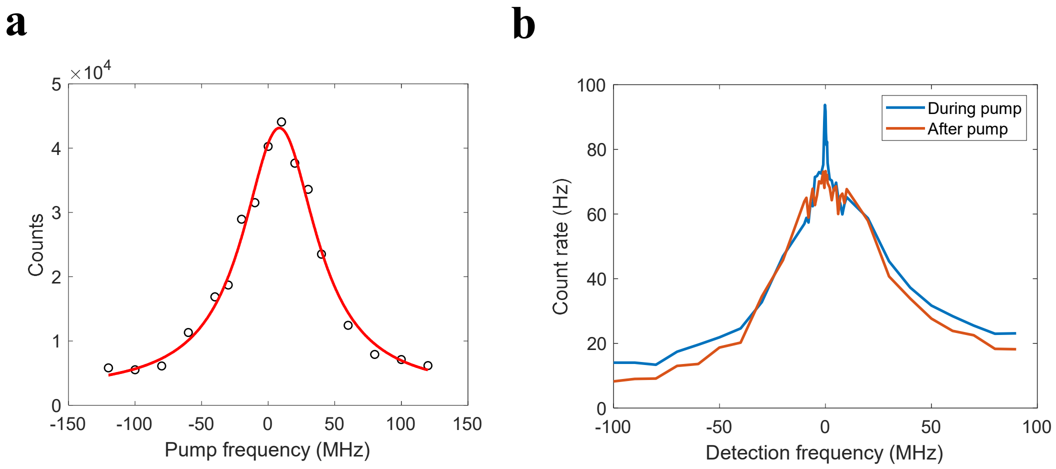

Figure 6.18: **PL measurements with 200 μs pulse on and 2 ms pulse off.** (a) PL strength vs. excitation frequency, with a fixed detection frequency. (b) PL strength vs. detection frequency, with a fixed excitation frequency. Pump on refers to the emission during the pump, and pump off to the emission right after the pump is turned off.

and filter linewidths. In conclusion, we posit that the difference in noise emission during the pump and after the pump is the thermal noise contribution, and confirm that the spectral lineshapes for both this thermal noise and the PL align with our expectations.

6.4 Detailed system calibration

The total M2O efficiency for the dataset shown in Fig. 6.10 is 3.4×10^{-5}. In addition to the 0.76% from the chip, this is comprised of the chip to fiber coupling efficiency, pump filtering setup insertion loss, the SNSPD detector efficiency, and various fiber component losses. The chip-to-fiber coupling efficiency was determined to be approximately 30%, by measuring the reflected power of an off-resonant CW input. We believe this comes from slight angular misalignment and mode mismatch after reflection and could be improved with packaging that incorporates tilt control. The circulator port 2 to 3 loss is 70%. The pump filtering system insertion loss was measured to be 2.5%. This comes from various individually measured fiber component losses: 2 isolators, each ~80% transmission; 4 optical switches, each ~80% transmission; free-space broadband filter, ~50% transmission due to the fiber coupling; and 2 narrowband fiber-coupled cavities, each ~50% transmission. The SNSPD detection efficiency is independently measured to exceed 90%. Finally, by measuring the count rate of a heavily attenuated laser with known power going to the chip and through the filters, we obtain the total detection efficiency of 0.45%, roughly matching the individually measured component efficiencies. We note another ‘calibration-free’ method to extract the transduction efficiency, as demonstrated in other works[37, 41]. Following this method, we first measure each of the four individual S-parameters of the system: R_{OM}: -35.3 dB (data shown in Fig. 6.2); R_{MO}: -53.2 dB (data shown in Fig. 6.2); T_{OO}: -6.6 dB (numbers mentioned above); T_{MM}: -41.1 dB (numbers measured in the next subsection). With the above numbers, one can extract the efficiency as $\eta = \sqrt{\frac{R_{MO}R_{OM}}{T_{MM}T_{OO}}}$ = -20.4 dB = 0.91 %. This is very close to the efficiency from our current detailed calibration method (1.1%), a difference of 0.8 dB. However, we note the small discrepancy is likely from a small drift of the input optical photon polarization along the fibers in the cryostat, which is difficult to stabilize and ultimately affects the photon flux reaching the device. Also, when performing the O2M experiment, the microwave resonator gets a bit more detuned (~ 2 MHz) due to the continuous optical illumination after weeks, this lowers the efficiency a little bit as well.

Noise thermometry

HEMT calibration

To measure the temperature of the microwave resonator under optical excitation, the microwave output port of the chip (port 3 of the cryogenic circulator) is connected to a low-noise cryogenic amplifier (HEMT) at 4K with superconducting NbTi cables. The HEMT output comes out of the refrigerator and the output power is measured by a spectrum analyzer for CW measurements or mixed down and digitized for pulsed measurements.

In order to back out the power output from the chip, the gain and noise of the entire measurement chain must first be calibrated. Here the gain is composed of the HEMT and any room-temperature amplifiers used, as well as loss from the cables and connections. The noise is dominated by the HEMT as it is held at 4K with a gain of ~40dB, the amplified Johnson noise at the output is much larger than room-temperature. This calibration is done by adding a variable noise source before the HEMT and measuring the output power as a function of this noise. The output power P_{out} can be expressed as [88, 89]:

$$P_{out} = \hbar\omega GB(\frac{1}{e^{\frac{\hbar\omega}{k_B T_N}} - 1} + N_{HEMT} + \frac{1}{2}) \tag{6.4}$$

where ω is the frequency, G is the net gain of the output line, B is the measurement

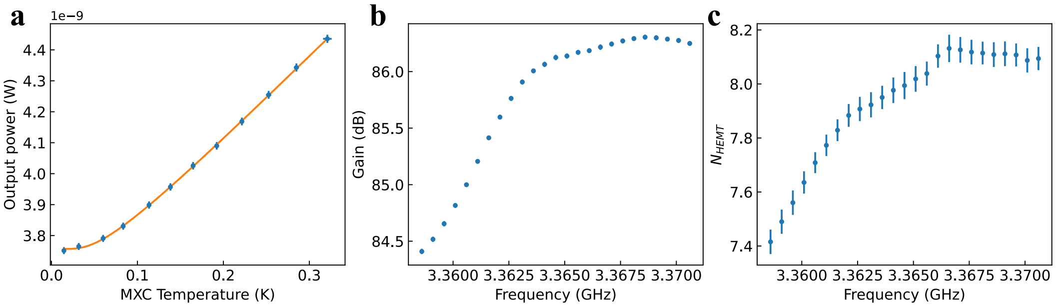

Figure 6.19: **HEMT calibration.** (a) The measured output power vs. fridge mixing chamber temperature for a certain frequency, fit to equation6.4. (b) Extracted gain of the output line from the fit for different frequencies. (c) Extracted added noise of the HEMT.

bandwidth, T_N is the temperature of the noise source, and N_{HEMT} is the added noise of the HEMT. Here we use the device as a noise source, and heat the device up with a resisitive heater on the mixing chamber plate. We allow ample time for the entire mixing chamber plate and all components that are thermally lagged to it to thermalize (~1 hour) before performing measurements. The output power as a function of the thermometer reading is measured and fit to Eq. 6.4.

The extracted gain and added noise are used to convert the measured output power to microwave resonator output with optical pulses applied in Fig. 6.11c and Fig. 6.12.

Microwave mode noise

Applying the calibration to the raw data, we back out the output power directly at the output port of the resonator S_{out}. However, the quantities of interest are the resonator photon occupancy N_{res} and waveguide photon occupancy N_{wg}. To derive these quantities, we follow the formalism described in [89]. We start with the driven Tavis-Cummings Hamiltonian, only considering the spin-microwave resonator coupling:

$$H = \hbar\omega_a a^\dagger a + \frac{1}{2}\hbar\omega_{at} J^z + \hbar g(a^\dagger J^- + J^+ a) + i\sqrt{\kappa_c}A_{in}(a^\dagger - a) + i\sqrt{\kappa_i}A_{env}(a^\dagger - a) \tag{6.5}$$

where ω_a is the resonator frequency, a is the resonator mode, ω_{at} is the spin frequency, $J^z, J^\pm$ are the collective spin operators, g is the spin-resonator coupling strength (although inhomogeneous, later will take the collective coupling strength), κ_c is the resonator external coupling rate, A_{in} is the waveguide photon flux, κ_{in} is the resonator internal loss rate, and A_{env} is the resonator photon flux. The corresponding equations of motion are:

$$\begin{aligned}\dot{a} &= -i\omega_a a - \frac{\kappa}{2}a - igJ^- + \sqrt{\kappa_c}A_{in} + \sqrt{\kappa_i}A_{env} \\ \dot{J^-} &= -i\omega_{at}J^- - \frac{\Gamma}{2}J^- + igJ^z a\end{aligned} \tag{6.6}$$

where we have introduced resonator decay rate κ and spin inhomogeneous linewidth Γ. Fourier transform the operators to the frequency domain:

$$\begin{aligned}a(\omega) &= \frac{\sqrt{\kappa_c}A_{in} + \sqrt{\kappa_i}A_{env} - igJ^-}{\kappa/2 - i\Delta} \\ J^-(\omega) &= \frac{igJ^z(\omega)a(\omega)}{\Gamma/2 - i\Delta_{at}}\end{aligned} \tag{6.7}$$

where $\Delta = \omega - \omega_a$ and $\Delta_{at} = \omega - \omega_{at}$.

$$\begin{aligned}a(\omega) &= \frac{\sqrt{\kappa_c}A_{in} + \sqrt{\kappa_i}A_{env}}{\kappa/2 - i\Delta} + \frac{g^2J^z(\omega)}{(\kappa/2 - i\Delta)(\Gamma/2 - i\Delta_{at})}a(\omega) \\ &= \frac{\sqrt{\kappa_c}A_{in} + \sqrt{\kappa_i}A_{env}}{\kappa/2 - i\Delta + C}\end{aligned} \tag{6.8}$$

where $C = -\frac{g^2J^z(\omega)}{\Gamma/2 - i\Delta_{at}}$. Using input-output formalism $A_{out} = -A_{in} + \sqrt{\kappa_c}a$:

$$\begin{aligned}A_{out}(\omega) &= -A_{in} + \sqrt{\kappa_c}(\frac{\sqrt{\kappa_c}A_{in} + \sqrt{\kappa_i}A_{env}}{\kappa/2 - i\Delta + C}) \\ &= \frac{\kappa_c - \kappa/2 + i\Delta - C}{\kappa/2 - i\Delta + C}A_{in} + \frac{\sqrt{\kappa_i\kappa_c}}{\kappa/2 - i\Delta + C}A_{env}.\end{aligned} \tag{6.9}$$

The power spectral density for an operator A is

$$S_{AA}(\omega) = \int_{-\infty}^{\infty} d\tau e^{i\omega\tau}\langle A^\dagger(0)A(\tau)\rangle. \tag{6.10}$$

To get $S_{out}(\omega)$, first find the autocorrelation of the output field in the time domain:

$$\begin{aligned}\langle A^\dagger_{out}(0)A_{out}(\tau)\rangle &= (\frac{1}{2\pi})^2\langle\int_{-\infty}^{\infty} d\omega\int_{-\infty}^{\infty} d\omega' e^{-i\omega'\tau}\langle A^\dagger_{out}(\omega)A_{out}(\omega')\rangle \\ &= (\frac{1}{2\pi})^2\langle\int_{-\infty}^{\infty} d\omega\int_{-\infty}^{\infty} d\omega' e^{-i\omega'\tau} \\ &\frac{(\kappa_c - \kappa_i - 2C_R)^2/4 + (\Delta - C_i)^2}{(\kappa/2 + C_R)^2 + (\Delta - C_i)^2}\langle A^\dagger_{in}(\omega)A_{in}(\omega')\rangle \\ &+ \frac{\kappa_i\kappa_c}{(\kappa/2 + C_R)^2 + (\Delta - C_i)^2}\langle A^\dagger_{env}(\omega)A_{env}(\omega')\rangle.\end{aligned} \tag{6.11}$$

Here we have taken the expectation value of C such that $\langle J^{z\dagger}(\omega)J^z(\omega')\rangle = -N\delta(\omega-\omega')$, where N is the population in the spin ground state. We define C_R and C_i as the real and imaginary parts of C, respectively. The autocorrelators of the spectral densities of the photon fluxes are:

$$\begin{aligned}\langle A_{in}^{\dagger}(\omega)A_{in}(\omega')\rangle &= \bar{N}_{wg}\delta(\omega-\omega')\\ \langle A_{env}^{\dagger}(\omega)A_{env}(\omega')\rangle &= \bar{N}_{res}\delta(\omega-\omega')\end{aligned} \tag{6.12}$$

Plug these in:

$$\begin{aligned}\langle A_{out}^{\dagger}(0)A_{out}(\tau)\rangle = (\frac{1}{2\pi})^2 &\int_{-\infty}^{\infty} d\omega \int_{-\infty}^{\infty} d\omega' e^{-i\omega'\tau}\\ &\frac{(\kappa_c-\kappa_i-2C_R)^2/4+(\Delta-C_i)^2}{(\kappa/2+C_R)^2+(\Delta-C_i)^2}\bar{N}_{wg}\delta(\omega-\omega')\\ &+\frac{\kappa_i\kappa_c}{(\kappa/2+C_R)^2+(\Delta-C_i)^2}\bar{N}_{res}\delta(\omega-\omega')\\ &=\frac{1}{2\pi}\int_{-\infty}^{\infty} d\omega e^{-i\omega\tau}\frac{(\kappa_c-\kappa_i-2C_R)^2/4+(\Delta-C_i)^2}{(\kappa/2+C_R)^2+(\Delta-C_i)^2}\bar{N}_{wg}\\ &+\frac{\kappa_i\kappa_c}{(\kappa/2+C_R)^2+(\Delta-C_i)^2}\bar{N}_{res}.\end{aligned} \tag{6.13}$$

Plug this back into S_{out},

$$\begin{aligned}S_{out}(\omega) = &\int_{-\infty}^{\infty} d\tau e^{i\omega\tau}\frac{1}{2\pi}\int_{-\infty}^{\infty} d\omega e^{-i\omega\tau}(\frac{(\kappa_c-\kappa_i-2C_R)^2/4+(\Delta-C_i)^2}{(\kappa/2+C_R)^2+(\Delta-C_i)^2}\bar{N}_{wg}\\ &+\frac{\kappa_i\kappa_c}{(\kappa/2+C_R)^2+(\Delta^2-C_i)}\bar{N}_{res})\\ &=\frac{(\kappa_c-\kappa_i-2C_R)^2/4+(\Delta-C_i)^2}{(\kappa/2+C_R)^2+(\Delta-C_i)^2}\bar{N}_{wg}+\frac{\kappa_i\kappa_c}{(\kappa/2+C_R)^2+(\Delta-C_i)^2}\bar{N}_{res}.\end{aligned} \tag{6.14}$$

We can gain some physical intuition by looking at this quantity in the resonant case where $\Delta = \Delta_{at} = 0$ and rearranging terms:

$$S_{out}(\omega=\omega_a=\omega_{at}) = \frac{(1-\frac{2\kappa_i}{\kappa}-C_e)^2}{(1+C_e)^2}\bar{N}_{wg}+\frac{4\kappa_i\kappa_c/\kappa^2}{(1+C_e)^2}\bar{N}_{res} \tag{6.15}$$

where $C_e = \frac{4Ng^2}{\kappa\Gamma}$ is the spin-resonator cooperativity. This shows that the spins will absorb the photons in the waveguide and resonator, and S_{out} represents the output noise power after getting absorbed by the spins.

6.5 Photon interference between two independent transducers

To demonstrate scalability towards large-scale quantum networks, we prepare two transducer chips, where the microwave resonances are offset by 3.4 MHz from each other due to fabrication disorder, shown in Fig. 6.20. Despite this offset, the most

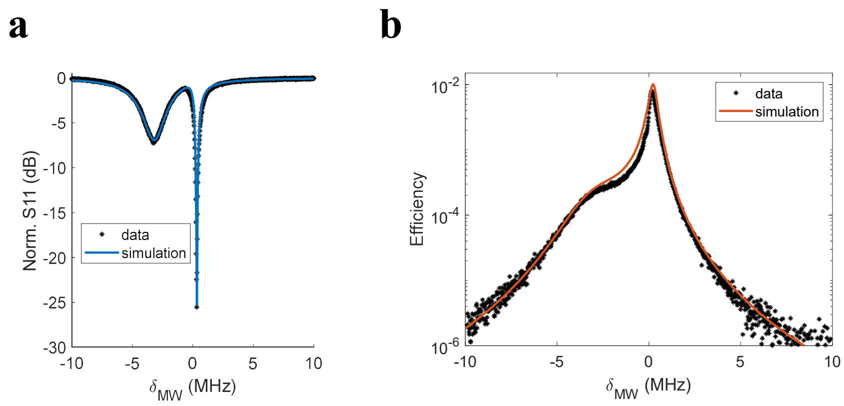

Figure 6.20: **Characterization of the second transducer for photon interference.** (a) MW reflection spectrum with the optical pump on, showing the spin resonator coupling. (b) Microwave-to-optical transduction at various input microwave frequencies with the same experimental conditions as (a).

efficient operating point still coincides at the spin frequency, showing its resistance to this disorder.

We simultaneously do CW M2O transduction on both devices, and interfere the output optical photons (Fig. 6.22). Specifically, we simultaneously send weak microwave photons to each transducer with two synchronized microwave generators. Separate optical pumps are also generated by splitting the pump lasers into two optical paths, each focused onto the circular transduction zone of the respective transducers. Due to the limited laser power, each transducer operates with $\sim 400\,\mu$W pump power. The transduced photons from each transducer, along with the reflected pumps, are collected and combined via a beam-splitter. On one of the output ports we measure the pump photon interference. The other output port goes through a high-extinction spectral filter to another SNSPD to detect only the interference between two transduced photons (Fig. 6.22a). Based on the phase measured on the pump interference, we correct the initial phase and average the interference over 1000 data traces for both the pump detection and the transduction detection.

In Fig. 6.21, a single shot time trace of pump photon interference detected on SNSPD is shown. This raw data set shows the beating oscillation frequency at 50 kHz. Therefore, we repeatedly take this data set and use the reflected pump interference as a reference to correct for the initial phase of the interference of the transduced photons (Fig. 6.22b). Here the oscillation frequency is 50 kHz corresponding to the intentionally added offset between the two pumps, with a Gaussian decay envelope ($\sim 596\,\mu$s) attributed to the phase correlation time between the two independent

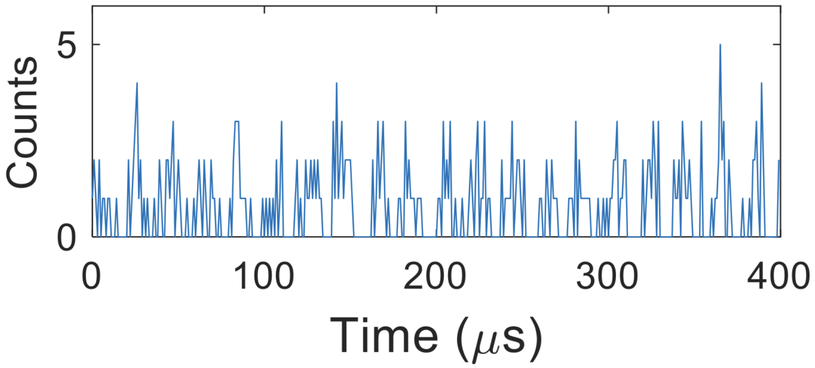

Figure 6.21: **A single shot time trace of the photon interference on SNSPD.** Pump interference detected on SNSPD. The

optical paths.

Then, we tune the phase difference $\Delta\phi$ between the two weak input microwave fields. Since the pump does not sense the phase change, the pump interference overlaps for different $\Delta\phi$ (Fig. 6.22c, top). On the other hand, $\Delta\phi$ will imprint onto the transduced photons. We measure the phase shift in transduction interference for different $\Delta\phi$, demonstrating the phase-coherent nature of the transducer (Fig. 6.22c, bottom). This dual M2O-transducer experiment showcases the ease of interconnecting multiple transducers for our REI platform due to its inherently matching optical transitions, and thus its potential for entangling remote quantum nodes. This dual M2O-transducer experiment showcases the inherent frequency lock in atomic platforms and also the potential towards entangling remote quantum nodes.

6.6 Cascaded two transducers towards optical control of superconducting qubits

Furthermore, to demonstrate the ability to optically probe and detect superconducting qubits, we cascade two transducers together with a cryogenic microwave link (Fig. 6.23a). Separate optical pumps are generated by splitting the pump lasers into two optical paths. The O2M path goes through a weakly driven electro-optical modulator and sent to the first chip to perform O2M transduction. Similarly, due to the limited laser power, each transducer operates with ~ 400 μW pump power. We note that the generated microwave photons can be used to probe qubits, as shown in previous studies [39, 90]. Instead, here we connect them by a microwave link, where the microwave photons are captured by the second transducer and converted back to optical photons, illustrating the ability to optically readout a qubit state. The

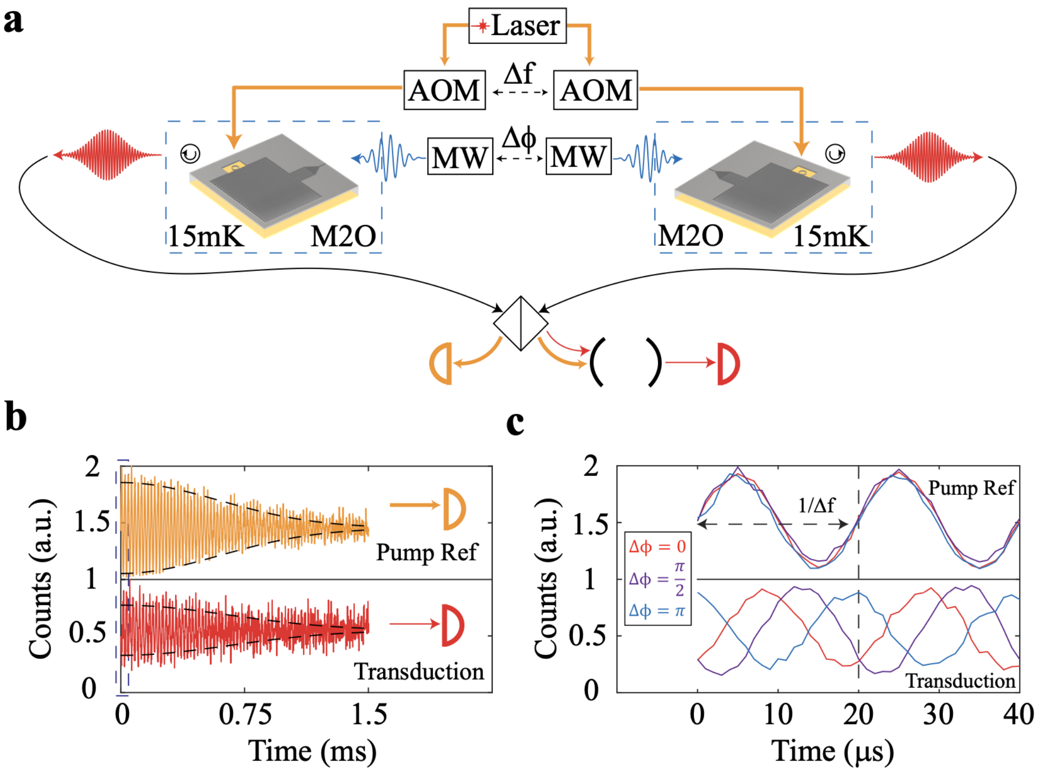

Figure 6.22: **Photon interference between two independent transducers.** (a) Dual M2O configuration. Two transducers are operated at the same time where the weak input microwave photons are phase shifted by $\Delta\phi$ and optical pumps are frequency shifted by $\Delta f = 50$ kHz. The output photons are combined on a beamsplitter and one port is sent to an SNSPD for phase referencing via the pump (b, upper). The other port goes through a narrow frequency filter to spectrally select only the transduction photons, and its interference is detected on another SNSPD (b, lower). A Gaussian decay envelope is observed due to the relative phase drift (596 ± 6 μs) between two optical paths. (c) A zoom-in on the interference, where different phase shifts between microwave inputs are implemented and measured.

output of the final M2O signal is split into two paths for heterodyne detection of the cascaded O2M-M2O, and transduced photon interference through a high-extinction spectral filter. On the heterodyne detection side, optical photons beating are measured on a spectral analyzer. The total efficiency agrees with the product between O2M and M2O efficiency and chip collection factors (Fig. 6.23b), where the lack of excess loss shows the advantage of matching spin transitions.

By interfering the input optical photons with the final transduced photons (intentionally frequency shifted by 50 kHz), we measure an intensity correlation between the two independent optical paths, confirming that the frequency was preserved throughout the entire transduction process (Fig. 6.23c). We note the Gaussian decay envelope of around 359 μs, similar to Fig. 6.22b, which we also attribute to the phase correlation time of the independent optical paths.

6.7 Discussion – why REI?

With all the measurement results presented above, an interesting topic can be discussed here now – why REI for transduction? I summarized the key points here and will discuss them one by one:

1. **Ultra-strong nonlinearity**
2. **Scalability**
3. **Synchronization**
4. **Versatility**

First, the current transducer efficiency is $\sim 1\%$ with refer-to-input added noise as 1.24 photons. The chip only requires a microwave resonator with $Q_{mw} \sim 1K$ but not an engineered optical cavity. The chip interference did introduce a Fabry-Perot optical mode, with $Q_{op} \sim 3K$ based on the free-spectral range and the finesse. This loose fabrication requirements with measured $\sim 1\%$ efficiency already indicate that the material has a very strong effective $\chi^{(2)}$ nonlinearity. As calculated in Section 3.5, this nonlinearity is found to be only related to the material properties $\chi^{(2)}_{eff} = \frac{4}{\epsilon_0 c h^2}\frac{\rho d^2 \mu}{\Gamma_e \Gamma_o}$, where for 340ppm ^{171}Yb^{3+}:YVO$_4$, this number is $\sim 10^7$ pm/V. This is a direct comparison to other conventional nonlinear materials (like LiNbO$_3$ with $\chi^{(2)} = \frac{1}{2}n^4 r_{15} \sim 450$ pm/V). Another way to look at this, is to think about the intrinsic nonlinearity, that is the efficiency per pump power per all the quality factors – $\frac{\eta}{P_{pump} Q_e Q_o Q_p}$. This gives a comparison between all the transducer platforms as usually the efficiency increases linearly with more pump power and better quality

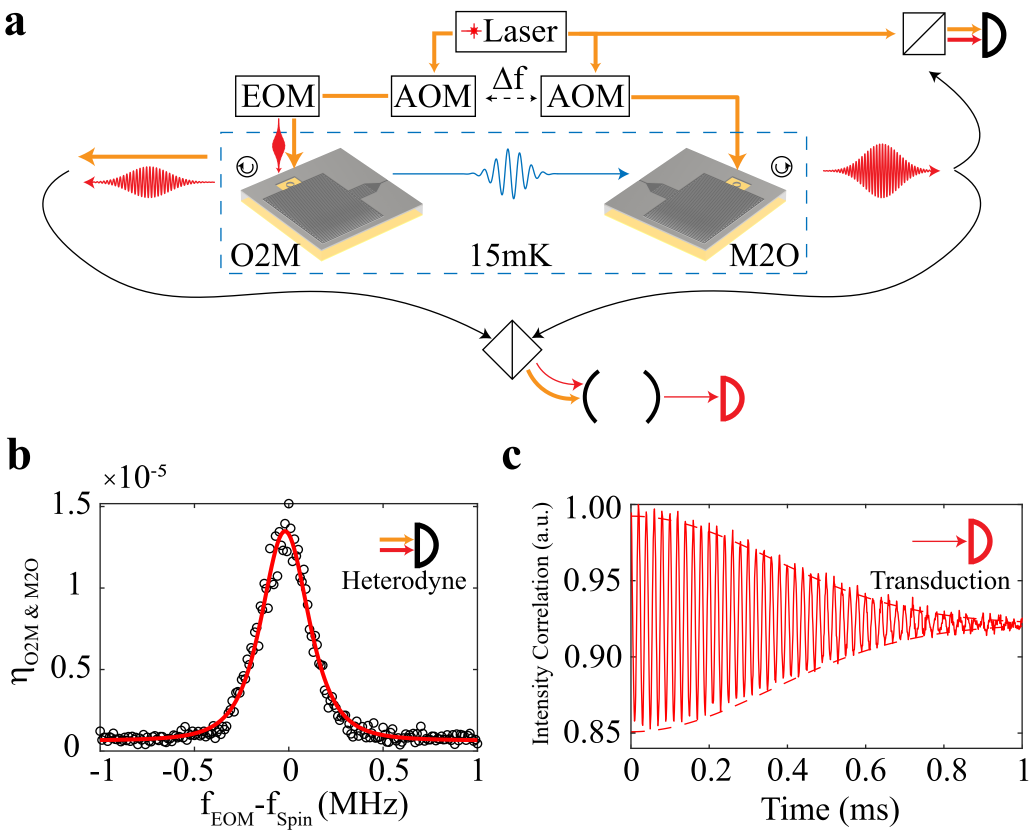

Figure 6.23: **Casacaded O2M and M2O transducer towards optical control of superconducting qubits.** (a) Cascaded O2M to M2O configuration. Two transducers are simultaneously operated where the optical pump is frequency shifted by $\Delta f = 50$ kHz. Weak optical photons are sent to the first transducer to perform O2M, from which the second transducer captures the transduced microwave photons and performs M2O. The final optical output is then both measured via heterodyne method and combined with the first input optical light for an intensity correlation measurement. (b) The total O2M-M2O efficiency at different input optical photon frequencies. We use the product of two Lorentzian functions for fitting (red line), which captures two sequential transduction processes. (c) The intensity correlations between the optical input and the transduced output. A Gaussian decay envelope ($359 \pm 2\ \mu$s) is observed due to the phase drift from the two separate optical paths.

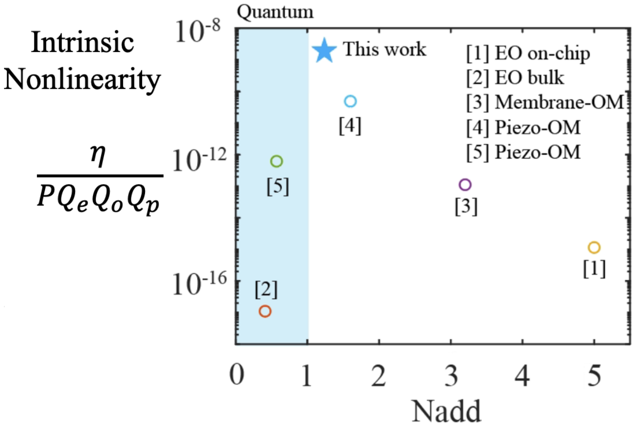

Figure 6.24: **Intrinsic nonlinearity between different platforms.** As defined in the text, $\frac{\eta}{P_{pump}Q_eQ_oQ_p}$ describes the efficiency per pump power per quality factors in all the fields. This factor is proportional to $[\chi^{(2)}]^2$ as calculated in Section 3.5. For each reference, [1] is Xu Y, et al. Nature Communications 12.1 (2021): 4453. [2] is Sahu, et al. Nature Communications 13.1 (2022): 1276 [3] is Brubaker. Physical Review X 12.2 (2022): 021062. [4] is Jiang, et al. Nature Physics 19.10 (2023): 1423-1428. [5] is Mirhosseini, et al. Nature 588.7839 (2020): 599-603.

factors in each fields. This $\frac{\eta}{P_{pump}Q_eQ_oQ_p}$ is meaningful as it is just proportional to $[\chi^{(2)}]^2$ as calculated in Section 3.5. Therefore, by looking into the literature, we summarize the performance in Fig. 6.24. We found the REI-platform discussed here is almost in the quantum regime, but significantly large in terms of this intrinsic nonlinearity number.

Second, the REI-based device footprint is relatively small for future scalability considerations. The large feature currently is the capacitor of the resonator, on the order of hundreds micrometers. As the REIs are already doped into a host crystal, lots of fabrication process can be done on this piece of substrate. Therefore, one does not need to be limited to a bulky setup.

Third, as the system is an atom-based platform, the operation frequencies are absolutely locked to REI transitions. This unique feature makes the transducers automatically frequency-matched hence suitable for the future remote entanglement application. Since in this case, photon interference needs to be done to generate entanglement based on heralding protocols and photon indistinguishability is a prerequisite. Although, other platforms can always achieve this by doing a resonator post-tuning (e.g., local oxidization via AFM [22]) or an extra step of optical frequency conversion (e.g., commercial electro-optic modulators). Another extra step will always complicate the fabrication process (potentially lower the Qs) or lower

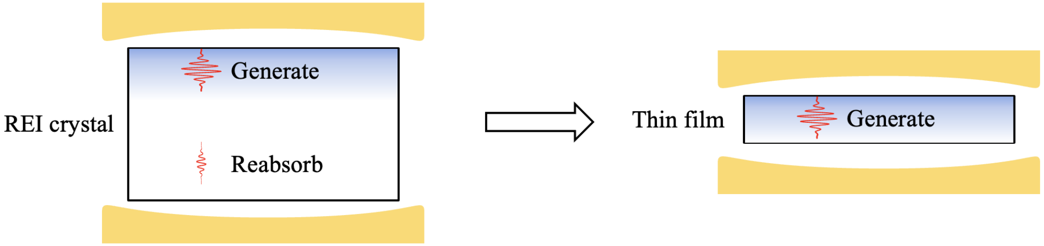

Figure 6.25: **Diagram of an optical cavity with REI thin film.** By utilizing a REI thin film, a good mode matching between the microwave and optical fields inside REI materials can be achieved. Hence, lowering the number of atoms that only couple to the optical field but not the microwave, behaving as an optical absorber and also as parasitic ions for O2M tasks.

the final efficiency from another step.

Lastly, REI-platform is not only a candidate for quantum transduction application but also a toolbox for quantum communications and cavity quantum electrodynamics studies. Among the applications, single photon sources based on REIs has been achieved in [13, 14]. Efficient quantum memories and multimode operations have been demonstrated in [66, 67]. Entanglement generation has also been recently achieved with single rare-earth ions in [68]. On the CQED side, quantum thermalization and many-body phenomenon have been observed in REI system [65, 91]. Also, as we will see in the next two chapters, we observe novel CQED effect from a tunable spin-inverted system. Therefore, transducing superconducting qubit signals via REI platform will give the qubit a native connection to other developed REI-based technologies.

Going back to the intrinsic nonlinearity argument, the number is huge, but the actual chip efficiency is the key number one would care for real applications. Therefore, REI platform still needs to further improve the efficiency. Based on our current results, adding a better optical cavity is the way to go. However, directly adding the cavity may not be the wisest option, the optical re-absorption will extinguish the transduced signal in the current setup, as shown in Fig. 6.25. A thin film is better to further optimize the mode overlap between the microwave and optical fields. On one side, we do not want to have parasitic ions that only couple to the microwave field but not the optical (only absorb the microwave photon but not transducing). On the other side, parasitic ions that only appear in the optical domain is also detrimental, as the O2M task will suffer the same as the parasitic ion argument.

REI thin film has been demonstrated. For example, research groups have developed a technology by bonding a REI chip to a substrate and polishing the chip down to tens of μm thickness [81]. Experiments have been demonstrated based on this type of chip architecture. With these discussions in mind, the next section will cover potential future improvements that utilize the thin film technology.

6.8 Further improvements

For the reduction of added noise

Currently, the noise is primarily from PL and resonator thermal occupancy within the 2 μs transduction window. With some technical improvements, there are a few avenues to decrease the added noise.

First, the PL emits isotropically, but collected light is limited to the NA of the lens system used. The current NA is ~0.1, which can further be reduced to collect less PL. Theoretically, the collection efficiency of the transduced photons that are emitted directionally will be unaffected by a lower NA. Experimentally however, there is always a finite angle misalignment in the setup, and a larger NA leads to better coupling. By adding fine tilt alignment, a more collimated beam could be used with a 10× smaller NA but the same beam waist. This would lower the PL by a factor of 10×.

Second, another way to lower the PL is by using a thinner sample, as the planar microwave resonator mode penetration is only a couple of micrometers. One idea to realize this is a REI-doped crystal bonded to a substrate, which would then be polished down to a desired thickness. We then require less initialization time, as a thinner crystal means less material that needs to be saturated at the optical pump frequency. With less initialization time, the PL should decrease, as well as the thermal noise. However, the REI properties in both the optical and microwave domains for a thin film require further studies, which could be worse than the normal bulk crystal due to surface stress and strain. Assuming all the properties are unchanged, with half the initialization time, we expect to halve the total added noise.

Third, growing a higher concentration sample is also useful. The effective $\chi^{(2)}$ nonlinearity is currently not as high as it could be. A higher concentration of Yb ions would bring the density up, linearly increasing the effective $\chi^{(2)}$. At the same time, the inhomogeneities typically get broader at higher concentrations, which would increase the transducer bandwidth that is limited by the spin linewidth currently. With a larger bandwidth, a shorter transduction pulse could be used, which will also cut down the photon collection time, lowering the noise effectively. For example, if we assume a 1 MHz bandwidth is achievable with the same efficiency, PL noise would be halved.

If all of the above improvements can be incorporated, the added noise can be decreased from the current 1.24 photons to about 0.2 photons.

For increasing efficiency

The current parameters, $C_e \sim 1$, $C_o \sim 0.2$, $C_a \sim 0.1$, give ~1% efficiency. Increasing C_o and C_a both to ~1 will bring the system to ~20% efficiency, while increasing C_e and $C_o \gg 1$ will bring the system to unit efficiency.

Without making C_o and C_a larger, simply increasing $C_e > 1$ will only hurt the efficiency in the on-resonance regime. To only improve C_o and C_a, one way is to incorporate a free-space optical cavity with Finesse ~ 10, then C_o will become 2 and C_a will become 1. The C_o can always be decreased to 1 by pumping the population or operating with some detuning. However, this optical cavity should be incorporated with a thin film, to avoid reabsorption. Assuming ion properties in the thin film are unchanged and a free-space tunable optical cavity with Finesse ~ 10 is reachable, then an efficiency of about 20% is achievable. We note that here the required Finesse is only ~ 10, which may be small enough to avoid excess noise from the increased circulating power.

Towards unit efficiency, working in the on-resonance regime would be difficult as it requires an ultra-large C_a, which means a strong pump and hence likely more noise. However in the adiabatic regime, one only needs large C_e and C_o, albeit with detunings. For this, other than the aforementioned improvements (thin film and free-space tunable optical cavity), a higher concentration sample will directly boost the number of atoms per volume, and hence the cooperativities linearly. Assuming the concentration is 6× higher with unchanged ion properties, microwave cavity Q is 10k and the optical cavity finesse is ~ 100, then $C_e \sim 10$, $C_o \sim 10$. With $C_a = 0.01$, unit efficiency is achievable in the adiabatic regime. The noise performance remains to be investigated in the experiment as there have so far been no transduction experiments in the adiabatic regime due to the requirement of large cooperativities in both microwave and optical domains.

Moving towards hybrid quantum networks, future experiments will be focused on optical access and entanglement generation between remote superconducting qubits. Meanwhile, interfacing superconducting qubits with single REIs or ensembles will also be investigated towards building a hybrid quantum network with disparate physical platforms.

6.9 Summary

In this chapter, we present the measurement results of a REI-based on-chip transducer between microwave and optical fields. Without an engineered optical cavity, the chip efficiency is 0.76% (3.4×10^{-5} including the pump filtering system) with an added noise down to 1.24(9) photons under pulsed operation with 500 kHz bandwidth. We further demonstrate dual transducer interference experiments that show scalability and the capacity to drive and readout qubits via optical fibers, an essential step towards the remote entanglement of superconducting qubits. The achieved efficiency with low optical and microwave resonator quality factors comes from the ultra-strong effective $\chi^{(2)}$ non-linearity in this REI-based material. Similar efficiency has been achieved for example in $LiNbO_3$, but required optical cavities with quality factors on the order of millions due to the quadratic scaling of efficiency with $\chi^{(2)}$ in the low-cooperativity regime [25, 92, 93]. The lack of a high-finesse optical cavity in our device lends itself to scalability in the context of robust fabrication, and the absolute atomic frequencies alleviate the need for precise frequency matching between different devices. Moving towards hybrid quantum networks, future experiments will be focused on optical access and entanglement generation between remote superconducting qubits. Meanwhile, interfacing superconducting qubits with single REIs or ensembles will also be investigated towards building a hybrid quantum network with disparate physical platforms.

Chapter 7

CAVITY QUANTUM ELECTRODYNAMICS STUDY WITH A TUNABLE SPIN-INVERTED ENSEMBLE

From the previous chapter, we have discussed a transducer between microwave and optical fields with rare-earth ion doped crystals. To achieve it, a superconducting microwave resonator and a natural optical mode are utilized. However, the chip is more than a frequency transducer. It is also a platform with strong coupling to the spin ensembles in the excited state, ready for cavity quantum electrodynamics study. Since the resonator is coupled to a three-level system, one could individually address the three transitions. Hence, the excited-state spin ensemble can be prepared to be in either a collective spin-up state or a collective spin-down state. In the spin-down case, other than strong couplings that have been observed, a novel transparency window created by the spin ensemble has been observed as well - collectively-induced transparency (CIT). It was firstly observed in the optical domain in 2023 but has not yet been reported in the spin domain. The narrow spectral feature of the transparency window as well as the large depth make it fundamentally attractive for microwave switching and frequency reference. On the other side, by preparing to the spin-up state, with enough population inversion to trigger the process, continuous-wave maser phenomena is observed. With more inversion from high pump power, periodic superradiant pulses are generated from the spin-inverted ensemble. Interestingly, since the chip is also a microwave-to-optical transducer, synchronized optical pulses are generated naturally, with phase coherence to microwave pulses.

With a quick summary of new findings, this chapter will first go through the theory of the spin-inverted system coupled to resonators. We will first visit the collective-induced transparency derivation, which is a combination of summaries from the results presented in [65] and new derivations by considering three-level systems instead of two levels. Numerical simulations will be presented using the new three-level system model. Next, I will go through the theory of superradiance burst, which is also a combination of summaries from the results presented in [94] and new derivations of the three-level system in our scenarios. Numerical simulations on superradiant bursts and periodic synchronized microwave and optical emissions will also be presented.

7.1 Theory of spin resonator coupling

Ensembles of two-level systems coupled to a resonator have been extensively studied in theory and experiments [95–98]. Here, I will go through some important ideas of the theory to pave the way for the next section of simulating three-level systems.

First, considering two-level systems coupled to a resonator $(a, a^\dagger)$:

$$\mathcal{H} = \hbar\omega_c a^\dagger a + \Sigma_i E_{1,i}\sigma_{11,i} + \Sigma_i E_{2,i}\sigma_{22,i} + \hbar\Sigma_i g_i(a^\dagger\sigma_{12,i} + \sigma_{21,i}a) \tag{7.1}$$

where ω_c is the cavity frequency, $E_{1/2,i}$ is the energy for the first/second level, $\sigma_{ij} = |i\rangle\langle j|$ is the atomic operator, g_i is the coupling strength between each individual atom to the resonator. One could solve the system dynamics by calculating the operator evolution and input-output theorem:

$$\begin{aligned}
\dot{a} &= -i\omega_c a - \frac{\kappa_a}{2}a - i\Sigma_i g_i\sigma_{12,i} - \sqrt{\kappa_{a,c}}A_{in} \\
\dot{\sigma}_{12,i} &= -(i\omega_{12,i} + \gamma_2)\sigma_{12,i} - ig_i(\sigma_{11,i} - \sigma_{22,i}) \\
\dot{\sigma}_{11,i} &= \gamma_1\sigma_{22,i} - ig_i(a^\dagger\sigma_{12,i} - \sigma_{21,i}a) \\
\dot{\sigma}_{22,i} &= -\gamma_1\sigma_{22,i} + ig_i(a^\dagger\sigma_{12,i} - \sigma_{21,i}a) \\
A_{out} - A_{in} &= \sqrt{\kappa_{a,c}}a
\end{aligned} \tag{7.2}$$

where κ_a is the cavity decay rate, $\kappa_{a,c}$ is the external coupling rate, γ_1 describes the spontaneous emission decay rate and γ_2 describes the dephasing rate of the coherence. $A_{in}^\dagger A_{in}$ describes the input photon flux, which can be represented by cavity mean photon number μ as

$$\begin{aligned}
\sqrt{\kappa_{a,c}}A_{in} &= \frac{\kappa_a}{2}\sqrt{\mu} \\
\mu &= \frac{P_{in}}{\hbar\omega}\frac{\kappa_{a,c}}{(\frac{\kappa_a}{2})^2 + (\delta)^2}
\end{aligned} \tag{7.3}$$

where P_{in} is the actual input power to the port. With this, one could calculate the cavity reflection spectrum by simply evaluating

$$|\frac{A_{out}}{A_{in}}|^2 = |1 + \frac{2\kappa_{a,c}}{\kappa_a}\frac{\langle a\rangle}{\sqrt{\mu}}|^2. \tag{7.4}$$

By taking a look at the dynamics of mode a and the cavity reflection spectrum in eqn. 7.4, one would find that if there is no atomic couplings, $\langle a\rangle = -\sqrt{\mu}$ by plugging μ to the dynamics for replacing A_{in}. This makes sense as the the cavity photon number should just be the input flux. The minus sign comes from the definition of the input-output port. In this case, the cavity reflection will just become as

$$|\frac{A_{out}}{A_{in}}|^2 = |1 - \frac{2\kappa_{a,c}}{\kappa_a}|^2. \tag{7.5}$$

Hence, we see by tuning the kappa ratio, one would change the cavity from under-couple ($\frac{2\kappa_{a,c}}{\kappa_a} < 1$) to critical-couple ($\frac{2\kappa_{a,c}}{\kappa_a} = 1$) and lastly to over-couple ($\frac{2\kappa_{a,c}}{\kappa_a} > 1$). Thinking about the contribution of the atomic couplings, one could view it as the atom adds additional terms in κ_a such that the cavity reflection will be different at various detunings.

There are two special cases worth mentioning here, that would be useful to understand the experimental data in the next chapter. One is the strong coupling regime, the other is the collectively induced transparency in two-level system.

Strong coupling regime

First, the strong coupling regime. I will show a key result from this paper [95] [1]. By considering weak excitation regime ($\sigma_z = \sigma_{22} - \sigma_{11} \approx 1$), one would have the reflection spectrum written as

$$R(\omega) = |1 - \frac{i\kappa_{a,c}}{\omega - \omega_c + i\kappa/2 - W(\omega)}|^2 \tag{7.6}$$

with

$$W(\omega) = \Omega^2 \int \frac{\rho(\omega')}{\omega - \omega' + i\gamma_2/2} d\omega' \tag{7.7}$$

where $\Omega = \sqrt{\Sigma_i g_i^2}$ describes the ensemble coupling strength and $\rho = \Sigma_o g_i^2 \delta(\omega - \omega_i)/\Omega^2$ is the discrete format describing the atomic distribution. Considering a simple case where the atomic distribution is a Dirac delta function centered at the cavity frequency ($\rho = \delta(\omega - \omega_c)$), therefore one would have $W(\omega) = \frac{\Omega^2}{\omega - \omega_c + i\gamma_2/2}$. Plugging this into the cavity reflection equation, we will find two poles (denominator is zero) as:

$$\lambda_\pm = \omega_c \pm \sqrt{\Omega^2 - (\frac{\kappa_a - \gamma_2}{4})^2}. \tag{7.8}$$

The strong coupling reaches when $\Omega \gg \kappa_a, \gamma_2$. In this case, the cavity spectrum will split into two doublets centered at $\omega_c + \Omega$ and $\omega_c - \Omega$, with the separation equals to twice of the ensemble coupling strength, as shown in Fig. 7.1(b).

Collectively induced transparency

This is a newly observed phenomenon in disordered systems in 2023 [65]. The key part of observing the phenomena is (1) a strong enough coupling such that the ensemble-cavity cooperativity is large; and (2) an inhomogeneous broadened

---

[1] I encourage people who are interested in this topic to read this detailed paper.

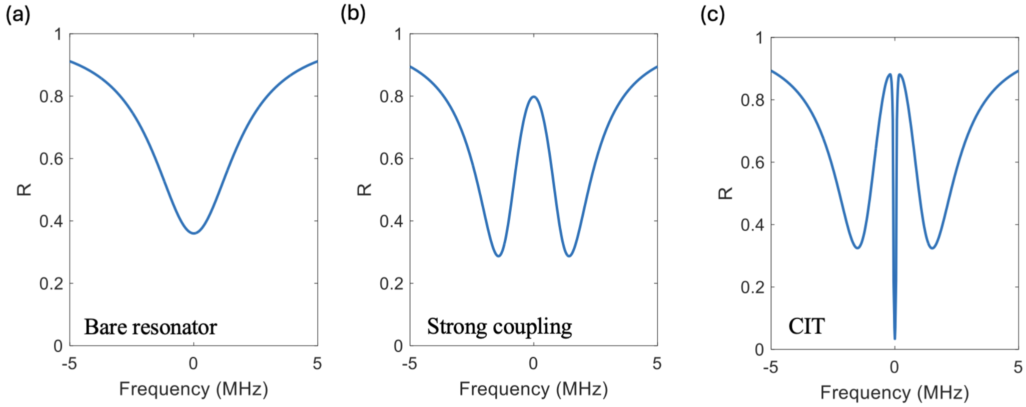

Figure 7.1: **A schematic for different resonator coupling patterns.** (a) The bare resonator with over-coupling kappa ratio. (b) A strong coupling pattern which splits the original resonator dip into two polaritons. (c) A CIT pattern due to an inhomogeneous ensemble strongly coupled to a resonator field.

ensemble. Without going into details and re-deriving the formulation, I will refer to this thesis [99] and mention the key equations that are critical to understanding.

Following the equation 7.4, by plugging in the two-level system dynamics, where $\langle a \rangle$ is related to $\sqrt{\mu}$, $\sigma_{22,i}$ and $\sigma_{11,i}$, one could simplify the equation to

$$R = |1 - \frac{2\kappa_{a,c}}{\kappa_a}\frac{1}{1+x}|^2 \tag{7.9}$$

where the parameter $x = -\Sigma_i \frac{2g_i^2\langle\sigma_{22,i}\rangle - \langle\sigma_{11,i}\rangle}{\kappa_a(\gamma_2 + i\Delta)}$ fully describes the modification from atomic couplings to the resonator field. One analytical equation can be solved by assuming (1) a Lorentzian distribution of the ions; (2) intermediate power (μ); (3) on-resonance condition; (4) high cooperativity; (5) enough inhomogeneity. With these assumptions, one could get

$$x = \frac{1}{\frac{\Delta_{inh}\kappa_a}{2Ng}\sqrt{\frac{\mu}{\gamma_1\gamma_2}} - 1} + \frac{8i(\omega_L - \omega_0)}{\frac{\Delta_{ihn}^2\kappa_a}{Ng^2}}. \tag{7.10}$$

With these two equations, the CIT intuitions are the following. First, the atomic coupling will modify the cavity decay rate κ_a. When μ is infinite, hence $x \longrightarrow 0$, the cavity at the center will see no atomic effect but a bare cavity with $R = |1 - \frac{2\kappa_{a,c}}{\kappa_a}|^2$. By tuning the μ, hence $x > 0$, one would effectively modify the cavity kappa ratio here with the power. If starting with an over-coupled cavity, one would observe the cavity center becomes critical-couple and further under-couple by tuning the x. In the optical domain, an over-coupled cavity is not trivial to fabricate. But this is relatively easy in the microwave domain by geometry engineering. Therefore, this kappa ratio tuning across the critical-coupling regime has not been observed in [65] but is in the microwave circuit, shown in the next chapter.

7.2 Simulation of CIT with three-level systems

To understand the CIT phenomena in our system with tunable population in each levels, we can rewrite the system Hamiltonian by adding extra terms. But the intuition is the same as discussed in the previous subsection. Here, by having an extra level, we can manipulate the amount of population in the spin manifold and further tune the spin population difference with microwave driving. Therefore, the optical pump power in the system is a knob of initialization. The microwave power is the one to saturate the system with the description of μ as covered above.

With these in mind, we could start with the system Hamiltonian as

$$\begin{aligned}\mathcal{H} =&\hbar\omega_{o,c}a^\dagger a + \hbar\omega_{e,c}b^\dagger b + \sum_k E_{g,k}\sigma_{gg,k} + \sum_k E_{e_1,k}\sigma_{e_1e_1,k} + \sum_k E_{e_2,k}\sigma_{e_2e_2,k} \\ &+ \sum_k \hbar g_{o,k}(a^\dagger\sigma^-_{o,k} + h.c.) + \sum_k \hbar g_{e,k}(b^\dagger\sigma^-_{s,k} + h.c.) \\ &+ \sum_k \hbar\Omega_k(\sigma^-_{p,k} + h.c.)\end{aligned} \tag{7.11}$$

where a is the optical mode and b is the microwave mode. Since in our system, the optical cavity is a formation from two reflective surfaces with broad linewidths, it covers both two optical transitions at the same time. One could write a_1 and a_2 modes to consider the two different coupling terms or use a classical driving form $\Omega = g_o a$ to replace one of the ion-cavity coupling terms. The two are equivalent and that is why in the simulation formulation, sometimes the optical cavity couples from $|1\rangle$ to $|3\rangle$ but later for maser derivation, it couples from $|1\rangle$ to $|2\rangle$. With the Hamiltonian, we then calculate the dynamics of each relevant operator in the Heisenberg picture:

$$\begin{aligned}
\dot{a} &= \frac{i}{\hbar}[\mathcal{H}, a] = -i\omega_{o,c}a - \frac{\kappa_o}{2}a - i\Sigma g_{o,k}\sigma^-_{o,k} \\
\dot{b} &= -i\omega_{e,c}b - i\Sigma g_{e,k}\sigma^-_{s,k} - \frac{\kappa_e}{2}b - \frac{\kappa_e}{2}\sqrt{\mu} \\
\dot{\sigma}^-_{o,k} &= -(i\omega_{e_2,g} + \gamma_o)\sigma^-_{o,k} + ig_{o,k}(\sigma_{e_2e_2,k} - \sigma_{gg,k})a - ig_{e,k}\sigma^-_{p,k}b + i\Omega_k\sigma^-_{s,k} \\
\dot{\sigma}^-_{p,k} &= -(i\omega_{e_1,g} + \gamma_o)\sigma^-_{p,k} + ig_{o,k}\sigma^+_{s,k}a - ig_{e,k}b^\dagger\sigma^-_{o,k} + i\Omega_k(\sigma_{e_1e_1,k} - \sigma_{gg,k}) \\
\dot{\sigma}^-_{s,k} &= -i(\omega_{e_2,e_1} + \gamma_s)\sigma^-_{s,k} - ig_{o,k}\sigma^+_{p,k}a + ig_{e,k}(\sigma_{e_2e_2,k} - \sigma_{e_1e_1,k})b + i\Omega_k\sigma^-_{o,k} \\
\dot{\sigma}_{e_2e_2,k} &= -\gamma_1\sigma_{e_2e_2,k} + ig_{o,k}(a^\dagger\sigma^-_{o,k} - \sigma^+_{o,k}a) + ig_{e,k}(b^\dagger\sigma^-_{s,k} - \sigma^+_{s,k}b) \\
\dot{\sigma}_{e_1e_1,k} &= -\gamma_1\sigma_{e_1e_1,k} + ig_{e,k}(-b^\dagger\sigma^-_{s,k} + \sigma^+_{s,k}b) + i\Omega(\sigma^-_{p,k} - \sigma^+_{p,k}) \\
\dot{\sigma}_{gg,k} &= \gamma_1\sigma_{e_1e_1,k} + \gamma_1\sigma_{e_2e_2,k} + ig_{o,k}(-a^\dagger\sigma^-_{o,k} + \sigma^+_{o,k}a) + i\Omega(-\sigma^-_{p,k} + \sigma^+_{p,k}).
\end{aligned} \tag{7.12}$$

With the equations, one could encode with multiple atoms, where each atom will have 6 equations. Therefore, it adds up to 6N+2 equations. We care about the steady-state solution of the system of N atoms. From Comsol simulations, we get the mode volume for the resonator is 580 $(\mu m)^3$, which leads to ~ 10 Hz single-ion coupling rate at the center of the inductor circle. Higher coupling strength up to ~ 200 Hz can be achieved for the location that is close to the inductor. Since the mode profile is relatively flat, we consider a 10 Hz homogeneous electrical coupling rate between the spin and the resonator. Therefore, for a 1 MHz coupling strength (measured experimentally, as shown in Fig. 5.5), the corresponding ensemble number is $N = (\frac{g_{tot}}{g_{single}})^2 = 10^{10}$. This large number is reasonable. If we consider the ensemble number from the interaction zone of the gaussian beam, we will have $N = \rho\pi r^2 D$, where $\rho = 5 \times 10^{24}/m^3$ is the number density for 340ppm ^{171}Yb^{3+}:YVO$_4$ concentration, $r = \frac{\omega_o}{2\sqrt{2ln[2]}} = 12\mu m$ is the gaussian beam radius considering the half width at half maximum (HWHM) and $D = 8\mu m$ is the mode penetration depth considering 50% mode energy. This calculation gives $N = 1.8 \times 10^{10}$, pretty well capturing the system behavior from the ensemble coupling strength. With these analyses, we assign the single-ion coupling rate as 10 Hz and consider the ensemble size as 10^{10}.

To calculate the result, one way is to directly solve the steady state solution by setting 6N+2 equations equal to 0. However, the equation sets are not linearized. One needs to use an iterative method to find the solutions by a roughly current initial guess. Another way is to solve all the ODE equations together. Even if the equations are coupled to each other, as long as a time step is defined, the program can always solve the increments for each parameter and hence get the temporal trajectory. This method is more time-consuming than the steady-state solver, as one needs to evaluate 6N+2 equations for all the time steps. But this will always give you an answer compared to the steady state solver that the result may not be converged, depending on the initial guess. For the equations, creating 60 billion of equations and solve together is computationally hard in either an ODE solver or a steady-state solver. For the sake of time, I randomly generate 10^{10} atoms from the Gaussian distribution and group the atoms into hundreds of subsets, where each group is considered as identical atoms in the simulation, saving the computational space. Because the spin inhomogeneity is $\Delta_{inh} = 2\pi \times 160$ kHz, the coherence time $1/\gamma_2$ is unknown for this concentration, but at least be bounded by the excited state lifetime $\tau_e = 267\mu$s. This gives the group of ions bounded by $N_{bound} = \frac{\Delta_{inh}}{1/(2\pi\tau_e)} = 270$, which makes the hundreds of subset group reasonable.

As shown in Fig. 7.2, a convergence test on the the number of identical atomic groups is performed. In each case, a ODE solver runs for solving $6N_{group} + 2$ equations together up to 100 μs. We see the the system behavior, both the resonator reflection (R) and the ensemble coupling strength ($g_{e,tot}$, is about to be steady after $N_{group} = 100$, which agrees with our expectation. In Fig. 7.3(a), the resonator reflection at zero detuning is plotted. We observe that it is about steady after 400 μs. In Fig. 7.3(b), the ensemble averaged populations are plotted. The populations are undergoing a slow change over time, due to the slowest time constant set in the simulation. At 400 μs, the population is almost stable, where the last 5 % changes happens from $N_2 = 0.198$ to $N_2 = 0.208$ in the next 600 μs. For the considerations of the resonator reflection and the sake of time, we use $t_{end} = 400\mu$s in the later experiment as a termination of the ODE solver, assuming the behavior is almost similar as the steady state.

Next, we fixed the $N_{group} = 2^7 + 1 = 129$ and run the time convergence test, as shown in Fig. 7.3. The system will have temporal behavior when the optical pump starts to apply. The longest time scale that is set in the simulation is the spin-phonon relaxation ($\gamma_{1s} = 1$ ms) and the optical T_1 as 300 μs. The key point is to find when the system is roughly steady in terms of the resonator reflection.

Hence, with a fixed N_{group} and termination time, we could simulate the CIT effect at different optical pump powers and different microwave probe powers. As shown in Fig. 7.4, we change the optical pump powers and microwave probe powers. On the top plot, a $\Omega = 0.22$ MHz is used, where we observe some resonator splitting patterns. Since the microwave probe power used is relatively small, we only observe

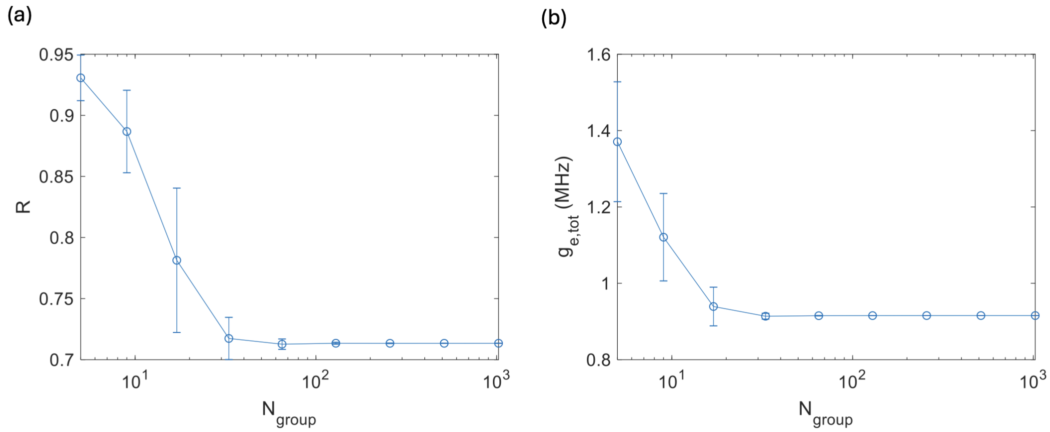

Figure 7.2: **Convergence test of the CIT simulation on N_{group}.** (a) The resonator reflection at zero detuning vs different N_{group}. (b) The ensemble coupling strength vs different N_{group}. The system behavior is stable when $N_{group} > 100$.

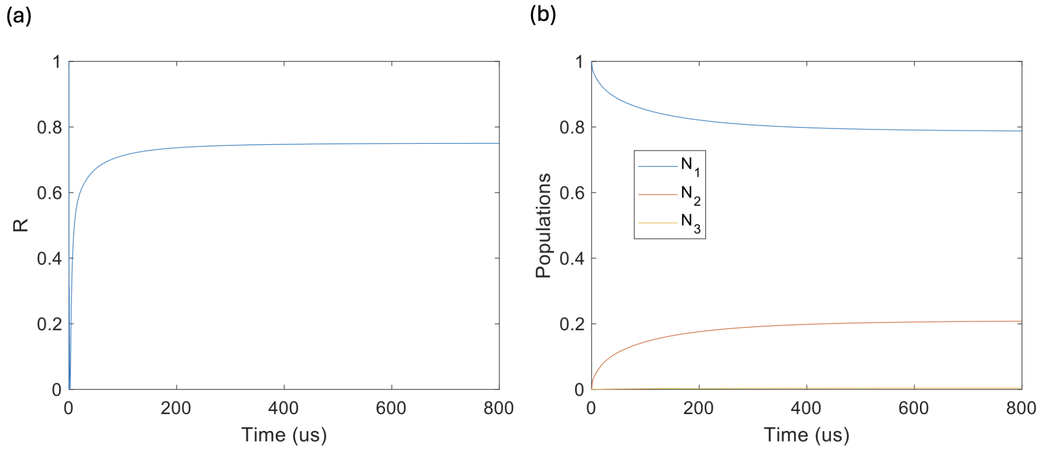

Figure 7.3: **Convergence test of the CIT simulation on the evolution time.** (a) The resonator reflection at zero detuning vs system evolution time. (b) The ensemble averaged populations at different energy levels vs system evolution time.

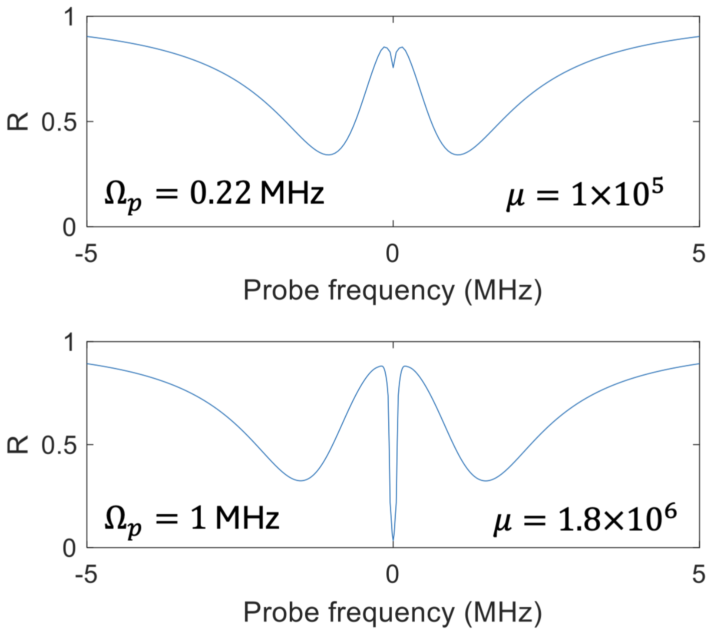

Figure 7.4: **CIT simulation results at different conditions.** Top: A CIT simulation with weak optical pump power and weak microwave probe power. Only a small CIT phenomenon is observed at the center. Bottom: A CIT simulation with high optical and microwave powers. A sharp CIT dip is observed at the center.

a weak CIT window on the top. On the bottom plot, we increase the optical pump power to $\Omega = 1$MHz, a clear splitting pattern is observed on the original resoantor profile. A sharp CIT dip is also captured with $\mu = 1.8 \times 10^6$, corresponds to a similar probe power used in the experiments. Also, we notice that the dip surpasses the orginal resonator dip (set $\kappa_c/\kappa_t = 0.8$ in the simulation). This is the effect of locally tuning the resonator kappa ratio to critical coupling point. The corresponding microwave power is referred as critical powers μ_c.

7.3 Gain of a spin-inverted amplifier

In the previous sections, we show how to calculate the ion-cavity coupling spectrum, specifically for the strong coupling regime and the CIT regime. This is done by initializing the system into the collective spin-down state. With the three-level systems, we can also apply the pump at the highest transition frequency, and hence starting with the spin-up state. With this, spin inversion will be achieved, where novel quantum dynamics can be studied. To understand the system, I will first discuss the gain of a spin-inverted system, in other words, an amplifier. The idea is shown in Fig. 7.6. This is not a new topic and the amplifier has been extensively

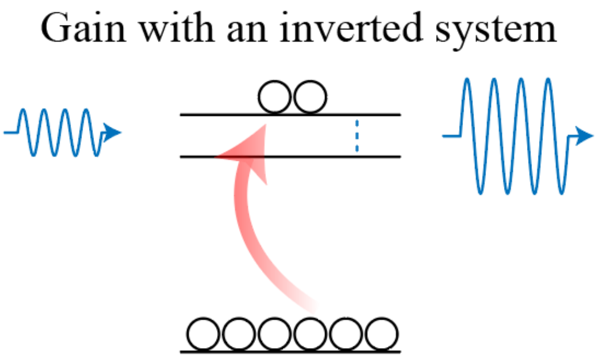

Figure 7.5: **Schematic of an amplifier based on an inverted system.** Spin inversions are created by pumping the three-level systems on the highest transition frequency. A weak input would trigger the stimulated emission process, hence amplify the signal strength.

studied and used in real experiments. I acknowledge this paper [100], where a maser amplifier has been derived clearly and achieved at room temperature. The derivations are relatively simple so I will summarize the key results here.

Similar to Eqn. 7.13, with spin inversion the sign of atomic coupling will be flipped, showing as:

$$R(\omega) = |1 - \frac{i\kappa_{a,c}}{\omega - \omega_c + i\kappa/2 + W(\omega)}|^2. \tag{7.13}$$

For a Lorentzian lineshape of the inhomogeneity, the density function and the corresponding $W(\omega)$ can be calculated:

$$\begin{aligned} \rho &= \frac{\Delta/2}{\pi}\frac{1}{(\Delta/2)^2 + \omega^2} \\ W(\omega) &= \frac{\Omega^2}{\omega - \omega_r + i\gamma/2 + i\Delta/2} \end{aligned} \tag{7.14}$$

where γ is the atomic dephasing rate and Δ is the inhomogeneous linewidth. For rare-earth ion systems, usually we will have $\Delta \gg \gamma$, which then allows us to neglect the contribution from γ. With the coupling terms, we can plug it back into the cavity reflection spectrum and get

$$\begin{aligned} R(\omega) &= |1 - \frac{i\kappa_{a,c}}{\omega - \omega_c + i\kappa/2 + \frac{\Omega^2}{\omega-\omega_r+i\Gamma/2}}|^2 \\ &= |\frac{2i\delta_c + (\kappa_{a,c} - \kappa_{a,i}) + \frac{4\Omega^2}{\Gamma+2i\delta_s}}{-2i\delta_c + (\kappa_{a,c} + \kappa_{a,i}) - \frac{4\Omega^2}{\Gamma+2i\delta_s}}|^2 \end{aligned} \tag{7.15}$$

where I use $\Gamma = \Delta + \gamma$, $\delta_i = \omega - \omega_i$ where i could be the cavity or the spin frequency and $\kappa_{a,c/i}$ represents the coupling/internal decay rate of the resonator. Assume the

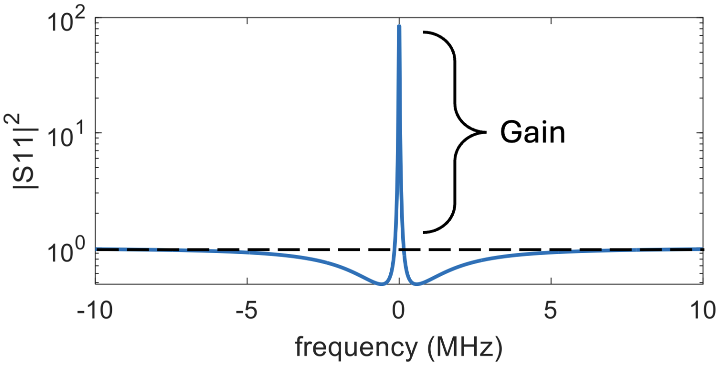

Figure 7.6: **Simulation of a microwave amplifier.** Numerical calculation using Eqn. 7.16 with $\kappa_{a,c}/\kappa = 0.8$ and $\frac{4\Omega^2}{\Gamma} = 0.9\kappa$.

atom and cavity are on-resonance to each other and only consider the on-resonance case ($\delta_c = \delta_s = 0$), we have

$$R(\omega) = |\frac{\kappa_{a,c} - \kappa_{a,i} + \frac{4\Omega^2}{\Gamma}}{\kappa_{a,c} + \kappa_{a,i} - \frac{4\Omega^2}{\Gamma}}|^2. \tag{7.16}$$

From the above equation, we see the $R(\omega)$ could be higher than unity, contrasting to the spin-down case where $R(\omega) = |\frac{\kappa_{a,c}-\kappa_{a,i}-\frac{4\Omega^2}{\Gamma}}{\kappa_{a,c}+\kappa_{a,i}+\frac{4\Omega^2}{\Gamma}}|^2$ can never surpass 1. The reason is that we have spin inversion here and the stimulated emission process would happen with a small trigger on the signal. For example, if the cooperativity is 0.9 ($C = \frac{4\Omega^2}{\Gamma\kappa}$) and the kappa ratio for coupling is 0.8 ($\frac{\kappa_{a,c}}{\kappa}$), then $R(\omega) = 100$, an amplifier with 20 dB gain at the center of the profile, as shown in Fig. 7.6. We note that keep increasing C to 1 ($\frac{4\Omega^2}{\Gamma} = \kappa$) will reach an instability point where maser oscillation would happen due to an accumulation of enough population inversion. That would generate signals even without a weak input, hence leading the gain to infinity. Experimental results of the microwave amplifier will be shown in the next chapter.

7.4 Theory of superradiance burst

As discussed in the previous chapter, C>1 would trigger the maser/laser process. Here, I would cover another emission process that is stronger than normal emission – superradiance. Superradiance is a many-body quantum phenomenon due to a group of atoms collectively and coherently contributing to the emission. It has been studied in theory and experiments [101–103]. The unique property of it is the relationship with the number of atoms. In a typical emission process, the emission strength is linear with the number of emitters, where each emitter contributes individually to the power. In superradiance, one would think about each emitter contributing individually to the electric field, and hence quadratically enhancing the field strength. Another uniqueness of superradiance is the temporal behavior. By exciting the system with a pump pulse, decay at a much faster speed (faster than the Purcell-enhanced emission) will be observed. Furthermore, if the system is with good coherence and enough population inversion is prepared, a superradiant burst with a delay from the pump will be observed. We experimentally observe this superradiant burst behavior, which will be presented in the next chapter. Here, I will go through the theory on how to understand superradiance and how to understand delayed bursts. A fully derivation can be found in [94]. Here I will review the key results with some discussions for our system.

First, we start with a Hamiltonian for N spins with two energy levels:

$$\mathcal{H} = \hbar\omega_c a^\dagger a + \Sigma_i (E_{1,i}\sigma_{11,i} + E_{2,i}\sigma_{22,i}) + \hbar\Sigma_i g_i (a^\dagger \sigma_{12,i} + \sigma_{21,i} a) + i\hbar\eta(a^\dagger - a) \quad (7.17)$$

where η is the drive of the system. Solving the equations in the Heisenberg picture by adding dissipation, we have

$$\begin{aligned} \dot{a} &= -i\omega_c a - i\Sigma_i g_i \sigma_{12,i} + \eta - \frac{\kappa}{2} a \\ \dot{\sigma}_{12,i} &= -(i\omega_{12} + \gamma_\perp)\sigma_{12,i} - ig(\sigma_{11,i} - \sigma_{22,i})a \\ \dot{\sigma}_{22,i} - \dot{\sigma}_{11,i} &= -2\gamma_{\|}\sigma_{22,i} + 2ig(a^\dagger \sigma_{12,i} - \sigma_{21,i} a). \end{aligned} \quad (7.18)$$

Assuming the cavity decay rate is fast, so we can adiabatically eliminate the cavity mode by setting $\dot{a} = 0$, which gives a relationship between a and $\Sigma_i \sigma_{21,i}$ with the drive term. We then plug this back into the equation of $\sigma_{12,i}$ and $\dot{\sigma}_{22,i} - \dot{\sigma}_{11,i}$ term, summing over all the atoms and represent the equation via the collective spin operator:

$$\begin{aligned} \dot{S}_z &= \frac{4g\eta}{\kappa} S_y - \gamma_{\|}(S_z + \frac{N}{2}) - \frac{4g^2}{\kappa} S_+ S_- \\ \dot{S}_- &= -\gamma_\perp S_- + \frac{4ig\eta}{\kappa} S_z + \frac{4g^2}{\kappa} S_z S_- \end{aligned} \quad (7.19)$$

where $S_z = \frac{1}{2}\Sigma_i \sigma_{22,i} - \sigma_{11,i}$, $S_y = \frac{1}{2}\Sigma_i i\sigma_{21,i} - i\sigma_{12,i}$, $S_+ = \Sigma_i \sigma_{21,i}$ and $S_- = \Sigma_i \sigma_{12,i}$. The result in Eqn 7.19 is informative. First, looking at the S_z equation, the first term describes the drive, the second term describes the longitudinal decay and the last term is the many-body term for enhancing the decay rate. For a single atom, $S_+ S_-$ is $S_z + \frac{1}{2}$, which is the Purcell-enhanced decay rate from the atom-cavity interaction. For multi-particle systems

$$S_+ S_- = \Sigma_i \sigma_{21,i}\sigma_{12,i} + \Sigma_{i\neq j}\sigma_{21,i}\sigma_{12,j}. \quad (7.20)$$

The first term is the same as before, with N terms inside. The second sum describes the quantum correlations between different atomic operators that could interfere with each other and hence enhance the emission process. This sum contains N^2 terms, responsible for the non-linear behavior of the superradiance phenomenon. Also, since the emission strength is the evolution rate of spin inversion, we will have $I \propto \frac{4g^2}{\kappa} \langle S_+ S_- \rangle$. This suggests that if the spin state is in a fully spin-up state, there is no $S_\pm$ and hence no emission at the time. It will emit when the coherence term $S_\pm$ is maximized, which leads to a delay of the burst.

On the other side, one could also regroup the S_- equation into

$$\dot{S}_- = -(\gamma_\perp - \frac{4g^2}{\kappa} S_z) S_- + \frac{4ig\eta}{\kappa} S_z \tag{7.21}$$

where the first term is the decay/gain term of the coherence and the second term describes the drive. From here, one can see that a critical condition is when $\frac{4g^2}{\kappa\gamma_\perp} = 1$. After this point, S_- will experience an exponential gain instead of decay, showing as the masing threshold. One point that needs to be noted, is that we did not consider inhomogeneities in the above equations, which would modify $\gamma_\perp$ to an integral from each atom considering $\gamma_\perp$ and inhomogeneity Γ.

Lastly, one could analytically solve the equations by considering a pure $|J, M\rangle$ collective angular momentum state. Although the experiment may not exactly generate a pure state like this, but the analytical result gives intuitions on how to understand the system behavior. With the $|J, M\rangle$ state, we further assume no driving strength ($\eta = 0$ as we already initialize the system in $|J, M\rangle$ state) and ignore the longitudinal decay as it is too slow for the dynamics we are interested, the equation will become:

$$\begin{aligned} \langle J, M| \dot{S}_z |J, M\rangle &= -\frac{4g^2}{\kappa} \langle J, M| S_+ S_- |J, M\rangle \\ \dot{S}_z &= -\frac{4g^2}{\kappa} (\frac{N}{2} - S_z + 1)(\frac{N}{2} + S_z) \end{aligned} \tag{7.22}$$

where we take $J = \frac{N}{2}$ and $M = S_z$. Following this paper [104], we get[2]

$$S_z(t) = -\frac{N}{2} \tanh[\frac{2Ng^2}{\kappa}(t - t_d)] \tag{7.23}$$

where $t_d = \frac{\kappa}{2Ng^2} log(\tan\frac{\theta}{2})$ and $M = -\frac{N}{2}\cos\theta$. We found the delay is inverse proportional to the cooperavitity and related to the initial spin state. A fully inverted

---

[2] I notice the result is solved by ignoring the '+1' in the first bracket. It is okay for large N where a billion and a billion plus one does not matter. The result would be slightly different. Since the goal is to learn some intuitions from analytical solution, this assumption should be fine.

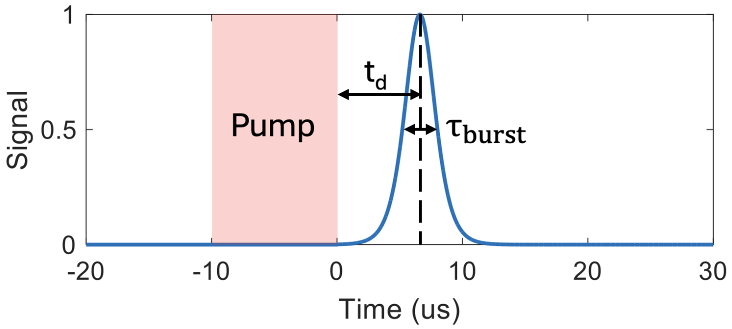

Figure 7.7: **Simulation of a superradiant burst.** Numerical calculation using Eqn. 7.24 with $N = 2^9$, $g = 2\pi \times 10$ Hz, $\kappa = 2\pi \times 4$ MHz and $\theta = 0.99\pi$.

system ($\theta = \pi$) will have infinite delay time. This is because we ignore the quantum fluctuation in the system, which could kick the polarization vector a little but trigger the whole emission process. In the next three-level system simulation, I will show the same simulation with and without the quantum fluctuation term, which shows nothing in the lack of the fluctuation term. Next, we can get the emission profile, which is the one got experimentally measured, as:

$$I \propto \left\langle \dot{S}_z \right\rangle = \frac{N^2 g^2}{\kappa} sech^2 [\frac{2Ng^2}{\kappa}(t - t_d)] \tag{7.24}$$

with a FWHM (full width at half maxima) $\tau_{burst} = \frac{\kappa}{Ng^2} log(\sqrt{2} + 1)$. The intensity shows the quadradic dependence on the number of atom and the burst delay is inverse proportional to the cooperavitity. A illustration of the solution is shown in Fig. 7.7 using Eqn. 7.24.

7.5 Simulation of periodic superradiance with three-level systems

Now we can go through the full calculation for the superradiance with three-level systems. First, I will go through the same formulism as described in the previous section. For a two-level system, one would only need to have the S_z and S_- to solve the full system. However, in a three-level system, there are five equations to solve, which makes it almost impossible to have an analytical solution. However, similar intuition could be learned by looking at the contribution from each term, without providing an analytical solution. Lastly, we implement a numerical simulation for the system. The method and results will be discussed here.

First, the system Hamiltonian is

$$
\begin{aligned}
\mathcal{H} =& \hbar\omega_{o,c}a^\dagger a + \hbar\omega_{e,c}b^\dagger b + \sum_k E_{1,k}\sigma_{11,k} + \sum_k E_{2,k}\sigma_{22,k} + \sum_k E_{3,k}\sigma_{33,k} \\
&+ \sum_k \hbar g_{o,k}(a^\dagger\sigma_{12,k} + \sigma_{21,k}a) + \sum_k \hbar g_{e,k}(b^\dagger\sigma_{23,k} + \sigma_{32,k}b) \\
&+ \sum_k \hbar\Omega_k(\sigma_{13,k} + \sigma_{31,k}) + \hbar\eta_b(b^\dagger + b) + \hbar\eta_a(a^\dagger + a).
\end{aligned}
\tag{7.25}
$$

We note the Hamiltonian is pretty much the same as Eqn. 7.11, but here I shift the optical cavity to σ_{12} instead of σ_{13} and use a classical drive term to describe the dynamics on σ_{13}. The reason is similar as mentioned before, that the cavity is broad enough. Since we will only do classical drive on one of the transitions, we can use Ω to replace $ga/ga^\dagger$ but leave the other arm for the optical cavity coupling. By doing this, we avoid using another input coupling term to describe the drive strength. Another difference here is the two extra quantum flucuation terms, describing by η_b and η_a. This is the one as mentioned in the previous section, that one needs a small kick on the polarization vector to be away from a fully spin-up state, such that the superradiance will happen. Mathematically, since our optical cavity is too board and the cooperativity is small, the main kick happens through the microwave side. Therefore, in the later derivation, I will set $\eta_a = 0$ for simplicity. After writing the Heisenberg equations in the three-level system, we have:

$$
\begin{aligned}
\dot{a} &= \frac{i}{\hbar}[\mathcal{H}, a] = -i\omega_{o,c}a - \frac{\kappa_o}{2}a - i\Sigma g_{o,k}\sigma_{12,k} \\
\dot{b} &= -i\omega_{e,c}b - i\Sigma g_{e,k}\sigma_{23,k} - \frac{\kappa_e}{2}b - i\eta_b \\
\dot{\sigma}_{12,k} &= -(i\omega_{12} + \gamma_o)\sigma_{12,k} + i\Omega_k\sigma_{32,k} - ig_{o,k}(\sigma_{11,k} - \sigma_{22,k})a - ig_{e,k}b^\dagger\sigma_{13,k} \\
\dot{\sigma}_{23,k} &= -i(\omega_{23} + \gamma_s)\sigma_{23,k} - ig_{e,k}(\sigma_{22,k} - \sigma_{33,k})b + ig_{o,k}a^\dagger\sigma_{13,k} - i\Omega_k\sigma_{21,k} \\
\dot{\sigma}_{13,k} &= -(i\omega_{13} + \gamma_o)\sigma_{13,k} - ig_{e,k}\sigma_{12,k}b - i\Omega_k(\sigma_{11,k} - \sigma_{33,k}) + ig_{o,k}\sigma_{23,k}a \\
\dot{\sigma}_{11,k} &= \gamma\sigma_{22,k} + \gamma\sigma_{33,k} - i\Omega(\sigma_{13,k} - \sigma_{31,k}) - ig_{o,k}(a^\dagger\sigma_{12,k} - \sigma_{21,k}a) \\
\dot{\sigma}_{22,k} &= -\gamma\sigma_{22,k} - ig_{e,k}(b^\dagger\sigma_{23,k} - \sigma_{32,k}b) - ig_{o,k}(\sigma_{21,k}a - a^\dagger\sigma_{12,k}) \\
\dot{\sigma}_{33,k} &= -\gamma\sigma_{33,k} - i\Omega(\sigma_{31,k} - \sigma_{13,k}) - ig_{e,k}(\sigma_{32,k}b - b^\dagger\sigma_{23,k})
\end{aligned}
\tag{7.26}
$$

Again we can adiabatically eliminate the cavity mode and plug the result back into the differential equations, then we have

$$\begin{aligned}\dot{S}_{33} - \dot{S}_{22} = -\gamma(S_{33} - S_{22}) - \frac{8g_e^2}{\kappa_e}S_{32}S_{23} - i\Omega(S_{31} - S_{13}) + \frac{4g_o^2}{\kappa_o}S_{21}S_{12} \\ - \frac{4g_e\eta_b}{\kappa_e}(S_{23} + S_{32})\end{aligned} \tag{7.27}$$

$$\dot{S}_{23} = -\gamma_s S_{23} + \frac{2g_e^2}{\kappa_e}(S_{33} - S_{22})S_{23} + \frac{2g_e\eta_b}{\kappa_e}(S_{33} - S_{22}) - i\Omega S_{21} - \frac{2g_o^2}{\kappa_o}S_{21}S_{13}. \tag{7.28}$$

This is the dynamics of spin population difference and the spin coherence term, which would contribute to the masing effect. Clearly, with an extra level, the equations are with more terms. First, in $\dot{S}_{33} - \dot{S}_{22}$ equation, the first term is the spontaneous decay, the second term is the interference term from the many-body interaction that is responsible for the N^2 dependence. The third term is the driving term to supply the population difference. The fourth term is another many-body term from the atom-cavity interaction in the optical domain. With good coherence in the optical domain, this could also be another N^2 term. However, in our case, the optical coherence is not ZEFOZ transitions, which we measure hundreds of ns coherence time. Therefore, this only contributes the diagonal term, which is N dependence but not N^2. Also, in our system, $g_o \sim 8$ kHz, but $\kappa_o \sim 100$ GHz. This leads to a tiny $\frac{g_o^2}{\kappa_o}$, presenting pretty much no Purcell enhancement on the optical transitions. Since this is much smaller than the spontaneous decay term γ, we can ignore it. The last term is the quantum fluctuation term. Assuming an optical pump has been applied and turned off, by ignoring the quantum fluctuation term, we found $\dot{S}_{33} - \dot{S}_{22} = -\gamma(S_{33} - S_{22}) - \frac{8g_e^2}{\kappa_e}S_{32}S_{23}$, which is the normal decay and the enhanced decay. In this case, the system evolution decays back to the two-level system case.

A similar analysis can be applied to the $\dot{S}_{23}$ equation. Here, we have $\dot{S}_{23} = -(\gamma_s - \frac{2g_e^2}{\kappa_e}(S_{33} - S_{22}))S_{23}$ considering the pump has been turned off and ignoring the quantum fluctuation term. $S_{21}S_{13}$ term can also be neglected as it contains an optical coherence term that dephases quickly without presenting the N^2 term from quantum correlation. We found this also decays back to the two-level system case, where the maser will be triggered if $\frac{2g_e^2}{\kappa_e}(S_{33} - S_{22}) \gg \gamma_s$. However, to fully capture the temporal behavior, one needs to run a numerical simulation with 6N+2 equations. Similar to the CIT simulation, here I generate a random sampling from a Gaussian distribution of 10^{10} atoms, and bundle atoms into hundreds of groups, where in each group the atomic frequencies are similar to the sample and hence treating them as identical atoms.

The convergence has been tested in the CIT simulation. Here, the code is exactly the same other than a few ODEs have been modified to accommodate the drive on different optical transitions. Setting $N_{group} = 129$, as concluded from the previous convergence test, we model the periodic superradiant burst behavior with Eqn. 7.26. By simulating the system up to 1 ms, we clearly observe this periodic behavior. The beginning emission is sharp and large, due to the system at that time is a highly coherent state without any dephasing yet and no population in the second level. Later, the behavior becomes stable and constant, showing as well in the population dynamics in each energy level. Here, we calculate the population via an ensemble averaging, meaning $N_i = \Sigma_k P_i N_{i,k}$. We clearly observe the periodic dynamics on the spin inversion.

Discussion on the periodic behavior

Although it is almost impossible to perform an analytical solution to the equations, we can try to gain some intuition by looking at different terms. Here, no analytical equation is derived, but the goal is to see why there is periodic behavior. By ignoring the $\frac{4g_o^2}{\kappa_o}$ and η_b terms, we can simplify the dynamics of $S_{33} - S_{22}$ and S_{23} as

$$\begin{aligned}\dot{S}_{33} - \dot{S}_{22} &= -\gamma(S_{33} - S_{22}) - \frac{8g_e^2}{\kappa_e} S_{32}S_{23} - i\Omega(S_{31} - S_{13}) \\ \dot{S}_{23} &= -[\gamma_s - \frac{2g_e^2}{\kappa_e}(S_{33} - S_{22})]S_{23} - i\Omega S_{21}.\end{aligned} \tag{7.29}$$

We see after creating a population inversion ($S_{33} - S_{22}>1$), S_{23} will increase exponentially as long as $\frac{2g_e^2}{\kappa_e} > \gamma_s$. But at the same time, $\dot{S}_{33} - \dot{S}_{22}$ has an enhanced decay term as $S_{32}S_{23}$. Noticing $S_{32}S_{23}$ is a real positive number, it quickly diminishes the inversion to $S_{33} = S_{22}$. However, there is a continuous optical pumping term Ω, feeding the population inversion. Therefore, when the inversion reaches a certain point, fast emission will be triggered to release the population inversion, and another cycle of inversion accumulation will go on. This ongoing cycle makes the system continuously emit superradiant bursts, with the periodicity related to the optical pumping rate and the microwave cooperativity that controls the threshold of the burst. An illustration of the periodic behavior is shown in Fig. 7.10.

7.6 Intuitive understanding of superradiance

After revisiting the simulated model, the key component to generate the superradiance is the S_z and S_{23} term which feedback to each other as shwon in Fig. 7.10. Hence, a two-level system is enough to capture the physics – a spin ensemble coupled

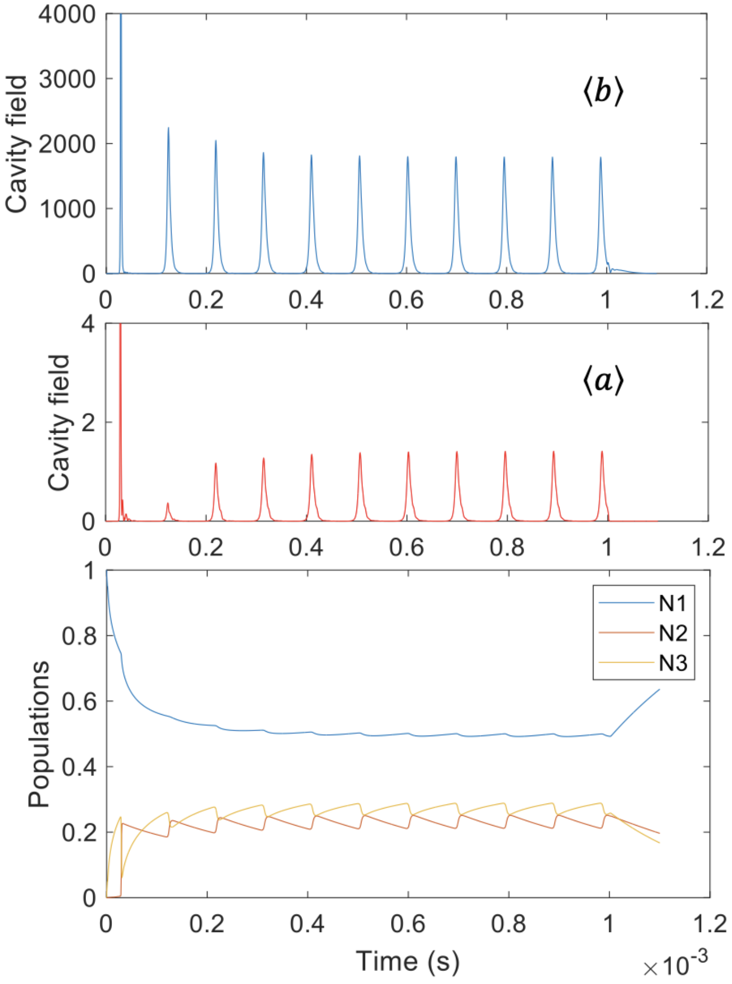

Figure 7.8: **Simulation of the periodic superradiant burst.** Top: Calculated microwave field $\langle b \rangle$ from the equations derived in Eqn. 7.26. Middle: Calculated optical field $\langle a \rangle$. Bottom: Calculated population in three different levels after averaging over the whole ensemble. Periodic dynamics are observed, showing in both the emission pattern and the populations. Here, we use $\delta_{e,c} = 2\pi \times 2$ MHz, $\Omega = 0.8$ MHz with 129 different groups of atoms from a 10^{10} Gaussian random sampling.

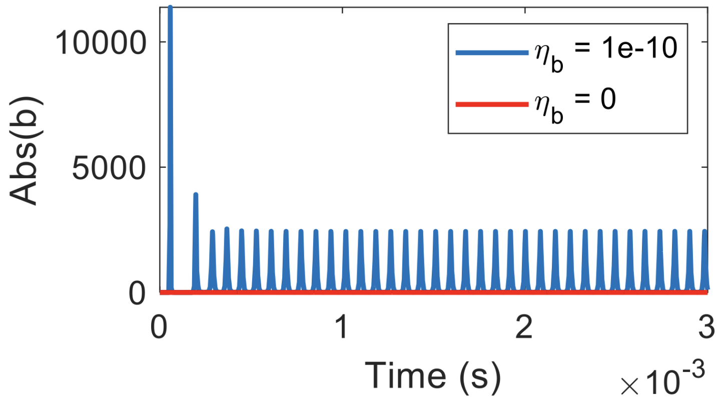

Figure 7.9: **Simulation with and without η_b.** A small noise fluctuation will trigger the superradiant process.

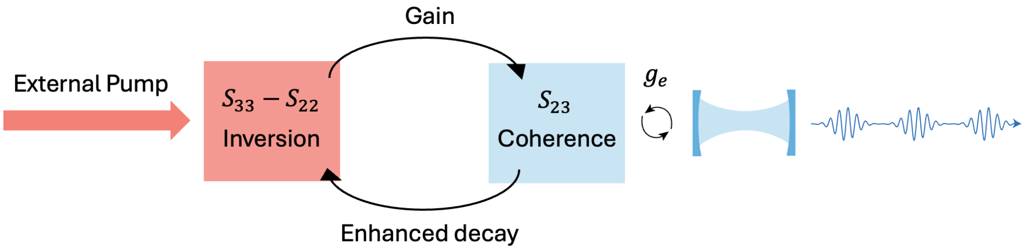

Figure 7.10: **Illustration of the periodic superradiant burst.** The spin inversion $S_{33} - S_{22}$ term will help boost the coherence S_{23} with a gain, while the S_{23} will enhance the decay of spin inversion, which leads to superradiant emissions. This behavior would go on under a CW drive where inversions could be accumulated to the threshold.

to a resonator and a pump for generating the inversion:

$$\begin{aligned}
\mathcal{H} &= \hbar\omega_c b^\dagger b + \Sigma_k E_{1,k}\sigma_{11,k} + \Sigma_k E_{2,k}\sigma_{22,k} + \hbar g \Sigma_k (b^\dagger \sigma_k^- + \sigma_k^+ b) \\
\dot{S}^- &= -\Sigma_k i\delta_k \sigma_k^- - \gamma_2 S^- + \frac{2g^2}{\kappa} S_z S^- + \frac{2g}{\kappa} S_z \eta_b \\
\dot{S}_z &= -2\gamma_1 S_{22} + 2DS_{11} - \frac{8g^2}{\kappa} S^+ S^- - \frac{4g\eta_b}{\kappa}(S^+ + S^-)
\end{aligned} \tag{7.30}$$

where $b, b^\dagger$ is still the microwave resonator mode, $S^- = \Sigma_k \sigma_{12,k}$, $S_z = \Sigma_k(\sigma_{22,k} - \sigma_{11,k})$, $S^+ = (S^-)^\dagger$, $\gamma_{1,2}$ is the T_1 and T_2 dephasing rate, η_b is the noise fluctuation operator and D is the repumping rate of the inversion. Here we adiabatically eliminate the resoantor mode and plug it into the atomic operator dynamics.

The physics is clear again here. In the S^- equation, the first term describes the disorder of the system; the second term describes the dephasing process from the T2 process; the third term describes the inversion induced gain ($\frac{2g^2}{\kappa} S_z$) and the last

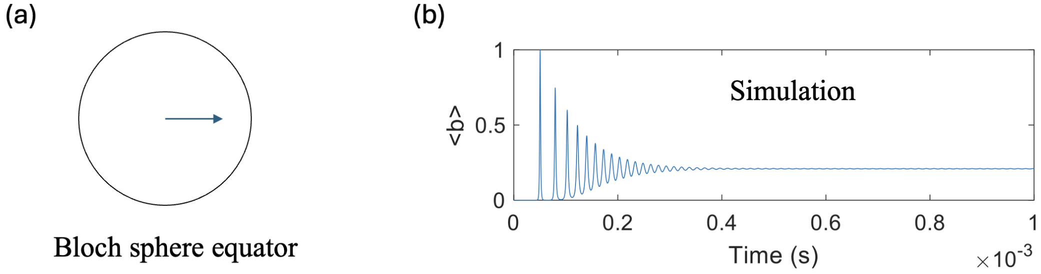

Figure 7.11: **Superradiance in identical atoms.** (a) The Bloch vector illustration. (b) A numerical simulation of the superradiance in identical atoms.

term triggers the superradiance. Similarly in the S_z equation, the first term is the depopulation from T1 process; the second term is the repumping process; the third term is enhanced decay from ensemble coherence ($\sim \frac{g^2N^2}{\kappa}$) and the last term is from the noise fluctuation operator.

No disorder

For the system without disorder, the first term in S^- vanishes. If we ignore the η_b term, the governing equations will then become to two coupled ODEs:

$$\begin{aligned} \dot{S}^- &= (-\gamma_2 + \frac{2g^2}{\kappa} S_z) S^- \\ \dot{S}_z &= (D - \gamma_1)N - (D + \gamma_1)S_z - \frac{8g^2}{\kappa} S^+ S^- \end{aligned} \tag{7.31}$$

In this case, all the atoms experience the same dynamics ,or equivalently, the Bloch vector are all overlapped, as shown in Fig. 7.11(a). A numerical simulation is performed and presented in (b). Some pulses are observed as well, but finally converge to a steady-state emission. The physics behind is straightforward (Fig. 7.12). The cavity field is proportional to ensemble coherence. The ensemble coherence (S^-) undergoes a dephasing from T_2 process and a gain from the inversion. At the beginning, the pumping process quickly generates inversion, which extend the coherence vector. However, the coherence feedbacks to the inversion and introduce an enhanced decay. This shows as the pulses at the beginning of the simulation. Afterwards, the system finally converges to a steady-state coherence vector due to the population related pumping term. Hence, steady-state emission is reached, as shown in the simulation. At this point, $\dot{S}^- = 0$, which gives $S_z = \frac{\gamma_2 \kappa}{2g^2}$

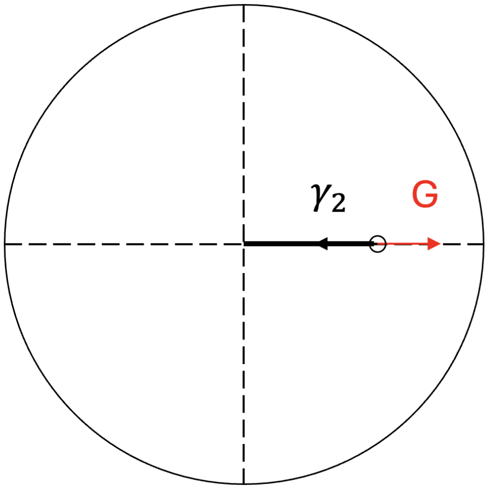

Figure 7.12: **Illustration of superradiance mechanism in identical atoms.** The view of the coherence plane in Bloch sphere. The Bloch vector undergoes a decay that shrinks the vector length, as well as a gain that extend the vector length. A balance will reach when the gain and the dephasing process cancel each other.

With disorder

For system with disorder, one cannot directly solve the governing equations with only two ODEs. The disorder term $\Sigma_k i\delta_k \sigma_k^-$ cannot be summarized into as a single term only with $S^- = \Sigma_k \sigma_k^-$. Therefore, one needs to solve the dynamics of each atom's coherence and sum together to get the ensemble coherence (equivalently, the cavity field):

$$\begin{aligned}\dot{\sigma}_k^- &= -(i\delta_k + \gamma_2)\sigma_k^- + \frac{2g^2}{\kappa}\sigma_{z,k}S^- \\ \dot{S}_z &= (D-\gamma_1)N - (D+\gamma_1)S_z - \frac{8g^2}{\kappa}S^+S^-\end{aligned} \tag{7.32}$$

An illustration of the coherence vectors is shown in Fig. 7.13(a). Instead of the vectors pointing towards the same direction, now each vector will have an angle due to the relative detunings. A numerical simulation is performed in (b). Again, continuous-wave superradiance can be achieved. The physics behind is similar to the idential atom case, shown in Fig. 7.14. Although the vector now has an angle, a new balance can be achieved between the dephasing, the detuning and the gain, causing the steady-state emission.

However, this detailed balance point will break down at higher pump powers. An intuitive understanding of it is that the gain term changes with more number of atoms while the detuning and dephasing is the same. An illustration of the periodic

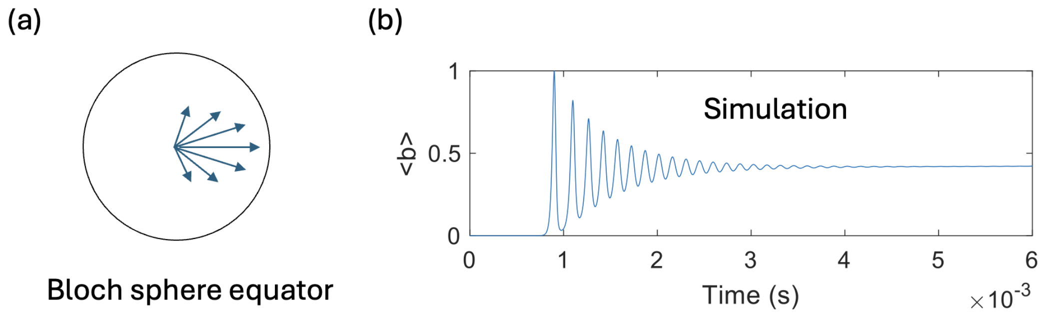

Figure 7.13: **Superradiance in disordered systems.** (a) The Bloch vector illustration. (b) A numerical simulation of the superradiance in disordered systems.

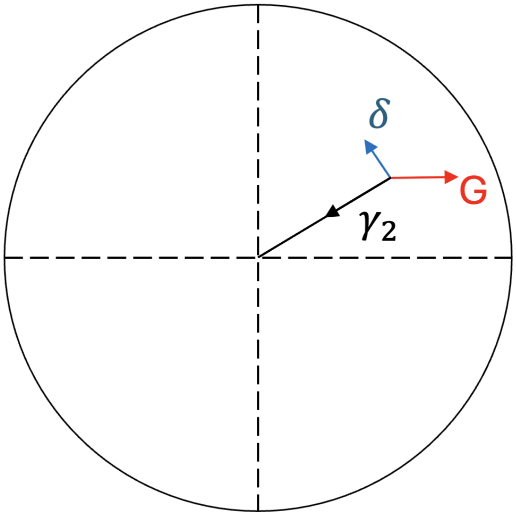

Figure 7.14: **Illustration of superradiance mechanism in disorder systems.** The view of the coherence plane in Bloch sphere. Each vector experience the dephasing, detuning and the gain term. When the three term gets balanced in the coherence plane, a steady-state emission is established.

superradiance is shown in Fig. 7.15(a). The system will develop the ensemble coherence at the beginning. But the vector will not be stabilized here due to the imbalance, causing the vectors to precess on the coherence plane. This terminates the emission as the ensemble coherence quickly vanishes and the system will decay back to the starting point afterwards. Another emission cycle will start when the system accumulates enough population inversion. A simulation of the whole ensemble is shown in Fig. 7.15(b). On the left, the σ_x over time is shown. Similar to a Ramsey experiment, the precession of the vectors causing the σ_x component oscillates based on the detunings. A summation of a vertical cut represents the

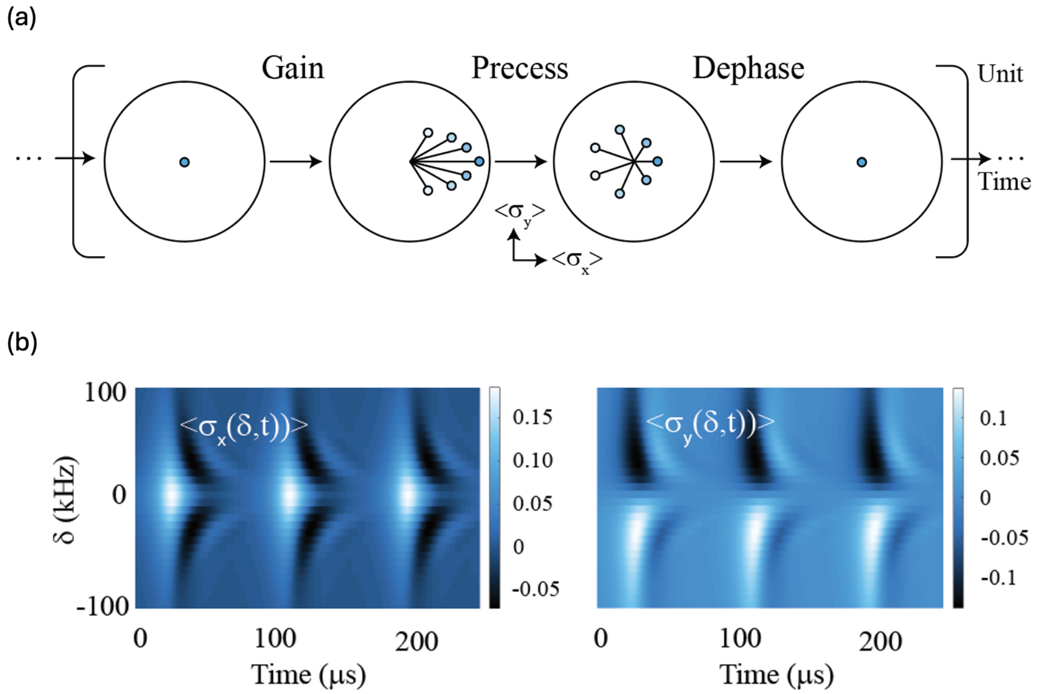

Figure 7.15: **Illustration of periodic superradiance mechanism in disorder systems.** (a) The view of the coherence plane in Bloch sphere. Now the balance breaks at higher pump powers, causing the Bloch vector to precess in the coherence plane. This terminates the emission and the system decays back to the starting point. After enough population gets accumulated, another cycle starts. (b) A simulation of the whole ensemble dynamics for three consequent superradiant pulse.

ensemble coherence at that moment, while a horizontal cut represents each atoms dynamics at that detuning. On the right, the σ_y over time is shown. Since the vectors are rotating based on the detuning, half of the ensemble rotaets clockwise and the other half rotates counter clockwise.

Lastly, one can confirm this periodic superradiance by simulating a same parameter set but including the disorder term or not, shown in Fig. 7.16. Clearly, at higher pump powers, the disorder will turn the continuous emission into periodic patterns, as discussed above.

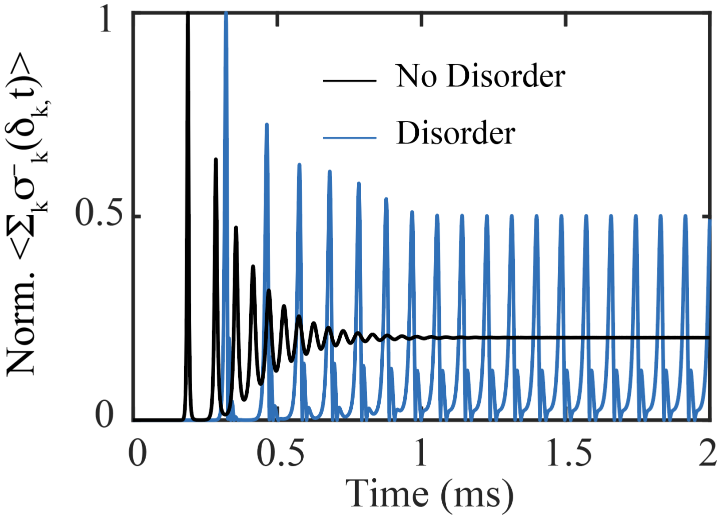

Figure 7.16: **Simulation of a same parameter set with and without disorders.** At higher pump powers, the disorder will turn the continuous emission into periodic patterns.

Chapter 8

MEASUREMENTS OF THE TUNABLE SPIN-INVERTED ENSEMBLE

In this chapter, I will describe the experimental results of the cavity quantum electrodynamics with the spin system. Specifically, I will first talk about the CIT phenomenon, how it appears with different microwave probing power, how the phase changes around the CIT dip, and the optical pump power dependence on the CIT dip. On the other side, by initializing the system into a spin-up state, microwave amplification and superradiance has been measured.

8.1 Experimental results on CIT in the spin domain

With the optical pump connecting between $|g\rangle$ and $|e_1\rangle$ level, we can tune the ensemble spin-resonator coupling strength via the optical pump power ($g_{tot} = g\sqrt{N}$), where the optical pump power controls the excited state population. To start, we first calibrate the microwave resonator lineshape, as shown in Fig. 8.1. From the single port resonator S11 fit, we get $\kappa = 2\pi \times 4$ MHz with the input coupling ratio $\kappa_c/\kappa = 0.8$.

Having the resonator aligned with the spin ensemble, we slowly increase the input microwave power. In the transduction measurement, we always probe the system with low microwave power and transduce single-photon level signals to the optical domain. Here the input microwave power needs to be increased significantly to observe the CIT effect. By turning on the optical power at 400 μW with weak enough microwave power, we observe a strong coupling pattern where the microwave resonator dip is split. Increasing the microwave power to ~ -80dBm level to the input port of the chip, a weak transparency window at the center pops up, showing the CIT effect. Further increasing the power will drastically sharpen the CIT window to about 35dB level, as shown in Fig. 8.2.

As discussed in the previous chapter, higher probe power would drive the spin transitions at the same time while probing the resonator field. This spin-driving modifies locally the coupling strength between the ensemble and the resonator, hence changing the reflection of the cavity spectrum. Specifically, the key equation

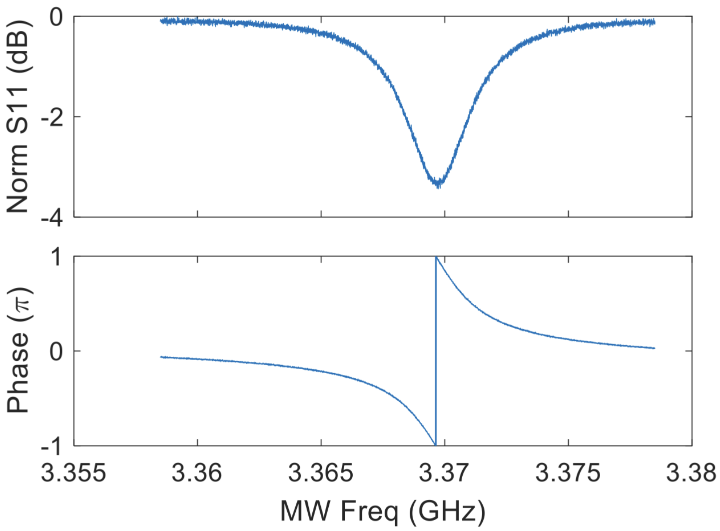

Figure 8.1: **Bare microwave resonator calibration.** The top shows the power of the reflection and the bottom shows the phase of the reflected signal.

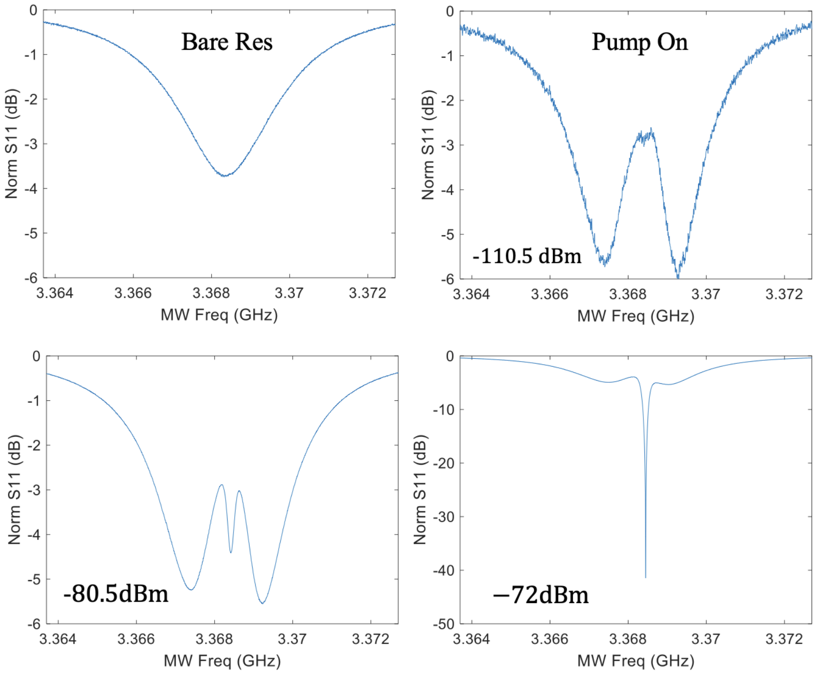

Figure 8.2: **CIT in spin domain with different microwave probe power.** By increasing the microwave probe power, a small transparency window is observed in the center of the strong coupling pattern, known as CIT. With high enough powers, a local critical coupling is realized, as explained in the text.

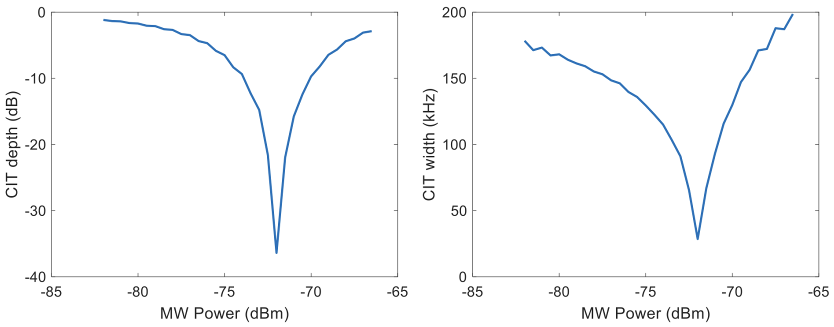

Figure 8.3: **CIT depth and width at different microwave power.** Left: CIT depth in dB scale. Right: CIT width in kHz.

here is

$$R = |1 - \frac{2\kappa_c}{\kappa}\frac{1}{1+x}|^2 \tag{8.1}$$

where x describes the modification due to the ensemble coupling. Since the resonator starts in the over-coupled regime, there is a critical point $x = \frac{2\kappa_c - \kappa}{\kappa} = \frac{\kappa_c - \kappa_i}{\kappa_c + \kappa_i}$ where a local critical coupling can be realized. Combined with the expression of x shown in Eqn. 7.10, we get

$$\mu_c = \gamma\gamma_s(\frac{\kappa_c}{\kappa_c - \kappa_i})^2\frac{C_e^2}{g^2} \tag{8.2}$$

where we see the critical power is quadratic dependent on the microwave cooperativity. Also, since this effect only happened with an over-coupled regime, $\kappa_c > \kappa_i$ should be with the system, avoiding the singularity of the equation.

Increasing the microwave power beyond the critical point will pass the critical coupling and further move into the local under-coupled regime. Hence, by fully sweeping the input microwave power, we could resolve this critical power as shown in Fig. 8.3. The critical point should in principle show a dip at real 0 which corresponds to minus infinity dB. However, experimentally searching the point is rather hard as it is only a specific number of frequency at a number of probing power. The data shown in Fig. 8.3 is with 5 kHz frequency step and 0.5 dB power step and Fig. 8.4 is with 10 kHz and 0.2 dB power step. The CIT linewidth is shown in Fig. 8.3, where we observe a linewidth down to 30 kHz. The CIT depth of about 35dB is not changed at different pump powers or better resolutions, meaning either the detection noise floor is not enough or the step needs to be further refined.

In Fig. 8.4, we repeat the microwave power measurement at different optical pump power. The pump power determines the amount of population in the excited state spin manifold, hence controlling the microwave cooperativity C_e. With small

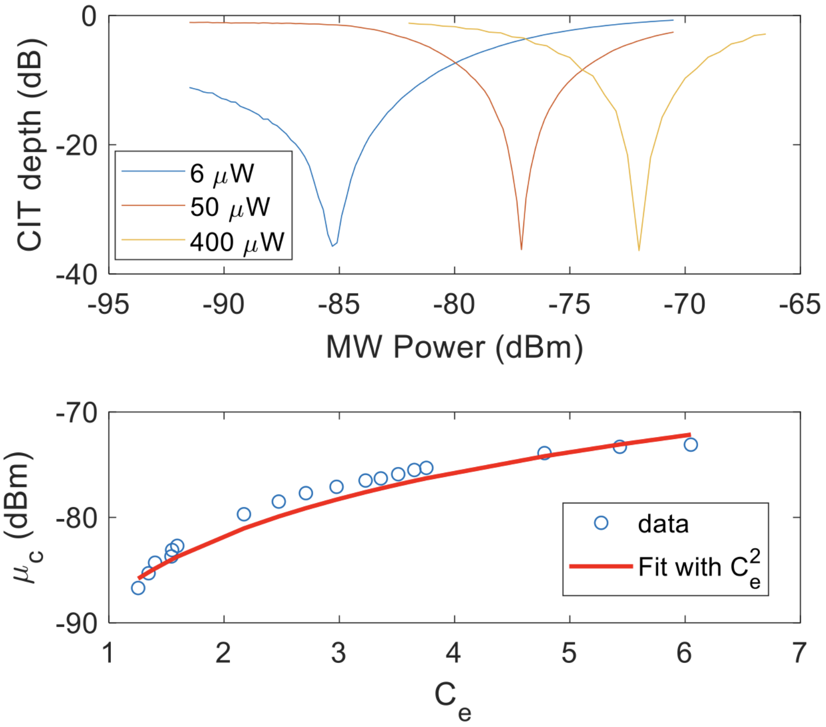

Figure 8.4: **The critical power at different cooperativity.** Top: CIT depth vs microwave power scan at different optical pump powers. Bottom: Extracted critical powers μ_c vs microwave cooperativity C_e, where the relationship between optical pump power and C_e is individually calibrated.

microwave powers, we could first measure the spin-resonator coupling to calibrate the relationship between the pump power and cooperativity. With this mapping, by extracting the critical power at each optical pump power, we get the relationship between μ_c and C_e, as shown in the bottom of Fig. 8.4. Based on Eqn. 8.2 we just derived, we fit the data with a quadratic curve, which explains the data. The discrepancy comes from the fact that the resonator center frequency will shift due to the optical illumination, which lowers the C_e at higher pump powers.

Lastly, for the full picture, the spin-resonator coupling at different optical powers is calibrated, shown in Fig. 8.5. At each power, a weak microwave probe is used to avoid the CIT condition, and each coupling spectrum is fitted using the same fitting model as the transduction section. We note the fitting at low microwave powers may not be correct. The fitting will always give a number, but lower coupling means less N. Under this circumstance, the CIT effect happened with less μ_c, which deepens the spin transition. Therefore, the fitting captures the CIT structure as if higher coupling strengths are there.

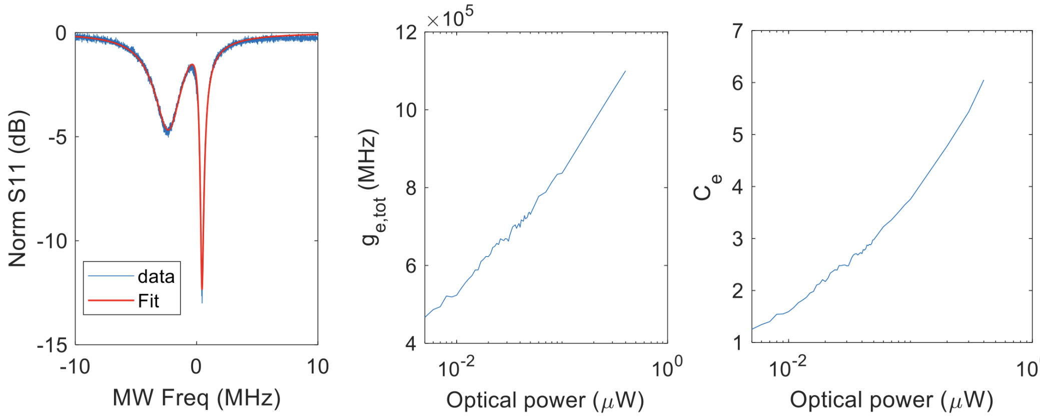

Figure 8.5: **Spin coupling strength vs optical pump power.** Left: An example of fitting the 400 μW power data. Middle: The ensemble coupling strength vs optical pump power. Right: The microwave cooperativity C_e at different optical pump power.

8.2 Microwave amplifier

The CIT phenomenon is achieved by initializing the system into the collective spin-down state. Here, by using the other optical pump arm that connects to the spin-up level, we create spin inversion in the system. With small inversions not yet triggering the superradiant emission, we observe the microwave amplifier effect, as shown in Fig. 8.6. As discussed in the previous chapter, amplification can be captured by Eqn. 7.16. With optical detuning, we could modify the equation in terms of N for the fitting, which goes as:

$$R(\omega_{op}) = |1 - \frac{i\kappa_c}{i\kappa_t/2 + \frac{1}{i\Gamma_s/2} C_e \kappa_t \Gamma_s/4 \frac{(\Gamma_o/2)^2}{(\omega_{op}-\omega_0)^2+(\Gamma_o)^2}}|^2 \tag{8.3}$$

where ω_o is the center of the optical transition frequency, $\Gamma_{o/s}$ is the optical/spin inhomogeneity, $\kappa_{c/t}$ is the microwave resonator decay rate in coupling port or in total. With the model, we can set C_e and Γ_o as the fitting parameter to generate the curve shown in Fig. 8.6, which we extract $C_e = 0.86$ and $\Gamma_o = 105$ MHz. We notice that this is below the maser threshold as C_e is smaller than 1. Experimentally, we have also not observed any masing effect at this pump power level yet.

8.3 Superradiant burst generation under a pulsed excitation

Superradiant bursts are delayed emissions from the excitation pulses. As discussed in the previous chapter, the mechanism behind this is the feedback between the spin inversion $S_{33} - S_{22}$ and the spin coherence S_{23}. By initializing the system to $|e_2\rangle$

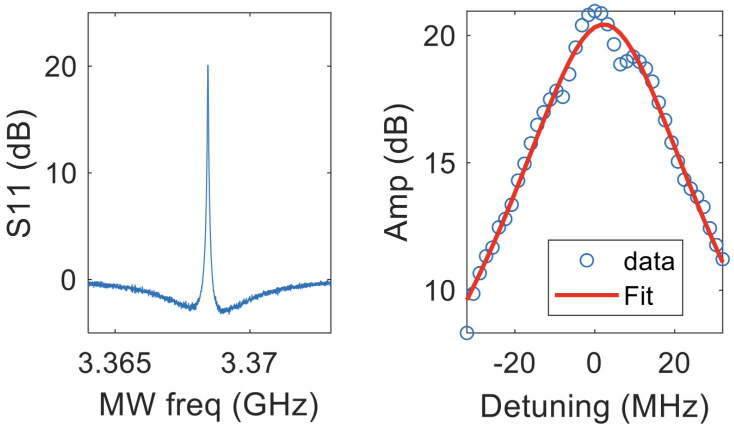

Figure 8.6: **Microwave amplification with spin inversion.** Left: A measurement of the microwave amplifier with 5 μW pump power. Right: The amplification vs optical pump detuning. A model considering both the amplification and a Lorentzian profile is fitted for 5 μW optical pump power. See the main text for more details.

state with a fast pulse, the system can be described by a collective spin-up state $|J, M\rangle$ where $J = N_3/2$. N_3 is the population in $|e_2\rangle$ level. Here, all the atoms are in $|e_3\rangle$ when considering the subsystem of $|e_2\rangle$ and $|e_3\rangle$, we have $M = -J\cos\theta$ where θ is π. After the pulse is turned off, the system evolves under Eqn. 7.19, where strong emissions will be triggered when the Block vector is on the equator, as shown in Fig. 8.7. Fig. 8.7c shows an example of the superradiant burst. τ_d and τ_w are labeled for the delay time and the burst width, which will be discussed later. We also observe other revivals of the burst, as also have been observed in [105].

From theoretical calculation, the burst delay τ_d is inversely dependent on the number of atoms involved in the process, as the collective coupling strength is the one that matters. Hence, we could scan in optical pump frequency, effectively controlling the number of atoms by addressing them at different locations across the optical inhomogeneity, as shown in Fig. 8.8. We use 1 mW optical pump power for 50 μs pulse initialization. Short initialization is important to make sure the system has not decayed significantly and also allows us to map the number of atoms from the optical detuning. In each optical detuning, we collect 300 copies of the burst data. Since the burst is triggered by another random process (e.g., quantum fluctuation), the delay time varies between the copies and leads to an uncertainty shown in the error bars in Fig. 8.8(a). From the calculation, we have $t_d \approx \frac{\kappa}{4Ng^2} log(\tan^2(\frac{\theta}{2}))$. The equation is very sensitive to the tipping angle θ (near π), which is experimentally hard to prevent. Hence, we do an inverse-Lorentzian fit to the results instead of

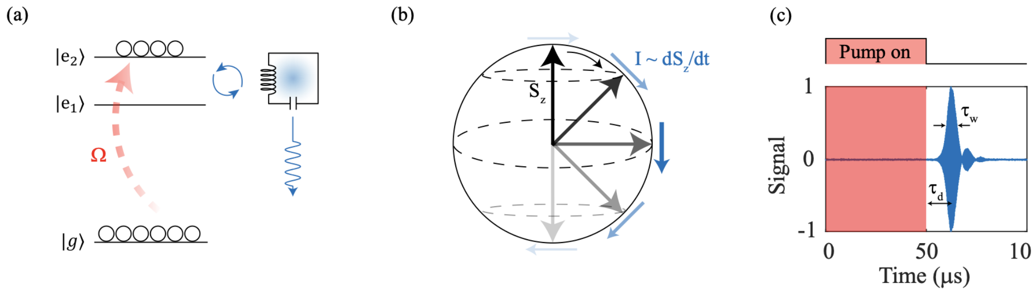

Figure 8.7: **Schematic of superradiant burst.** (a) A drawing of the system dynamics. A pulsed optical pump is sent from $|g\rangle$ to $|e_2\rangle$. The accumulated population inversion will build up the spin coherence, which in turn speeds up the decay process of the inversion. (b) A Bloch sphere model for the burst understanding, where the Bloch vector is at the north pole at the beginning. A small kick from quantum fluctuations or system decay will change and move the vector away from the pole and hence speed up the decay. (c) An example of the measured burst signal. τ_d is the burst delay and τ_w is the burst width.

direct calculation. An inverse of the Lorentzian profile is a quadratic function, which shows as the dashed line on top of the data. From the fitting, we get the optical linewidth is 77 MHz, which roughly agrees with the individual calibrated linewidth of 92 MHz. The pulse width is also analyzed in Fig. 8.8(b). From the calculation, $\tau_w = \frac{\kappa \cosh \sqrt{2}}{Ng^2}$. Hence, we use another inverse of Lorentzian to fit the data. The error bars are much smaller as the quantum fluctuations control the delay but not the shape of the emission. From the fit, we get the $\Gamma_o = 92$MHz, which agrees with the calibration. The burst strength is analyzed shown in Fig. 8.8(c). From the calculation, we have $I \approx \frac{N^2 g^2}{\kappa}$. Therefore, we fit the data with the Lorentizian-square profile, which we extract $\Gamma_o = 79$ MHz, similar to the other two results.

Next, we measure the second correlation $g^{(2)}$ of the superradiant burst. The $g^{(2)}$ of an optical superradiance has been measured to be $g^{(2)}(0) = 1.2$ from [106]. A $g^{(2)}$ of microwave superradiance has not been measured, to my knowledge. The reason is that there is no microwave single photon detector. However, our chip naturally forms a microwave-optical converter, which generates the optical counter-part of the microwave superradiance. Here, we use another separate chip to do the conversion job, shown in Fig. 8.9. Since the burst is delayed from the optical illumination, we did not get the optical part naturally from the same single chip. We first measured the $g^{(2)}$ of the burst to be 1.2, same as calibrated in the optical domain. Next, we add a microwave pulse trigger into the experimental pulse sequence. Since the burst is generated from a random kick, the output superradiant has an uncertainty in term of

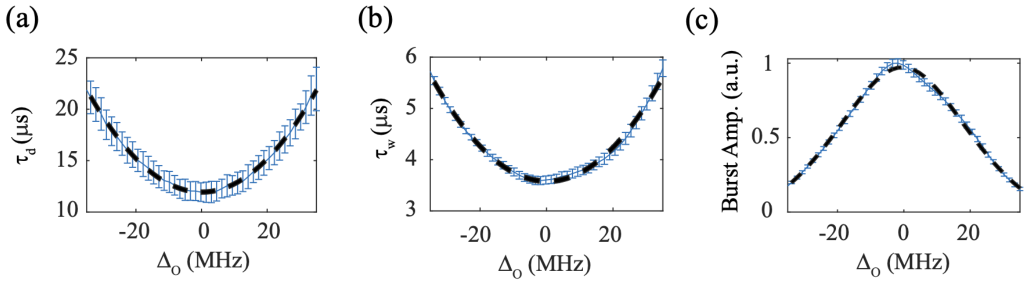

Figure 8.8: **Superradiant burst with different numbers of atoms.** By sweeping the detuning of the excitation pulse, we effectively change the number of atoms inside the spin manifold. (a) The burst delay at various optical detuning. (b) The burst width at various detuning. (c) The burst strength at various detuning. Dashed lines in (a) and (b) are the fits based on an inverse of the Lorentzian profile. The dashed line in (c) is a fit based on a square of the Lorentzian profile. Details are discussed in the main text.

the photon arrival time. With a trigger microwave pulse, one can artificially control the burst time, eliminating the uncertainty. This has been demonstrated in [105] where a controllable quantum storage is claimed. Here, with a microwave trigger, the $g^{(2)}(0)$ gradually changes from 1.2 to 1, as the burst arrival times are fixed. This demonstrate the superradiant burst arrival time can be stablized via external triggers, and behave as a classical coherent pulse with a fixed photon arrival time. On the other side, this also shows that without the microwave trigger, the $g^{(2)}(0) = 1.2 > 1$ is due to the photon arrival uncertainties..

8.4 Superradiance emission under a CW drive

After we understand the superradiant behavior under the pulse mode, now we move to the CW mode. The phenomenon is rather novel than a continuous masing effect. Rather, we observe CW and periodic microwave superradiance. I will go through the performances and discuss the data here, respectively.

First, we send in optical pump powers into the chip, connecting the transitions between $|g\rangle$ and $|e_2\rangle$, as shown in Fig. 8.10. With small spin inversion, the masing will not happen, but the microwave amplification effect, as discussed in the first section of this chapter. As the pump power increases, The masing starts to happen at a knee of $\sim 8\mu W$, shown in Fig. 8.10(b), where the y-axis is the integrated output power on a spectral analyzer. A simulation curve of N_s^2 is calculated on top, indicating the quadratic dependence of the emission power on the number of atoms.

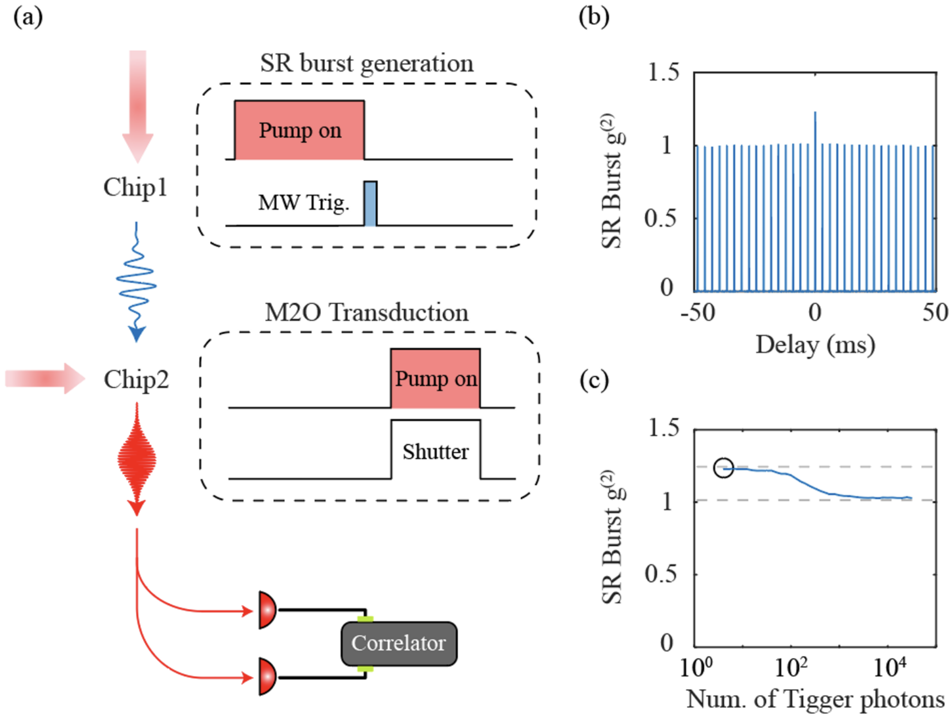

Figure 8.9: **Second correlation measurements of the superradiant burst.** (a) The experimental setup for the measurements. One chip is to generate the burst and the other chip is to conver the burst into optical photons. The pump time is 40 μs with 400 μW. A microwave trigger is followed the optical excitation for 1 μs duration. The optical output from the second chip is collected and split into two path for two SNSPDs measurements. (b) A $g^{(2)}$ measurement example. (c) The $g^{(2)}(0)$ of superradiant burst vs the trigger strength.

As the schematic of dynamics shown in Fig, 8.10(a), populations are pumped to the spin-up state. After enough inversion accumulated, it goes into superradiance, where the population quickly decays into the spin-down state. At the same time, the optical T_1 decay is also going on, which releases the population from $|e_2\rangle$ and $|e_1\rangle$ back to $|g\rangle$. The important part is the decay of $|e_1\rangle$. Because any population back to $|g\rangle$ will undergo an optical pumping process back to $|e_2\rangle$. Hence, the optical T_1 decay plus the optical pumping effectively creates a population inversion feeding from $|e_1\rangle$ to $|e_2\rangle$, which helps to create the inversion continuously or periodically. There is still a weak optical mode on both of the optical arms. However, the Purcell decay from coupling is calculated to be 3 mHz, which is too slow compared to the T_1 process.

One thing worth discussing here is what simulation needs to be calculated. Since later, we will see the maser is not continuous, one can not do a steady-state simulation

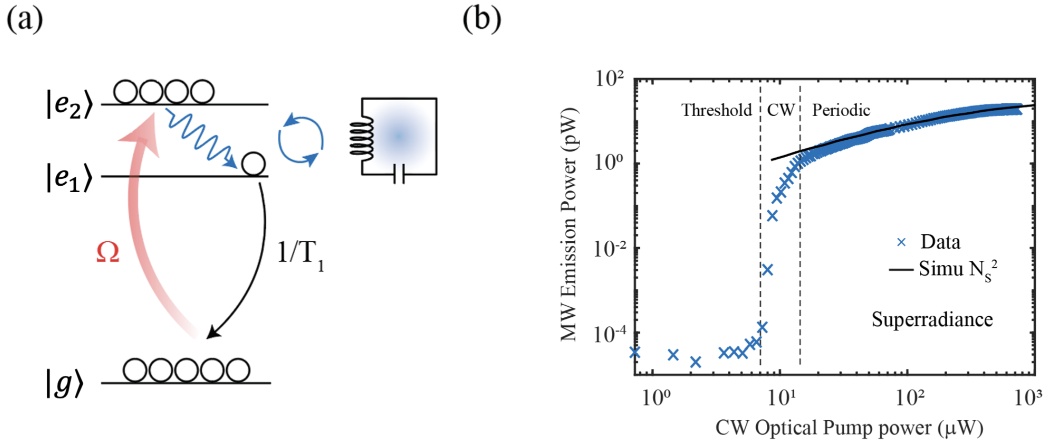

Figure 8.10: **Superradiance emission at different CW optical pump power.** (a) A schematic of the system dynamics. The optical T_1 process combined with the optical pumping forms an effective pumping from $|e_1\rangle$ back to $|e_2\rangle$, feeding the spin inversion. (b) The masing curve at different optical pump power. A masing knee is around 8 μW. A simulated total population square in the spin manifold is plotted on top, indicating the quadratic dependent of the masing emission power.

by setting all the differential equations to zero and finding a saturated population. Rather, one needs to do an ODE solver and find the oscillation behavior. Here, as described in the previous chapter, a full three-level system simulation is implemented and calculated at various pump powers. At each power, the population within the spin manifold is calculated. Although the periodic behavior will happen, it is between $|e1\rangle$ and $|e2\rangle$ where the S_z changes rapidly but not $N_{e1} + N_{e2}$. This can also be viewed in Fig. 7.8, where the pulse happens but $N_{e1} + N_{e_2}$ is almost constant. $N_{e_1} + N_{e_2}$ also describes the maximum J that the collective spin state could achieve. Hence, by calculating the total population in the spin manifold and squaring it with a fit constant on the front, we see nice agreements between the simulation and the data. The area before the masing knee is not captured as here is only calculating the population. At the masing knee, we measure the turning point at 8μW, corresponding to $g_{e,tot} = 0.5$MHz from an independent calibration via the spin-resonator coupling spectrum, which gives the cooperativity at this point to be 1.6. There are two phenomenons along the masing curve, which I will discuss one by one.

CW superradiance

At low pump powers, we observe a continuous masing effect right above the knee. A temporal trace taken on the oscillascope is shown in Fig. 8.11(a). A frequency

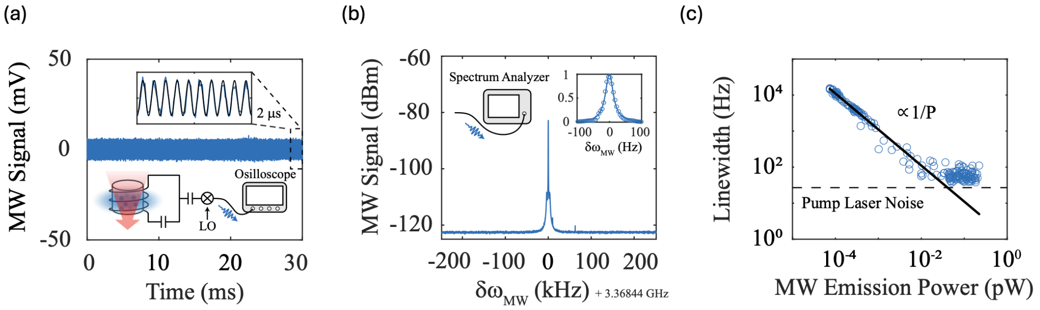

Figure 8.11: **Regime I: Continuous superradiance.** (a) A temporal trace of the continuous microwave emission. (b) A frequency spectrum of the CW maser. A zoom-in scan featuring a 30 Hz linewidth is showing on the top right corner. (c) The linewidth vs emission power by scanning the pump detuning, effectively tuning the number of atoms inside the system. A Schawlow-Townes limit line fit shows as the black line on top.

spectrum is plotted in Fig. 8.11(b), where a zoom-in spectrum is taken on the top right. Here, we observe a narrow emission of 30 Hz linewidth, with 25 dB above the noise floor. To further study the maser linewidth, we perform a laser detuning scan. To see the relationship between the linewidth and the emission power, increasing the pump power is not the proper knob. Higher pump power will start the periodic emission, where the system is not anymore in the CW regime. Hence, we keep pump power the same, and scan the input laser frequency. More optical detuning will pump less atoms into the excited spin manifold, hence change the emission profile. By implementing this detuning scan, we observe the linewidth change as well as the emission power. With careful calibration on the detection system, we observe an inverse relationship between the linewidth and the power. A black line is a fit to the noise broadened Schawlow-Townes limit [107–110]:

$$\Delta f = \frac{\hbar\omega}{4\pi P_{out}} n_{incoh} (\frac{\Gamma\kappa}{\Gamma+\kappa})^2 \tag{8.4}$$

where P_{out} is the total output emission power, $n_{incoh} = n_{th} + \frac{1}{2} + \frac{N_{e1}}{S_z} + \frac{1}{2}$ is incoherent photon number inside the resonator and the spin collective mode, Γ is the gain medium linewidth and κ is the resonator linewidth. The fitting results extract $n_{incoh} = 6.8$ from the system, corresponding to 1K system temperature if assuming all are thermal noise.

Other than the incoherent photons broadening the emission linewidth, the system also experience an correlated laser noise. As shown in Fig. 8.12, different pump frequencies generates different emission frequency. This microwave-optical frequency

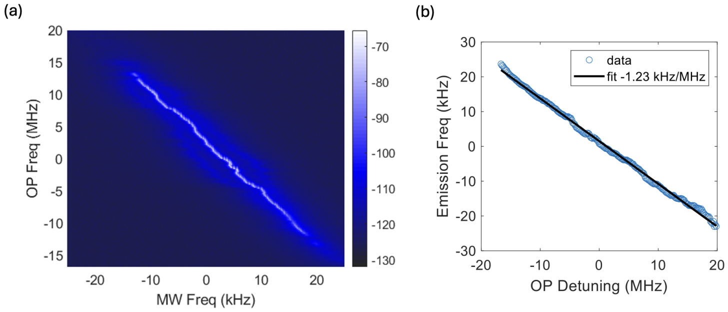

Figure 8.12: **Maser frequency at different optical pumping frequency.** (a) Microwave emission spectra at different pump laser frequencies. A correlation between the spin transition and the optical transition frequencies are detected. (b) A fit to the correlation, showing a slope of ∼ -1.23 kHz/MHz.

correlation might come from a correlated g-tensor in the ground and excited state. Hence, any laser frequency noise will imprint to the microwave emission, with a slope of ∼ -1.23 kHz/MHz. The pump laser is frequency locked to a seed laser via heterodyne method, where the seed laser locks to a stable cavity. We carefully calibrate the laser linewidth via the PDH error signal, which shows a 22 kHz linewidth. This corresponds to 27 Hz limit of the microwave emission, explaining the boundary of Fig. 8.11(c).

Periodic superradiance

At higher optical pump powers, the system undergoes periodic superradiance as the gain cannot balance the detuning and dephasing. A temporal trace is shown in Fig. 8.13. In frequency domain, a periodic structure should correspond to a comb-like spectra, as shown in Fig. 8.14(a). By zooming into one of the lines, a 49 Hz linewidth is observed as shown in the insert. Here, the teeth seperation of 12.3 kHz corresponds to the periodicity in time domain (81 μs). At the same time, optical periodic emissions are observed as well. This is due to the $\chi^{(2)}$ nature of the material, hence a build-in transduciton process happens. As calibrated in Chapter 6, we have the conversion from microwave coherence to optical coherence based on the continuous optical pump. The detection noise floor is elevated due to the room temperature photo-diode being used here comparing to a HEMT at 4K stage for microwave detection.

Since the optical bursts are generated from the coherent transduction, the phase of the optical emission should follow the phase of the microwave emission. To measure it, we down-convert both the microwave and optical signals to 5 MHz oscillations.

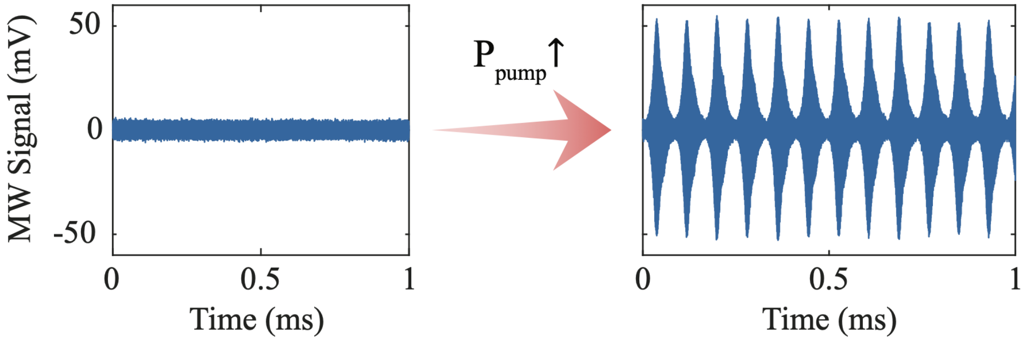

Figure 8.13: **Regime II: Periodic superradiance under a CW drive.** With higher pump powers, the emission changes into a periodic burst pattern.

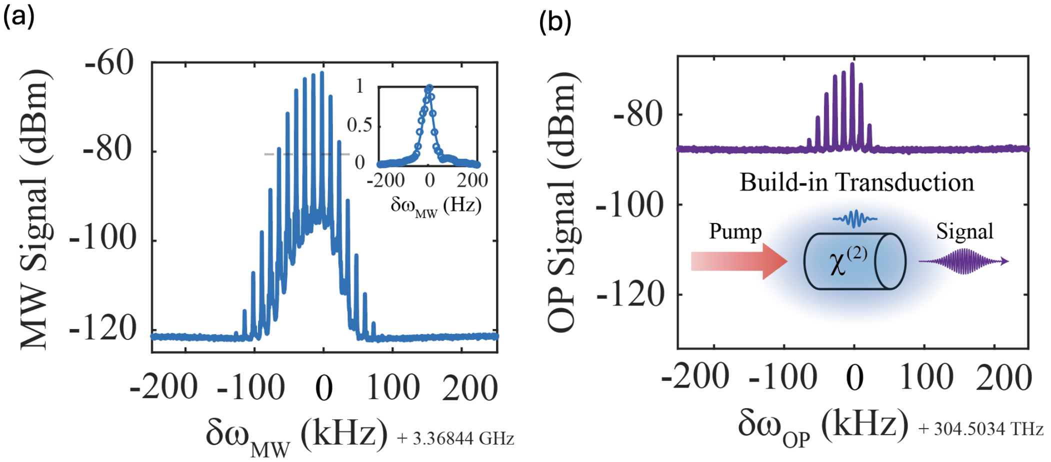

Figure 8.14: **Frequency domain measurements of the periodic superradiance.** (a) A frequency spectrum of the periodic superradiance. A zoom-in scan features a linewidth of 49 Hz for one of the teeth. The teeth separation here is 12.3 kHz, corresponding to 81 μs in time domain. (b) A frequency spectrum of the optical emission at the same time. Same comb-like features are observed due to the build-in transduction process from the $\chi^{(2)}$ nature of the material.

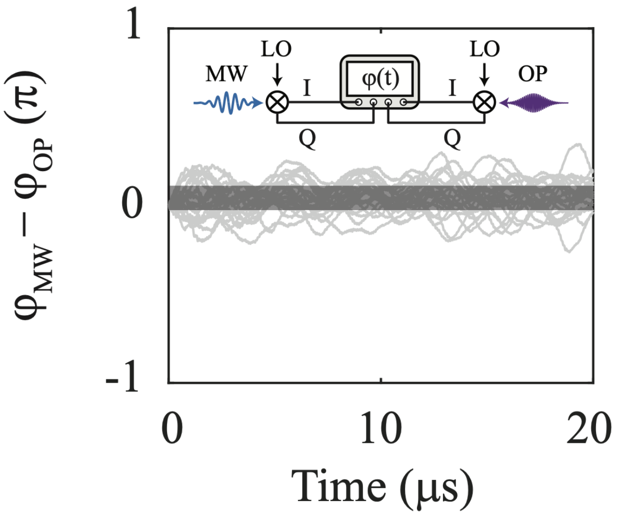

Figure 8.15: **Phase difference between the microwave and optical emission.** Due to the coherent process of transduction, the phase of the optical emission follows the phase of the microwave emission. Here we down-convert both fields to 5 MHz carrier frequency and extract the phase via the IQ quadratures. Shaded area represents the standard deviation of the phase fluctuation.

By analyzing the IQ quadratures of the signal, the phase in each emitted burst can be extracted, as plotted in Fig. 8.15. The standard deviation of the phase fluctuation is 0.06π.

As described in Chapter 7, the periodicity comes from the accumulation of the spin inversion. Hence, by putting different numbers of atoms into the spin manifold, the required S_z to achieve the emission threshold will be different ($Ns * S_z \sim$ constant). Specifically, assuming the pumping is an exponential process, we have

$$\begin{aligned} \frac{4g^2 N_{accm}}{\kappa\Gamma} = 1 \Rightarrow \tau = \frac{1}{D} log \frac{N_f - N_i}{N_f - \frac{\kappa\Gamma}{4g^2}} \\ \tau \approx \frac{1}{D} \frac{\kappa\Gamma}{4Ng^2 r_f} \end{aligned} \tag{8.5}$$

where N_{accm} is the accumulated population inversion, D is the repumping rate, N_f is the final saturated population inversion, N_i is the intial population inversion and r_f is the saturation factor depending on the drive Rabi frequency. Here, we find the period is inversely proportional to the total number of atom inside the spin manifold. To implement the periodicity tuning in experiments, we scan the input pump laser detunings. Due to the inhomogeneity in the optical domain, exciting the ensembles at different frequency inside the inhomogeneity would put different amount of atoms

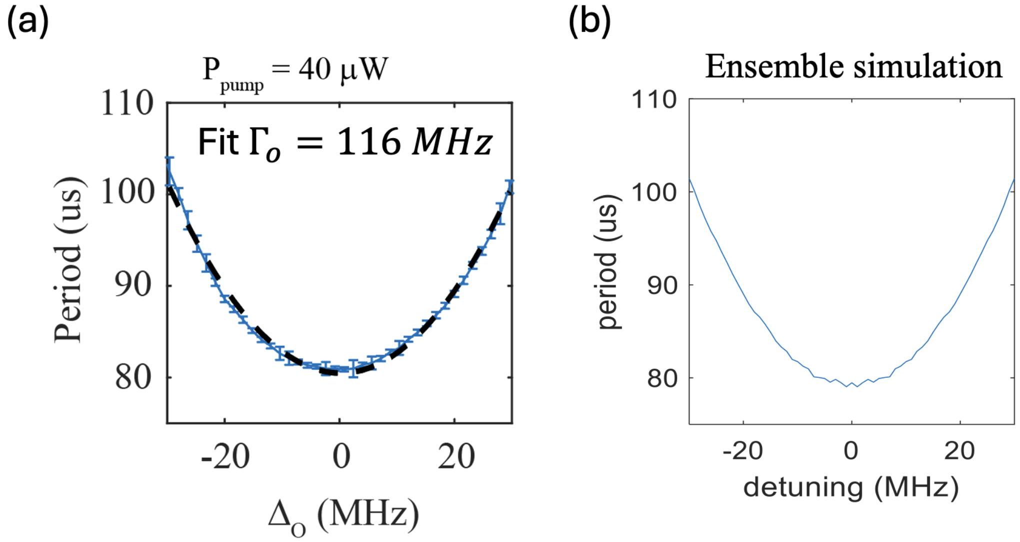

Figure 8.16: **Periodicity tuning via number of atom.** (a) Experimental data of the periodicity tuning. By scanning the optical detunings through the inhomogeneous ensemble, different number of atoms are excited to the spin manifold. (b) Simulation of the periodicity tuning.

into the spin manifold. Remembering an inverse of Lorentzian distributions of the inhomogeneity profile ($1/N$) would become a quadratic function. The experimental data is shown in Fig. 8.16(a). A quadratic fit is shown as the black dash line on top, featuring a 116 MHz ensemble linewidth in optical domain. This agrees to an independent measurement of the optical inhomogeneity (92 MHz) as measured in Chapter 5. A ensemble simulation is performed in (b), which agrees with the measured result well.

8.5 Summary

In this chapter, I described the experimental results with a tunable spin ensemble strong coupling to a resonator field. The large cooperativity (~ 6) enables a group of novel phenomenons in the cavity quantum electrodynamics area.

By pumping the system into the collective spin-down state, we observe strong couplings that split the resonator mode. By tuning the probe microwave powers, we are effectively tuning the S_z inside the spin manifold, which modifies the reflection spectrum of the resonator. At critical powers, the resonator would become critical coupled locally due to the spin-resonator couplings, which is the CIT effect. We achieved an extra 35 dB attenuation of the input microwave power wth a window size of 30 kHz. We further studied the microwave critical power dependence on the pumping strength. With higher pump powers, we observe the critial power moves to higher valves, from which we find a quadratic dependence of the crital power on the microwave cooperativities, agreeing with the theoretical calculations.

On the other side, by pumping the system into the collective spin-up state, we created controllable spin inversion inside the system. With weak inversions, we observe microwave amplification effect due to the stimulated emission process. The measured gain is up to 20 dB before the masing threshold. To further study the gain profile, we scan the input optical pump frequency, effectively modifying the numbers of atoms in the spin manifold. We fit to a theoretical model and extract the optical linewidth as 105 MHz with $C_e = 0.86$.

Turning on more pump powers will tune the system into a maser. Interesting, as the chip is a transducer at the same time, we get maser and the corresponding laser together automatically. Here, we identify two operations of the maser. In the first operation, by just surpassing the masing threshold, we observe CW masing effect, where the measured emission linewidth is inversely proportional to the emission power. We fit the result to a Lorentzian profile and extract down to 30 Hz emission linewidth. The linewidth-power shows an inverse relationship, governing by the noise-broadeden Schawlow-Townes limit. In the second operation, the maser undergoes a periodic dynamics. Therefore, instead of a single frequency peak, we observe a comb-like spectrum with the periodicity changes linear with the number of the atoms. At the same time, synchronized optical emissions are observed as well due to the build-in transduction process, featuring the in-phase property with the microwave emission. To understand the physics behind, we build a model to calculate the temporal behaviors of three-level systems coupled to a resonator field, which captures the system periodicity.

Moving into the pulsed operation, we observe superradiant bursts. The delay time, burst width and burst strength are analyzed showing different dependence on the number of atoms, agreeing with the theoretical expectations. Further, we measure the second-order correlation function of the burst, showing a control of the delay time by trigger the system with a weak microwave pulse.

With these results, we demonstrate the cavity quantum electrodynamics of a tunable spin-inverted system. We first-time observed the collectively induced transparency window in the spin domain since it is first discovery in 2023. Starting with an over-coupled resonator, one could effectively tune the system into critical coupling and further into under coupled regime. We also observe periodic superradiance phenomenon that is sychronized and coherent between the microwave and optical fields. These results in the many-body CQED area pave the way for on-chip tunable superradianct light source and inform the ensemble-based platforms with further undertanding for quantum interconnect applications.

Chapter 9

CONCLUSIONS

In this thesis, I present a new chip design and the measurement results for scalable interfaces between microwave and optical photons.

I first studied different rare-earth ion doped crystals for on-chip transducers, where Er^{3+}:YVO_4 is identified as a promising material for telecom applications and $^{171}\mathrm{Yb}^{3+}$:YVO_4 is identified as an ultra-strong effective $\chi^{(2)}$ material for transduction. Next, a simple transduction formalism is derived based on mode coupling theory, where the efficiencies are characterized only by microwave, optical, and atomic cooperativities. By learning from past REI-based transducers, a new transducer architecture is designed utilizing a planar superconducting microwave resonator and a free-space optical mode, avoiding various issues faced in hybrid devices and nanobeam designs.

The chip is fabricated under standard cleanroom processes and then characterized under cryogenic temperatures. We measured 0.76% chip efficiency with an added noise refer-to-input down to 1.24(9) photons. The performance is more than three orders of magnitude higher than the previous demonstration with solid-state ensembles, and it is the first time that the added noise process is calibrated, which is very close to the quantum level.

A unique advantage of atom-based platforms is frequency matching. To further demonstrate this, we prepare two transducer chips and measure the photon interference between the two. By shifting the phase of input microwave photons, we observe the corresponding phase change on the output optical photons, demonstrating the phase coherent nature of the transducer and the frequency matching from the photon interference.

Next, I demonstrated the chip is not only a transducer but also a nice platform for cavity quantum electrodynamics studies. With the control of a tunable three-level system, for the first time we report collectively induced transparency in the spin domain, where a critical power was identified for local kappa ratio tuning of the resonator. With enough spin-inversions, synchronized coherent superradiance in microwave and optical fields are detected. The superradiance can be emitted continuously, where a noise-broadened Schawlow-Townes limited linewidth is measured.

Periodic superradiance is detected with strong optical drives. We unravel the mechanism of this phenomenon with models and simulations. At the same time, optical emissions are observed due to the build-in transduction process. The synchronization between the microwave and optical field in terms of temporal shape and phase information makes it applicable for microwave and optical interfaces. The different superradiance behavior paves the way toward a on-chip tunable superradiance light source, and the understanding of the CQED system informs the solid-state community for the next generation of quantum interconnect devices.

Outlook

The ways to further improve the transducer performance have been discussed in Chapter 6. A key question following is, what milestones one could achieve with quantum transducers? The final goal of the transducer is to bring quantum information inside the superconducting circuit outside the cryogenic environment. Towards this aspect, one could demonstrate remote entanglement between two superconducting qubits mediated by transducers. For this, one needs to operate the system with high enough efficiency, bandwidth, and repetition rate to have enough entanglement attempts before qubit dephasing.

Specifically, a throughput rate that one cares about is $R_{en} = \eta BWR$, where η is the transduction efficiency, BW is the bandwidth and R is the pulse on/off ratio between conversion and cooling of the transducer. Depending on different entanglement protocols, this R_{en} needs to be higher fast enough (e.g., higher than the dephasing rate of the qubit) to demonstrate the remote entanglement with >50% fidelity. Currently, our device shows $R_{en} = 38$ Hz for $n_{add} < 2$. This is too slow for the remote entanglement task as the current qubit T_2 is around tens of μs. To further improve the numbers, the current devices need to improve efficiencies and lower the noise, as discussed in Chapter 6. Higher bandwidth could be achieved by exploring higher concentration samples, where the spin inhomogeneity [1] would be broader. Also, more cooling needs to be considered to increase the repetition rate. For example, superfluid helium could be explored for another cooling channel for the superconducting resonators. Better kappa ratio engineering could be applied hence one could radiatively cool the resonator with another cold bath [2]. Another novel experimental one could think about is to entangling a superconducting qubit with a

---

[1] The current limiting factor on the transducer bandwidth.

[2] For example, with the kappa ratio infinitely approaching one, only the waveguide temperature will contribute to the thermal occupancy of the resonator.

single rare-earth ion. Here, one could use the single optical photon emitted from the single emitter for the entanglement. A high-efficiency frequency converter around 984nm needs to be developed. The optical photon emit from single Yb^{3+} is will be 6 GHz away from the transduction signal. The spin qubit coherence time is long enough compared to the superconducting qubit, hence the requirement would be again on the qubit coherence time.

On the synchronized emission between microwave and optical fields, it paves the way for SPDC generation of the REI-based device. With the current chip design, generating microwave-optical photon pairs from the SPDC process is doable. However, the uncoupled area that this 10μm below the top surface would reabsorb the single optical photon, which destroys the photon pair generation. Although one could play the same trick as the current to first optically saturate the system, the required initialization time (e.g., 20μs in the current transducer measurement), is long enough to start a superradiant burst. To overcome this issue, one needs to have a thin film of the REI material, hence less absorption and less initialization time can be applied. With this, the microwave-optical photon pair generated from the SPDC process should be detectable.

For the superradiance, currently, the optical part is driven by a natural conversion process from the spin coherence. An optical cavity with good finesse on the optical arm would help generate pure optical superradiance at the same time, which might benefit from the narrow spin linewidth as they are connected to each other via an optical pump. With technical efforts, the pump laser linewidth could be improved and hence may not be a limiting factor on the superradiance linewidth. The thermal contribution from the resonator could be suppressed by the aforementioned methods, which leads to quantum-limited linewidths.

For the CIT, one nice application for it would be a fast microwave switch. The attenuation is largely enough but the dynamics is relatively slow. Better resonator geometry could be designed to make single-ion coupling strength large, hence improving the temporal response.

BIBLIOGRAPHY

[1] Richard P. Feynman. “Simulating physics with computers.” In: *International Journal of Theoretical Physics* (1982), pp. 467–488.

[2] Peter W. Shor. “Polynomial-time algorithms for prime factorization and discrete logarithms on a quantum computer.” In: *SIAM Review* 41.2 (1999), pp. 303–332.

[3] Don Coppersmith. “Modifications to the number field sieve.” In: *Journal of Cryptology* 6 (1993), pp. 169–180.

[4] Frank Arute et al. “Quantum supremacy using a programmable superconducting processor.” In: *Nature* 574.7779 (2019), pp. 505–510.

[5] H. Jeff Kimble. “The quantum internet.” In: *Nature* 453.7198 (2008), pp. 1023–1030.

[6] Nicolas Gisin et al. “Quantum cryptography.” In: *Reviews of Modern Physics* 74.1 (2002), p. 145.

[7] J. Ignacio Cirac et al. “Distributed quantum computation over noisy channels.” In: *Physical Review A* 59.6 (1999), p. 4249.

[8] Juan Yin et al. “Satellite-based entanglement distribution over 1200 kilometers.” In: *Science* 356.6343 (2017), pp. 1140–1144.

[9] Matteo Pompili et al. “Realization of a multinode quantum network of remote solid-state qubits.” In: *Science* 372.6539 (2021), pp. 259–264.

[10] Can M. Knaut et al. “Entanglement of nanophotonic quantum memory nodes in a telecom network.” In: *Nature* 629.8012 (2024), pp. 573–578.

[11] David L. Moehring et al. “Entanglement of single-atom quantum bits at a distance.” In: *Nature* 449.7158 (2007), pp. 68–71.

[12] Laurent J. Stephenson et al. “High-rate, high-fidelity entanglement of qubits across an elementary quantum network.” In: *Physical Review Letters* 124.11 (2020), p. 110501.

[13] Jonathan M. Kindem et al. “Control and single-shot readout of an ion embedded in a nanophotonic cavity.” In: *Nature* 580.7802 (2020), pp. 201–204.

[14] Salim Ourari et al. “Indistinguishable telecom band photons from a single Er ion in the solid state.” In: *Nature* 620.7976 (2023), pp. 977–981.

[15] Philip Krantz et al. “A quantum engineer’s guide to superconducting qubits.” In: *Applied Physics Reviews* 6.2 (2019).

[16] Paul Magnard et al. “Microwave quantum link between superconducting circuits housed in spatially separated cryogenic systems.” In: *Physical Review Letters* 125.26 (2020), p. 260502.

[17] Simon Storz et al. “Loophole-free Bell inequality violation with superconducting circuits.” In: *Nature* 617.7960 (2023), pp. 265–270.

[18] Nicholas J. Lambert et al. “Coherent conversion between microwave and optical photons—an overview of physical implementations.” In: *Advanced Quantum Technologies* 3.1 (2020), p. 1900077.

[19] Nikolai Lauk et al. “Perspectives on quantum transduction.” In: *Quantum Science and Technology* 5.2 (2020), p. 020501.

[20] Jake Herschel Lebi Rochman. *Microwave-to-Optical Transduction Using Rare-Earth Ions.* California Institute of Technology, 2022.

[21] Google Quantum AI and Collaborators. “Quantum error correction below the surface code threshold.” In: *Nature* (2024).

[22] Utku Hatipoglu et al. “In situ tuning of optomechanical crystals with nano-oxidation.” In: *Optica* 11.3 (2024), pp. 371–375.

[23] Sebastian Borówka et al. “Continuous wideband microwave-to-optical converter based on room-temperature Rydberg atoms.” In: *Nature Photonics* 18.1 (2024), pp. 32–38.

[24] Rishabh Sahu et al. “Quantum-enabled operation of a microwave-optical interface.” In: *Nature Communications* 13.1 (2022), p. 1276.

[25] Yuntao Xu et al. “Bidirectional interconversion of microwave and light with thin-film lithium niobate.” In: *Nature communications* 12.1 (2021), p. 4453.

[26] Jeffrey Holzgrafe et al. “Cavity electro-optics in thin-film lithium niobate for efficient microwave-to-optical transduction.” In: *Optica* 7.12 (2020), pp. 1714–1720.

[27] Timothy P. McKenna et al. “Cryogenic microwave-to-optical conversion using a triply resonant lithium-niobate-on-sapphire transducer.” In: *Optica* 7.12 (2020), pp. 1737–1745.

[28] Rishabh Sahu et al. “Entangling microwaves with light.” In: *Science* 380.6646 (2023), pp. 718–721.

[29] Markus Aspelmeyer, Tobias J Kippenberg, and Florian Marquardt. “Cavity optomechanics.” In: *Reviews of Modern Physics* 86.4 (2014), pp. 1391–1452.

[30] Mohammad Mirhosseini et al. “Superconducting qubit to optical photon transduction.” In: *Nature* 588.7839 (2020), pp. 599–603.

[31] Wentao Jiang et al. “Efficient bidirectional piezo-optomechanical transduction between microwave and optical frequency.” In: *Nature Communications* 11.1 (2020), p. 1166.

[32] Xu Han et al. “Cavity piezo-mechanics for superconducting-nanophotonic quantum interface.” In: *Nature Communications* 11.1 (2020), p. 3237.

[33] Matthew J. Weaver et al. “An integrated microwave-to-optics interface for scalable quantum computing.” In: *Nature Nanotechnology* 19.2 (2024), pp. 166–172.

[34] Simon Hönl et al. “Microwave-to-optical conversion with a gallium phosphide photonic crystal cavity.” In: *Nature Communications* 13.1 (2022), p. 2065.

[35] Srujan Meesala et al. “Non-classical microwave–optical photon pair generation with a chip-scale transducer.” In: *Nature Physics* (2024), pp. 1–7.

[36] Srujan Meesala et al. “Quantum entanglement between optical and microwave photonic qubits.” In: *Physical Review X* 14.3 (2024), p. 031055.

[37] Reed W Andrews et al. “Bidirectional and efficient conversion between microwave and optical light.” In: *Nature physics* 10.4 (2014), pp. 321–326.

[38] Benjamin M. Brubaker et al. “Optomechanical ground-state cooling in a continuous and efficient electro-optic transducer.” In: *Physical Review X* 12.2 (2022), p. 021062.

[39] RD Delaney et al. “Superconducting-qubit readout via low-backaction electro-optic transduction.” In: *Nature* 606.7914 (2022), pp. 489–493.

[40] Alkim Bozkurt et al. “A quantum electromechanical interface for long-lived phonons.” In: *Nature Physics* 19.9 (2023), pp. 1326–1332.

[41] Han Zhao et al. “Quantum-enabled continuous microwave-to-optics frequency conversion.” In: *arXiv preprint arXiv:2406.02704* (2024).

[42] Jingshan Han et al. “Coherent microwave-to-optical conversion via six-wave mixing in Rydberg atoms.” In: *Physical Review Letters* 120.9 (2018), p. 093201.

[43] Hai-Tao Tu et al. “High-efficiency coherent microwave-to-optics conversion via off-resonant scattering.” In: *Nature Photonics* 16.4 (2022), pp. 291–296.

[44] Aishwarya Kumar et al. “Quantum-enabled millimetre wave to optical transduction using neutral atoms.” In: *Nature* 615.7953 (2023), pp. 614–619.

[45] Xavier Fernandez-Gonzalvo et al. “Cavity-enhanced Raman heterodyne spectroscopy in Er 3+: Y 2 SiO 5 for microwave to optical signal conversion.” In: *Physical Review A* 100.3 (2019), p. 033807.

[46] Jake Rochman et al. “Microwave-to-optical transduction with erbium ions coupled to planar photonic and superconducting resonators.” In: *Nature Communications* 14.1 (2023), p. 1153.

[47] Sacha Welinski et al. “Electron spin coherence in optically excited states of rare-earth ions for microwave to optical quantum transducers.” In: *Physical Review Letters* 122.24 (2019), p. 247401.

[48] Alexander Anferov et al. "Superconducting qubits above 20 GHz operating over 200 mK." In: *PRX Quantum* 5.3 (2024), p. 030347.

[49] Tian Zhong et al. "High quality factor nanophotonic resonators in bulk rare-earth doped crystals." In: *Optics Express* 24.1 (2016), pp. 536–544.

[50] Mouktik Raha et al. "Optical quantum nondemolition measurement of a single rare earth ion qubit." In: *Nature Communications* 11.1 (2020), p. 1605.

[51] Ioana Craiciu et al. "Multifunctional on-chip storage at telecommunication wavelength for quantum networks." In: *Optica* 8.1 (2021), pp. 114–121.

[52] Tian Zhong et al. "Nanophotonic coherent light–matter interfaces based on rare-earth-doped crystals." In: *Nature Communications* 6.1 (2015), p. 8206.

[53] John G Bartholomew et al. "On-chip coherent microwave-to-optical transduction mediated by ytterbium in YVO4." In: *Nature communications* 11.1 (2020), p. 3266.

[54] Ali K. Hamze et al. "Design rules for strong electro-optic materials." In: *npj Computational Materials* 6.1 (2020), p. 130.

[55] Anatole Abragam and Brebis Bleaney. *Electron paramagnetic resonance of transition ions.* OUP Oxford, 2012.

[56] JA Capobianco et al. "Optical spectroscopy, fluorescence dynamics and crystal-field analysis of Er3+ in YVO4." In: *Chemical physics* 214.2-3 (1997), pp. 329–340.

[57] Charles W. Thiel, Thomas Böttger, and Rufus L. Cone. "Rare-earth-doped materials for applications in quantum information storage and signal processing." In: *Journal of Luminescence* 131.3 (2011), pp. 353–361.

[58] Tian Xie et al. "Characterization of Er3+: YVO4 for microwave to optical transduction." In: *Physical Review B* 104.5 (2021), p. 054111.

[59] Thomas Böttger et al. "Spectroscopy and dynamics of Er3+: Y2SiO5 at 1.5 μ m." In: *Physical Review B—Condensed Matter and Materials Physics* 74.7 (2006), p. 075107.

[60] Sebastian Probst et al. "Anisotropic rare-earth spin ensemble strongly coupled to a superconducting resonator." In: *Physical Review Letters* 110.15 (2013), p. 157001.

[61] Manjin Zhong et al. "Optically addressable nuclear spins in a solid with a six-hour coherence time." In: *Nature* 517.7533 (2015), pp. 177–180.

[62] Tian Zhong and Philippe Goldner. "Emerging rare-earth doped material platforms for quantum nanophotonics." In: *Nanophotonics* 8.11 (2019), pp. 2003–2015.

[63] Subhojit Dutta et al. "Integrated photonic platform for rare-earth ions in thin film lithium niobate." In: *Nano Letters* 20.1 (2019), pp. 741–747.

[64] Likai Yang et al. “Controlling single rare earth ion emission in an electro-optical nanocavity.” In: *Nature Communications* 14.1 (2023), p. 1718.

[65] Mi Lei et al. “Many-body cavity quantum electrodynamics with driven inhomogeneous emitters.” In: *Nature* 617.7960 (2023), pp. 271–276.

[66] Morgan P Hedges et al. “Efficient quantum memory for light.” In: *Nature* 465.7301 (2010), pp. 1052–1056.

[67] Dario Lago-Rivera et al. “Telecom-heralded entanglement between multimode solid-state quantum memories.” In: *Nature* 594.7861 (2021), pp. 37–40.

[68] Andrei Ruskuc et al. “Scalable Multipartite Entanglement of Remote Rare-earth Ion Qubits.” In: *arXiv preprint arXiv:2402.16224* (2024).

[69] Guokui Liu and Bernard Jacquier. *Spectroscopic properties of rare earths in optical materials.* Vol. 83. Springer Science & Business Media, 2006.

[70] George F. Koster. “Properties of the thirty-two point groups.” In: (1963).

[71] Richard Conger Powell. *Symmetry, group theory, and the physical properties of crystals.* Vol. 824. Springer, 2010.

[72] Zundu Luo and Yidong Huang. *Physics of solid-state laser materials.* Springer, 2020.

[73] Marina N. Popova et al. “Crystal field and hyperfine structure of Er 3+ 167 in YP O 4: Er single crystals: High-resolution optical and EPR spectroscopy.” In: *Physical Review B* 99.23 (2019), p. 235151.

[74] Robert Marino et al. “Energy level structure and optical dephasing under magnetic field in Er3+: LiYF4 at 1.5 μm.” In: *Journal of Luminescence* 169 (2016), pp. 478–482.

[75] Jonathan M. Kindem et al. “Characterization of Yb 3+ 171: YVO 4 for photonic quantum technologies.” In: *Physical Review B* 98.2 (2018), p. 024404.

[76] Lewis A. Williamson, Yu-Hui Chen, and Jevon J. Longdell. “Magneto-optic modulator with unit quantum efficiency.” In: *Physical Review Letters* 113.20 (2014), p. 203601.

[77] Xu Han et al. “Microwave-optical quantum frequency conversion.” In: *Optica* 8.8 (2021), pp. 1050–1064.

[78] Tian Xie et al. “Scalable microwave-to-optical transducers at single photon level with spins.” In: *arXiv preprint arXiv:2407.08879* (2024).

[79] Mankei Tsang. “Cavity quantum electro-optics.” In: *Physical Review A* 81.6 (2010), p. 063837.

[80] Haowei Xu et al. “Efficient Quantum Transduction Using Anti-Ferromagnetic Topological Insulators.” In: *arXiv preprint arXiv:2308.09048* (2023).

[81] Alexander Ulanowski, Benjamin Merkel, and Andreas Reiserer. "Spectral multiplexing of telecom emitters with stable transition frequency." In: *Science Advances* 8.43 (2022), eabo4538.

[82] Chetan Deshmukh et al. "Detection of single ions in a nanoparticle coupled to a fiber cavity." In: *Optica* 10.10 (2023), pp. 1339–1344.

[83] Daniel A. Steck. *Quantum and atom optics.* http://steck.us/teaching., 2007.

[84] Morten Kjaergaard et al. "Superconducting qubits: Current state of play." In: *Annual Review of Condensed Matter Physics* 11.1 (2020), pp. 369–395.

[85] Nur Ismail et al. "Fabry-Pérot resonator: spectral line shapes, generic and related Airy distributions, linewidths, finesses, and performance at low or frequency-dependent reflectivity." In: *Optics Express* 24.15 (2016), pp. 16366–16389.

[86] David S. Sumida and Tso Yee Fan. "Effect of radiation trapping on fluorescence lifetime and emission cross section measurements in solid-state laser media." In: *Optics Letters* 19.17 (1994), pp. 1343–1345.

[87] Felix R. Graf et al. "Photon-echo attenuation by dynamical processes in rare-earth-ion-doped crystals." In: *Physical Review B* 58.9 (1998), p. 5462.

[88] William Hease et al. "Bidirectional electro-optic wavelength conversion in the quantum ground state." In: *PRX Quantum* 1.2 (2020), p. 020315.

[89] Mingrui Xu et al. "Radiative cooling of a superconducting resonator." In: *Physical Review Letters* 124.3 (2020), p. 033602.

[90] Georg Arnold et al. "All-optical single-shot readout of a superconducting qubit." In: *arXiv preprint arXiv:2310.16817* (2023).

[91] Mi Lei et al. "Quantum thermalization and Floquet engineering in a spin ensemble with a clock transition." In: *arXiv preprint arXiv:2408.00252* (2024).

[92] Wei Fu et al. "Cavity electro-optic circuit for microwave-to-optical conversion in the quantum ground state." In: *Physical Review A* 103 (5 May 2021), p. 053504. DOI: `10.1103/PhysRevA.103.053504`.

[93] Alfredo Rueda et al. "Efficient microwave to optical photon conversion: an electro-optical realization." In: *Optica* 3.6 (2016), pp. 597–604.

[94] Andreas Angerer et al. "Superradiant emission from colour centres in diamond." In: *Nature Physics* 14.12 (2018), pp. 1168–1172.

[95] Igor Diniz et al. "Strongly coupling a cavity to inhomogeneous ensembles of emitters: Potential for long-lived solid-state quantum memories." In: *Physical Review A—Atomic, Molecular, and Optical Physics* 84.6 (2011), p. 063810.

[96] Gavin Dold et al. “High-cooperativity coupling of a rare-earth spin ensemble to a superconducting resonator using yttrium orthosilicate as a substrate.” In: *Physical Review Applied* 11.5 (2019), p. 054082.

[97] Gavin G.G. King et al. “Probing strong coupling between a microwave cavity and a spin ensemble with Raman heterodyne spectroscopy.” In: *Physical Review B* 103.21 (2021), p. 214305.

[98] Robert J. Thompson, Gerhard Rempe, and H. Jeff Kimble. “Observation of normal-mode splitting for an atom in an optical cavity.” In: *Physical Review Letters* 68.8 (1992), p. 1132.

[99] Mi Lei. *Many-Body Cavity Quantum Electrodynamics and Spin Dynamics with an Ensemble of Rare-Earth Ions.* California Institute of Technology, 2024.

[100] Tom Day et al. “A Room-Temperature Solid-State Maser Amplifier.” In: *arXiv preprint arXiv:2405.07486* (2024).

[101] Herbert Walther et al. “Cavity quantum electrodynamics.” In: *Reports on Progress in Physics* 69.5 (2006), p. 1325.

[102] Jonathan D. Breeze et al. “Continuous-wave room-temperature diamond maser.” In: *Nature* 555.7697 (2018), pp. 493–496.

[103] Enrico Salvadori et al. “Nanosecond time-resolved characterization of a pentacene-based room-temperature MASER.” In: *Scientific Reports* 7.1 (2017), p. 41836.

[104] Michel Gross and Serge Haroche. “Superradiance: An essay on the theory of collective spontaneous emission.” In: *Physics reports* 93.5 (1982), pp. 301–396.

[105] Wenzel Kersten et al. “Triggered superradiance and spin inversion storage in a hybrid quantum system.” In: *Physical Review Letters* 131.4 (2023), p. 043601.

[106] Carlo Bradac et al. “Room-temperature spontaneous superradiance from single diamond nanocrystals.” In: *Nature Communications* 8.1 (2017), p. 1205.

[107] Justin G. Bohnet et al. “A steady-state superradiant laser with less than one intracavity photon.” In: *Nature* 484.7392 (2012), pp. 78–81.

[108] S.J.M. Kuppens, Martin Van Exter, and J.P. Woerdman. “Quantum-limited linewidth of a bad-cavity laser.” In: *Physical Review Letters* 72.24 (1994), p. 3815.

[109] Hudson A. Loughlin and Vivishek Sudhir. “Quantum noise and its evasion in feedback oscillators.” In: *Nature Communications* 14.1 (2023), p. 7083.

[110] Liang Jin et al. “Proposal for a room-temperature diamond maser.” In: *Nature Communications* 6.1 (2015), pp. 1–8.

[111] U. Ranon. “Paramagnetic resonance of Nd3+, Dy3+, Er3+ and Yb3+ in YVO4.” In: *Physics Letters A* 28.3 (1968), pp. 228–229.

Appendix A

^{167}ER:YVO$_4$ HYPERFINE STRUCTURES

This is an extension of the spectroscopic work I have done in [58]. Here I will go through the theoretical calculation and the experimental results of ^{167}Er:YVO$_4$ hyperfine structures.

A.1 Set up the problem

^{167}Er has nuclear spin I = 7/2 which expands the state space into 16 dimensions. To model the nuclear spin effect, we use the Hamiltonian from [55]:

$$H_{eff} = \mu_B B \cdot g \cdot S + I \cdot A \cdot S + I \cdot P \cdot I. \tag{A.1}$$

In the axial symmetry, the spin Hamiltonian becomes:

$$\begin{aligned} H_{eff} =& \mu_B B \left[g_{//} B_z S_z + g_\perp \left(B_x S_x + B_y S_y \right) \right] \\ &+ A_{//} S_z I_z + A_\perp \left(S_x I_x + S_y I_y \right) + P_{//} \left[I_z^2 - \frac{1}{3} I(I+1) \right]. \end{aligned} \tag{A.2}$$

The last term is the nuclear electric quadrupole term, which only appears in I≥1 cases.

A.2 Study the $I \cdot A \cdot S$ term

Consider B field is zero, and $P_{//}$=0. Therefore, we only study the $I \cdot A \cdot S$ term:

$$H_{eff} = A_{//} S_z I_z + A_\perp \left(S_x I_x + S_y I_y \right) = A_\perp S \cdot I + (A_{//} - A_\perp S_z I_z). \tag{A.3}$$

The Hamiltonian could be simplified into the following form:

$$\begin{aligned} H = A_\perp S \cdot I + (A_{//} - A_\perp) S_z I_z &= A_\perp \frac{F^2 - I^2 - S^2}{2} + (A_{//} - A_\perp) S_z (F_z - S_z) \\ &= A_\perp \frac{F^2 - I^2 - S^2}{2} + (A_{//} - A_\perp)(S_z F_z - S_z^2) \\ &= A_\perp \frac{F^2 - I^2 - S^2}{2} + (A_{//} - A_\perp)(S_z F_z - \frac{1}{4}). \end{aligned} \tag{A.4}$$

From the last line, we see the system could split into two type of hyperfine structure with F=4 and F=3. Also, we notice the energy levels of $|F, \pm m_F\rangle$ are degenerate, since flipping the F_z requires flipping S_z as well (also I_z). For example:

$$\begin{aligned} |F=4, m_F=3\rangle &= \frac{1}{\sqrt{8}}\,|I_z=+\frac{7}{2}, m_s=-\frac{1}{2}\rangle + \frac{\sqrt{7}}{\sqrt{8}}\,|I_z=+\frac{5}{2}, m_s=+\frac{1}{2}\rangle \\ |F=4, m_F=-3\rangle &= \frac{1}{\sqrt{8}}\,|I_z=-\frac{7}{2}, m_s=+\frac{1}{2}\rangle + \frac{\sqrt{7}}{\sqrt{8}}\,|I_z=-\frac{5}{2}, m_s=-\frac{1}{2}\rangle\,. \end{aligned} \tag{A.5}$$

These are the intuitive understanding, since at low external field, F_z, S_z, I_z and F cannot be good quantum numbers at the same time. A better way to see the degeneracy is to solve the 16 by 16 matrix and find the eigenvalues. By solving the system, we found:

$$\begin{aligned} E &= -\frac{1}{4}A_{//} \pm \frac{1}{2}[A_{//}^2 m_F^2 + A_\perp^2(I(I+1)+\frac{1}{4}-m_F^2)]^{\frac{1}{2}} \\ &= -\frac{1}{4}A_{//} \pm \frac{1}{2}[A_{//}^2 m_F^2 + A_\perp^2(16-m_F^2)]^{\frac{1}{2}}. \end{aligned} \tag{A.6}$$

Truly, we see the energy levels are degenerate about $\pm m_F$ (see the Fig. A.1 below). The ± sign is F=4 and F=3 hyperfine structure. However, one fact needs to be pointed out is that the eigen state here is not purely $|F, m_F\rangle$ type state. The reason is because $|F, m_F\rangle$ is related to $|I, m_I\rangle$ and $|S, m_S\rangle$ through fixed Clebsch-Gordan coefficient. But the system we are solving here gives the coupling coefficient depending on the number of $A_{//}$ and $A_\perp$. However, use m_F but not use F is okay, since actually the eigenstates are truly having a definite m_F value. Therefore, in the following discussion, I will still use m_F labels but use 'F' instead of F.

For the m_F=0 state, we call it ZEFOZ state. The reason would be discussed in the next section. It is worthwhile to pointing out that the double degeneracy we have here is not the Kramer's degeneracy. There is no time reversal symmetry here. The degeneracy is due to our axis symmetry type Hamiltonian.

Asides: Thinking the ^{171}Yb:YVO$_4$ system

For ^{171}Yb:YVO$_4$, we have $S = \frac{1}{2}$ and $I = \frac{1}{2}$. Therefore, under this understand, only $I \cdot A \cdot S$ term would split the system into 'F' = 1 and 'F' = 0 states, with totally 4 levels. However, in 'F' = 1 state, $m_F = \pm 1$ states should be degenerate. Therefore, the total level structures would be as shown in Fig. A.2. The 'F' = 1, m_F=0 state should be $\frac{1}{\sqrt{2}}(|\uparrow\Downarrow\rangle + |\downarrow\Uparrow\rangle)$ state. The degenerate 'F' = 1, m_F=±1 states should be $|\uparrow\Uparrow\rangle$ and $|\downarrow\Downarrow\rangle$ states. The 'F' = 0, m_F=0 state should be $\frac{1}{\sqrt{2}}(|\uparrow\Downarrow\rangle - |\downarrow\Uparrow\rangle)$ state. Also,

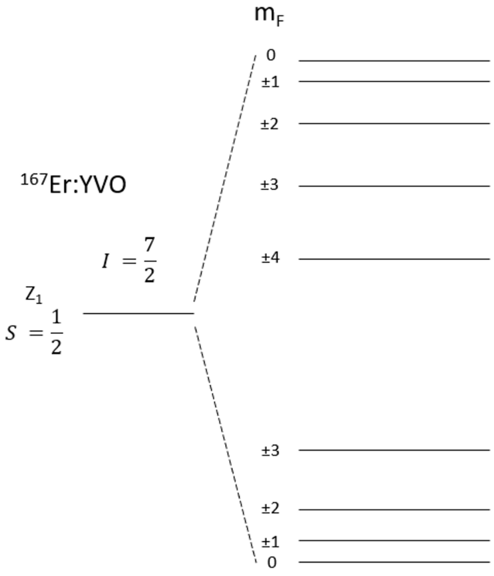

Figure A.1: ^{167}**Er:YVO$_4$ hyperfine structure considering the $I \cdot A \cdot S$ term.** The ±m_F are degenerate due to the axis symmetry type Hamiltonian.

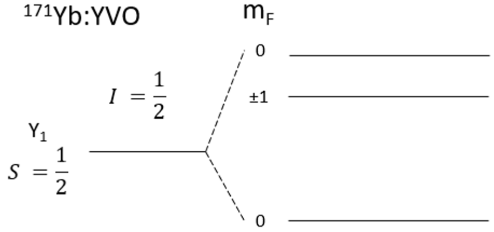

Figure A.2: ^{171}**Yb:YVO$_4$ hyperfine structure considering the $I \cdot A \cdot S$ term.** The ±m_F are degenerate due to the axis symmetry type Hamiltonian.

using the previous calculated energy equations, we could get the energy levels as:

$$\begin{aligned} E &= -\frac{1}{4}A_{//} \pm \frac{1}{2}[A_{//}^2 m_F^2 + A_\perp^2(I(I+1) + \frac{1}{4} - m_F^2)]^{\frac{1}{2}} \\ &= -\frac{1}{4}A_{//} \pm \frac{1}{2}[A_{//}^2 m_F^2 + A_\perp^2(1 - m_F^2)]^{\frac{1}{2}} \end{aligned} \tag{A.7}$$

which gives $E = \frac{A_{//}}{4}, \frac{-3A_{//}}{4}, \frac{-A_{//}+2A_\perp}{4}, \frac{-A_{//}-2A_\perp}{4}$. The results agree with [75]. The sequence of the energy level structure (e.g., $m_F = \pm 1$ or $m_F = 0$ is higher) is depending on the sign of g and A parameters.

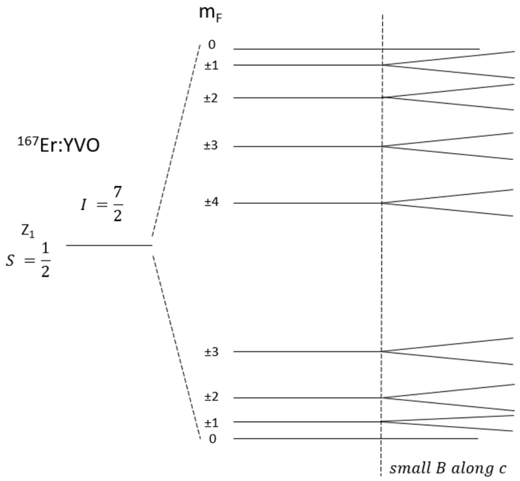

Figure A.3: ^{167}**Er:YVO$_4$ hyperfine structure considering the $I \cdot A \cdot S$ and the electronic Zeeman term.** Schematic showing the energy levels under small magnetic fields along c-axis.

A.3 Add the electronic Zeeman term

Now we add some magnetic field into the consideration. For simplicity, let us only consider B along z case:

$$H = \mu_B g_{//} B_z S_z + A_{//} S_z I_z + A_{\perp}(S_x I_x + S_y I_y). \tag{A.8}$$

Clearly, the introduced magnetic field would split the previous degenerate $\pm m_F$ state. We could also precisely diagonalize this Hamiltonian and see the eigen-energy:

$$\begin{aligned} E &= -\frac{1}{4}A_{//} \pm \frac{1}{2}[(\mu_B g_{//} B_z + A_{//} m_F)^2 + A_{\perp}^2(I(I+1) + \frac{1}{4} - m_F^2)]^{\frac{1}{2}} \\ &= -\frac{1}{4}A_{//} \pm \frac{1}{2}[(\mu_B g_{//} B_z + A_{//} m_F)^2 + A_{\perp}^2(16 - m_F^2)]^{\frac{1}{2}}. \end{aligned} \tag{A.9}$$

Here, we see that two $m_F = 0$ states are having the energy of:

$$E_{m_F=0} = -\frac{1}{4}A_{//} \pm \frac{1}{2}[(\mu_B g_{//} B_z)^2 + 16A_{\perp}^2]^{\frac{1}{2}} \tag{A.10}$$

which does not have the first order B field dependence. This property is not valid for all other $m_F \neq 0$ states. Another special case is $m_F = \pm 4$, where the energy levels are:

$$E_{m_F=\pm 4} = \frac{7}{4}A_{//} \pm \frac{1}{2}\mu_B g_{//} B_z \tag{A.11}$$

where the two levels would evolve linearly with the external magnetic field, without any bending structures, as shown in Fig. A.3.

A.4 Add the nuclear electric quadrupole term

Now let us consider the full Hamiltonian with B//c condition:

$$H_{eff} = \mu_B g_{//} B_z S_z + A_{//} S_z I_z + A_{\perp}(S_x I_x + S_y I_y) + P_{//}[I_z^2 - \frac{1}{3} I(I+1)] \tag{A.12}$$

From the previous trick we use, we could modify the Hamiltonian to:

$$\begin{aligned} H_{eff} &= \mu_B g_{//} B_z S_z + A_{//} S_z I_z + A_{\perp}(S_x I_x + S_y I_y) + P_{//}[(F_z - S_z)^2 - \frac{1}{3} I(I+1)] \\ &= \mu_B g_{//} B_z S_z + A_{\perp} S \cdot I + (A_{//} - A_{\perp}) S_z I_z + P_{//}[F_z^2 - 2F_z S_z + S_z^2 - \frac{1}{3} I(I+1)] \\ &= \mu_B g_{//} B_z S_z + A_{\perp} \frac{F^2 - I^2 - S^2}{2} + (A_{//} - A_{\perp})(S_z F_z - \frac{1}{4}) \\ &+ P_{//}[F_z^2 - 2F_z S_z + \frac{1}{4} - \frac{1}{3} I(I+1)]. \end{aligned} \tag{A.13}$$

Again, we would see the energy levels are still degenerate about $\pm m_F$ states, since flipping F_z would also flip S_z. However, still this type of understanding is intuitive, since S_z, I_z, F_z, F are not good quantum numbers together. The better way is still to diagonalize the 16 by 16 matrix here and see the energy levels:

$$\begin{aligned} E = &-\frac{1}{4} A_{//} + P_{//}(m_F^2 + \frac{1}{4} - \frac{1}{3} I(I+1)) \\ &\pm \frac{1}{2}[(\mu_B g_{//} B_z + (A_{//} - 2P_{//}) m_F)^2 + A_{\perp}^2 (I(I+1) + \frac{1}{4} - m_F^2)]^{\frac{1}{2}}. \end{aligned} \tag{A.14}$$

The ZEFOZ states are still preserved:

$$E_{m_F=0} = -\frac{1}{4} A_{//} - 5P_{//} \pm \frac{1}{2}[(\mu_B g_{//} B_z)^2 + 16 A_{\perp}^2]^{\frac{1}{2}}. \tag{A.15}$$

Another special pair of linear states are also preserved:

$$E_{m_F=\pm 4} = \frac{7}{4} A_{//} \pm \frac{1}{2} \mu_B g_{//} B_z. \tag{A.16}$$

We see the effect of this nuclear electric quadrupole term are just changing the initial splitting energy slightly. Now we fully study the Hamiltonian, let us see ^{167}Er:YVO$_4$ cases.

A.5 ^{167}Er:YVO$_4$ hyperfine structures for different crystal levels

Z1 levels

First looking at Z1 spin is because we have all the parameters for Z1 from Ranon's paper [111]. Plug in all the parameters and use the eigen energy we derived before, we have the energy levels as shown in Fig. A.4.

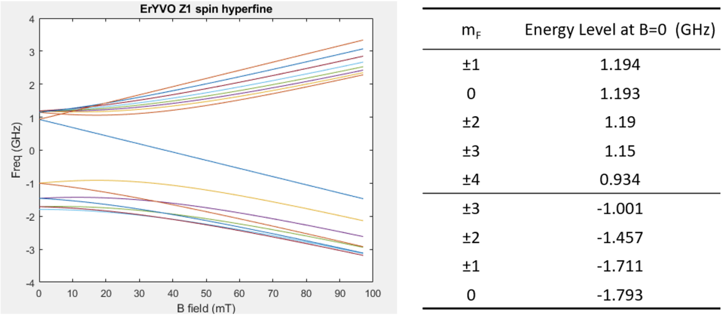

m_F	Energy Level at B=0 (GHz)
±1	1.194
0	1.193
±2	1.19
±3	1.15
±4	0.934
±3	-1.001
±2	-1.457
±1	-1.711
0	-1.793

Figure A.4: ^{167}**Er:YVO$_4$ Z1 hyperfine levels with B field along c-axis.** Left: a full evolution to ~ 100mT. Right: The energy levels at zero field.

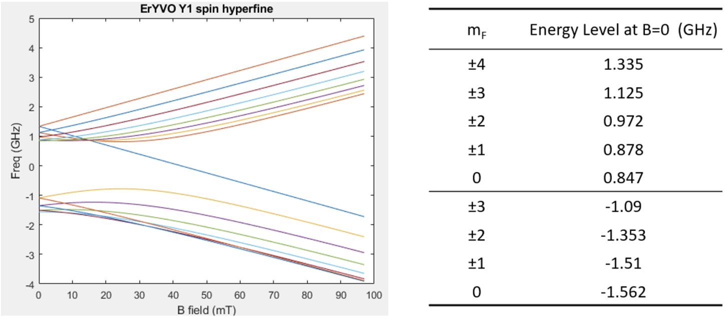

m_F	Energy Level at B=0 (GHz)
±4	1.335
±3	1.125
±2	0.972
±1	0.878
0	0.847
±3	-1.09
±2	-1.353
±1	-1.51
0	-1.562

Figure A.5: ^{167}**Er:YVO$_4$ Y1 hyperfine levels with B field along c-axis.** Left: a full evolution to ~ 100mT. Right: The energy levels at zero field.

We clearly see two ZEFOZ states and two special linear states on the right figure. The ZEFOZ states are pretty near to the other states. Due to the nuclear electric quadrupole term, the $m_F = \pm 1$ states are lifted and therefore slightly higher than the ZEFOZ state by ~ 1 MHz. This makes the Z1 spin hyperfine system hard to use, since the ZEFOZ state spin transitions ($\Delta m_F = 0$) are near to the $\Delta m_F = \pm 1$ transitions by only 1MHz. The next nearest $\Delta m_F = 0$ transitions are between $\Delta m_F = \pm 1$, which is 80MHz away. One idea would be let $B_{ac}//c$, therefore we are only access to the $\Delta m_F = 0$ transitions, and the next transition is 80MHz away.

Y1 levels

The Y1 hyperfine levels are shown in Fig. A.5. Again, we clearly see two ZEFOZ states and two special linear states on the right figure. We see in the Y1 case, the zero field structures are again being lifted by the nuclear electric quadrupole interaction. The ZEFOZ transition between $m_F = 0$ states are ~30MHz away from $\Delta m_F = \pm 1$ transitions and also another $\Delta m_F = 0$ transition.

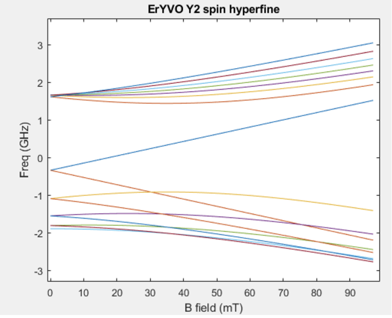

m_F	Energy Level at B=0 (GHz)
0	1.6621
±1	1.6616
±2	1.653
±3	1.611
±4	-0.343
±3	-1.097
±2	-1.555
±1	-1.813
0	-1.897

Figure A.6: **^{167}Er:YVO$_4$ Y2 hyperfine levels with B field along c-axis.** Left: a full evolution to ~ 100mT. Right: The energy levels at zero field.

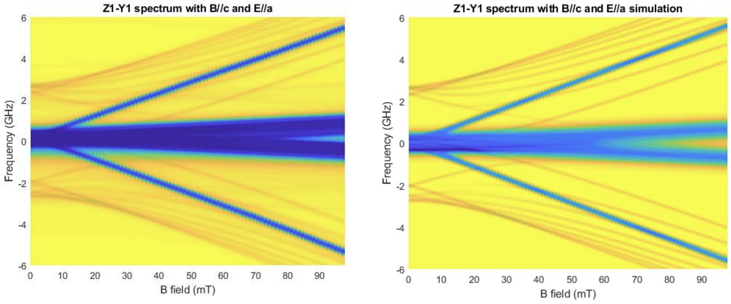

Figure A.7: **^{167}Er:YVO$_4$ Z1-Y1 optical transmission spectroscopic data.** Left: The experimental data with B//c. Right: The simulation.

Y2 levels

The Y2 hyperfine levels are shown in Fig. A.6. We see in the Y2 case, the 'F' = 4 and 'F' = 3 are flipped, since we use $A_{Y_2,//} < 0$;. The ZEFOZ transition between $m_F = 0$ states are less than 1MHz away from $\Delta m_F = 1$ transitions and ~ 80MHz away from another $m_F = 0$ transition.

A.6 Optical spectroscopic data of the hyperfine transitions

We perform a high-resolution optical spectroscopy through the sample. An external magnetic field along c-axis is scanned. The Z1 to Y1 spectrm is shown in Fig. A.7. We could fit to the Z1-Y1 experimental data and learn Y1 hyperfine parameters, where we get $A_{Z1,\perp}$ = 746.8 MHz, $A_{Z1,//}$ = 367.6 MHz, $A_{Y1,\perp}$ = 603.2 MHz, $A_{Y1,//}$ = 596.8 MHz, $P_{Z1,//}$ = 41.7 MHz, $P_{Y1,//}$ = 41.7 MHz, $g_{Z1,//}$= 3.544 and $g_{Y1,//}$= 4.51. We notice the simulation captures the main structures pretty well. The transition linewidth and strength are set manually with Gaussian distribution. The transition strength operator in the code is using σ_x for the hyperfine transitions.

The Z1 to Y2 spectrm is shown in Fig. A.8. We could fit to the Z1-Y2 experimental

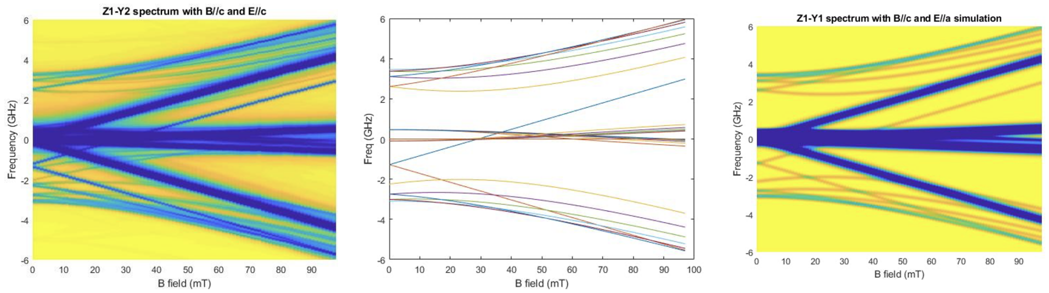

Figure A.8: ^{167}**Er:YVO$_4$ Z1-Y2 optical transmission spectroscopic data.** Left: The experimental data with B//c. Middle: Simulations of the transitions for $\Delta m_F = 0$ Left: The simulation.

data and learn Y2 hyperfine parameters, where we get $A_{Z1,\perp}$ = 746.8 MHz, $A_{Z1,//}$ = 367.6 MHz, $A_{Y2,\perp}$ = 890.4 MHz, $A_{Y2,//}$ = -362.8 MHz, $P_{Z1,//}$ = 41.7 MHz, $P_{Y2,//}$ = 41.7 MHz, $g_{Z1,//}$= 3.544 and $g_{Y2,//}$= -2.74.

Appendix B

NIOBIUM SPUTTER OPERATIONS

Here I will write down the detailed steps to operate the niobium sputter that is maintained by ourselves, as shown in Fig. B.1.

First, the metal mounting piece should be cleaned if there are too much visible dirt on it. One could use solvent and sonication to clean the piece. Next, the chip for sputtering needs to be well-cleaned, following the standard cleaning recipe – Acetone, IPA, DI water with sonication. Inside the sputter room, here is the sequence for using the sputter. Valve numbers are shown in Fig. B.2.
1. Open the control knob for N2 and air on the wall. Open two cooling water knobs near the gas controls.
2. To load the sample, Open v3 and v4. Put the sample holder in and make sure it is flat. Close v3, v4. open the load lock pump and v2; when the pressure is ~ 6e-5 on the pump, close v2, Load lock pump.
On the gauge, pressure IG measures the pressure inside the deposition chamber down to 1e-10. Pressure A measures the pressure inside the deposition chamber down to 1e-4. Pressure B measures the pressure on the load lock
3. To transfer the sample, open v5, and make sure the plate inside the chamber is at 290 degrees. Move the handle on the transfer arm to the 1st marker line on the left and rotate (clockwise if looking from the left of the sputter to the right) by 90 degrees and move the transfer arm back to the end, rotate back. Close v5. Switch the pressure to MV (before opening Ar).
4. Open the Ar gas bottle and the second on/off valve on the gas control panel.
5. Rotate the sample plate to 200 degrees (the chip will be facing us now so no deposition); open the Ar flow rate monitor, and the power supply power (switch on the left back, then turn the key to lock, click output to off, ‘actual’ button is to change the reading), the Ar knob on the back of the sputter, the growth monitor power.
6. Then we can rotate v6 to make the gauge A pressure ~3.5e-3 Torr. This pressure needs to be calibrated every few months to make sure the sputtered film has little stress.
7. After ~ 5mins when the pressure is stabilized, turn on the high-voltage output.
8. Wait until the power supply output is counting to 5mins, start the growth monitor (open), rotate the sample to 20 degrees (facing the target so starts sputtering), and

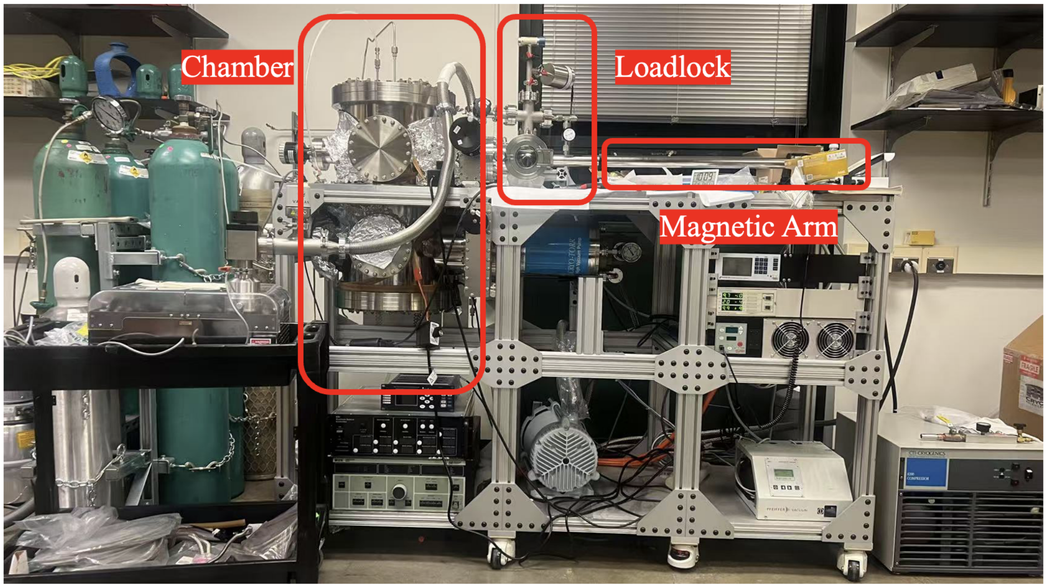

Figure B.1: **Overview of the niobium sputter.** A full picture of the niobium sputter setup.

open the deposition shutter.

9. Then we can see the growth, we want 1.5kA. When it is about the number we want (0.03kA away from the desired thickness), close the deposition shutter, rotate the sample back to 290 degrees, close the power supply output, and close the Ar knob on the back of the sputter.

10. Fully open v6 to let the pressure pump down

11. To transfer the sample out, make sure the sample plate is at 290 degrees. Open v5 and move the handle on the transfer arm to the 2nd marked line on the left, rotate 90 degrees (clockwise if looking from the left of the sputter to the right), push the arm to the 1st marked line, then rotate back and move the transfer arm back to the end. Close v5. Switch to ‘UHV’

12. Close v2 and the load lock pump. Open v3 and v4 to take the sample out

13. Click degas on the pressure panel and clear the growth monitor

14. Put the sample holder back. Close v3 and v4. Open v2 and the load lock pump. When the pressure is on the pump is ~ 6e-5, close v2 and the pump. Close everything at the end: Ar gas bottle and on/off valve on the control panel, the Ar flow rate monitor, the power supply, the growth monitor, the N2 and air valve, and two cooling water valves.

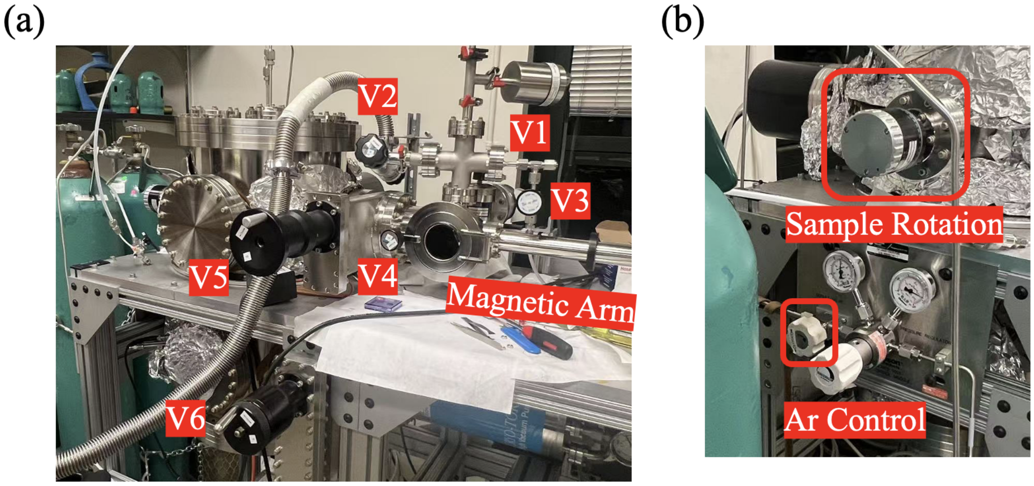

Figure B.2: **Valves labeling of the niobium sputter.** (a) The valves related to control the sampling loading and chamber operation. (b) The Ar control and sample rotation knob.